SORPTION BEHAVIOR OF SELECTED RADIONUCLIDES ON NATURAL CLAY MINERALS

By

PARVEEN KUMAR VERMA

CHEM01201304005

Bhabha Atomic Research Centre, Mumbai

A Thesis submitted to the

Board of Studies in Chemical Sciences

In partial fulfillment of requirements

for the Degree of

DOCTOR OF PHILOSOPHY

of

HOMI BHABHA NATIONAL INSTITUTE

October 2018

Homi Bhabha National Institute[1]

Recommendations of the Viva Voce Committee

As members of the Viva Voce Committee, we certify that we have read the dissertation prepared by Shri Parveen Kumar Verma entitled **"Sorption behavior of selected radionuclides on natural clay minerals"** and recommend that it may be accepted as fulfilling the thesis requirement for the award of Degree of Doctor of Philosophy.

Chairman - Prof. S. Kannan		**Date:** 1.10.18
Guide / Convener – Prof. P. K. Mohapatra		**Date:** 1.10.18
Examiner – Prof. Radha Tomar		**Date:**
Member 1- Prof. C.P. Kaushik		**Date:** 1/10/18
Member 2- Prof. G.G. Pandit		**Date:** 1/10/2018
Member 3- Dr. P.S. Dhami		**Date:** 1/10/2018

Final approval and acceptance of this thesis is contingent upon the candidate's submission of the final copies of the thesis to HBNI.

I/We hereby certify that I/we have read this thesis prepared under my/our direction and recommend that it may be accepted as fulfilling the thesis requirement.

Date: 26/10/2018

Place: Mumbai

26.10.2018

Signature

Guide

STATEMENT BY AUTHOR

This dissertation has been submitted in partial fulfillment of requirements for an advanced degree at Homi Bhabha National Institute (HBNI) and is deposited in the Library to be made available to borrowers under rules of the HBNI.

Brief quotations from this dissertation are allowable without special permission, provided that accurate acknowledgment of the source is made. Requests for permission for extended quotation from or reproduction of this manuscript in whole or in part may be granted by the Competent Authority of HBNI when in his or her judgment the proposed use of the material is in the interests of scholarship. In all other instances, however, permission must be obtained from the author.

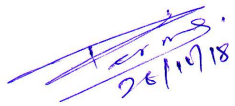

(Parveen Kumar Verma)

DECLARATION

I, hereby declare that the investigation presented in the thesis has been carried out by me. The work is original and has not been submitted earlier as a whole or in part for a degree/diploma at this or any other Institution / University.

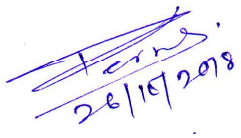

(Parveen Kumar Verma)

List of Publications arising from the thesis

Journal: Published (07)

1. Cs^+ sorption onto Kutch clays: Influence of competing ions A.S. Semenkova, M.V. Evsiunina, **P. K. Verma**, P.K. Mohapatra, V.G. Petrov, I.F. Seregina, M.A. Bolshov, V.V. Krupskaya, A.Y. Romanchuk, and S.N. Kalmykov, Applied Clay Science, 166, 2018, 88-93.
2. Np(V) uptake by various clays. A. S. Semenkova, A. Yu Romanchuk, Victoria V. Krupskaya, B.V. Pokidko, O. V. Dorzhieva, A. V. Sobolev, I. A. Presnyakov, **P. K. Verma**, P. K. Mohapatra, S. N. Kalmykov, *Applied Geochemistry,* **2018**, 92, 1-8.
3. Np(V) uptake by bentonite clay: Effect of accessory Fe oxides/hydroxides on sorption and speciation**. P. K. Verma,** A.Yu. Romanchuk, I. E. Vlasova, V. V. Krupskaya, S. V. Zakusin, A. V. Sobolev, A.V. Egorov, P.K. Mohapatra, S. N. Kalmykov; *Applied Geochemistry,* **2017**, *78*, 74-82.
4. Effect of different complexing ligands on europium uptake from the aqueous phase by kaolinite: Batch sorption and fluorescence studies; **P. K. Verma**, P.K.Mohapatra; *RSC Adv*., **2016**, *6*, 84464-84471.
5. Spectroscopic investigations onto sorption of uranium on suspended bentonite: effects of pH, ionic strength and complexing anions. **P. K. Verma**, P. N. Pathak, M.Mohapatra, A. K. Yadav, S. N. Jha, D. Bhattacharyya, and P. K. Mohapatra, *Radiochim. Acta,* **2015**, *103(4)*: 293–303.
6. Sorption of metal cations on suspended bentonite: effects of pH, ionic strength and complexing anions. **P. K. Verma**, P. N. Pathak, P. K. Mohapatra, *Radiochim. Acta,* **2014**, *102(5)*: 401–409.
7. Influences of different environmental parameters on the sorption of trivalent metal ions on bentonite: batch sorption, fluorescence, EXAFS and EPR studies. **P. K. Verma**, P. N. Pathak, P. K. Mohapatra, S. V. Godbole, R. M. Kadam, A. A. Veligzhanin, Y. V. Zubavichus and S. N. Kalmykov. *Environ. Sci.: Processes Impacts*, **2014**, *16*, 904–915.

Communicated / under preparation

1. Structural investigation of Europium complex on kaolinite-humic acid/citric acid binary system: fluorescence and EXAFS studies.
2. Eu (III) sorption onto different clays: effect of interlayer cation and form of clay.

Conferences (06)

1. Structural investigation of Europium Complex at kaolinite-humic acid/citric acid binary system: fluorescence and EXAFS studies; O-23, in SESTEC-2018, May 23-26, 2018, BITS Pilani, K.K. Birla Goa campus, Goa, India
2. Neptunium uptake studies onto bentonite of different origin: from characterization to thermodynamic modeling, ***P.K.Verma***, A.Yu. Romanchuk, I.E. Vlasova, V.V. Krupskaya, V.G. Petrov, S.N. Kalmykov, P.K. Mohapatra, OP-28, TIE-27,p.149 in SESTEC-2016, May 17-20, 2016, IIT Guwahati, Guwahati.
3. Luminescence Studies on the Sorption and Speciation of Europium onto Kaolinite in the presence of Humic Acid; ***P.K. Verma***, M. Mohapatra, P. K. Mohapatra, in MIGRATION-2015.
4. Spectroscopic investigations on the sorption of uranium onto suspended bentonite. ***P.K. Verma***, P.N. Pathak, M. Mohapatra, P.K. Mohapatra, SS-1, p.242 in SESTEC-2014, February 25-28, 2014, TSH, Anushaktinagar, Mumbai.
5. Sorption behavior of Eu(III) on bentonite: Batch Studies and Modeling, ***P.K. Verma***, P.N. Pathak, P.K. Mohapatra, in NUCAR -2013, February 19 –23, 2013, Jabalpur, M.P.
6. Time-Resolved Fluorescence Investigations on the complexation of Eu(III) with citric acid, ***P.K. Verma***, P.N. Pathak, P.K. Mohapatra, S.V. Godbole, in NUCAR -2013, February 19 –23, 2013, Jabalpur, M.P.

26/10/2018

(Parveen Kumar Verma)

Dedicated to My Family

ACKNOWLEDGMENTS

This dissertation would not have been accomplished without the support and encouragement of numerous people including my well-wishers, friends, and colleagues who contributed in many ways to the successful completion of this Thesis. Firstly, I would like to express my sincere gratitude to ***late Dr. P.N. Pathak***, who has introduced me to the subject of "actinide speciation". I would like to express my sincere gratitude to my research guide ***Prof. P.K Mohapatra*** for his continuous support, patience, motivation, and enthusiasm. His encouragement, knowledge, and experience helped me a lot during the course of my Ph.D. work. Besides my advisor, I would like to thank ***Prof. B.S. Tomar (Ex-chairmen, doctoral committee)***, ***Prof. S. Kannan (chairmen, doctoral committee***) and other members of my doctoral committee**;** ***Prof. C.P. Kaushik, Prof G.G Pandit*** and ***Dr. P.S. Dhami*** for their time, encouragement, thoughtful ideas and critical evaluation during the course of my Ph.D.

I am very thankful to ***Prof. P.K. Pujari***, Associate Director, Isotope (RC & I) group and Head, Radiochemistry Division, B.A.R.C., Mumbai for his interest, continuous support and motivation, which helped me a lot during the course of my Ph.D. work.

My sincere thanks to ***my lab mates*** for all their precious help, valuable discussions, and cooperation. I am heartily thankful to my collaborators from other labs and divisions for their help, cooperation and suggestions during the course of the work. I would also like to thank my colleagues ***Dr. M. S. Murali, Dr. A. Bhattacharyya, Dr. S. Ansari, Shri D. R. Prabhu, Dr. D. Raut, Dr. B. Mahanty, Dr. R.B. Gujar, Shri A.S. Kanekar*** and my seniors ***Dr. (Mrs.) Neelam, Dr. Ajay B. Patil, Dr. Pankaj Kandwal*** with **all other members of RCD** for their help, encouragement, and support during the course of my research work.

I would like to thanks, our collaborators at **MSU, Moscow, Russia,** especially ***Dr. A. Yu Romanchuk*** and ***Prof S.N. Kalmykov*** for their valuable suggestions, scientific discussions and cooperation. I would like to express my sincere gratitude to my other lab mates at ***MSU, Moscow, Russia.***

I am blessed to have friends who are a constant source of laughter, joy, and support. I would like to thank all my dear friends who always stood by me and lend constant encouragement and support. I would also like to thank all ***my training school batch mates*** for their warm friendship and support. I would like to acknowledge my ***teachers*** since my childhood; I would not have been here without their guidance, blessings, and support. Finally, I would like to acknowledge the people who mean the world to me, ***my family***. I would like to thank ***my parents*** for their unconditional love, support, faith, encouragement and confidence in me. They have been my driving force and inspiration in all pursuits of my life. I owe all my accomplishments to them. My ***brother (Rajesh Kumar Verma)*** has been a constant source of love and confidence and his belief and hope helped in overcoming all the hurdles of my life. I would like to express my gratitude towards my wife ***Sonam Verma*** who always stood by me and encouraged me up at every step of life, without her love and understanding I would not have been able to make it.

I would like to thanks ***DST (India)*** and ***RFBR (Russia)*** for providing me the opportunity to work under the Indo-Russian Joint collaborative project. This helped me a lot to build my knowledge and understanding of the subject.

Lastly, I would like to thank everybody who was important in the successful realization of this thesis, as well as apologizes that I could not mention everyone personally.

CONTENTS

SYNOPSIS

The distribution of radionuclides in the near-surface environment, aquifers etc. from nuclear weapons testing or from accidental events, such as Fukushima (2011), Chernobyl (1986), etc. is of potential concern for humanity for now and will be of great concern in the future as well [1]. Although scientific understanding and efforts are being made in this direction to understand the associated radiation risks on global scale, the assessment of radiation doses that the populace might receive, either by exposure from radionuclides in ecosphere or by internal ingestion (*via* food), requires a good understanding of the long-term behavior of radionuclides in the environment [1]. This knowledge forms the basis for the prevention goals of radiation protection. The other source of radioactive contaminants is from the deep repository sites used for long-term disposal of high-level radioactive waste (HLW) generated inform fuel cycle activities. The possibility of radioactive release from accidental events (e.g. Fukushima, Chernobyl, etc.) can be minimized by best of engineered safety measures applied at the nuclear facilities. On the other hand, the safety of a repository site used for HLW burial in vitrified glass blocks is related to its capacity to confine radioactivity and isolate it from the biosphere. The evaluation of the mobility of radionuclides in groundwater condition, in contact with the deep geological repository, requires the understanding of aqueous chemistry, geochemistry, and hydrology of both the radionuclides and the material used for the engineered barrier system (EBS) in deep geological repositories [1]. There is a need, therefore, to experimentally determine the sorption coefficients and retardation factors of different radionuclides on various clays under the different chemical condition and finally to model the generated data to understand the factors controlling the mobility of the given radionuclides under a given set of chemical/physical conditions. The influence of the specific conditions prevailing at a repository site must also be taken into account while estimating the radionuclide mobility from a repository. The origin of the clay minerals and the chemical treatment it undergoes has a significant influence on their surface properties. These

differences can alter the sorption behavior of the radionuclide onto these minerals. Bentonite, a 2:1 aluminosilicate, was found to be a promising candidate as the backfill material in EBS due to its favorable chemical and physical properties under deep geological repository conditions. Bentonites are known to have efficient radionuclide retention capacity, low hydraulic conductivity, high cation exchange, and adsorption capacities, very low anion diffusion capacity and low transport capacity of positively charged radionuclides, good swelling capacity, etc. [2]. The interactions between the radionuclide and bentonite decide its final fate in the geosphere. In this context, it is necessary to understand different aspects of radionuclide sorption reactions onto bentonite such as the kinetics, thermodynamics, sorption mechanisms (e.g., ion exchange, surface complexation/precipitation) of actinides to model the contribution of these reactions to the sorption in natural environments. This requires a proper understanding of the sorbed species on natural minerals. Various spectroscopic techniques, e.g., EXAFS (Extended X-ray Absorption Fine Structure), EPR (Electron Paramagnetic Resonance) and TRLFS (Time-Resolved Laser Fluorescence Spectroscopy) have been used to obtain information on the nature of the sorbed species. TRLFS is a useful means of identifying sorbed species onto clay minerals during different chemical processes. Different excitation and emission spectra of a luminescent metal ion (viz. Eu(III)) and its decay lifetimes can be used to differentiate between the chemical species in the aqueous phase and those present at the mineral water interface.

The natural soil contains a variety of natural organic matter (NOM) such as fulvic and humic acid (HA) in very low concentrations along with other organic acids such as citric acid (cit), oxalic acid (OA), and inorganic complexing anions *i.e.* sulphate (SO_4^{2-}), phosphate (PO_4^{2-}), carbonate (CO_3^{2-}), etc due to natural and anthropogenic activities [1,3]. The complexation of radionuclides with these organic/inorganic anions distributed in soil and natural waters system plays an important role in the determination of the metal ion toxicity, bioavailability and its transport of in the biosphere [1]. A large volume of R&D

work is ongoing to understand the sorption, migration and speciation behavior of different radionuclides of several contaminated sites, such as the Hanford Site, Nevada Test Site, Savannah River Site, etc [1]. The sorption reactions at the clay surface play an important role in the immobilization/retention of radionuclides. The majority of the literature on surface complexation modeling (SCM) describes the adsorption of metal ions (M^{n+}) by different pure or synthetic mineral phases under well-defined conditions [4-6]. The complexity of natural soil systems makes it very difficult to apply the concept of any SCM to soil and/or natural sediments. To simulate sorption onto well-characterized natural samples, two basic modeling approaches were proposed: (*i*) the component additivity approach and (*ii*) the generalized composite approach. The component additivity approach is based on summing the sorption of individual components in the complex mixture [7]. To simplify the model, it is important to determine the mineral components that dominate sorption. However, the identification of mineral components that dominate sorption in natural sediments is a challenging task. Even if quantitative and/or qualitative data analysis was performed, further understanding of the combined behavior towards radionuclide sorption under the given physical or chemical conditions is quite complicated. Furthermore, the components can be distributed quite unevenly. For example, iron oxide/hydroxide minerals may coat clay minerals which can influence the sorption process [7-9].For Radionuclides such as Eu(III) and Np(V) sorption has been previously studied onto pure or pre-treated clay minerals but their sorption onto natural raw bentonite clays (without treatment) are still scarce or lacking.

In the present thesis work, natural bentonites of different origins and kaolinite (commercial) were thoroughly characterized by host of physical techniques such as X-ray Fluorescence (XRF), X-ray diffraction (XRD), Fourier Transform Infrared (FTIR), BET (surface area), High Resolution Transmission Electron Microscopy (HR-TEM), Scanning Electron Microscopy (SEM), Mössbauer spectroscopy, etc. The nature of iron phases in natural bentonite and its relative content was determined, wherever possible, using

Mössbauer spectroscopy. Sorption of actinides (Am(III), Np(V), U(VI)) or their homologs *i.e.* Eu(III)) and fission product ions viz. Cs(I) and Sr(II) onto bentonite of different origin, the chemical form has been investigated using batch sorption, thermodynamic modeling, and spectroscopic studies. The natural bentonite of different origins showed interesting profiles for Np(V) and Eu(III) sorption and the results are compared with different forms of bentonite and with other class of clay minerals (*i.e.* kaolinite). Attempts are made to identify the phases in the composite natural bentonite responsible for Np(V) and Eu(III) sorption using SCM and by independent experiments. Different ionic forms of bentonite were used to understand the effect of interlayer cation on Np(V) and Eu(III) sorption. The effects of different chemical conditions such as pH, ionic strength, surface coverage, presence of inorganic/organic complexants, etc on the sorption of Eu(III) and U(VI) onto bentonite and kaolinite (for Eu(III) only) have also been investigated Spectroscopic techniques such as UV-vis, TRFS and EXAFS revealed the speciation of U(VI)/Eu(III) at the clay surfaces in the presence and absence of the complexing agents. The dissertation has been divided into six Chapters and a brief description of each Chapter is given as follows.

CHAPTER 1: INTRODUCTION

In this Chapter, the various pathways and mechanisms of radioactivity release into the environment are discussed. An overview of the interface between nuclear fuel cycle and environment are given starting from 'front end' process of nuclear fuel cycle *i.e.* uranium mining to 'back-end' process of HLW disposal in deep geological repositories. The major nuclear accidents and their impact on the environment are mentioned in brief. The worldwide efforts on the management of land contaminated by nuclear legacy waste such as Rocky Flat and geological disposal of HLW are highlighted. The possible interaction of released radionuclides with clay/oxide surfaces are discussed in brief and the techniques to understand the interaction mechanism are listed. The process and environmental factors such as the presence of complexing agents in soil that can affect the radionuclide migration are

discussed. The difficulties and challenges of working with natural clay systems are also presented. The mechanistic approach for surface complexation modeling (SCM) and a short account of different approaches used for SCM (*i.e.* component additivity and generalized composite) are given. Finally, the literature on the understanding of the sorption and speciation of radionuclides onto mineral water interface are given along with the motivation for the present dissertation.

CHAPTER 2: EXPERIMENTAL

The outline of various experimental procedures and instrumentation are discussed in this Chapter. The reagents used, their source and purities are given. The concentration and the preparation of stock solutions of various reagents and the metal ions are also given in this Chapter. The basic principles of radiation detectors are briefly discussed and the methods used for the radiometric assay of radionuclides such as ^{241}Am, ^{237,239}Np, ^{233}U, ^{152,154}Eu, ^{137}Cs, ^{90}Sr, etc are discussed to ascertain their radiochemical purities. The clay preparation (different ionic forms, iron deficient clays, etc.) and their characterization by various physical techniques such as XRF, XRD, FTIR, BET (surface area), HR-TEM, SEM, Mössbauer spectroscopy are also discussed along with their instrumentation. Methods for achieving different chemical condition such as varying pH, ionic strength, complexing agents, surface coverage etc. are also discussed. The basics of SCM and various approaches are given.

The evolution of Chapter is as follows; brief detail of the methods used for the characterization of different clays and HA used in the experiments, description of various radionuclides and fission products, their sources, concentration, purities and assaying methods. For redox active radionuclides such as Np(V), the methods (*i.e*. solvent extraction, UV-vis or Eh-pH (Pourbaix diagram) for ascertaining the particular oxidation state are discussed. Procedures of the batch sorption experiments, % sorption calculation with the development of surface complexation modeling to model the sorption data are addressed. The

various techniques for surface speciation (EXAFS, TRLFS etc.) are also discussed with emphasis on their nature and local coordination of the formed surface complexes.

CHAPTER 3: CHARACTERIZATION OF CLAYS OF DIFFERENT ORIGIN

This Chapter lists out the results of various techniques (such as XRD, FTIR, XRF, HR-TEM, etc) used to get an idea about the elemental composition, phases, Fe(II)/Fe(III) speciation, size and structural distribution of clay minerals, which is a must to begin as these factors influence the interaction between the actinides and the clay minerals. The XRD pattern and FTIR data of commercial bentonite show the predominance of montmorillonite and quartz. The measured zeta potential of bentonite suspension showed negative values from pH ~ 2 to ~ 9 and no isoelectric point (pH at which zeta potential is zero) was observed. Similar titrations performed on HA samples showed two pk_a values suggesting the presence of carboxylic and phenolic moieties in HA. For kaolinite, the well-resolved and sharp peaks in the XRD pattern with four well-resolved peaks at 3695, 3669, 3650 and 3619 cm^{-1} and two peaks at 937 cm^{-1} and 912 cm^{-1} in FTIR suggests the ordered nature of the sample. The specific surface area (in m^2/g) was found to be 23.04 and 38.04 for kaolinite and bentonite respectively, from BET measurements. The bentonite clays of natural origin *i.e.* those originating from Kutch, Rajasthan, Khakassia are enriched with smectite (montmorillonite), with some admixture of other clay minerals (*i.e.* chlorite, kaolinite), as well as carbonates, quartz, different iron oxides/hydroxides and other minerals in relatively small amounts. Na-form and Ca-form of clay were identified and estimated due to the different position of the (001) reflection. The presence of iron oxide/hydroxide nanoparticles was confirmed by HR-TEM. The specific surface area determination shows a higher value for Kutch bentonite (150 m^2/g) followed by Rajasthan bentonite (50 m^2/g) and lowest for Khakassia bentonite (15 m^2/g), from BET measurements.

CHAPTER 4: SORPTION AND MODELING STUDIES ON COMMERCIAL CLAYS

In this Chapter, the results of sorption and speciation of actinides and fission products onto clays (bentonite and kaolinite) of commercial origin are discussed. Batch sorption studies are carried out to understand the interaction of different metal cations such as U(VI), Am(III), Eu(III), Sr(II), and Cs(I) with bentonite clay with varying pH in the range, 2–9. The effects of other experimental parameters such as ionic strength (0.01–1 M $NaClO_4$), clay to metal ion concentration ratio and the presence of complexing agents on Eu(III) and U(VI) sorption have also been investigated. The sorption of the metal ions follows the trend, Am(III) ~ Eu(III) > Cs(I) > Sr(II). The higher sorption of Cs(I) compared to Sr(II) may be due to its lower hydration and affinity towards interlayer space. The sorption of Eu(III) and U(VI) has been found to be invariant with the change in the ionic strength of the medium, suggesting inner sphere complexation on the bentonite surface. Near quantitative sorption of Eu(III), /Am(III) has been observed in the entire pH range and with the marginal influence of the presence of OA and CO_3^{2-} on the sorption profiles. However, the presence of EDTA suppresses the sorption of Eu(III) ion onto the bentonite possibly due to non-interacting anionic species. Surface complexation modeling shows the predominant formation of Eu(III) complexes with silanol sites up to pH < 7 beyond which aluminol sites play an important role for Eu(III) sorption. The U(VI) sorption increased with increasing pH up to pH 6 beyond which a decrease was seen, which could be attributed due to the formation of anionic uranium-carbonate species. The U(VI)-bentonite suspension in the presence/absence of different complexing ligands shows bi-exponential luminescence decay profiles. The luminescence quenching for the U(VI) is seen with carbonate, citrate (cit) and for surface sorbed U(VI). EXAFS studies are also carried out to understand the local coordination of Eu(III) and U(VI) sorbed onto bentonite under different experimental conditions. Eu(III) sorption and speciation have been studied on a kaolinite–water interface in the presence of

different complexing ligands, such as OA, cit, and HA. Eu(III) sorption follows anion-exchange (outer-sphere) mechanism up to pH~6 beyond which, surface complexation (inner-sphere) is predominantly responsible for the Eu(III) sorption. The addition of complexing ligands modifies the sorption profiles. Fluorescence studies have shown that the nature of the Eu(III) complexes formed onto the kaolinite surface is different in the presence of different complexing agents.

CHAPTER 5: SORPTION AND MODELING STUDIES ON NATURAL CLAYS

The results of sorption and speciation of actinides (*i.e.*, Np(V) and Eu(III) (surrogate for Am(III)) onto clays of natural origin (mainly the bentonite clay) were discussed and compared with the bentonites of different ionic forms and clays of different class (*i.e.*, 1:1 and 1:2). The batch sorption studies on thoroughly characterized bentonite of different natural origins (Kutch, Rajasthan (India), Khakassia(Russia), FEBEX (Spain)) and thermodynamic modeling of sorption data are carried out to understand the role of iron-containing accessory phases/minerals on the sorption of Np(V) and Eu(III) onto these clays. The initial sorption studies suggested that Np(V) sorption follows an inner-sphere complexation mechanism whereas for Eu(III) its outer-sphere complexation at lower pH followed by inner sphere at higher pH for all the studied clays. The % sorption of Np(V) was found to be different onto the bentonites of different origin. The SCM using component additivity approach (with available surface complexation data from literature) revealed the dominant role of the Fe-phases (*i.e.*, goethite) accessory phase, which is present as nanoparticles, in Np(V) sorption at trace concentrations of Np(V) (~10^{-14} M). This is also supported by the combination of α-track radiography with SEM-EDX using ^{237}Np(V) sorbed onto the bentonites of different origin. The role of iron-containing phase for Np(V) sorption is also proven independently by carrying out Np(V) sorption studies with clays before and after removal of the iron phase. The effect of interlayer cation was also investigated and the data was modeled using the component additivity approach of SCM. The effect of interlayer cation onto Np(V) sorption

is also discussed. The Eu(III) sorption has also been carried out to illustrate the important role that accessory minerals can play in Eu(III) sorption. The % sorption of Eu (III) has been found to be similar (except Kutch clay) on clays of different origin at 10^{-11} M but are found to be different at 10^{-6} M Eu(III). Thermodynamic modeling has been done to further support the observations.

CHAPTER 6: SUMMARY AND CONCLUSIONS

This is the final Chapter and summarises the work carried out as part of this thesis. In brief, the sorption and speciation of actinides (^{241}Am, ^{237,239}Np, and ^{233}U) and fission products (^{152,154}Eu, ^{137}Cs, and ^{90}Sr) are discussed on to the bentonites of commercial and natural origin. The effect of different complexing agents and other chemical conditions are addressed with respect to Eu(III) and U(VI) sorption onto different clays. The Np(V) sorption onto natural bentonite of different origins is discussed and the role of the accessory Fe-phase present in natural bentonites towards Np(V) has been highlighted. The results of SCM are supported with other independent experimental methods, to validate the role of Fe-phases towards Np(V) sorption. The effect of the ionic form of bentonite towards Np(V) sorption is discussed. Eu(III) sorption results onto bentonites of different origin and onto kaolinite are discussed. Role of different complexing agents towards Eu(III) sorption onto kaolinite and bentonite has also been discussed.

As can be seen in this dissertation, characterization of clays of natural origin is a challenging task, but once done, can help one to predict the sorption of the given radionuclide (*i.e.*, Np(V) in the present case) using component additivity approach of SCM. The present dissertation highlight that the accessory phase, even in minor concentrations, can play a decisive role towards the sorption of particular actinides (*i.e.*, Fe-phase for Np(V) sorption in the present case).

REFERENCES

1. R.E. Hester and R.M. Harrison, Issue 32 (Environ. Sci. Technol.), Nuclear Power and Environment, RSC publishing, 2011.
2. C. Steefel, J. Rutqvist, C. F. Tsang, H.H. Liu, E. Sonnenthal, J. Houseworth and J. Birkholzer, Reactive transport and coupled THM processes in engineering barrier systems (EBS), LBNL Report, 2010.
3. F.J. Stevenson, Humus Chemistry, genesis, Composition, Reactions, A Wiley-Inter science publication, 1982.
4. W. Stumm, J. J. Morgan, Aquatic Chemistry, Third Edition, A Wiley-Inter science publication, 1996.
5. W. Stumm, Chemistry of the solid water Interface, A Wiley- Inter-science publication, 1992.
6. H. Geckeis, J. Lützenkirchen, R. Polly, Th. Rabung, M. Schmidt, Chem. Reviews, (2013) 113, 1016-1062.
7. J.A. Davis, J.A. Coston, D.B. Kent, C.C. Fuller, Environ. Sci. Technol. (1998) 32, 2820-2828.
8. W. Dong, T. K. Tokunaga, J. A. Davis, J. Wan; Environ. Sci. Technol., (2012) 46 (3), 1565–1571.
9. W. Dong, J. Wan; Environ. Sci. Technol., (2014) 48 (12), 6569–6577.

LIST OF ABBREVIATIONS

Alpha Hydroxy Isobutyric Acid	HIBA
Brunauer- Emmett- Teller	BET
Cation Exchange Capacity	CEC
Citric Acid	cit
Component Additivity	CA
Constant Capacitance Model	CCM
Diffuse Layer Model	DLM
Distribution Coefficient	KD
Electron Paramagnetic Resonance	EPR
Energy Dispersive X-Ray Spectroscopy	EDX
Engineered Barrier System	EBS
Extended X-Ray Absorption Fine Structure	EXAFS
Fission Products	FP
Fluorescence Studies	FS
Fulvic Acid	FA
Generalised Composite Approach	GCA
High-Level Waste	HLW
High Purity Germanium Detector	HPGe
High Resolution-Transmission Electron Microscopy	HR-TEM
Humic Acid	HA
Humic Substances	HS
Inductively Coupled Plasma-Atomic Emission Spectroscopy	ICP-AES
Intermediate Level Waste	ILW
Liquid Scintillation Counting	LSC

Low-Level Waste	LLW
Multi Channel Analyzer	MCA
Natural Organic Matters	NOM
Neel Temperature	TN
Nonelectrostatic Model	NEM
Nuclear Energy Agency	NEA
Nuclear Magnetic Resonance	NMR
Oxalic Acid	OA
Photo Multiplier Tube	PMT
Point of Zero Charge	PZC
Scanning Electron Microscopy	SEM
Selective Area Electron Diffraction	SAED
Surface Complexation Modeling	SCM
Time-Resolved Fluorescence Spectroscopy	TRFS
Time-Resolved Laser Induced Fluorescence Spectroscopy	TRLFS
Ultraviolet Visible	UV-vis
X-Ray Absorption Fine Structure Spectroscopy	XAES
X-Ray Absorption Near Edge Spectroscopy	XANES
X-Ray Diffraction	XRD
X-Ray Photoelectron Spectroscopy	XPS

LIST OF FIGURES

CHAPTER 3

CHAPTER 5

LIST OF TABLES

1

GENERAL INTRODUCTION

The wide distribution of radionuclide contaminants in the near-surface environment, aquifers, geosphere etc. aroused from nuclear weapons testing or from accidental events, such as Fukushima (2011), Chernobyl (1986), etc. is of potential concern for humanity for now and will be of great concern in the future as well [1-8]. Although scientific understanding and efforts are being made to evaluate the associated radiation risks and its consequences on global scale, the assessment of radiation doses that the populace might receive in long-term, either by exposure from these radionuclides in ecosphere or by internal ingestion (*via* food), requires a thorough understanding of the long-term behavior of these radionuclides in the environment. This knowledge forms the basis for the prevention goals to be adopted for radiation protection. The overall scheme of electricity generation from nuclear fuel involves several processes which have direct or indirect interference with the environment [9].

The difference in processes and their interference with environment gives varieties of wastes starting from uranium and its decay products in the tailings arising from mining and processing of uranium ore, to a range of nuclear wastes of varying chemical /physical composition and associated radio activities (**Fig 1.1**). Most of the actinides isotopes are α-active with long half-lives ($t_{1/2}$) and are both radio and chemo-toxic in nature. They can enter into the food chain through numerous pathways and their presence, even in very small amounts, can cause serious health hazards [10]. The nuclear weapon tests in the past have

produced global fallouts detectable in different parts of the world. The use of nuclear power in energy production creates long-lived actinides which might be released into the ecosystem during the various nuclear fuel cycle-related activities (**Fig. 1.1**). For example, uranium is extracted from crushed ores by acid or alkali leaching and then further purified using solvent extraction and ion exchange processes. The tailings arising from these processes contain most of the decay product radionuclides (Radium (Ra) and below). Some of the common problems associated with the tailings are Radon emanation, leaching of contaminants including radionuclides, heavy metals into groundwater. These contaminants primarily affect the aquifers bodies, air, and soil quality and later on directly or indirectly affect the human

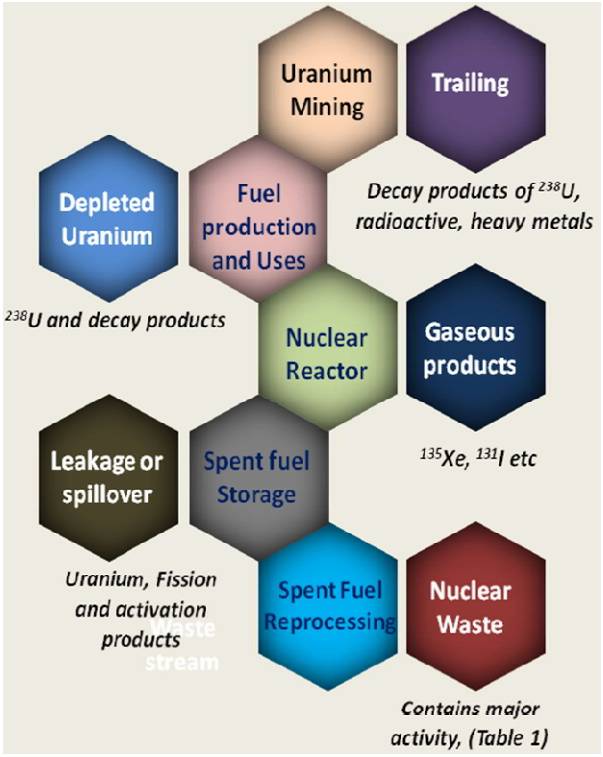

Fig. 1.1. Different stages in the nuclear fuel cycle and its associated waste.

population nearby [11]. Other processes such as uranium enrichment; fuel fabrication, etc are associated with their own waste streams and require safe management. However, the major sources of radioactive wastes are found in the back end of the nuclear fuel cycle. The consequences of the accidents such as Chernobyl in the former Soviet Union and more recent

one at Fukushima Daiichi in Japan renewed the interest in understanding the transport behavior of radionuclides in the environment and their associated hazards.

1.1. NUCLEAR ENERGY

To meet the growing demand for energy, we need reliable, affordable and clean electricity. To achieve this, nuclear energy capacity must expand and the goal of supplying 25% of the electricity in 2050 through the construction of 1000 GW of new nuclear capacity was set

Table 1.1. List of long-lived fission products and transuranics in High-level Waste

Nuclide	Half-life d:day,y: year	Decay mode	Nuclide	Half-life d:day,y: year	Decay mode
Fission products			**Fission products**		
^{99}Tc	2.1 x 10^5 y	β	^{154}Eu	8.8 y	γ
^{90}Sr-^{90}Y	28.5 y	β	^{106}Ru-^{106}Rh	368 d	γ
^{93}Zr	1.5 x 10^6 y	β	^{125}Sb	2.77 y	γ
^{107}Pb	6.5 x 10^6 y	β	**Transuranics**		
^{135}Cs	2 x 10^6 y	β	^{237}Np	2.14 x 10^6 y	α
^{147}Pm	2.62 y	β	^{238}Pu	87.74 y	α
^{151}Sm	93 y	β	^{239}Pu	2.41 x 10^4 y	α
^{155}Eu	4.96 y	β, γ	^{240}Pu	6.5 x 10^3 y	α
^{129}I	1.57 x 10^7y	β, γ	^{241}Pu	14.4 y	β
^{134}Cs	2.06 y	β, γ	^{241}Am	4.32 x 10^2 y	α
^{137}Cs	30.17 y	β, γ	^{243}Am	7.3 x 10^3 y	α
^{144}Ce-^{144}Pr	284 d	β, γ	^{244}Cm	18.11 y	α
^{152}Eu	13.33 y	γ	^{245}Cm	8.5 x 10^3 y	α

[12]. The global electricity demand is rising very fast and the requirements will get doubled by 2050. To avoid dangerous levels of climate change, we require at least 80% of electricity to be generated from non-fossil fuel or from low-carbon sources viz. nuclear, wind, hydro, solar etc., which is only ~34% today. At present, the nuclear energy is used by ~30 countries

and supplies only ~11% of global electricity consumption. The nuclear energy is generated by neutron-induced fission of ^{235}U, ^{233}U, and ^{239}Pu to sustain chain reaction [13]. Due to this neutron-induced fission of fissile elements such as ^{235}U, ^{233}U, ^{239}Pu, etc. an enormous amount

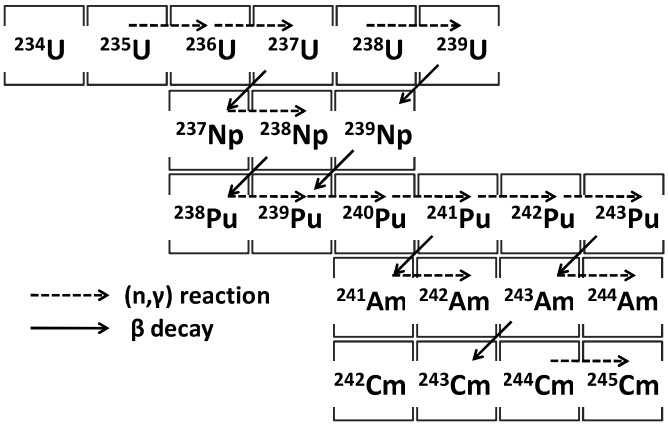

Fig. 1.2. Scheme for the production of transuranic in the uranium-fuelled nuclear reactor by (n, γ) reaction followed by β decay.

of energy (200 Mev) is released with the simultaneous generation of various fission products (most of which are highly radioactive) (**Table 1.1**). Thus, the benefit of nuclear energy production comes with the inevitable hazards of long-lived radionuclides. Long-lived α-emitting actinides such as ^{241}Am, ^{243}Am, ^{245}Cm, and ^{237}Np are also produced as activation products and are present in significant quantities in nuclear waste (**Fig. 1.2**). Due to their long half-life, there is a long-term radiological risk to the environment from these radionuclides. The sustainable development of nuclear energy program for future applications largely depends on the safe management of the radioactive nuclear waste. The source and composition of radioactive waste generated at various stages of the nuclear fuel cycle were discussed below.

1.1.1. Nuclear Fuel Cycle

The steps involved in the life of the fissile element such as ^{233}U, starting from milling mining to radioactive waste management are referred, collectively, to as the nuclear fuel cycle. The

nuclear fuel cycle is broadly classified into two parts, viz. the front end and the back end of the nuclear fuel cycle. The front end of the nuclear fuel cycle starts with the mining of the uranium ore, milling, conversion, enrichment, fuel fabrication, reactor operation, etc. whereas the back end of nuclear fuel cycle starts after the removal of the spent fuel from the reactor, its temporary storage, and finally its reprocessing to recover the valuables, and treatment and subsequent disposal of the radioactive waste [14-17]. At each stage of the nuclear fuel cycle, radioactivity can be released into the environment (**Fig.1.1**).

1.1.2. Waste from the "Front End"

In general, uranium mining is done in open or in an underground facility. Most of the available ores are lean sources of uranium (0.1 to 0.2% of uranium) suggesting large quantities of ore have to be mined to get sufficient natural uranium for fuel fabrication. The waste pile rock after mining releases radon gas continuously due to the decay of long-lived ^{226}Ra and the radioactivity can be released into the environment even after shut down of the mine due to the seepage of water. The ores obtained from the uranium mines are subjected to various chemical processes to get uranium in the form of yellow cake (U_3O_8) leaving behind a large inventory of liquid waste tailings with small amounts of un-extracted uranium and other decay products of uranium. These tailings emit γ-radiations >20 times of the natural background levels. The decay of ^{226}Ra to the radioactive gas ^{222}Rn is another major concern for the uranium tailings even after shut down of the mill. The tailing piles are also subjected to seepage and/or erosion in long-term and can contaminate the ground and surface water. The conversion of yellow cake to the usable form of the fuel in reactors does not produce radioactive waste of much significance. A significant quantity of radioactive elements is produced during the burning of the fuel in the nuclear reactor. More than 99.9% radioactivity is retained in the uranium fuel rods after burn up and only 0.1% of the total radioactivity is distributed to other parts of the reactor.

1.1.3. Waste from the "Back End"

Majority of the radioactive wastes arise from various activities in the back end of the nuclear fuel cycle. The nuclear fuel bundles coming out from the nuclear reactor, after reaching the desired burn up , are referred to as the "spent fuel". In natural or enriched uranium-fuelled reactor, ^{235}U undergoes neutron-induced fission to produce various fission products which are radioactive in nature and are a major contributor of radiation dose in the waste. The transuranic elements such as Np, Pu, Am, and Cm are formed by successive neutron capture reactions involving ^{238}U have long half-lives and contribute significantly to the radiotoxicity of the nuclear waste. The spent fuel is usually allowed to cool for several years (cooling period) in the water pool to facilitate the decay of the short-lived fission products and other radionuclides and also to reduce the heat burden (due to the decay heat) prior to further processing. The timeline for the radionuclide decay with associated decay heat and radiotoxicity was shown in **Fig. 1.3.** In general, ^{137}Cs, ^{90}Sr, and ^{238}Pu are the dominant sources of both heat and radioactivity which last for several hundreds of years after that the major radioactivity contributors are ^{238}Pu, ^{239}Pu, ^{240}Pu, ^{241}Am, ^{151}Sm, ^{237}Np, ^{99}Tc, etc. The radionuclides of concern after 10^4 years are ^{239}Pu, ^{240}Pu, ^{243}Am, ^{99}Tc and ^{237}Np while the radioactivity present in the nuclear waste after 10^5 year is mainly due to some of the long-lived fission products (^{99}Tc, ^{135}Cs, ^{93}Zr, ^{129}I) and actinides ($^{234,235,238}U$, ^{242}Pu, ^{237}Np) activity with the combined activity of their decay products.

1.1.4. Types of Nuclear Fuel Cycle

The nuclear fuel cycle, based on the management of spent fuel, can be categorized into two types viz. open and closed fuel cycles. The open fuel cycle implies the disposal of highly active waste without any reprocessing whereas the closed fuel cycle generates a complex array of radioactive waste depending upon on schemes undertaken for nuclear fuel reprocessing. The closed nuclear fuel cycle offers an option for recovery of valuables from the high-level radioactive waste. The management and disposal of radioactive waste add to

other sources of radioactive contaminants in the geosphere. In a closed fuel cycle, the spent nuclear fuel is subjected to aqueous reprocessing (PUREX process) to recover the valuables such as Plutonium, useful fission products, and depleted uranium. The concentration of the aqueous PUREX raffinate (by vaporization followed by acid killing) results in the high-level

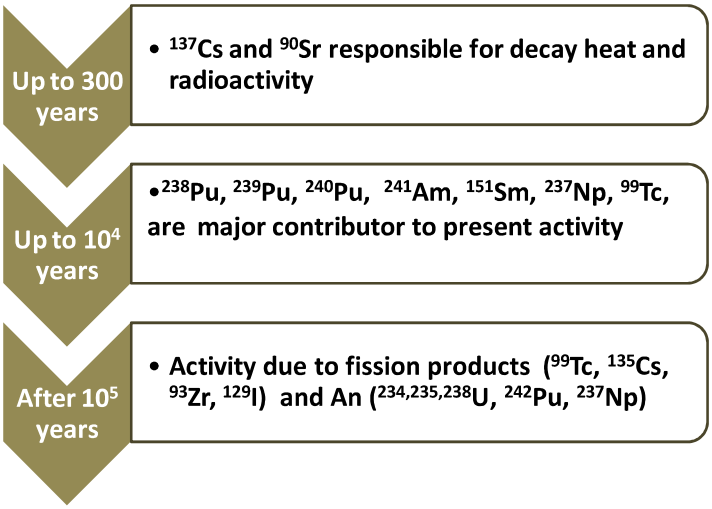

Fig. 1.3. Timeline for radioactivity remained in the nuclear waste from different radioactive elements present in the back end of the nuclear fuel cycle.

radioactive waste (HLW). The HLW contains small amount of unrecovered U and Pu during the PUREX process, minor actinides (*i.e.* Am, Cm, Np), fission and activation products along with the structural elements and process chemicals. The HLW is potentially hazardous for millions of years, due to the presence of long-lived minor actinides and other fission products in it.The safe disposal of the HLW is a challenging task in the back end of the nuclear fuel cycle. Apart from this, ion exchange resins, chemical sludge, reactor components, reprocessing equipments, etc. are other added sources of radioactive waste in the back end of the nuclear fuel cycle.

1.2. CATEGORIZATION OF NUCLEAR WASTE

Radioactive wastes can be broadly categorized into three categories, based on the radioactivity content in the waste, namely, low-level waste (LLW), intermediate level waste

(ILW) and high-level waste (HLW) **(Fig. 1.4)**. A very brief description of the different types of radioactive wastes is given in the following sections.

1.2.1. Low-Level Waste (LLW)

The nuclear waste with radioactivity of less than millicurie/ liter is called low-level waste (LLW). Some of the predominant sources of LLW are decontamination of equipments, radioactive laboratories, hospitals (using radiopharmaceuticals), various chemicals used in the nuclear fuel cycle, etc. The LLW contains small amounts of short-lived radionuclides and therefore, when stored for a sufficiently long time, most of the radioactive isotopes decay to their stable daughter products. It is less hazardous compared to other class of radioactive

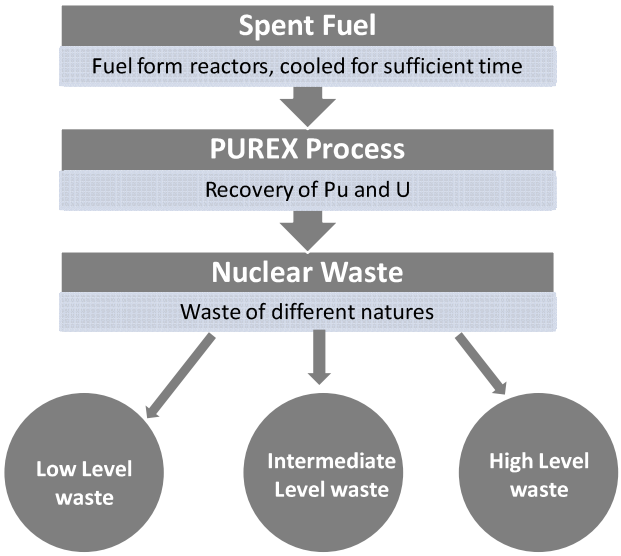

Fig. 1.4. Production of nuclear waste from the nuclear reactor and their categorization based on the radioactivity content.

wastes but must be disposed off carefully as compared to the normal industrial wastes. The LLW comprises of ~90% of the total volume of the radioactive wastes generated, but has < 1% radioactivity associated with it. In general, the solid LLWs are compressed or incinerated before their final burial in shallow landfill sites.

1.2.2. Intermediate Level Waste (ILW)

Intermediate level waste (ILW) requires more attention as compared to LLW but significantly less as compared to HLW (vide infra), as they have radioactivity in the range of millicurie/ liter (mCi/L) to curie/ liter (Ci/L) and may require special shielding. The ILW waste contains long-lived radionuclides in moderate to large quantities. Chemical sludge, resins, nuclear reactor parts, reprocessing equipment, contaminated equipment of weapon decommissioning are part of ILW. It comprises ~7% of the total volume of the radioactive waste with ~4% of the associated radioactivity. The ILW waste can be solidified in concrete matrices before final disposal.

1.2.3. High-Level Waste (HLW)

High-level waste (HLW) is defined to contain radioactivity >1 curie/ liter (Ci/L) of the waste. It makes up 3% of the total radioactive waste volume with >95% of the total radioactivity produced in nuclear fuel reprocessing. The HLW contains minor actinides (Am, Cm, Np), uranium, plutonium and fission products. The HLW generates considerable amounts of decay heat and requires interim cooling before its final disposal. It also requires special shielding during handling and transportation. The associated radioactivity of the HLW due to the presence of long-lived minor actinides possesses major challenges in its final disposal. Efforts are being made worldwide by scientists of various streams to meet the challenges in both, the development of suitable methods for separation of the minor actinides from HLW and its safe long term disposal.

1.3. CHEMISTRY OF LANTHANIDES AND ACTINIDES

The work carried out in this present dissertation pertains to the sorption and speciation of actinides/lanthanides and other fission products onto the mineral-water interface. To understand the subject of speciation which has a significant role in the sorption and migration of radionuclides it is essential to understand the chemistry or more specifically aqueous

chemistry of actinides and lanthanides. Hence, a brief survey of the solution chemistry of actinide/ lanthanide is of considerable relevance.

1.3.1. Solution Chemistry of Actinides/Lanthanides

Any chemical interaction of metal ion, M^{n+}, in the aqueous phase is governed by its speciation under given chemical/physical conditions. The actinides can exist in multiple oxidation states which give a challenging but interesting speciation of actinide in the aqueous media [18]. The trivalent oxidation state is the most stable oxidation state for lanthanides. However, this is not the case with actinides, at least in the case of the early members of the series. The 5*f* electrons of the actinides feel lesser attraction from the nuclear charge compared to the 4*f* electrons of the lanthanides. The higher stability of the tetra positive ions (M^{+4}) of the early actinide elements is mainly due to the smaller values of fourth ionization potential of the 5*f* electrons compared to those of 4*f* electrons in the lanthanides. Thus, Thorium (Th) exists in the aqueous phase only as Th(IV) while the trivalent oxidation state (M^{3+}) becomes prominent only for the transplutonium elements. All the oxidation states of actinides are well known except for the 7+ states for Np and Pu which exist in their alkaline solutions. The higher oxidation state of actinide ((M(V), M(VI)) ions exist in acidic solution as oxygenated cations, viz. MO_2^+ and MO_2^{2+} and known as actinyl ions. Actinides such as Plutonium are known to exist in various oxidation states simultaneously due to very close redox potential values of its different oxidation states. The M^{3+}/M^{4+} and MO_2^+/MO_2^{2+} couples are reversible, as these involve the transfer of single electron whereas, other couples, such as the M^{4+}/MO_2^+ couple, are irreversible and the equilibrium is attained slowly as they involve the formation or breaking of the metal oxygen bonds.

1.3.2. The Hydrolysis of Actinides

In view of the large ionic potentials (charge / ionic radius ratio) of actinides, the actinide ions in different oxidation states exist as strongly hydrated ions in aqueous media in the absence

of complexing anions. The actinide ions in trivalent and tetravalent oxidation states are present as M^{3+} and M^{4+}, respectively, whereas the penta and hexavalent oxidation states are highly prone to hydrolysis as compared to their lower oxidation states and exist as partially hydrolyzed oxo ionic species, viz. MO_2^+ and MO_2^{2+} with the further possibility of hydrolysis at higher pH values. The oxygen atoms at the axial positions of these actinyl ions are not basic in nature and hence, do not coordinate with protons. The effective charge on the actinyl ion is 2.3 ± 0.2 and 3.3 ± 0.1 in MO_2^+ and MO_2^{2+} moieties, respectively which is greater than the ionic charge on the entire molecular entity making the coordinating field in the case of molecular ion proportionately stronger. The degree of hydrolysis for the actinide ions decreases with the decrease in their effective charge, *i.e.*, $M^{4+} > MO_2^{2+} > M^{3+} > MO_2^+$, which has similarity with their complex formation properties [18]. The hydrolysis of the actinide ions can be represented by the following generic equation **1.1**,

$$M^{n+} + aH_2O \leftrightarrow M(H_2O)_a^{n+} \leftrightarrow M(OH)_a^{(n-a)+} + aH^+ \qquad \textbf{(1.1)}$$

The hydrolytic behavior of a particular oxidation state, within the actinide series, is different for different actinides; for example, Th(IV) is quite different from that of other tetravalent actinide ions i.e. Pu(IV) and U(IV). For U(IV) and Pu(IV), the hydrolysis starts with a simple monomeric reaction of the type given in **Eq. 1.1** followed by slow irreversible polymerization of the hydrolyzed products. For Th(IV), however, different polymeric species can exist even in very dilute solutions. The polymer formation of Pu(IV) is irreversible whereas for Th(IV) is reversible. The hydrolytic behavior of some of the trivalent actinides such as Cm(III), Cf(III) and Am(III) are well studied and shows higher hydrolysis constant values for the actinides when compared to their lanthanides analogs.

1.3.3. Complexation of Actinides

The actinide ions (An^{m+}) in the aqueous media exhibit a strong tendency to form complexes with different ligands. This property of the actinides is widely exploited in devising various

chemical methods for their separation and purification. One of the most important factors that control the strength of complex formation is the ionic potential (*vide supra*) of the metal ions of a given oxidation state. Higher ionic potential allows better electrostatic attraction between oppositely charges ionic species *i.e.* between cations and anions and hence can lead to the stronger complex formation (steric factors are assumed to be absent). The complexing strength of the actinide ions in different oxidation states is similar to their hydrolytic behavior, *i.e.* $M^{4+} > MO_2^{2+} > M^{3+} > MO_2^{+}$. For actinide ions of the same oxidation state, the complexing ability increases with their atomic number due to a decrease in their effective ionic size (actinide contraction) resulting in an increase in the ionic potential [19]. The above generalized approach may be valid in cases where the complexation is primarily ionic in nature. There are other complexation reactions where hybridization involving 5*f* orbitals, the steric effect of ligands and hydration of metal ions also affect the tendency of complexation. For simple inorganic or organic anionic ligands, the tendency of complex formation with a given actinide ion generally vary in the same manner as the ability of the ligands to bind with hydrogen ion [20]. For monovalent ligands, the complexing tendency decreases in the order: $F^- > CH_3COO^- > SCN^- > NO_3^- > Cl^- > Br^- > I^- > ClO_4^-$. The divalent anions form stronger complexes than the monovalent anions and their complexing ability decreases in the order: $CO_3^{2-} > SO_3^{2-} > C_2O_4^{2-} > SO_4^{2-}$. The complexation ability of some of the commonly used organic ligands with a tetravalent actinide ion, for example, Th(IV) varies as EDTA > Citrate > Oxalate > HIBA > Lactate > Acetate [21].

1.4 . IMPACT OF RADIONUCLIDES ON THE ENVIRONMENT

The potential impact of a given radionuclide on the environment is mainly influenced by several factors such as its quantity, chemical form, and nature of radiation and half-life of the radionuclide. Long-lived radionuclides pose more risk as they exist for a longer duration as compared to short-lived radionuclides. Radioactive elements, whether natural or anthropogenic, are potential sources of radiation exposure to the living population through

various pathways [21-25]. The mining and processing of uranium and thorium bearing ores give rise to the production of wastes which possess potential radiological hazards to the environment [11]. For example, mining of uranium ore leaves residues which contain a higher concentration of ^{226}Ra compared to that in the original ore and thus, presenting a source of radon contamination. In the event of a major accident or nuclear explosion, various radionuclides having very different chemical, physical and radiological characteristics are released into the environment. The potential impact of long-lived radionuclides, such as ^{137}Cs, ^{90}Sr and minor actinides on the environment can be seen for many years after these events. Other potential sources of radiation hazard arise from the processes adopted in the management of spent nuclear fuel in the back end of the nuclear fuel cycle. The raffinate emanating out of the PUREX process generally contain small amounts of un-extracted U, Pu along with a host of fission products such as ^{99}Tc, ^{107}Pd, ^{93}Zr, $^{135,137}Cs$, ^{90}Sr and minor actinides such as Am, Np, Cm with a large volume of lanthanide ions as well as activation products and is termed as high active waste which upon concentration is termed as the high level liquid waste (HLLW). Long-lived radionuclides including many minor actinides are of great environmental concern. Till now, the most accepted conceptual approach for HLLW management is to vitrify the radioactive waste oxide it in a glass matrix followed by its burial in a deep geological repository. Since the half-lives of the minor actinides concerned range between several hundred to millions of years, the surveillance of HLLW for such a long period is practically impossible from both economical as well as environmental safety point of view. Moreover, the possibility of decay heat and radiation damage of the vitrified mass of the HLW due to the beta/gamma emitting fission products such as ^{137}Cs and ^{90}Sr cannot be ruled out in the first 100-300 years. Therefore, it may create a possible risk of leaching from the vitrified mass and leads to migration of long-lived alpha-emitting minor actinides from the repository to the environment.

1.5. THE SOURCES OF RADIONUCLIDES IN THE ENVIRONMENT

The primary sources of the radionuclides in the environment are nuclear weapons testing and nuclear energy program-related activities over the past 70 years [10]. The other sources include the accidental or inadvertent release of radioactive materials from various nuclear facilities and medical centers using radioactive sources for societal benefit. The use of depleted uranium in weapons production also adds up as one more source of radionuclides in

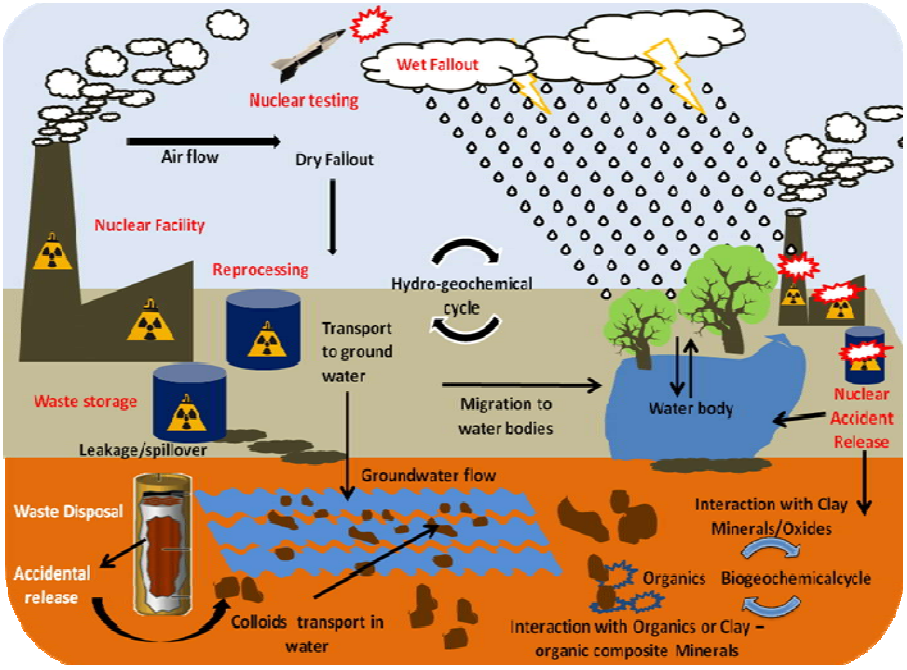

Fig. 1.5. The sources and possible ways of radionuclide's leaching and their interaction with the geo-sphere.

the environment [26-27]. The environmental pathways of some of the key processes controlling radionuclide transporting into the environment are depicted in **Fig. 1.5**. The radionuclide transport in the ecosystem is mainly controlled by the atmospheric or aquatic system, through a surface aquifer or terrestrial systems in groundwater. Although the nuclear weapons testing is one of the primary sources of low-level global radionuclide contaminant via the atmosphere, other sources of radionuclide can cause a high level of contamination at localized sites, and spreading of these contaminations can occur by aquatic pathways and

represent a potential media for uptake into the food chain. Such uptakes are a real concern for humanity over a long period of time. Various geochemical factors controlling the migration of radioactive contaminants into the atmospheres are discussed later in this Thesis. Some of the potential sources of radioactive contaminants are discussed as follows.

1.5.1. Nuclear Weapons

Nuclear weapons testing accounts for the major (>10^8 TBq) fraction of the total radioactivity released into the atmosphere [26-27]. Most of the released radionuclides are short-lived and decayed, hence, the radioactivity declined sharply from their peak in the 1960s. Further decay was very slow mainly due to the presence of long-lived ^{14}C ($t_{1/2}$: 5730 years) in the atmosphere. The dry or wet fallout from the atmospheric weapons testing also caused contamination of surface water and terrestrial environment. The fallout can be local, *i.e.* within a few 100 km from the test side; regional *i.e.* up to several thousand km from the test side; or global. The level of spread of these fallouts depends primarily on the altitude and latitude of the explosion site and its yield [26-28]. Though the activity from these fallouts was often found to be of low level and widely dispersed, a considerable level of activity was found at certain places. For example, in the USA alone there are over 70 million m^3 of contaminated land and over 1800 million m^3 of water at Department of energy facilities used for weapons productions [29]. At Mayak Production Association (Chelyabinsk, Russia) a significant level of Pu contamination exists at the sites and its nearby area used for weapons-grade Pu production and accidental discharge [30-32]. Around 10^5 TBq of radioactive contaminants were discharged as liquid waste into the Techa River between 1949 to1956. The major associated activities were $^{89\text{-}90}S$, ^{137}Cs, rare earth isotopes, and ^{95}Zr - ^{95}Nb and ruthenium isotopes [31-33]. The same site also has ~7.4 x 10^4 TBq activity released due to liquid waste tank explosion causing the contamination in the area of approximately 20 x 10^3 km^2 with a concentration of 4000 $Bq{\cdot}m^{-2}$ [30,34] Underground testing of weapons caused contamination of the subsurface geosphere due to ^3H, fission products and other actinides. At

Nevada Test site in the USA ~10^7 TBq of radioactivity was released into the subsurface during 828 tests. Some of the radionuclides of concern are ^{3}H, ^{137}Cs, ^{90}Sr, $^{239,241}Pu$, ^{85}Kr. $^{152,154}Eu$ and ^{151}Sm. The inventory changes with time as new isotopes will emerge as daughter products and others will decay. The remaining activity of the subsurface will be dominated by long-lived radionuclides such as U, Pu, Np and Am [35-37].

1.5.2. Nuclear Accidents

Accidental release of radioactive contaminants from nuclear facilities are localized sources of contamination and these sources are, in general, less significant contributors to the environmental radioactivity as the probability of such occurrences are low but if released can also lead to long-term effects onto the environment. Some of the largest releases from such events have been due to Kyshtym, Chernobyl and Fukushima. For example, the 1989 report of International Atomic Energy Agency (IAEA) suggests that the Kyshtym explosion results in ~74 TBq of beta and gamma emitting radionuclides (10% of total release) in the wider environment comprising mainly ^{95}Zr, ^{106}Ru, ^{106}Rh, ^{95}Nb, ^{144}Ce and ^{144}Pr, and ^{90}Sr. The area contaminated by ^{90}Sr was ~23000 km^2 with $3.7x10^3$ bq m^{-2} of ^{90}Sr contamination density [38]. At Chernobyl, ~1.76 x 10^{18} Bq of ^{131}I and ~80 $x10^3$ TBq of ^{137}Cs were released into the environment whereas, at the Fukushima-Daiichi reactor site accident in 2011, ~1.5 x 10^{17} TBq of ^{131}I and ~1.2 x 10^{16} Bq of ^{137}Cs were released into the local environment [39]. These nuclear accidents can be minimized by best of engineered safety measures used in the nuclear facilities and with better management to minimize the human error.

1.5.3. Nuclear Fuel Cycle

The nuclear fuel cycle is another major source of radioactive contaminants (in the form of radioactive wastes) leading to the environmental contaminations [29, 40]. By waste volume, the largest source is from Uranium mining and milling operations in front end of the nuclear fuel cycle (vide supra) [41]. These activities have produced ~937 x 10^6 m^3 of tailings, with

associated activities ranging from <1 to >100 Bq/g [41, 42]. The waste mainly contains uranium and its decay products, including the radioactive gas, radon (Rn) [42]. The radioactive waste arising from the nuclear reprocessing facilities causes high localized level of contamination. The leakage from the storage facility is also a contributor of radioactive contaminants to the environment [43-47]. For example at the Hanford site (USA), an estimated 570 m^3 of waste having ~3.7 x 10^4 TBq of activity has benne released into the subsurface from leaking underground tanks [29]. The radioactive contaminants released from the nuclear fuel cycle vary at every stage and need special attention and require specified waste treatment methodology before final disposal. The depleted uranium, by-product of fuel enrichment facilities, is another waste that has less activity but has associated health hazards due to both its radiological and chemical toxicities [48-49].

1.5.4. Naturally Occurring Radioactive Materials

Naturally occurring isotopes are present everywhere and serve a constants background of dose for humanity since the inception of the earth. The dose received can be either due to primordial (^{40}K, ^{238}U, ^{232}Th) sources or of cosmic origin (from cosmic ray) [27, 50]. The decay products of the primordial sources (^{238}U, ^{232}Th) can cause significant problems with respect to environmental contamination, but their concentration varies with the local geology [27, 51]. The migration and hence associated risk from these primordial sources can be significantly enhanced by industrial processes such as mining and milling for uranium or thorium [52, 53]. The processes such as the production of phosphate, oil production and combustion of coal also contribute to the radioactive contaminants in the environment [54, 55]. The radioactivity quantity in different types of coal ranges from 21-309 Bq/kg for ^{226}Ra; 12-435 Bq/kg for ^{238}U; 7.5-56 Bq/kg for ^{232}Th and 6-398 Bq/kg for ^{40}K [55, 56]. The release of naturally occurring radioactive isotopes from these industrial activities is a relatively minor source of contamination compared to other sources.

1.6. ENVIRONMENTAL BEHAVIOR OF RADIOACTIVE CONTAMINANTS

The waste arising from a different source varies in their physical and chemical forms and also with respect to their associated radioactivity. The waste contains a range of radioactive isotopes with a range of half-life from several days to millions of years. The chemistry of different radioactive elements differs and hence, the remediation strategies. The radioactive contaminants with long life, higher quantity, high activity, and easy bioavailability are of great concern to the environment. **Table 1.2** lists some of the key environmental contaminants with their major decay modes and half lives. Most of the contaminants listed in the table are present in the significant quantities due to the sources discussed earlier. For example, ^{60}Co is used in medial and other industrial processes requiring radiation source while ^{238}U and ^{222}Rn are naturally occurring and so on. The bioavailability some of these radionuclides are of concern as it is the major pathway to be a part of the food chain and hence, can directly affect the population. ^{222}Rn exists as a gas and can be inhaled and is the second leading cause of pulmonary cancer in USA [57]. $^{90}Sr(II)$ resembles the chemical properties of Ca(II) and can be accumulated in the bones. $^{137}Cs(I)$ resembles K^+ and can be transported into the living cells by K^+ transport channels. The ^{99}Tc and ^{129}I (as part of T3 or T4 hormone) can be accumulated in the Thyroid gland [58, 59]. The fate of these radionuclides in the environment depends on several factors but the oxidation states of the radionuclides play a significant role. Chemical properties, such as complexation and hydrolysis, bioavailability, and transport of the radionuclides depend on its oxidation properties, particularly for redox active elements such as Pu and Np. The existence of actinides in multiple oxidation states (**Table 1.2**) complicates its chemical behaviors in the aqueous media. Uranium generally exists as uranyl ion (UO_2^{2+}) in the +VI oxidation state but U(IV) is also stable under reducing conditions [60]. The most stable and dominant oxidation state for Neptunium is +V (as NpO_2^+) though other oxidation states are also possible. For plutonium, +IV is the most stable one but as in the case of uranium and neptunium, the other

oxidation states can also prevail depending upon the local chemical environments. The higher oxidation states of actinides (An(V, VI)) tend to be more aqueous soluble and are more mobile in the environment, whereas the actinides in the tetravalent (An(IV)) state are more prone to hydrolysis and polymerization reactions due to higher ionic potential [18, 22-25].

Table 1.2: Some of the key radio-contaminants to the environment

Radionuclide	Prevailing Oxidation state	Half-life	Major decay mode
Fission Products			
^{99}Tc	+IV, +VII	2.15x10^5 y	β
^{90}Sr	+II	29.1 d	β
^{137}Cs	+I	30.17 d	γ
^{129}I	+I, 0, +V	1.57x10^7 y	β,γ
Actinides			
^{238}U	+III, +IV, +V, +VI	4.47x10^9 y	α
^{238}Pu	+III, +IV, +V, +VI, +VII	87.7y	α
^{239}Pu	+III, +IV, +V, +VI, +VII	2.41x10^6 y	α
^{240}Pu	+III, +IV, +V, +VI, +VII	6.55x10^5 y	α
^{241}Pu	+III, +IV, +V, +VI, +VII	14.4 y	β
^{241}Am	+III, +IV, +V, +VI, +VII	432.7 y	α
^{237}Np	+III, +IV, +V, +VI, +VII	2.14x10^6 y	α
^{222}Rn	0	3.8 d	α
^{60}Co	+II, +III	5.27y	β,γ

Out of the fission products listed in **Table 1.2**, cesium (Cs) and strontium (Sr) show stable oxidation states of +I and +II, respectively but technetium and iodine are redox active. The stable oxidation states of the Cs and Sr make their chemistry unaffected by the nearby redox environment but are of potential concern due to their bioavailability [58-61]. Cs being in the

+I oxidation state interacts weakly with different ligands and tends to bond via electrostatic interactions rather than strong covalent bonding. Its high solubility makes it more mobile in the environment and interaction with the surface of the mineral may serve as a predominant mechanism for its retardation. Sr(II) also do not complex very strongly but can be precipitated with calcium sulfate and carbonate [61-63]. Technetium mainly exists as an anionic moiety (TcO_4^-) in the +VII oxidation state. The +IV oxidation state of Tc is possible under reducing conditions. TcO_4^- is soluble and mobile whereas Tc(IV) exists as insoluble TcO_2 [40]. Iodine (I) can exist in different oxidation states (*i.e.*, -I, 0, +V) in the environment [61]. In the aqueous environment, iodine exits mainly as IO_3^- and I^-, but in soil system, it can be present as organic species as well. The ^{60}Co chemistry is relatively simple with just +II and +III oxidation states. Co(II) is most stable and is more aqueous soluble then Co(III) and hence, is more important from the environmental point of view [64-65].

1.7. RADIONUCLIDE TRANSPORT IN ENVIRONMENT

1.7.1. In Atmosphere

The radionuclides can enter the ecosystem in various forms depending upon the origin of contaminant and the physical or chemical form of the radioisotope. The transport of suspended radionuclides is mainly governed by its size; larger size particle has more probability of settling down as compared to a particle of smaller diameter [10]. Once released into the environment the fate of the radionuclides depends on the prevailing near field meteorological conditions. For atmospheric releases due to nuclear weapons testing depends strongly on the height and yield of the explosion. The refractory radionuclides such as ^{95}Zr, Pu and ^{144}Ce are released in particulate form and hence, tend to deposit readily with less distribution than the volatile isotopes such as ^{137}Cs and ^{131}I [66-67]. The localized transport of radioactive contaminants occurs with the use of depleted uranium (DU) weapons and uranium mining. The mass (10% -35%) of the DU weapons convert into an aerosol (size <5μm) after hitting the target [11]. The distribution of DU aerosol was controlled by the

prevailing meteorological condition, with the risk of re-suspension into the atmosphere due to wind or anthropogenic activities [68-70].

1.7.2. In Aquatic System

The transport behavior of radionuclides depends on its aqueous speciation, which controls the solubility, bioavailability, and reactivity of given radioactive contaminants [19, 21-25]. The chemical speciation depends on various factors such as biogeochemical conditions, E_h, pH, the presence of complexants, natures of minerals systems present nearby and interplays

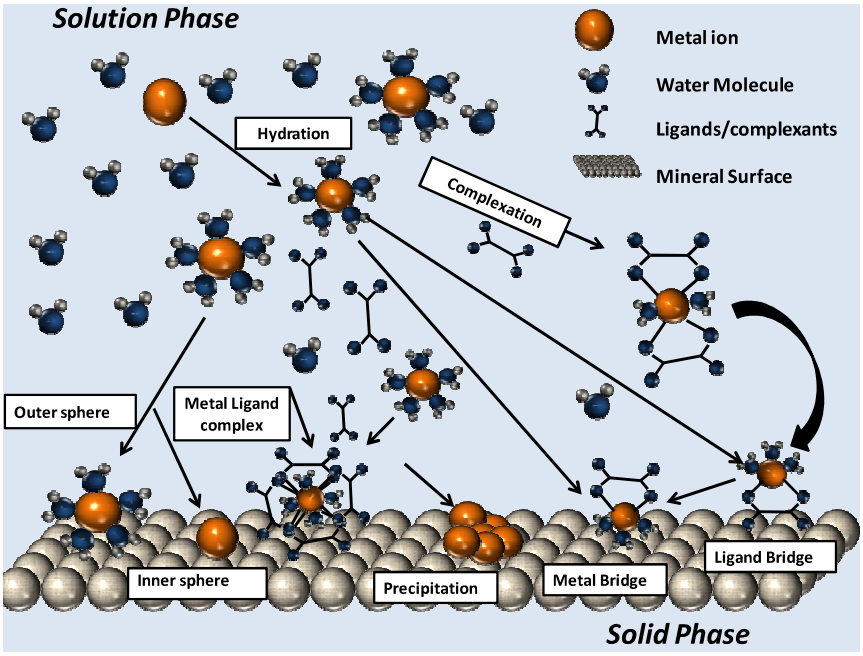

Fig. 1.6: Some of the key processes governing transport or retardation of the metal ion in the aquatic media.

between these factors [22-24, 71-72]. The various processes at minerals water interfaces were depicted in **Fig. 1.6**. Processes such as sorption, precipitation, or ion exchange with the interlayer the cation of minerals can retard the migration of radionuclides in the geosphere [71]. The water in the environment has varying biogeochemical cycles depending upon the nearby meteorological condition. It can be fresh water or saline, with neutral pH, low ionic strength, oxidizing conditions etc.

The water in certain regions can be rich in organic matters or other complexants due to decomposition of flora or fauna in its vicinity. The chemical condition of water affects the speciation of metal ions. For examples, the proposed conceptual management of HLW produced after the spent fuel reprocessing was its vitrification and storage in deep geological repositories. The safety of a deep geological repository site, to avoid radioactive contaminants, used for HLW burial in vitrified glass blocks is related to various long terms factors such as the behavior of buried radionuclides, including best of engineered barrier system (EBS) designed for its isolation. The performance of a deep geological repository can be decided by its capacity to confine radioactivity and isolate it from the biosphere for billions of years. The evaluation of the migration or mobility of radionuclides in groundwater conditions, in contact with the deep geological repository, requires the understanding of the aqueous chemistry, geochemistry, and hydrology of both the present radionuclides and the material used for the engineered barrier system (EBS) in deep geological repositories. There is a need, therefore, to experimentally determine the sorption coefficients/percentage sorption and retardation factors of different radionuclides on different clays under various chemical/physical conditions of water and finally to model the generated data with different theoretical approaches/models to understand the factors controlling the migration of the given radionuclides under a given sets of chemical/physical conditions. The influence of the specific conditions prevailing near the repository site must also be taken into consideration while estimating the radionuclide mobility from a repository site. The origin of the clay minerals and the chemical treatment it undergoes before it comes into contact with any radio-contaminant has a significant influence on their surface properties and hence, on its interaction with the radionuclides. These differences can alter the sorption behavior of a given radionuclide onto these clay minerals.

1.7.2.1. Clay Minerals

The interaction of radionuclide with the clay mineral can either enhance or retarded the mobility of the radionuclides in the aquatic medium.. The sorption property of the clay minerals is dependent on various factors such as its structure, interlayer cation and charge on its surface. A number of mechanisms can be responsible for actinide transport or retardation in the geosphere. The interaction mechanism of the metal ion, a radioactive contaminant in the present case, with the mineral surfaces can be of ion exchange, chemisorption or physisorption type. In the ion exchange process, the sorbing metal ions exchange with other similarly charged ions within the mineral structure or from the interlayer spacing. For example, Cs(I) undergo cation exchange reaction with mineral surfaces which is the key controlling factor retarding the Cs(I) transport in the aquifers [62]. The binding of the sorbing metal ion with covalent bonding to form the inner-sphere complex is termed as chemisorption reaction [63, 73]. The binding of the metal ion with the mineral surface occurs at specified sites and the strength of interaction depends on both, the chemical properties of the metal ion and the mineral surface properties. Uranyl ion (U(VI)) binds with goethite, hydrated ferric oxide and mica (muscovite, chlorite) surface through the formation of inner-sphere complexes [73-75]. The weak interaction by Van der Waal's forces termed as physisorption and the complex thus formed is called the outer-sphere complex [76]. This interaction is relatively weak and the desorption of the metal ion from the mineral surface by an alteration in geochemical properties is readily possible. Sr(II) interacts with many surfaces like ferrihydrite, bacteriogenic iron oxide, calcite and kaolinite in this manner [73,77-79].

The irregularities at the mineral surface serve more reactive sites for metal ion sorption, microbially dissolution and other processes at the mineral surface [73]. The steric environment of the surface site in combination with the chemical and physical nature of ligand/complexants present near the surface has a direct influence on the affinity of the surface site for a particular metal ion. For example, montmorillonite, vermiculite and

micaceous minerals like illite, biotite has a high affinity for Cs(I) on their edge and step sites [80-82]. Over the period of time, the Cs(I) ion can diffuse into the interlayer of the sheet silicates making the desorption process irreversible [83]. The sorption process is also dependent on the acidity and ionic strength of the solution. At higher acidities, the protonation of the mineral surfaces occur altering their overall charge and hence, can alter the mechanism and extent of interaction between the mineral surfaces and the sorbing mental ions [84]. In alkaline conditions, although the surface is preferentially negatively charged, the interaction of the metal ion with the hydroxide ions (OH^-) decreases the charge on the metal ions and hence, can reduce the sorption on the mineral surfaces. Higher ionic strength reduces the activity of the metal ion and also alters the effective charge onto the mineral surface, in both the cases decreasing the complexation of the metal ion with the surface of the mineral. The higher ionic strength can also cause desorption of the metal ions. Desorption of the metal ions is significant in seawater conditions due to higher pH and ionic strength of seawater. Out of various classes of clay minerals, the smectite group clay minerals, such as bentonite (a 2:1 aluminosilicate of smectite family) are considered as candidates for buffer material in deep geological repositories [85]. In general, it consists of a nanometer/micrometer scale of 2:1 clay minerals (mainly Montmorillonite) and micrometer scale of macro-grains (mainly quartz) [86]. The physical and chemical properties of bentonite are mainly characterized by its hydrated or water saturated forms. It is a dark-grey to brownish clay-rich mineral composite consists mainly of montmorillonite, with minor concentrations of cristobalite, zeolite, and quartz, among others. It has a 2:1 layered phyllosilicate (smectite) structure, in which one alumina octahedral sheet is sandwiched between two silica tetrahedral sheets. The layered structure expands in contact with water and both the interlayer sites as well as ionizable hydroxides surface sites are available for interaction with the metal cation sorption. Bentonite is known to have efficient radionuclide retention capacity, low hydraulic conductivity, high cation exchange, and adsorption capacities, low anion diffusion capacity,

low transport capacity of positively charged radionuclides with good swelling capacity, etc. Bentonite is very suitable for isolating radioactive waste canisters (having vitrified HLW) due to its very low anion diffusion capacity and low transport capacity of positively charged radionuclides [85-88]. Thus, it acts as a good buffer around the waste canisters. With its high swelling potential, it can help in self-sealing of openings within the EBS system and gaps between the bentonite with the nearby rocks and with radioactive waste canister. The thermal conductivity of bentonite is adequate to conduct heat away from the canister and helps in the cooling of the latter. Further, it has good colloid and microbial filtration capability. Initially, the bentonite (buffer material) installed around the waste canisters in a deep geological repository is partially saturated with water. Slowly the heat released from radioactive waste inside the canister enhances the temperature at the near-field of the bentonite-rock system due to the decay heat generated from the radionuclides. On the other hand, water is taken up from the rock-water interface at the outer part of the buffer system which leads to the swelling of the bentonite in the nearby region. In short, bentonite is known to be promising candidate as the backfill material for EBS of a deep geological repository due to its favorable chemical and physical properties under deep geological repository conditions and the knowledge of interaction of various radionuclides with this backfill material is necessary to assess the performance of any deep geological nuclear waste disposal site. Bentonite is considered as a good candidate for EBS in many countries. The interaction mechanism between the radionuclide and bentonite decide its final fate into the geosphere. In this context, it is necessary to understand various aspects of radionuclide sorption reactions onto bentonite such as kinetics, thermodynamics, sorption mechanisms (e.g., ion exchange, surface complexation/precipitation) of radionuclides to model the contribution of these reactions to the overall sorption process in the natural environmental conditions. This requires a proper understanding of the sorbed species, its nature, and form of complex, on the natural minerals. Various spectroscopic techniques, e.g., EPR (Electron Paramagnetic Resonance), EXAFS

(Extended X-ray Absorption Fine Structure), and TRLFS (Time-Resolved Laser Fluorescence Spectroscopy) have been used to obtain information about the nature of the sorbed species onto clay surfaces [84, 89-96]. TRLFS is a useful means of identifying sorbed species onto clay minerals under different chemical/physical conditions. The difference in the excitation/ emission spectra of a luminescent metal ion (such as Eu(III)) and its decay lifetime can be used to differentiate among the various chemical species present in the aqueous phase and those present in the mineral water interface [89-90,96]. Besides pure bentonite, once the EBS systems are left of billions of years, the local wear and tear in EBS system can cause intermix of more natural sediment/mineral with the buffer material and the complex interplay between different sorption processes may occur. The radionuclides can also leach to a sufficient distance to come to the regions where admixtures of bentonite with other soil component are prevailing. In the event of a nuclear accident, the released radionuclides can interact with very different kind of soil system with completely different flora and fauna existing in those regions. With the possibility of all these hypothetical scenarios and understanding of nuclear accidents and other testing facilities, the effect of another soil component with bentonite and other clays on sorption and speciation of radionuclides is of paramount importance. The natural soil contains a variety of natural organic matter (NOM) such as a fulvic acid (FA) and humic acid (HA) in very low concentrations along with other decomposition products of plant and animal remains in the soil [97-99]. The decomposition process and other anthropogenic activities also contribute of simple organic acids such as citric acid (cit), oxalic acid (OA), and inorganic complexing anions *i.e.* sulfate (SO_4^{2-}), phosphate (PO_4^{2-}), carbonate (CO_3^{2-}), etc in the geosphere. The complexation of a given radionuclide with these organic/inorganic anions distributed in soil and natural water systems plays an important role in the determination of its radiotoxicity, bioavailability and transport behavior in the biosphere [97-98].

1.7.2.2. The Natural Organic Matters (NOMs)

The sorption properties of the mineral surface can be modified by the coating of organics onto the mineral surface. These coatings can add to more sites for complexation but can also block the active sites available for sorption. The coating of in organics has also profound effects on the sorption properties of the mineral surface. For example, the alumina coating onto kaolinite, illite and montmorillonite surfaces enhances Sr(II) sorption compared to the respective uncoated mineral surfaces. A biological, as well as natural organic matter (NOM), coating also modifies the reactivity of the mineral surface. The coating by the NOM depends on the mineral surface, natures of the NOM, its quantity, etc. The content of NOM in the natural soils varies widely from one place to the other even can vary at the same place with time and other natural or anthropogenic activities. The complex nature of NOM and the amount present in the soil system depend on various factors such as time, flora and fauna, climate and topography of the nearby ecosystem [99]. Humic substances, one of the important NOM, represent a complex mixture of molecules with varying size, shape, and reactivity. Humic substances are in general composed of three different fractions. The solubility of these fractions with the pH is used to distinguish between them, the humin fraction is insoluble under all pH conditions, whereas humic acid (HA) are insoluble at or below pH 2 and fulvic acid (FA) is soluble under all pH conditions [99-101]. HA contains various types of carboxylic, phenolic, enolic and alcoholic groups with other aromatic and aliphatic moieties [99,102]. The characterization of HA with respect to different functional groups can be done by optical or FTIR spectroscopy. In general, the total acidity was determined by Baryta adsorption method. The estimation of various OH containing groups requires various chemical transformation reactions. Being a polyprotic acid, the potentiometric titrations were also used for pKa determination of HA. The interaction of these HA either with clay minerals or with radionuclides alters the sorption of speciation of radionuclides. These are the various possibilities in which the clay mineral - metal ion

systems behave in the presence of HA. Humic acid complexation is affected by the pH of the solution, as the deprotonation of the functional groups is possible with increasing pH leading to stronger complexation ability of the ligand. The strength of the humate complex also depends upon the oxidation state of the metal ion. The stability of the HA metal complex decreases in the order U(IV) > Th(IV) > Am(III) > Eu(III) > U(VI) > Co(II) > Sr(II) as a result of electrostatic interaction between the two [60,103]. For redox active actinides such as Np and Pu, the reduction of the metal ions (*i.e.*, Np(VI) to Np(IV) and Pu(VI) to Pu(IV)) in the presence of HA are also reported [104].

1.7.2.3. Inorganic Complexants

The redox, co-precipitation and complexation reactions with inorganic anions such as carbonates also alter the interaction of the metal ions with the mineral surface. The strength of inorganic ligands complexing to the actinides decrease in the order $CO_3^{2-} \geq OH^- > HPO_4^{3-} \geq F^- \geq SO_4^{2-} > NO_3^- \geq Cl^-$[105].The complexation also varies with the charge of the actinide ion similar to their hydrolytic behavior (vide supra). Carbonate (or bicarbonate) is the most important inorganic anion present in the natural system and its concentration ranges from 10^{-5} M in surface water to 10^{-2} M in groundwater [106]. They can form stable negative complexes with the actinides, which has a lower affinity for the mineral surface and remains in the aquatic media, therefore, can increase the mobility of the actinides [63,107-108]. For example, the uranyl ion (U(VI)) has a very high affinity for the carbonate ion and forms $UO_2(CO_3)_2^{2-}$ or $UO_2(CO_3)_3^{4-}$ complex as shown in the equation 1.2 and 1.3 [107-108].

$$UO_2^{2+}{}_{(aq)} + 2HCO_3^- \rightarrow UO_2(CO_3)_2^{2-}{}_{(aq)} + 2H+ \qquad \textbf{(1.2)}$$

$$UO_2^{2+}{}_{(aq)} + 2HCO_3^- \rightarrow UO_2(CO_3)_3^{4-}{}_{(aq)} + H+ \qquad \textbf{(1.3)}$$

The Eh-pH diagram of uranium in the presence of inorganic carbon is given in **Fig. 1.7**.

In the natural media water serves as a dominant transport medium and hence, knowledge of the predominant actinide oxidation states and actinide speciation under different water

condition are essential. Pourbaix diagrams (also known as Eh-pH diagram) serve as a useful tool for addressing the actinide ion speciation as a function of pH and electrochemical potential of the media [108]. The prerequisite for the Pourbaix diagrams in water media for any radionuclide is to define the chemical stability area of water. The potential at which oxygen generation starts on the anode is defined as the upper stability limit of water whereas the potential at which the hydrogen gas is evolved from the surface of an immersed electrode defines the lower stability limit of water media. The upper or oxidizing limit and lower or reducing limits are defined by equation 1.4 and 1.5 respectively.

$$\tfrac{1}{2}\, O_2 + 2H^+ + 2e^- \rightarrow H_2O \qquad \textbf{(1.4)}$$

$$H_2O + e^- \rightarrow \tfrac{1}{2}\, H_2 + OH^- \qquad \textbf{(1.5)}$$

By using the Nernst equation, the relationship between potential and pH and pE were derived (equation 1.6 and 1.7) for the boundary of water as systems

$$pE = 20.75 - pH \qquad \textbf{(1.6)}$$

$$pE = - pH \qquad \textbf{(1.7)}$$

The above two equations can be compared to equations of a straight line with pE at y-axis and pH as the x-axis and define the working limit in the aquatic media or the stability field for water. Thus, water as a medium offers its solutes only a small electro potential window of stability. Within the stability zone of the aquatic system, the distribution of oxidation states and speciation of a particular actinide can be obtained by considering all its complexation and redox and reactions. **Fig. 1.7** shows Eh-vs-pH diagram calculated for uranium in water containing hydroxide and carbonate under an atmospheric condition at 298 K. From the Eh-pH diagram, the

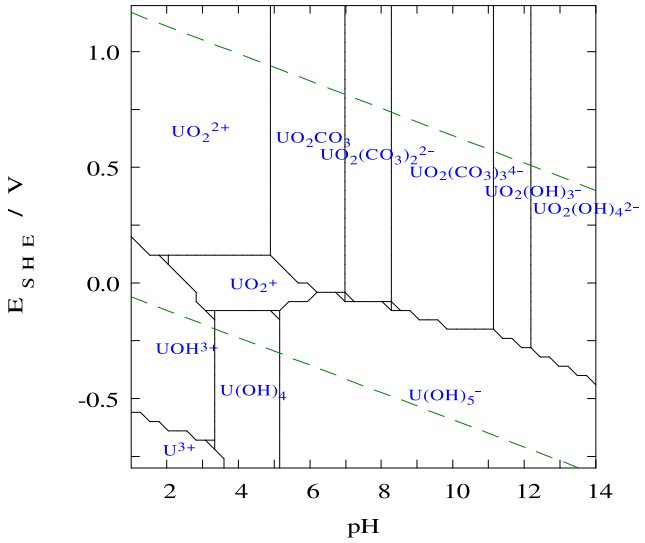

Fig. 1.7. The Eh-pH diagram for the U(VI) (10 nM) in the presence of carbonate (1 mM); T: 298K.

presence of negatively charged $UO_2(CO_3)_2^{2-}$ or $UO_2(CO_3)_3^{4-}$ dominates in oxidizing and mild reducing condition at pH > 6 [108]. In pH 5-6, less mobile $UO_2(CO_3)$ dominates and in acidic pH range (pH<5) the uncomplexed uranyl ion (UO_2^{2+}) dominates. In the absence of any complexing anion/ligands, the interaction between mineral surface and the clay are mainly of two types, inner-sphere complex formation, and outer sphere complex formation. In the inner sphere complex, the hydrated metal ions shed its primary hydration sphere and attach to the mineral surface by largely covalent bond, whereas in outer sphere complexation, the metal ions retain its primary hydration sphere and approach electrostatically to a critical distance (**Fig. 1.6**). In the presence of other inorganic or organic complexants such as simple organic acid, HA or inorganic anions, the interaction mechanism between the radionuclide with the clay minerals differs. Such alteration in the interaction mechanism can have a profound effect of the sorption properties of the clay minerals which can lead to entirely different pathways for the fate of radionuclides under those conditions. **Fig. 1.8** shows some of the possible ways of clay–radionuclides interactions in the presence of any external complexants.

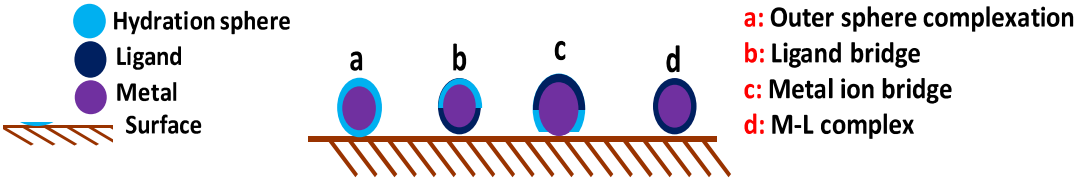

Fig. 1.8. The possible mode of interaction of metals ion with the clay surface in the presence of organic or inorganic complexants (shown as Ligand).

A large volume of research work is ongoing to understand the sorption, speciation and migration behavior of different radionuclides at several contaminated sites, such as the Hanford Site, Nevada Test Site, Savannah River Site, etc. Many such sites involved in the production, reprocessing or storage of nuclear materials/wastes have contributed to environmental radionuclide contaminant in various ways such as spillage, discharge, accidentals, and testing facilities. To understand the radionuclide migration behavior at these sites and for efficient remediation methodology, a wide range of disciplines are required with a lot of financial burdens.

1.8. THERMODYNAMIC MODELING OF SORPTION DATA

The experimentally obtained sorption or K_D data for a given radionuclide under the given experimental condition can be used for surface complexation modeling studies. These kinds of studies are essential for the prediction of long-term behavior and for understanding the transport of radioactive contaminants in the ecosystem [109]. Any surface complexation modeling (SCM) is started with the conceptualization of a mineral surface with chemical functional groups, mainly –OH, which can interact with the contaminants in the aqueous phase (a radioactive contaminant in the present case) with different modes such as inner or outer sphere complexation. The minerals (*i.e.* clay) can also have ion exchange sites for ion exchange reactions. The mineral surface can possess either variable charge or fixed charge density or both. The variable charge on these surfaces arises from the acid-base properties of the surface hydroxyl groups or from the surface complexation reaction, mainly by the inner

sphere complexation. Most of the oxides, including the iron oxides which are ubiquitous in many environmental systems, exhibit variable charged surfaces, and can also have several distinct sites on different surface planes. The permanent charge on the surface is a feature of many clay systems. The clay minerals are comprised of composite sheets with alumina octahedra and silica tetrahedra attached in different ways such as one alumina octahedron for one silica tetrahedron (1:1) or as described in the previous section systems containing one alumina octahedron sandwiched in between two silica tetrahedra (2:1). Substitution by any lower valent cation such as trivalent (Fe^{3+} or Al^{3+}) with Si in silica tetrahedral or any divalent with Al^{3+} in octahedral, gives rise to the fixed structural charge that is compensated by binding of external cations in cavities between the or on the outer planes. These cationic sites are suitable for cation exchange reactions with the aqueous phase cations. The ion exchange interactions are predominantly electrostatic in nature with relatively weak bonds without much change in the total surface charge. Many a time, a single mineral exhibits different site types on its surface such as ion exchange interlayer sites, surface complexation edge sites and planar face sites. The identification of surface site types and their estimation are very important for the development of SCM [110]. For both simple and complex assemblages, the number of surface sites can be estimated from the specific surface area of the solid phase. The cation exchange capacity or CEC is the number of ion exchange sites (can be estimated by different chemical methods) which involve replacing all exchangeable ions in clay with a particular index cation. All SCM is based on some basic chemistry principles, many of which are widely accepted equilibrium models for solution chemistry. These models are based on mass action laws representing chemical reactions.

The fundamental concepts for an SCM are as follows [110]:

- Selection of simple chemical components, which acts as building blocks to form all the chemical species needed under the given chemical condition. Simple ions or chemical elements are often selected as components for SCM. Other choices for

components are also possible as long as they meet the requirement that no component can be expressed as a combination of other already present components in the system.

- The spectroscopic or conceptual understanding is used to form the chemical species which can be formed by combining one or more components of the system.
- The basic definition of each species depends on the selected set of components.
- The charge neutrality and the mass balance requirement are a must, by which the combined concentrations of all species having a given component are governed by the fixed total quantity of that component in the system.
- The mass action equation for each species is derived, in which the activities of all chemical species and components involved in a chemical reaction are related by a log K value (thermodynamic stability constant).
- An underlying thermodynamic database is required for the stability constants of all relevant dissolved (and solid) species.

The SCM approach is based on a set of chemical reactions on the mineral surfaces; each has an equilibrium constant value. The surface sites are visualized as taking part in reactions in a similar way to any other entity present in the system. In the most commonly applied types of SCMs, some of the surface atoms (≡S) react with water to form surface hydroxyl groups with zero charges (≡SOH). These surface hydroxyl groups undergo acid-base reactions similar to ligands in solution chemistry forming either positively charged, i.e., $\equiv SOH_2^+$ or negatively charged, i.e., $\equiv SO^-$ surface moieties. The sites can also interact with metal ions in aqueous electrolyte solutions. The various reactions between the metal ions and the mineral surface are discussed in the modeling section of the experimental part (Chapter 2, Section 2.9).

The uptake of metal ions or protons at a mineral surface changes the surface charge; hence, an electrostatic interface layer model is often a component for the SCM to correct for the effects of varying surface charge on equilibrium constants. A number of electrostatic models for the interface have been proposed and applied to model the sorption data, such as the

diffuse layer model (DLM), triple layer model (TLM), and constant capacitance models (CCM) [110,111]. The two main differences between the various electrostatic models are the number of adsorption planes and how the relationships between the surface charge density and the electrostatic potential at these surfaces are defined. So the overall free energy of metal ion sorption process can be assumed as the sum of free energies of non-electrostatic (NES) or chemical contribution and electrostatic contribution (ES), equation 1.8 [110].

$$\Delta G_{\text{Sorption}} = \Delta G_{ES} + \Delta G_{NES} \qquad \textbf{(1.8)}$$

where $\Delta G_{\text{Sorption}}$ represents the free energy change for the overall sorption process and ΔG_{ES} and ΔG_{NES} are contributions from the electrostatic and non-electrostatic interaction to the overall sorption process. In cases where the chemical or non-electrostatic contribution to the free energy of adsorption (ΔG) dominates over the electrostatic contribution, a non-electrostatic model (NEM) can be used. These kinds of models often find their application in modeling natural materials where the electrostatic effects are difficult to quantify and the electrostatic terms become incorporated within equilibrium constants for various surface sorption reactions.

One of the key issues is how to describe and model these surface reactions. While a number of interactions of radionuclides with surface groups are possible, a distinction is often made between ‘inner-sphere’ and ‘outer-sphere’ surface complexes. When forming an inner-sphere complex, there is a direct bond between the surface and the adsorbed species. In contrast, a species forming an outer-sphere complex retains its shell of coordinated water molecules and therefore lies at a greater distance from the surface (**Fig. 1.6**). As a result, this species is associated with the surface mainly by electrostatic forces, which are weaker than the inner-sphere type bonds. There are several important types of radionuclide sorption reactions, including simple adsorption reactions, reactions involving simultaneous ligand sorption (to form ternary surface complexes), and reactions involving multiple surface sites

(multidentate sorption). Multiple sorbing species may attach to each site (polynuclear adsorption) at relatively high dissolved radionuclide concentrations (this is analogous to the formation of polynuclear solution complexes). Cations, such as uranyl (UO_2^{2+}), are known to bind to two or more surface oxygens, which can be represented as a bidentate binding [110]. In an SCM, an equilibrium constant (log K value) is associated with each type of the reaction, typically defined analogously to equilibrium constants in the aqueous chemistry although some surface reactions (like multidentate adsorption) require more specific formulation of the associated equilibrium constants. The details of the modeling are described elsewhere, but the key feature of any SCM approach is the incorporation of a range of realistic and relevant surface reactions. In recent years, more emphasis was given on the identification of the surface species by advanced techniques, particularly the synchrotron-based technique of extended X-ray absorption fine structure (EXAFS) spectroscopy, have provided very useful information about the local structure of the surface sorbed species. The EXAFS spectroscopy probes the local coordination environment (*i.e.,* the type of neighboring atoms, coordination number, and bond lengths) of the adsorbed species. EXAFS spectroscopy has been used to distinguish between sorption by ion exchange and binding to the edge sites. Similarly, EXAFS can be used to differentiate between various forms of adsorbed or precipitated species. A recent EXAFS study of Zn(II) sorption on montmorillonite surface demonstrated distinct crystallographic differences between sorption complexes formed at strong and weak sites [112].

The majority of the literature data on SCM describes the adsorption of metal ions by individually pure or synthetic mineral phases under well-defined chemical/physical conditions, whereas complexity of the natural soil systems makes it very difficult to apply the concept of any SCM to these systems. Two basic modeling approaches were proposed: (i) the component additivity approach and (ii) the generalized composite approach for the SCM of the natural system [113-114]. The generalized approach assumes the generic sites on the

mineral surface and iteratively fits the sorption data to get the best-fit parameters for log K value, whereas the component additivity approach is based on summing the sorption of individual components in the complex mixture. To use this approach, it is essential to determine the composition of the natural mineral. The model can be simplified if the components that dominate the sorption of the given metal ions known by other means. However, the identification of the mineral components that dominate the sorption of a given radioactive contaminant in natural sediments is a challenging task. Even if qualitative or quantitative data analysis of pure phases were made available, further understanding of the combined behavior of those components towards radionuclide sorption under the given physical or chemical conditions is quite complicated. Furthermore, the components can be distributed quite unevenly in size, a coating of other NOM or oxides, surface inhomogeneity, etc. For example, the coating of iron oxide/hydroxide minerals onto clay minerals influences the sorption of U(VI).

The inherent inhomogeneity of the natural sorbents with respect to their mineral composition and complexity due to the presence of natural organic matters makes the sorption and speciation studies of actinides in natural media a challenging task (*vide supra*). An attempt was made through this thesis to understand some of the underlying factors that play an important role in deciding the sorption and speciation of radionuclides in the natural environments. The compositional analysis for natural clay minerals are also a tedious task but essential for understanding of the radionuclide clay interactions. The objective of present dissertation, broadly, is to understand the sorption and speciation of radionuclides in the natural media, for which thorough characterization of clay minerals is extremely important. After characterization of clay minerals, emphasis was devoted to understand the role of different accessories phase present in the clay minerals towards the sorption of radionuclide (in the present case Np(V)). The individual experimental protocols were designed to get the information of most reactive phases responsible for Np(V) sorption. The effect of other

structural parameters of clay such as form of clay (1:1 or 1:2) and nature of interlayer cation onto radionuclide sorption was also studied. The presence of NOMs adds additional complexity to natural system and hence simple clay systems were chosen for better understanding of the radionuclide sorption onto clay-NOMs binary systems. Sorption studies were also done to understand the role of clay mineral structure and role of interlayer cation onto radionuclide sorption. Finally the experimental data were analysed using CA approach of SCM to get better insight into the sorption mechanism and to further support experimental observations.

1.9. SCOPE OF THE PRESENT THESIS

There is an ongoing risk of environmental contamination with radioactive ions such as actinides (U(VI), Th(IV), Pu(IV) and Am(III)), fission (Cs(I), Sr(II)) and activation (Np, Pu etc) products etc. due to increasing nuclear fuel cycle activity associated with the ever-increasing energy demand in the world. To meet these growing demands, we need reliable, affordable and clean electricity. Hence, there is always a need to study and access the level of contaminants in the environment, to find out better ways to retard their migration etc. In the present work the sorption of actinides (Am(III), Np(V), U(VI)) or their homologs i.e. Eu(III) and Gd(III)) and fission product ions viz. Cs(I) and Sr(II) onto bentonite of different origin, of different chemical form, have been investigated using batch sorption, thermodynamic modeling, and spectroscopic studies. The natural bentonites of different origins (*e.g.* India, Russia and Spain) and kaolinite (commercial) were thoroughly characterized by host of physical techniques such as X-ray Fluorescence (XRF), X-ray diffraction (XRD), Fourier Transform Infrared (FTIR), BET (surface area), High Resolution Transmission Electron Microscopy (HR-TEM), Scanning Electron Microscopy (SEM), Mössbauer spectroscopy, etc. The clays used in the present work are of variable composition both, with respect to their mineralogy and Fe containing phase and Fe speciation. It is of interest to see the effect of such variation in the mineralogy and Fe content of the clay onto the sorption and speciation

of radionuclides. The batch sorption experiments were carried out to understand the role of different aqueous condition onto the sorption behavior of given radionuclide on selected clay mineral. Some of the clays were chemically modified with respect to their interlayer cation form, or Fe- containing minerals. The sorption on these modified clays gives an indication that, these modification, if occur (change in cationic form) or if such kind of mineral is found, (or mineral with different Fe-phases and Fe-speciation), in nature can either increase or decrease the sorption and even sometimes the sorption does not change much. These studies help in predicting the migration of radio contaminants under a variety of experimental conditions. The effect of complexing agents on sorption onto clay surface was also studied, with small organic molecules such oxalic acid to complex humic acid, the effect of carbonate, an ambiguous inorganic complexants present in aqueous media, was also seen. The spectroscopic techniques such as EPR, EXAFS, and TRLFS studies were undertaken to probe the local structure of surface sorbed complexes. To further understand the sorption mechanism, surface speciation and the role of individual phases present in complex mineral assemblages toward metal sorption of the natural system, Thermodynamic modeling using SCM was done. To further support the results of theoretical modeling, certain experimental procedure was undertaken. The combinations of both theoretical modeling with the experimental finding were used to arrive at a suitable conclusion especially when working with a complex mineral system such as natural clays.

2

EXPERIMENTAL

2.1. INTRODUCTION

The present studies are mainly focused on understanding the sorption of radionuclides onto natural clay minerals vis-à-vis that onto others clays of commercial origins. Before going for the speciation and sorption studies at the mineral water interface it's very important to understand the clay system. The natural clays may contain other minor but important constituents, which can modify or affect the sorption of the given radionuclides to a great extent. In the present Chapter, a brief description of the clay sample has been given along with their characterization and speciation using techniques such as, X-ray diffraction (XRD), X-ray fluorescence (XRF), Scanning Electron Microscopy (SEM), High Resolution Transmission Electron Microscopy (HR-TEM), zeta potential measurement, BET surface area analysis, Electron Paramagnetic Resonance (EPR), UV-visible spectroscopy, Luminescence spectroscopy (LS), Inductively Coupled Plasma-Atomic Emission Spectroscopy (ICP-AES), Extended X-ray Absorption Fine Structure Spectroscopy (EXAFS), Mössbauer spectroscopy, radiometry, etc. Additionally, radiotracer preparation and techniques used for their assay have been discussed along with the relevant data analysis. In addition, the aqueous speciation of radionuclides, and different SCM used for modeling of sorption data have been discussed in brief.

2.2. PREPARATION AND PURIFICATION OF RADIOTRACERS

> ***Caution: working with the radiotracers requires a specialized facility like the glove box, fume hoods, dust mark etc. Utmost care must be taken when working with the radioactive elements.***

The environmental concentration of the radioactive contaminants can vary from place to place but in general, their concentration in the environment is very small and hence, the studies were carried out with respective radiotracers. The application of tracers also offers rapid quantification using radiometric analysis. The procurement, preparation and subsequent purification of various radiotracers used in the present studies are given below.

2.2.1. Uranium-233 (^{233}U)

^{233}U ($t_{1/2}$ = 1.59 x 10^5 y) tracer was produced by the neutron activation of ^{232}Th followed by its purification using a reported methods [115].^{233}U was separated from the bulk of the unconverted ^{232}Th using an anion exchange resin (Dowex 1×8 in Cl^- form) from 6 M HCl solution, to get rid of major decay products such as ^{228}Th (daughter product of ^{232}U) and others [116]. It is well known that uranium (VI) forms anionic complexes ($UO_2Cl_n^{(n-2)-}$; where n = 3 or 4) in 6 M HCl solution which is held onto the column containing the resin, whereas thorium and its daughter products will pass through the column. The uranium loaded column was washed with an excess of 6 M HCl to remove any adsorbed impurities. Finally, the loaded uranium was eluted with pH 2 solution (0.01 M HNO_3) and the eluted fraction was evaporated to dryness and one to two drops of concentrated $HClO_4$ was added and evaporated to dryness in succession for three times to destroy the organic impurities from the column and also to convert to uranium perchlorate. The final pH of the resultant solution was adjusted to 2 using very dilute $HClO_4$. The concentration of uranium in the ^{233}U stock solution thus obtained was ~ 10^{-5} M. The radiochemical purity of ^{233}U tracer was confirmed by α-spectrometry.

2.2.2. Americium-241 (^{241}Am)

^{241}Am ($t_{1/2}$ = 431y) was purified from its daughter product (*i.e.* ^{237}Np) by first reducing Np to its +IV oxidation state using hydroxylamine hydrochloride ($NH_2OH.HCl$) in 1 M HNO_3 and subsequently extracting the converted Np^{4+} ion using 0.5 M theonyl trifluoroacetate (TTA) in xylene. The aqueous phase after phase separation was devoid of any Np and contained the bulk of Am and hence, was evaporated to dryness and few drops of a mixture of concentrated HNO_3 and $HClO_4$ (5:1 ratio) was added to destroy any organic impurities. $HClO_4$ was added dropwise and evaporated to convert it to the perchlorate (ClO_4^-) form and the final pH of the stock solution was adjusted to 2 using very dilute $HClO_4$. The concentration ^{241}Am in the stock solution was maintained at ~ 10^{-5} M. The radiochemical purity of the product was ascertained by α-spectrometry.

2.2.3. Neptunium tracer (^{237}Np and ^{239}Np)

Both ^{239}Np, ($t_{1/2}$ = 2.35 days) and ^{237}Np ($t_{1/2}$ = 2.1x10^6 y) were used as the radiotracers for neptunium sorption studies. ^{239}Np was obtained from the decay of ^{243}Am by liquid-liquid extraction using 5% TOA (tri-*n*-octylamine) in toluene from HCl containing feed solution. The extraction cycle was repeated twice with fresh organic phases to maximize the uptake of ^{239}Np, followed by its stripping in Millipore water [117]. The resulting strip solution was evaporated to dryness and few drops of a mixture of concentrated HNO_3 and $HClO_4$ was added to remove traces of organic impurities. The concentration of ^{239}Np in the stock solution was maintained at ~ 10^{-13} M at pH 2 using dilutes $HClO_4$. The radiochemical purity of the product was ascertained by gamma-ray spectroscopy using a HPGe detector and also by alpha spectrometry. ^{237}Np was used from laboratory stock solution at pH 1 HNO_3. The ^{237}Np solution was dried and dilute $HClO_4$ was added to get Np in the perchlorate form. The final stock solution was prepared and kept at pH 2 ($HClO_4$).

2.2.4. Europium tracer (^{152,154}Eu)

The ^{152,154}Eu tracer was produced by neutron irradiation of Eu_2O_3 powder sealed in quartz for sufficient time. After a cooling period of 2-3 days, the irradiated Eu_2O_3 was dissolved in diluted $HClO_4$. The concentration of Eu(III) in the stock solution was 1×10^{-5} M. ^{152}Eu and was used as the laboratory stock.

2.2.5. Other radiotracers

Other radiochemical tracers such as ^{137}Cs, ^{90}Sr, etc were procured from BRIT (Board of Radiation and Isotope Technology), Mumbai and their radiochemical purity were ascertained by gamma-ray spectrometry.

2.3. ASSAY OF THE RADIONUCLIDES

The radionuclides used in the present study were quantified by different radiometric assay techniques. The α and/or β emitting radionuclides e.g. ^{233}U, ^{237}Np, ^{239}Np, and ^{90}Sr were be assayed in the sorption experiments by liquid scintillation counting whereas NaI(Tl) scintillation counter and HPGe detector were used for the estimation and checking the radionuclide purity of gamma-emitting radionuclides such as ^{152,154}Eu, ^{152}Eu ,^{241}Am, and ^{137}Cs.

2.3.1. Liquid Scintillation Counter (LSC)

The LSC was widely used for the quantitative analysis of alpha-emitting radionuclides used in the present study. The inherent advantage of this type of detector is their detection efficiency (~100%) which allows assay of low amounts of radioactivity with good precision. The LSC works on the principle that, when an ionizing radiation interacts with a scintillator material, a material that luminescence in a suitable wavelength region when interacted by charged particles, it emits photons which are collected by the photomultiplier tube (PMT) and produces a signal representative of the intensity of the photons falling on it. In the case, when a scintillator material emits photons in UV region, a wavelength shifter (to shift to visible

region) is added to the scintillator cocktail which has intermediate energy levels. This shifted wavelengths photons are subsequently recorded in the PMT (as photocathodes of most PMTs are compatible with visible light). The LSC is widely used for gross alpha activity and cannot be used for alpha spectrometry as they can't differentiate among alpha particles of different

Fig. 2.1. The LSC system used in the present studies.

energies. Many organic molecules are versatile scintillators for radiation measurements [118-119]. For gross α-counting using LSC, the α-emitting radionuclide was mixed with a liquid scintillation cocktail. The liquid scintillation cocktail comprises of three components in general, first a solvent like a dioxane or toluene, second, a scintillator like PPO (2,5-diphenyl oxazole) and third, a wavelength shifter such as POPOP [1,4-bis-2-(5-phenyl oxazolyl)-benzene]. The solvent acts as the main stopping medium and must be chosen in such a way to give efficient energy transfer from the radionuclide to the scintillating solute. In the present case, the concentration of the radiotracers was kept very low to mimic the natural conditions and hence, generally large volumes of aqueous aliquots (up to 1 mL) could be added to the

liquid scintillation cocktail. The Ultima Gold scintillation cocktail was employed for liquid scintillation counting. Each sample was counted at low background liquid scintillation counting Quantulus-1220, Perkin Elmer for sufficient time to minimize the statistical counting error (**Fig.2.1**).

2.3.2. NaI(Tl) Inorganic Scintillation Counter

Sodium iodide activated with thallium (0.1- 0.2%), NaI(Tl), is one of the most widely used inorganic scintillators for the assay of the gamma-ray emitting radionuclides. The interaction of NaI with the gamma-ray causes the excitation of the electrons from the valence band (VB) to the conduction band (CB) or for the ionization of atom. The de-excitation of the electrons from the CB to the VB leads to the emission of photons. The band gap in NaI crystal is of the order of 5-6 eV and hence the wavelength of the emitted photons lies in the UV range for which the PMT is not very sensitive and hence, Thallium is doped as a wavelength shifter. The relation between the energy and wavelength is given below:

$$E(ev) = 1239.84 / \lambda(nm) \qquad \textbf{(2.1)}$$

where E is energy in eV and λ is the corresponding wavelength in nm. The addition of thallium in the NaI crystal not only shifts the wavelength to higher values *i.e.,* to the visible

Fig. 2.2. The NaI(Tl) detector assembly used in the present studies.

region by creating intermediate levels in conduction bands but also increases the fluorescence yield of the detector. The efficiency of NaI(Tl) detectors is very good with an energy resolution of ~7% only at 662 keV. In the present work, a 3" x 3" well type NaI(Tl) detector coupled with a multi-channel analyzer (MCA) has been used for γ-counting. A suitable aliquot (generally ~1 mL) of the desired radioactive solution was taken in flat bottom glass tubes (γ tubes) for counting. Each sample was counted for sufficient time to get >10,000 counts to reduce the counting statistics error. **Fig. 2.2** shows the NaI(Tl) detector used in the present studies.

2.3.3. High Purity Germanium Detectors (HPGe)

To ascertain the radiochemical purity of the gamma emitting radionuclides used in the present work, HPGe (high purity germanium) detector coupled to a multi-channel analyzer (MCA) was used (**Fig. 2.3**). The HPGe detector was made up of exceptionally pure

Fig. 2.3. (a) Top view, (b) front view with (c) data acquisition system of the HPGe detector used for present studies.

germanium (Ge) with an impurity level of ≤ 10^{10} atoms/cm^3. HPGe is the most commonly used semiconductor detector for γ ray spectrometry. The high energy resolution (typically 1.9 keV at 1332 keV) of HPGe is the key in ascertaining the radiochemical purity of the given radionuclides, due to its low band gap energy (0.7 eV). The other advantage of an HPGe detector is that it can be stored at room temperature and only require cooling to liquid

nitrogen temperature during counting operations. In the present work, radiochemical purity of ^{239}Np, ^{241}Am, ^{152,154}Eu and ^{152} Eu was ascertained by an HPGe detector.

2.3.4. Solid State Nuclear Track Detector (SSNTD)

The SSNTDs were used for the detection of high energy charged particle such as α-particles. The two main steps in the SSNTD are the formation of latent tracks and their subsequent development by chemical leaching or other means. The high energy charged particles passing through a dielectric material (crystals, inorganic glasses & plastics) produce submicroscopic trails of continuous damage along their path. These trails consist of radiation damaged material and called as latent tracks as they are too small to be seen with the help of a microscope. Under certain favorable circumstances, such as after alkali leaching (6 M NaOH) at elevated temperature (~70ºC); they can be viewed under a microscope. In the present studies, α-track radiography and SEM-EDX studies were conducted to identify the local distribution of α-emitting radionuclides on bentonite samples at the micrometer scale. The CR-39 type polycarbonate film (TASTRAK PADC) was used for α-radiography. The tracks were developed using alkaline leaching at 75 ± 1 ºC for 6 h. The α-track images along with the corresponding areas of the solid samples were observed using an Olympus BX-51 optical microscope.

2.4. CLAY CHARACTERIZATION/MINERALOGICAL DETERMINATION

2.4.1. X-ray diffraction (XRD)

X-ray diffraction (XRD) is one the most widely used non-destructive techniques for characterization of solid materials of varying crystallinity and lattice systems. The non-destructive nature, ease of sample preparation and fast operation with high accuracy in determination of d-spacing made XRD, a versatile tool in the field of material chemistry. The XRD pattern varies from sharp peaks in crystalline materials to broad humps in amorphous systems. The Bragg's equation is given as follows,

$$n\lambda = 2d \sin\theta \qquad \textbf{(2.2)}$$

where n is the order of reflection, d is inter-planar distance while λ and θ are wavelength and incident angle of the X-rays, respectively. The XRD pattern of any materials is based on the scattering of X-rays by the parallel planes, an array of atoms, ions or molecules. Since the parallel arrays of atoms of the crystal lattice are analogous to the parallel lines of a diffraction grating, the inter-planar spacing between the planes could be successfully determined from

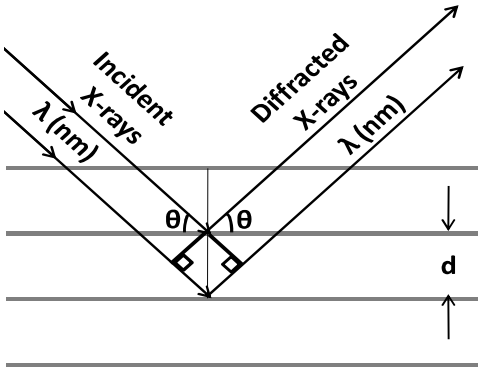

Fig. 2.4. Schematic representation of the Bragg's equation for X-ray diffraction.

the separations of bright fringes of the X-ray diffraction pattern (**Fig. 2.4**). The X-rays wavelength of (0.5 to 2 Å) has the same magnitude as the inter-planar spacing in the crystal lattice system. Therefore, crystal planes act like diffraction gratings for the impinging X-ray radiation. The electron cloud of the atoms act as scattering centers for X-rays and the scattered X-rays from two scattering centers may undergo constructive or destructive interference. The constructive interference occurs only at a set of particular angles defined by Bragg's Law (**equation 2.2**), which results in sharp peaks in the XRD pattern and are characteristic of a given material. In the present study, XRD was used to get the information about the composition of different clay samples, as well as other colloidal clay fractions (<0.5 mm), which were selected from a water suspension according to Stokes' law (without using of chemical dispersants).The -ray diffraction patterns were recorded with an Ultima-IV x-ray diffractometer (Rigaku) and the scans were recorded with the following conditions: Cu-K_α

radiation source, D/Tex- Ultra 1D-detector, scan range: 3.6- 65 2θ, scan speed: 5º/min, step: 0.02º 2 θ, intensity (max): ~2.5 x 10^4 counts. The identification of the mineral composition was done with the textural (oriented) samples prepared from clay suspension in the air-dried and ethylene glycol (EG) solvated states. The quantitative analysis was done using the Rietveld method in the BGMN program.

2.4.2. X-ray fluorescence (XRF)

The X-ray fluorescence (XRF) spectrometry is used for the elemental analysis of various clay samples used in the present study. The XRF is based on the principle that when the individual atoms were excited by an external energy source, they emit X-ray photons of characteristic wavelength or energy. Simply by counting the number of photons of a given energy emitted from the sample, the elemental composition of the sample can be identified and quantified. The identification of different elements by X-ray methods is possible due to the characteristic radiations emitted from the inner electronic shells of the atoms. When an electron beam of sufficient energy strikes a material, several processes were possible. The interaction may results in the emission of photons with a broad continuum of energies called, bremsstrahlung, or “braking radiation”, due to the deceleration of the electrons inside the material. Another consequence of the interaction between the electron- beam and the material is the ejection of photoelectrons (photoelectric effect) from the inner shells of the atoms making up the material. These photoelectrons have the kinetic energy, E-φ, which is the difference in energy between the incident particle energy (E) and the binding energy (φ) of the atomic electron. The ejected electron leaves a “hole” in the inner shell and after a brief period, the atomic electron rearranges rearrange and fill hole” position from a higher levels. By this way of relaxation, the atom undergoes fluorescence, or emission of X-ray photons whose energy is equal to the difference in energies of the initial and final states. The detection of this photon and by measuring its energy one can determine the specific element and its electronic transition from which the photons are originated. This gives the basis for XRF spectrometry,

where elements may be specified and quantified based on the emission of their characteristic x-rays from a sample that is being excited. The Fluorescence emission, however, is not the only process by which an excited atom can relax. It competes with the "Auger effect", which results in the emission on of a second photoelectron to regain the stability. The relative numbers of excited atoms that fluoresce are described by the fluorescence yield, which increases with increasing atomic number of the analyte element [120]. In the present studies, the chemical analysis was performed using XRF in accordance with the standard procedure using an Axiom AX spectrometer (PANalytical, Netherlands). The clay samples were dried at 110 ºC and were prepared by fusion with lithium borate at 1200 ºC. The iron (Fe) content in the clay samples was determined in the form of total Fe_2O_3, regardless of its actual valence state.

2.4.3. Mössbauer Spectroscopy

Mössbauer spectroscopy is a versatile tool that can be used to provide information about the local structure around the probe atom (*i.e.* ^{57}Fe in the present case). The key to the success of this technique is the discovery of recoil-less γ ray emission and absorption, referred to as the 'Mössbauer Effect', after its discoverer Rudolph Mössbauer, who first observed the effect in 1957 and received the Nobel Prize in Physics in 1961 for this work [121]. The Mössbauer spectroscopy is based on the magnetic behavior of iron in its crystal structure, but it operates on different dimensional scales. Whereas this technique gives information about the charge and coordination, the magnetometric methods are more sensitive to get the information about the type of magnetic coupling and to the magnetic domain status of Fe in different particles. The Mössbauer effect involves resonant absorption of γ-radiation between I = 1/2 and 3/2 nuclear energy from ^{57}Fe nuclei source to the samples containing iron oxides (**Fig. 2.5**). The Mössbauer spectra consist of a plot of the counts/transmission of γ-rays versus the velocity of the source. The horizontal movement of the source (^{57}Co for iron compounds) is required to match the nuclear environments of the absorber and the source and hence, absorption can

take place. In the absence of any magnetite field, the Mössbauer spectrum consists of one (if the absorbing atom, such as ^{57}Fe, is at a site of cubic symmetry) or two (other symmetry distorted from cubic) absorption maxima. But when a static magnetic field acts on the resonant nuclei (^{57}Fe), it splits the nuclear spin of the ground state (I = ½) into two and those of the excited state (I= 3/2) into four. This gives rise to six allowed transitions that can produce a 6-line spectrum (**Fig. 2.5**). The number and the position of the absorption maxima are determined by the hyperfine interactions between the resonant nuclei and their electrons surroundings. There can be three types of hyperfine interactions. Firstly, the electric

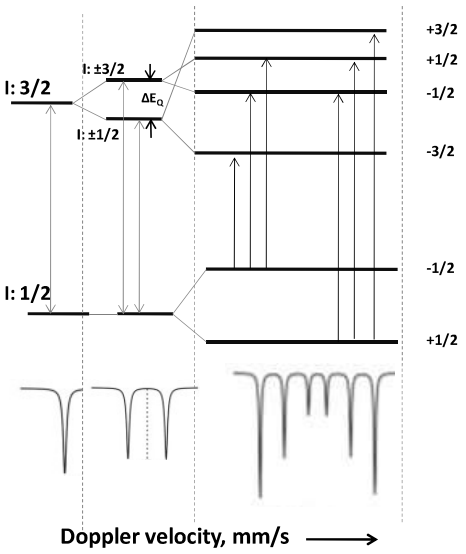

Fig. 2.5. Top: The shift in the nuclear energy levels of 57Fe as shifted by electrical monopole (left), as split by electrical quadrupole (center) or by magnetic dipole interaction (right), Bottom: The corresponding Mössbauer spectra involving transitions from different energy levels.

monopole interaction (δ parameter) is a function of the 's' orbital electron densities at the probe nucleus. This results in a displacement of the Mössbauer spectrum and is expressed as the the velocity of the source (mm/s) needed to counteract the displacement. This isomer shift (or chemical shift), δ, provides information about the coordination number (CN), valency and spin state of the Fe in the given sample. Secondly, the electric quadrupole interaction is

governed by the electric field gradient acting on the target nucleus. This quadrupole interaction or splitting, ΔEq, provides information about the site distortion, e.g., it increases with increasing distortion. Finally, the magnetic hyperfine field, B_{hf} , provides information about the valence and magnetic properties of the sample. Since the latter depends on temperature, the Mössbauer spectra are often recorded at variable temperatures, especially at liquid N_2 (78K) and liquid He (4.2K) which induces magnetic ordering in those oxides which have a Néel temperature (TN) below room temperature (RT) or are super paramagnetic at RT. The absorption data are usually fitted with one or more doublets and/or sextets each with its own set of parameters to get the information about the local environment around ^{57}Fe.

The Mössbauer spectra are used for the identification and characterization of Fe oxides phases in clay samples. This follows primarily from the fact that the different oxides of Fe order magnetically over a wide range of temperatures (78 K - 950 K). The Mössbauer parameters of the different magnetically ordered Fe oxides differ considerably and hence, allow unequivocal identification and sometime quantification in mixtures to be made. Mössbauer spectroscopy is insensitive to all isotopes except ^{57}Fe in the sample and it makes this technique very useful for natural systems where the iron oxides may be too low in concentration or in crystallinity to be detected by XRD. The Mössbauer spectroscopy can also give information about the particle size and isomorphous substitution. In addition, by applying an external magnetic field tone can distinguish ferrimagnetic phases from antiferromagnetic ones and may separate the two basic magnetic sub lattices in poorly crystalline and Al-substituted goethite [122]. In the present study, Mössbauer spectra at the ^{57}Fe nuclei were obtained by a MS-1104 Em-type spectrometer operating at constant acceleration mode. The spectra were recorded using a JANIS closed-cycle cryostat and the results were analyzed using the SpectrRelax program [123]. All the isomer shifts were given relative to the Mössbauer spectra of α-Fe at room temperature.

2.4.4. Zeta Potential Measurements

The surface of the various oxides and colloidal particles suspended in the aqueous phase has a small amount of charge, which may be strongly affected by the pH of the surrounding media. The solid particles in the aqueous solution can develop surface charge primarily in two ways. Firstly, the surface charge is developed due to the chemical reactions at the mineral surface, e.g., the surface hydroxyl groups (*i.e.* for oxides) varies with the pH of the solution and for most of the oxide surfaces a point of zero net proton charge (pZ_{npc}) can be obtained by varying the pH [111]. The second way of development of surface charge is due to lattice imperfections and/or an isomorphous substitution at the phase boundary or other planes. The charge generations by isomorphous substitution are common in clay minerals. For example, if some of the tetravalent Si atoms of the SiO_2 tetrahedra in the SiO_2 sheet of clay mineral are replaced by trivalent Al atom a negatively charged framework is developed. Similarly, the substitution by any divalent (*i.e.*, Mg^{2+}) cation in the trivalent Al-octahedral gives a negatively charged lattice. This developed surface charge at the particle surface affects the distribution of its counterions close to the surface which ultimately leads to the formation of the electric double layer around each particle. There exists a notional boundary within the diffusion layer inside which the ions and particles from a stable entity move

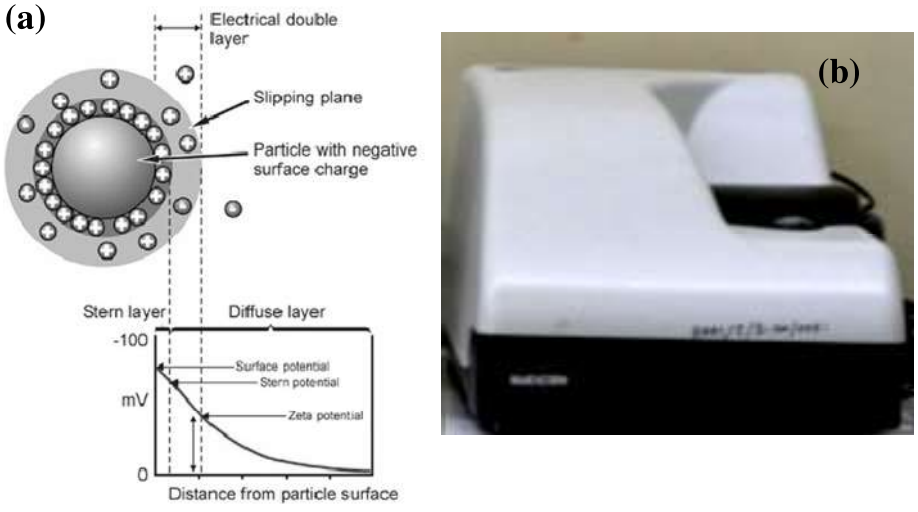

Fig. 2.6. Basics of the double layer (a) and actual instrument (b) used for present studies.

together, but any ions beyond this boundary do not travel with the particle. This boundary is often termed as a shear plane and the potential at this plane is called as the Zeta potential as shown in **Fig. 2.6**. The stability of any colloidal system is generally ascertained in terms of the magnitude of the zeta potential. Large negative or positive zeta potential values (≥± 30 mV) of the colloidal system generate mutual repulsion among particles and thus stabilize the colloidal solution, whereas low zeta potential values (≤ ±30 mV) offer less electrostatic repulsion hence, results in flocculation, so the system gets destabilized. The point where zeta potential becomes zero is called the iso-electric point or PZC (point of zero charge) and is one of the very important parameters used for characterizing the colloidal systems. The surface potential is not directly accessible by experimental measurements and can only be calculated from the experimentally determined surface charge. The zeta potential calculated for the electrophoretic mobility, which is defined as the velocity of a particle in an electric field, is typically lower than the surface potential calculated from the diffusion double layer theory. In true sense, the zeta potential reflects the potential difference between the shear plane and the bulk phase. The zeta potential can be computed from the electrophoretic mobility and other electrokinetic measurements.

The charged particles, suspended in an electrolyte solution, are attracted towards the electrode of opposite charge on the application of an electric field, but at the same time, their movement is opposed by the viscous forces acting on it. The particles start moving with a constant velocity when equilibrium is attained between the two opposing forces, The velocity *i.e.*, electrophoretic mobility of the particle is dependent on several factors such as the strength of the electric field, the dielectric constant (ε), the viscosity (η) of the medium and the Zeta potential of the particle (ζ). The electrophoretic mobility (U_E) and zeta potential (ζ) are related by the Helmholtz Smoluchowski equation given below:

$$U_E = \frac{2\varepsilon\zeta f(Ka)}{3\eta} \qquad \textbf{(2.3)}$$

where $f(Ka)$ is known as Henry's function and generally have two values either 1.5 or 1.0. $f(Ka)$ equal to 1.5 is used for electrophoretic determinations of zeta potential in aqueous media at moderate electrolyte concentrations which is referred to as the Smoluchowski approximation. For smaller particles in low dielectric constant media $f(Ka)$ becomes 1.0 (Huckel approximation) and allows simple calculation. In the present studies, the zeta potential of bentonite samples was determined with varying chemical conditions using Malvern, Zetasizer Nano ZS.

2.4.5. BET for Specific Surface Area Determination

BET surface area analysis was used for the measurement of the gross surface area of the clay material. This technique uses the BET theory, proposed by Brunauer-Emmett-Teller (BET), which explains the physisorption of gas molecules onto the solid surface. The BET theory corresponds to multilayer adsorption under the following hypotheses: (a) the gas molecules are physically adsorbed onto a solid in infinite layers at saturation pressure; (b) there is no interaction between each adsorption layer; and (c) the Langmuir theory can be applied to each layer. The resulting BET equation is given as:

$$\frac{1}{v(^{p}/_{p_0}-1)} = \frac{c-1}{v_{mc}}\left(\frac{p}{p_0}\right) + \frac{1}{v_{mc}} \qquad \textbf{(2.4)}$$

where p and $p_0$are the equilibrium and the saturation pressure of gas at the temperature of adsorption, v is the volume of adsorbed gas, and vmc is the volume of adsorbed gas for monolayer formation, c is the BET constant as given below.

$$c = e^{(E_1 - E_L)} \qquad \textbf{(2.5)}$$

where, E_1 and E_L are the heat of adsorption for the first and the Lth layers, respectively while E_L is the heat of liquification. The BET adsorption isotherm can be plotted as a straight line with $1/v[(p_0/p)-1]$ on the y-axis and (p_0/p) on the x-axis (**equation 2.5**). The slope and the

intercept of the resulting plots are used to calculate the monolayer adsorbed gas quantity ($v$mc), the BET constant (c) and the surface area of the material using the following equation:

$$A = \frac{v_{mc}Ns}{va} \qquad \textbf{(2.6)}$$

where N is the Avogadro's number,v is the molar volume of gas; s is the adsorption cross section of the adsorbing species, and a is the mass of the adsorbent (in g). In the present work, the surface area of the mineral oxides was determined using BET surface area analyzer (Sorptomatic 1990, CE Instruments, UK).

2.4.6. Inductively Coupled Plasma Atomic Emission Spectroscopy (ICP-AES)

ICP-AES is one of the most commonly used techniques for elemental analysis of analytes. The inherent advantages such as multi-element capability, high specificity, and low detection limits make this technique suitable for analysis of various samples. In this technique, a plasma source is used for the dissociation of the analyte into its constituent atoms or ions followed by their excitation to a higher energy level. They de-excitation of the constituent atoms to their ground state emits photons of a particular wavelength which is characteristic of the concerned element present in the analyte. In this work, we have used ICP-AES to access the extent of clay dissolution under specified experimental conditions.

2.4.7. Scanning Electron Microscopy-Energy Dispersive X-Ray Analyzer (SEM-EDX)

Scanning Electron Microscopy (SEM) gives high-resolution images of the sample surface by rastering a focused electron beam across the surface by detecting the secondary or backscattered electron signal whereas an Energy Dispersive X-Ray Analyzer (EDX or EDA) is used to provide elemental identification and quantitative compositional information. The combination of the two, SEM and EDX, serves as a unique tool for analyzing the multi-compositional natural samples. SEM is basically a high magnification microscope, which scans the sample with a focused electron beam to produce images of the sample. The primary

electron beam can interact with the sample in a number of ways, *i.e.*, (a) can generate low energy secondary electrons, which tend to emphasize about the topographical nature of the specimen under study; (b) can be backscattered to produce images with a high degree of atomic number (Z) contrast, and (c) can excite or ionize the atoms which emit x-rays or undergo Auger electron ejection during relaxation leading to shell-to-shell transitions. The emitted x-rays are characteristic of the elements in the top few μm of the sample and are measured by the EDX detector to get the elemental composition of the sample. In the present study, the elemental composition of the solid phase was determined by SEM-EDX (JEOL JSM-6380 LA with a JED 2300 analyzer).

2.4.8. High Resolution –Transmission Electron microscopy (HR-TEM)

Transmission Electron Microscopy (TEM) is a technique that uses the interaction of a beam of focused and energetic electrons with the sample which subsequently provides

Fig. 2.7. The HR-TEM facility used in the present studies

compositional, morphological, and crystallographic information. The emitted electrons from the filament pass through multiple electromagnetic lenses and make contact with the screen

where the electrons are converted into the light to obtain the image. The speed or wavelength of electrons determines the image resolution. The high-resolution transmission electron microscopy (HR-TEM) uses both the scattered and transmitted beams to create an interference image. It is basically a phase contrast image and can be as small as the unit cell of a crystal. In these cases, the outgoing modulated electron waves at very low angles interfere with itself during their propagation through the objective lens. All the electrons emerging from the specimen are combined at a point in the image plane. The HR-TEM has been extensively and successfully used for analyzing lattice imperfections and crystal structures in a variety of materials on an atomic resolution scale. In the present studies, the HR-TEM images of the clay samples were obtained with an aberration-corrected JEOL 2100 F operated at 200 kV (**Fig. 2.7**).

2.5. SOME TECHNIQUES FOR SPECIATION ANALYSIS

2.5.1. Ultraviolet-Visible (UV-visible) Spectrophotometry

The UV-Visible spectroscopy refers to an absorption spectroscopy in the ultraviolet-visible spectral region of electromagnetic spectrum. This can be used for both qualitative and quantitative determinations of the given species as the spectra obtained are characteristic of a

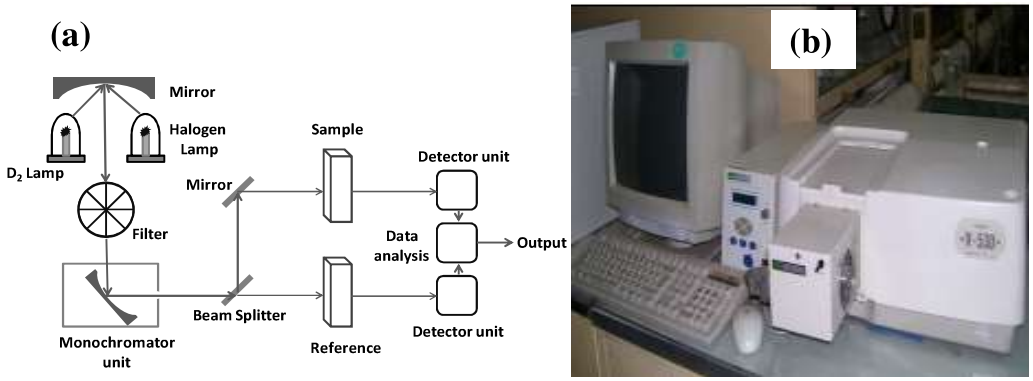

Fig. 2.8. The schematic layout of (a) UV-vis spectrophotometer instrument and (b) the instrument used for the present studies.

particular species. The UV-Visible spectrophotometry is based on the Lambert-Beer law which states that "Equal fractions of the incident monochromatic light are absorbed by successive layers of equal thickness and with an equal concentration of absorbing medium". Mathematically, it can be defined by **equation 2.7:**

$$A = \log ({}^{I_0}/_{I}) = \varepsilon c l \qquad \textbf{(2.7)}$$

where, I_0 and I are the intensities of the incident and the transmitted lights, A is the absorbance, ε is the molar extinction coefficient which is the characteristic of the absorbing species, c is the concentration of the absorbing species and l is the path length or thickness of the absorbing medium.

The absorption spectra of the samples can be used to get information about the structural changes in the species (*i.e.,* uranyl ions) before and after any chemical treatment. It can also be used to get information about the functional groups or conjugation in organic molecules (*i.e*., humic acid) as well as oxidation state of a metal ion in a particular species (*i.e.,* Np(V) oxidation or reduction). A schematic diagram of a standard spectrophotometer is given in **Fig. 2.8.** In the present studies, UV-Visible absorption spectra of the HA and uranium samples were recorded, using a Jasco V-350 UV/Vis spectrophotometer under different chemical conditions. The cation exchanged capacity (CEC) of some of the clay samples were also determined using the differences in the absorption of Cohex (cobalt hexaamine trichloride) before and after the equilibration with the respective clay mineral. The instrument has a resolution of 1 nm with a wavelength accuracy of ± 0.5 nm.

2.5.2. Electron Paramagnetic Resonance (EPR)

The Electron paramagnetic resonance (EPR) shares most of the theoretical description and other experimental concepts with the Nuclear Magnetic Resonance (NMR) spectroscopy. Some of the important characteristics of the EPR include its higher sensitivity at a given spin

concentration, its ability to observe long-range spin-spin interactions and its sensitivity to molecular motion at short time scales. The application of EPR is restricted to elements/ions those contain unpaired electrons. From the EPR technique, one can obtain information on the binding strength and structure of target metal complexes onto the clay from the analysis of spectral line shape and other EPR parameters. The modifications in the coordination environments induce changes in the line width and intensity. In the present studies, Gd(III) was used as the EPR probe to get information about the nature of coordination complexes at clay surface. The EPR spectra were recorded using a Bruker EMM 1843 spectrometer operating at the X-band frequency of 9.5 GHz equipped with 100 kHz field modulation and phase sensitive detection to obtain the first derivative signals (**Fig. 2.9**).

Fig. 2.9. The EPR instrument used in the present studies

2.5.3. Fluorescence Spectroscopy (FS)

The Fluorescence spectroscopy was used to understand the interaction mechanisms between luminescent metal ions with the chosen minerals and complexing ligands. FS is one of the most sensitive, non-invasive and widely used spectroscopic methods for speciation studies. In the FS studies, one can record the excitation spectra at a specified emission wavelength and

emission spectra at the specified excitation wavelength and a combination of specific excitation-emission wavelengths were used for the lifetime measurements.

The measured spectra with the lifetime analysis were used for the assignment of the complex stoichiometry and structure in both sorptions as well as complexation studies. The different species show the appreciable difference in any of the three parameters (or more) measured in the FS. In general, the emission spectra are characteristic of a given species and the selective excitation helps in the reduction of interferences from others species. Thus, the spectral characteristics and lifetime of species provide information about some of the important properties like oxidation states of metal ions, coordination numbers, the degree of hydration, covalence, etc. **Fig. 2.10** shows the typical layout of an FS instrument with the emission lines of Eu(III) ion. Some of the *f*-elements when excited at a suitable wavelength relax through intense emission in aqueous media. Some of the lanthanide and actinide fluorophores are Eu(III), Gd(III), Tb(III), U(VI), Am(III), Cm(III), Bk(III), Cf(III), and Pa(IV), etc. The characteristic emission or excitation spectra of these *f*-elements originate from *f-f* transitions (**Fig. 2.10**). Though the *f-f* transitions are not very much affected by the ligand field, valuable information can be extracted from the emission or excitation spectra and lifetimes measurement of these ions in a given chemical environment.

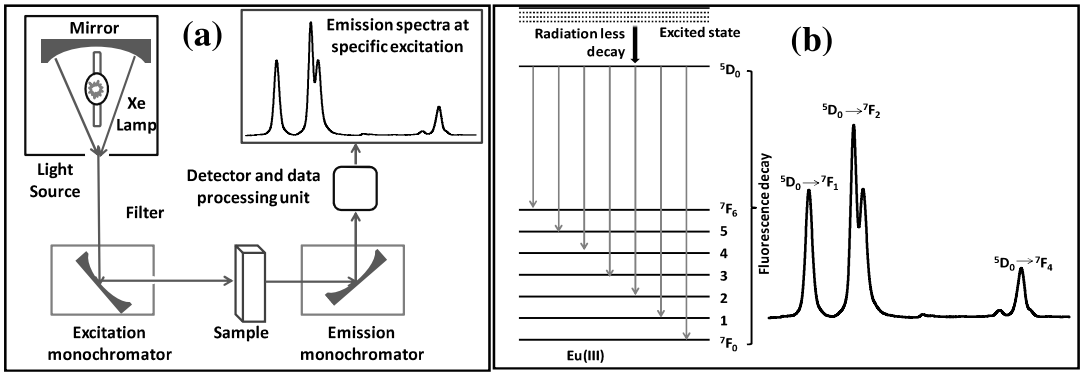

Fig. 2.10. The schematic layout for (a) FS instrument and (b) Eu(III) energy levels with representative emission spectra.

In the present studies, speciation of Eu(III) and U(VI) in aqueous solution and onto minerals water interface were analyzed using the FS. An Edinburgh CD-920 spectrometer equipped with an Ekspla-made tunable Nd: YAG NL310 laser as an excitation source was used for the fluorescence studies.

2.5.4. X-ray Absorption Fine Structure Spectroscopy (XAFS)

The X-ray Absorption Fine Structure (XAFS) spectroscopy gives an opportunity for studying, at the atomic and molecular scale, the local structure around a selected element that is contained within a material. The XAFS is unique in the sense that, it can be applied not only to crystals, but also to materials that possess little or no long-range ordering, amorphous systems, quasi-crystals, glasses, films, membranes, liquid, or even to the molecular gases. This versatility allows it to be used in a variety of disciplines including physics, chemistry, biology, environmental science, materials science, and geology. This XAFS spectroscopy covers both Extended X-ray Absorption Fine Structure Spectroscopy (EXAFS) and X-ray Absorption Near Edge Spectroscopy (XANES), which have their origin in quantum interference effects. The XAFS spectral region up to ~30 eV above the absorption edge is defined for XANES while beyond this limit the data is used for EXAFS analysis. **Fig. 2.11**

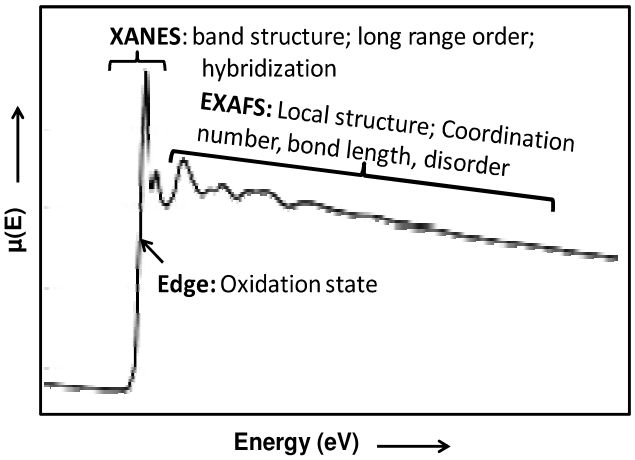

Fig. 2.11. The representative XAFS spectra showing various regions of XAFS (XANES, EXAFS etc.) and information obtained from them.

depicts a typical spectrum obtained in an XAFS experiment. The basic principle of XAFS lies in the fact that, when X-rays of sufficient energy impinge on a probe atom, electrons are ejected from the inner atomic orbital (*e.g.* 1s) due to the photoelectric effect. The "photoelectron" wave got scattered from the atoms surrounding the probe atom or X-ray absorbing atom and creates interference between the outgoing and the scattered parts of the photoelectron wave function. Basically, these quantum interference effects cause an energy-dependent fluctuation in the X-ray absorption probability, which is proportional to a measurable quantity, e.g. X-ray absorption coefficient (μ(E)). When properly decoded, these modulations in X-ray absorption coefficient provide crucial information about the local environment *e.g.*, atomic number, structural disorder, and thermal motions of neighboring atoms around the probe element. In the present study, the XAFS data for sorbed Eu(III) and U(VI) complexes onto clay surfaces were collected under varying chemical conditions. The beamline parameters, experimental condition, and data analysis are discussed in brief here. The EXAFS measurements in fluorescence mode have been carried out at the scanning EXAFS beamline (BL-09) of the INDUS-2 Synchrotron Source (2.5 GeV, 125 mA) at Raja Ramanna Centre for Advanced Technology (RRCAT), Indore, India. Its operational energy range is from 4 to 25 KeV with 200 mA current. The optical setup of beamline consist of an Rh/Pt coated collimating meridional cylindrical mirror followed by a Si(111) (2d = 6.2709 Å) based double crystal monochromator. The second crystal of DCM is a sagittal cylindrical crystal used for horizontal focusing. The metal ion sorbed clay samples on the glass plate is placed at 45° to the incident X-ray beam, and a fluorescence detector is placed at right angle to the incident X-ray beam for collection fluorescence intensity (I_f). One ionization chamber (IC) is placed prior to the sample to measure the incident flux (I_0). The absorbance of the sample as a function of energy was derived from these measurements. The energy-dependent absorption coefficient $\mu(E)$ has been converted to absorption function $\chi(E)$ defined by **equation 2.8** to take care of the oscillations in the absorption spectra :

$$\chi(E) = \frac{\mu(E) - \mu_0(E)}{\Delta\mu_0(E_0)} \qquad \textbf{(2.8)}$$

where E_0 is the energy at absorption edge eneergy, represents the bare atom background and $\mu_0 E_0$ is the step in the value at the respective metal absorption edge. The energy scale was converted to the photoelectron wave number scale (k) by using the following equation

$$k = \sqrt{\frac{2m(E - E_0)}{\hbar^2}} \qquad \textbf{(2.9)}$$

The goodness of fit of model data with experimental spectra has been determined by the value of the R_{factor} defined by **equation 2.10**:

$$R_{factor} = \sum \frac{[\mathrm{Im}(\chi_{dat}(r_i) - \chi_{th}(r_i)]^2 + [\mathrm{Re}(\chi_{dat}(r_i) - \chi_{th}(r_i)]^2}{[\mathrm{Im}(\chi_{dat}(r_i)]^2 + [\mathrm{Re}(\chi_{dat}(r_i)]^2} \qquad \textbf{(2.10)}$$

where, χ_{dat} and χ_{th} refer to the experimental and theoretical $\chi(r)$ values respectively and Re and Im referring to the real and imaginary parts of the respective quantities. The $x(E)$ (energy dependent absorption coefficient) has been converted to the $x(k)$ (wave number dependent absorption coefficient) where m is the mass of the electron. Finally, the $x(k)$ is weighted by k^3 to amplify the oscillation at higher k value and the functions $x(k)k$ are Fourier transformed in real or R space to generate the $x(R)$ versus R (or FT-EXAFS) spectra in terms of the actual distances from the center of the absorbing atom. Set of EXAFS data analysis program available within the IFEFFIT software package have been used for EXAFS data analysis. The ATHENA software was used for data reduction & Fourier transform to derive the $x(R)$ versus R spectra from the absorption spectra. ARTEMIS sotware was used for generation of the theoretical EXAFS spectra starting from an appropriate crystallographic

structure and finally fitting of the experimental data with the theoretical spectra using the FEFF 6.0 code.

2.6. MEASUREMENT OF DISTRIBUTION COEFFICIENT (K_D) OR % UPTAKE

Sorption of radionuclides at the mineral water interface plays an important role in deciding their fate in the natural systems. The most common way of ascertaining the performance of a solid phase toward radionuclide sorption is the determination of distribution coefficient (K_D) of the given radionuclide under a given set of conditions. The K_D value reflects the affinity of the solid surface for the metal ion of interest. Higher K_D value means better affinity. The K_D value for a given system can be calculated from the following equation (equation 2.11).

$$K_D = \frac{C_s}{C_l} \qquad \textbf{(2.11)}$$

where, C_s is the concentration of the metal ion (radionuclides in the present case) per gram of solid (*i.e.,* clay mineral) and C_L is the concentration of metal ion per mL of aqueous phase after attainment of the sorption equilibrium. Various species for a particular radionuclide can exist simultaneously for a given set of experimental conditions and hence, the K_D represents the gross distribution of the radionuclide at solid/solution interface without considering the nature of the exact species. The other very common parameter, which is commonly used in for sorption studies is to evaluate the distribution of radionuclide at solid /solution interface in % term (with respect to initial radionuclide concentration in the aqueous phase). The % sorption can be determined using the following equation.

$$Sorption\ (\%) = \frac{C_i - C_f}{C_i} \times 100 \qquad \textbf{(2.12)}$$

where, C_i and C_f are the initial and final concentration of the radionuclide in the aqueous phase after sorption onto the solid surface. The relationship between K_D and Sorption (%) is given as

$$Sorption\ (\%) = \frac{K_D}{K_D + 1} \times 100 \qquad \textbf{(2.13)}$$

2.7. BATCH SORPTION STUDIES

The batch sorption experiments were performed under ambient conditions. After several hours of preconditioning of the clay with the aqueous medium, an aliquot of radiotracer was added to clay suspension of known composition in predefined ionic strength maintained by $NaClO_4$. The pH values, in the desired range, were adjusted by the addition of dilute solutions of $HClO_4$ (Sigma-Aldrich) or NaOH (stock standard solution). The samples were agitated continuously using wrist hand shaker (Burrell, USA) to attain the sorption equilibrium; it may take days for some radionuclides. The final pH of the solution was measured and defined as, equilibrium pH, which was used for further data analysis. In ternary systems, involving complexing ions as well, suspensions were equilibrated with complexing anions, in a similar manner as mentioned above, with the difference that the complexing anions were added prior to radionuclide addition. The pH was measured using a pH electrode (Mettler Toledo or Lab India) calibrated against standard pH solutions (Merck). For studies involving higher ionic strength (1 M) solutions, the measured pH was corrected by using a suitable correction factor [124]. The correction factor was determined by measuring a series of known pH samples at different ionic strengths, and the difference in the measured pH values was taken as the correction factor for further experiments. A known volume of the suspensions was centrifuged using a high-speed centrifuge (Allegra 64R, Beckman Coulter or 3-30K sigma) for 15-20 minutes to remove the clay particles. This condition was sufficient to remove most of the clay particles. If required, dynamic light scattering measurements were used to confirm the absence of the floating particles after centrifugation. Aliquots of the supernatant solutions were mixed with scintillation cocktail (Ultima gold) for α or β-emitting radionuclides for the LSC assay (liquid scintillation counting using a Quantulus-1220, Perkin Elmer). For γ-emitting radionuclides, a well-type NaI(Tl) counting system was used. The % sorption was calculated as defined in equation 2.12. A blank experiment (without clay) was also performed

under the identical experimental conditions to account for the losses, if any, due to sorption of radionuclides onto the walls of the container used for the sorption experiments.

2.8. CLAY PREPARATION

In these studies, we have used clays of both natural as well as the commercial origin for sorption studies as indicated in **Table 2.1**. The majority of these studies were performed with natural bentonite samples from the Rajasthan and Kutch deposit (India) and 10 Hutor deposits (Khakassia, Russia), and a commercially available sample of FEBEX bentonite (Spain), bentonite (Aldrich) and kaolinite (Aldrich). The clay samples such as Kutch and FEBEX clay were treated for specific purposes and used for sorption studies. The FEBX clay was converted to Na and Ca-forms by shaking the clay suspension with 1M solution of NaCl or $CaCl_2$, respectively for 24 h, the procedure was repeated thrice, followed by washing with water. The solid phase thus obtained was separated from the liquids using high-speed centrifugation (20000 rpm for 20 minutes) (**Fig. 2.12**). The solid samples were kept overnight at 70°C for drying. To convert the original FEBEX clay into the Li-form, the clay was treated by a 1 M solution of LiCl for 24 h twice, washed with water and separated by centrifugation at 20000 rpm for 20 minutes. The solid mass was then heated at 250°C for 12 h. The original Kutch bentonite was also treated with 1 M $NaClO_4$ for 20 h, thrice, washed with water and separated by centrifugation at 20000 rpm for 20 minutes. The resultant solid was dried at 70°C for overnight. To remove iron oxides from the Kutch bentonite, the Kutch bentonite sample was treated with mixture of citrate buffer (composition: 0.13 M sodium citrate ($C_6H_5O_7Na_3$), 77 0.4 M sodium bicarbonate ($NaHCO_3$), and 0.53 M sodium chloride (NaCl) with reducing agent (sodium dithionite ($Na_2S_2O_4$)) at 80°C for ~2h (**Fig. 2.13)**. The ratio of reagents used for the iron oxide removal was 30 ml of buffer and 0.3 g of $Na_2S_2O_4$ per gram of Kutch bentonite. After this treatment, the obtained sample was washed with hydrochloric acid (pH 1) and converted to the Na-form (as for other clays). The fixations of interlayer cations in different bentonite samples were confirmed by XRD studies.

2.9. SURFACE COMPLEXATION MODELING (SCM) OF SORPTION DATA

The application of SCM provides a better understanding of the interaction between the radionuclide and the clay minerals. The scientific basis for the SCM is taken from aqueous complexation chemistry, assuming surface as a coordinating site with the surface hydroxyl group ≡SOH. An equilibrium constant (log K value) is defined for each type of the surface reaction, analogous to equilibrium constants in the aqueous chemistry although some surface reactions (like multidentate adsorption and ion exchange) require more specific formulation of the associated equilibrium constants (**Table 2.1**). The surface itself can undergo protonation or deprotonation reactions depending upon the pH of the system, like organic acids. Some of the common surface complexation reactions in the presence of metal ion and other complexants are given in **Table 2.2.** The key feature of any SCM approach is the incorporation of a range of realistic and relevant surface reactions.

Table 2.1: Source and treatment of studied clays

Name	Origin	Treatment
Kutch	The Kutch deposit, India	Crushed in a ball mill and sieved to size fractions < 75 μm; No chemical treatment
Purified Kutch		Fe-phase removal, see section 2.8
Rajasthan	Rajasthan, India	No chemical treatment
FEBEX	The Cortijo de Archidona deposit, Almería, Spain	Commercially Available, No additional treatment
Na-FEBEX		Conversion to Na-Form, see Section 2.8
Ca-FEBEX		Conversion to Ca-Form, see Section 2.8
Li-FEBEX		Conversion to Li-Form, see Section 2.8
Khakassia	The 10 Hutor deposits, Khakassia, Russia	Commercially Available, Na_2CO_3 treatment for Na-Form
Kaolinite	Aldrich	Commercially Available, No additional treatment
Bentonite	Aldrich	Commercially Available, No additional treatment

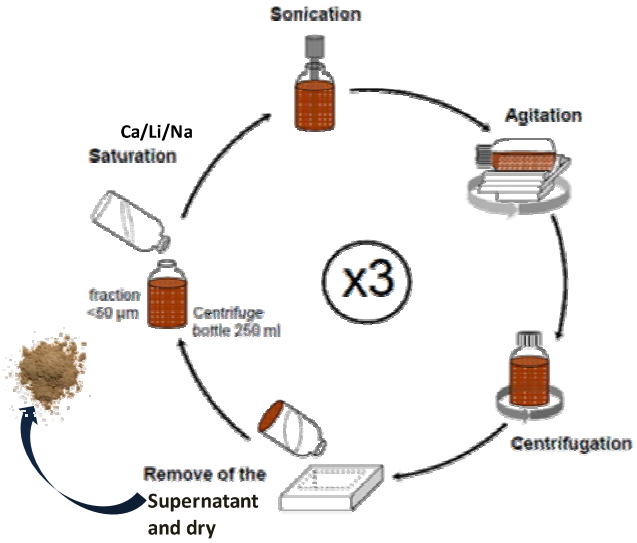

Fig. 2.12. Schematic for clay preparation of different interlayer cationic (Na/Ca/Li) form; T: 298K.

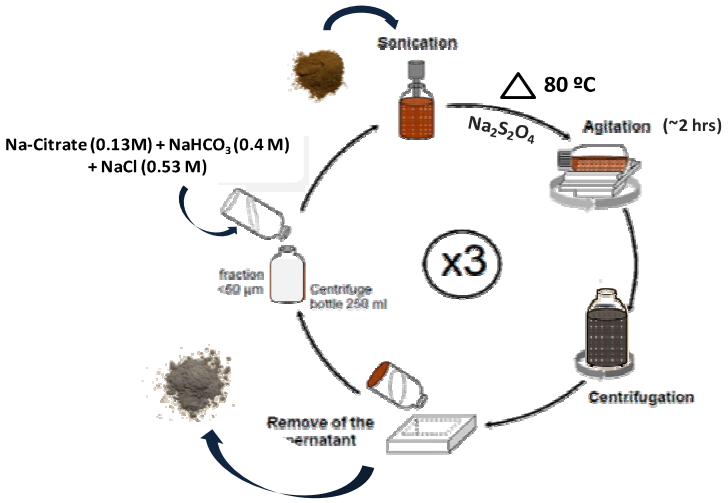

Fig. 2.13. Schematic for iron removal from Kutch bentonite

The complexity of natural systems makes it impossible to experimentally determine the radionuclide sorption systematically for all conceivable sets of experimental conditions. For modeling the sorption data in mineral assemblages, two major alternative approaches have emerged over the time. These are the component additivity (CA) and generalized composite approaches (GCA) [113-114]. The CA approach the mineral assemblage is considered as a substrate that is composed of a mixture of different identifiable minerals. In this case, surface

chemical reactions are known from independent studies of each mineral component of the complex mineral assemblage [113]. These single-mineral component SCMs were combined

Table 2.2. The Surface complexation reactions (typical of oxide surfaces) used for SCM of sorption data

Reaction type	Representative reaction
For pure oxide surface	
Surface hydroxyl protonation	. $\equiv SOH + H^+ \rightarrow \equiv SOH_2^+$
Surface hydroxyl deprotonation	. $\equiv SOH \rightarrow \equiv SO^- + H^+$
In presence of 'n' valent metal cation (M^{n+})	
Absorption of metal ion	. $\equiv SOH + M^{n+} \rightarrow \equiv SOM^{(n-1)} + H^+$
Absorption accompanied by hydrolysis	$\equiv SOH + M^{n+} + H_2O \rightarrow \equiv SOM(OH)^{(n-2)} + 2H^+$
Formation of binuclear complex	$\equiv SOH + 2M^{n+} + H_2O \rightarrow \equiv SOM_2^{(2n-1)} + H^+$
Surface acts in bidentate mode	$2 (\equiv SOH) + 2M^{n+} + H_2O \rightarrow (\equiv SO)_2M^{(n-2)} + 2H^+$
Ion exchange reaction	$X^-Na + M^{n+} \rightarrow XM^{n-1} + Na^+$
In presence of ligands / inorganic anions (L^{z-})	
Ligand attachment	$\equiv SOH + L^{z-} \rightarrow \equiv SOHL^{z-}$
Ligand exchange	$\equiv SOH + L^{z-} + H^+ \rightarrow \equiv SL^{1-z} + H_2O$
In presence of both 'n' valent metal cation (M^{n+}) and ligands / inorganic anions (L^{z-})	
Ternary complexation	$\equiv SOH + L^{z-} + M^{n+} \rightarrow \equiv SML^{n-z-1} + H^+$

in an additive fashion, taking care of the relative amounts of surface area of each mineral (*i.e.,* site concentration of each component) present in the substrate hence, called as CA modeling approach. Using this approach the adsorption by the mixture of mineral components can then be predicted in an equilibrium calculation, without any fitting of

experimental data for the mixture. However, it is generally very difficult to identify all (sorbing) solids in real natural systems or to ascertain whether their surface chemical property remains the same, as in their pure form, in the mineral assemblage. This gives rise to the GC approach wherein the surface of the composite mineral assemblage is considered to be too complex to be quantified in terms of the contributions of individual solid phases to adsorption and/or that the contribution of individual solid components is not simply additive [110]. In such cases, the metal ion sorption on the whole substrate can often be described by mass laws written in terms of some generic surface sites. The number of surface groups may be estimated from the specific surface area of the mineral assemblage or by other means. The stoichiometry and formation constants for each mass law equation are then determined by fitting experimental sorption data (pH edge under relevant conditions) for the mineral assemblage as a whole [110,125]. The GCA has generally been applied using a Non-Electrostatic Model (NEM) [126]. While the fitted mass action equations may not provide very accurate representations of the stoichiometry of the reactions at the molecular scale it can still be coupled with aqueous complexation reactions to provide SCM simulations of macroscopic sorption data as athe function of aqueous chemical conditions. In the present study, both approaches were used and the outcomes were explained based on the principles of aqueous complexation chemistry. The sorption data were modeled using the geochemical speciation software PHREEQC USGS, 179 2015) or FITEQL 4.0. The thermodynamic constants for aqueous speciation of actinides were taken from the NEA thermodynamic database [127].

3

CHARACTERIZATION OF CLAYS OF DIFFERENT ORIGIN

3.1. INTRODUCTION

The understanding of material/surface properties is essential before one can understand the sorption and speciation behaviors of the radionuclide at mineral-water interfaces. The identification and quantification of the mineralogical composition in natural sediments is a challenging task but has great relevance in understanding the mechanism of sorption and migration. For such complex systems, even if the quantitative and/or qualitative data of mineralogical composition were made, further understanding of their combined behavior under the given physical or chemical conditions is rather tough. In the present Chapter, the clays from both natural and commercial origin were thoroughly characterized by one or more physical techniques such as X-ray fluorescence (XRF), X-ray diffraction (XRD), Fourier Transform Infrared (FTIR), BET (surface area), High Resolution Transmission Electron Microscopy (HR-TEM), Scanning Electron Microscopy (SEM), Mössbauer spectroscopy, etc. The surface properties of bentonite were determined using the Gran plot. The cation exchange capacity and surface charge etc were also determined. The interaction of clay minerals with the humic acid was also studied.

This Chapter lists the results of the characterization of the clay materials using various techniques such as XRD, FTIR, XRF, HR-TEM, etc. to get an idea about the elemental

composition, phases, Fe(II)/Fe(III) speciation, size and structural distribution of the clay minerals, etc. This information is a pre-requisite for understanding the mechanism of sorption as these factors influence the interaction between the actinides and the clay minerals and hence governs their fate in the environmental system.

3.2. X-RAY DIFFRACTION (XRD)

The identification and quantification of clay minerals in soils are delicate issues due to the inherent complexity of the clay mineralogy encountered in the environmental system. This complexity occurs due to the important chemical and structural heterogeneity of clay minerals found in soils. Indeed, several different types of clay minerals (kaolinite, chlorite, smectite, illite, mica, etc.) can coexist within a wide range of particle sizes distribution (from nm to few μm). In order to improve the identification of the soil clay minerals, an approach having both sequential particle size fractionation and XRD profile modeling has been proposed. In the present case, XRD was used to investigate the mineral composition of clay samples, as well as colloidal clay fractions (<0.5 mm), that was separated from a water suspension according to Stokes' law, without using any chemical dispersants. The identification of the mineral composition was done with the textural (oriented) samples prepared from a bentonite suspension in the air-dried and ethylene glycol solvated states [128]. The final quantitative mineral composition was calculated using the Rietveld method using the BGMN program [129].

3.2.1. Clay Minerals without any Chemical Modification

The XRD data show that all the studied clay minerals consist of montmorillonite (main reflections – 15.2, 4.5, 2.55, 1.70, 1.501 Å) with a small admixture of quartz (3.34 Å), calcite (3.05 Å), goethite (4.17, 2.45, 2.28 Å) and hematite (2.69, 2.49 Å). The X-ray diffraction patterns for all the studied bentonite samples have a (001) reflection in the range of 12 Å to 15 Å. For Rajasthan, FEBEX and Kutch clay samples, the (001) reflection occurs at d =

12.8 Å,15.0 Å and d = 15.2 Å respectively mainly due to the presence of admixture of Na^+ and Ca^{2+}, Mg^{2+} forms of montmorillonite in these clays., whereas for Khakassia clay its d = 12.6 Å which indicates the predominant presence of Na^+ form montmorillonite . The non-basal reflection at d = 4.47 Å, 2.56 Å, 1.69 Å as well as some other small non-basal reflections have the same values for all the studied clay systems. The values of the (060)

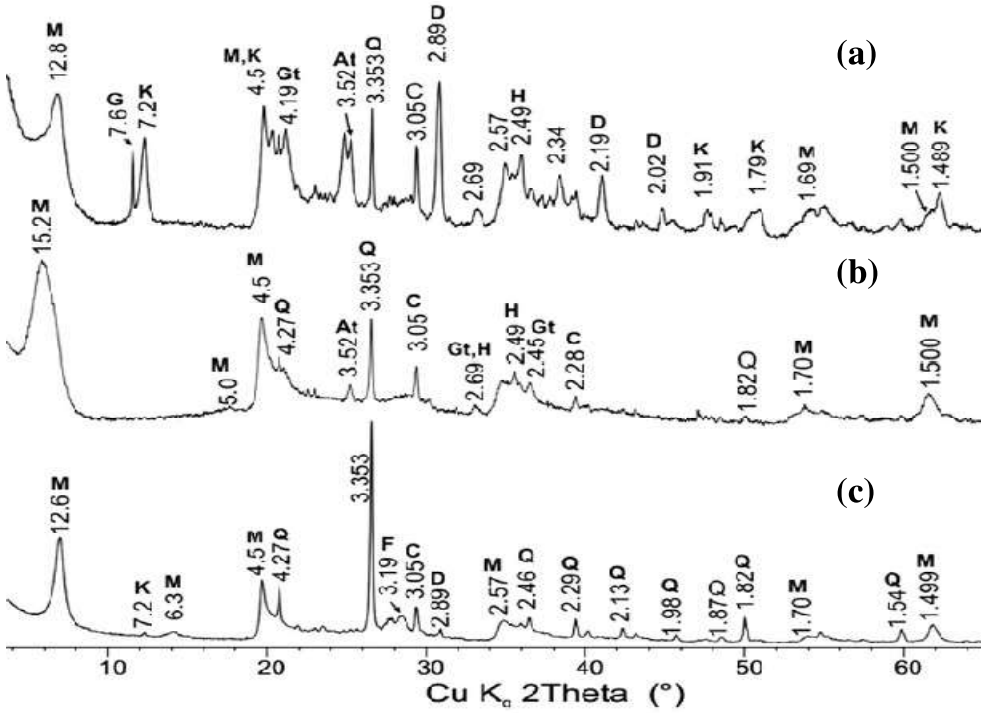

Fig. 3.1 X-Ray diffraction patterns collected for the non-oriented natural clays of (a) Rajasthan, (b) Kutch and (c) Khakassia bentonite clays. M: montmorillonite, K: kaolinite, Q: quartz, C: calcite, D: dolomite, At: anatase, G: gypsum, Gt: goethite, H: hematite, F: feldspar.

reflection of the Kutch and Rajasthan clays are higher than that of the Khakassia and FEBEX clays, which indicates the presence of iron in the 2:1 layer of montmorillonite. The strongest reflections of the admixed clay and non-clay minerals are shown in **Fig. 3.1**. The compositions of colloidal fractions <0.5 µm for Kutch, Rajasthan and Khakassia clay samples are found to be enriched in Na- montmorillonite (**Fig.3.2**), with basal reflections at $d_{(001)}$ = 12.5 Å, $d_{(002)}$ = 6.11-6.23 Å, $d_{(004)}$ = 3.12-3.13 Å and $d_{(006)}$ = 2.07 Å. The presence of kaolinite in the Rajasthan clay was identified by a series of basal reflections at $d_{(001)}$ = 7.16 Å,

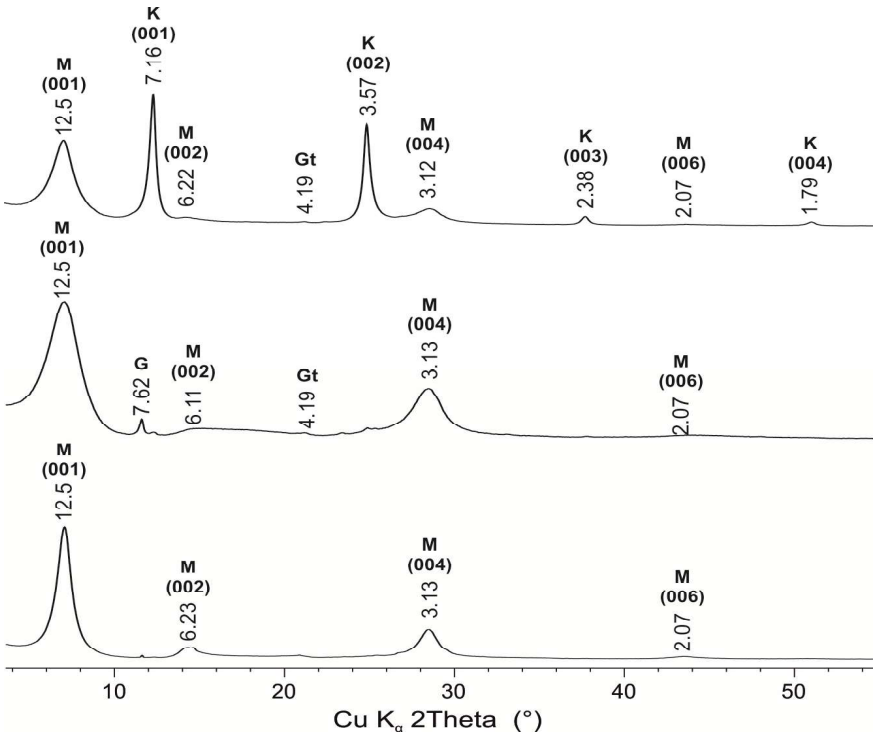

Fig. 3.2. X-Ray diffraction patterns collected for the oriented samples of colloidal fraction <0.5 μm separated from (a) Rajasthan, (b) Kutch and (c) Khakassia bentonite clays. M: montmorillonite, K: kaolinite, G: gypsum, Gt: goethite, (001) - basal reflections of clay minerals.

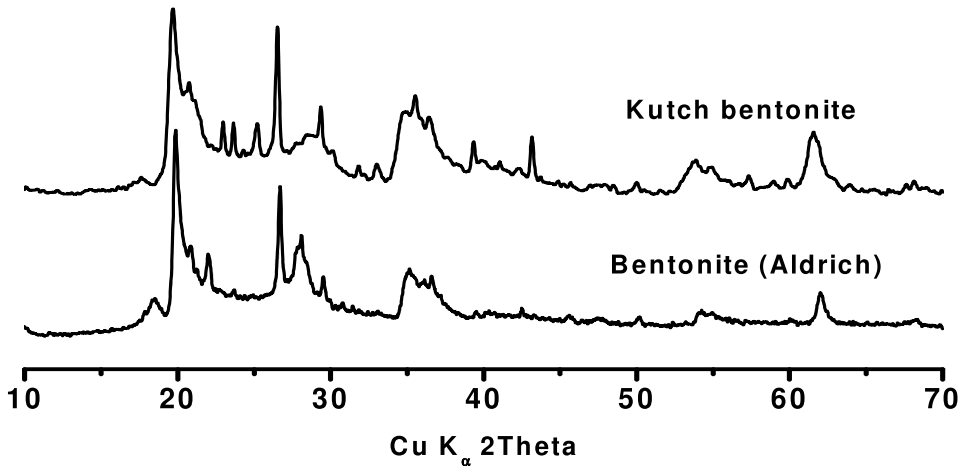

Fig. 3.3. XRD pattern of the Kutch bentonite and bentonite of commercial origin (Aldrich).

$d_{(002)}$ = 3.57 Å, $d_{(003)}$ = 2.38 Å, and $d_{(004)}$ = 1.79 Å. The sign of iron-containing minerals (*e.g.*, goethite) in the Rajasthan and Kutch clays was identified by the small reflection at d = 4.19

Å, and an admixture of gypsum in the Kutch clay sample was identified based on the small reflection at d = 7.62 Å. The XRD spectrum of Kutch bentonite is very similar to that of the bentonite procured from Aldrich (Fig.3.3). The FEBEX spectrum is free from admixture, except quartz (Fig 3.4). The spectrum is kaolinite clay sample (**Fig. 3.4**) mainly consist of kaolinite (7.19, 4.47, 3.58, 2.57, 2.34, 1.99, 1.67, 1.490 Å) with an admixture of quartz (3.35 Å), illite (10.0 Å) and smectite (12.6 Å). The mineral compositions are given in **Table 3.1.**

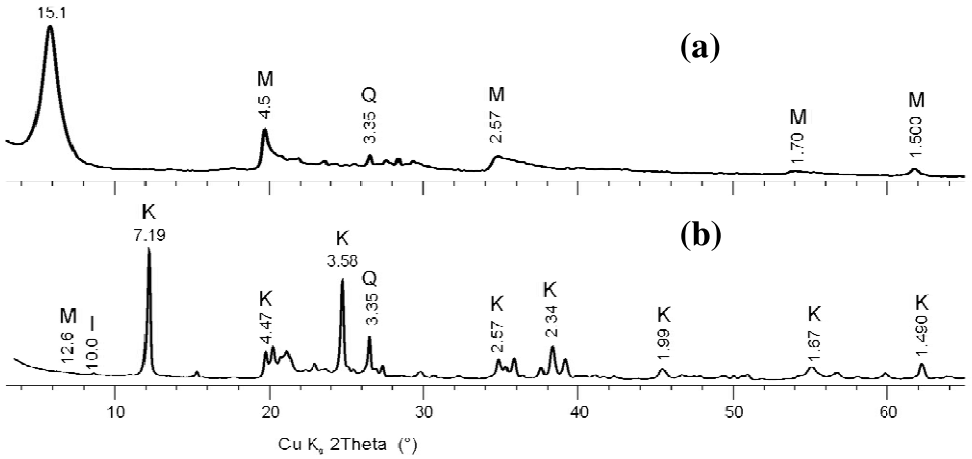

Fig. 3.4. XRD pattern of (a) FEBEX bentonite and (b) kaolinite clay of commercial origin (Aldrich).

3.2.2. Clay Minerals after Chemical Modification

As already discussed in Chapter 2, modifications in the clays were done to understand the role of these modifications onto radionuclide sorption. Before going for the sorption studies the modified clays were characterized using XRD and other relevant techniques. The different mono cationic form of the clay minerals can be characterized by the (001) basal reflections. The size (or hydration) of monocations in the interlayer of the clay minerals decide the width of interlayer spacing (d) and hence, according to Bragg law (see XRD in experimental techniques; Chapter 2, Section 2.4.1) the variation in the d causes variation in 2θ value, a measurable quantity in the XRD studies. The modification of the Kutch bentonite to its Na-form can be seen from the shift of basal plane reflection, $d_{(001)}$, from 15.2 Å in pure to $d_{(001)}$ = 12.6 Å for the modified sample. Similarly, for the FEBEX clay, the quality of the

Table 3.1. Composition and related properties of the studied bentonite

Sample	Kutch Clay	Purified Kutch Clay	Khakassia Clay	FEBEX Clay	Rajasthan	Kaolinite
Composition, mass (%)						
Na^+-Montmorillonite	23.6	83.4	65	59.5	32.8	4.5
Ca,Mg^{2+}-Montmorillonite	66.4	12.9		27.3	14.4	-
Illite	-	-	4.5	-		7.1
Kaolinite	-	-	1.3	-	26.4	76.2
Chlorite	-	-	2.2	-		-
Quartz	3.5	0.9	15.9	1.9	1.9	4.2
Albite	-	-	6.3	5.3		1.5
Microcline	-	-	-	3.2		6.5
Calcite	1.6	1.6	3.8	2	3.9	-
Dolomite	-	-	0.5		11.9	-
Anatase	1.1	1.2	-	-	2.9	-
Goethite	3	-	-	-	4.5	-
Hematite	0.7	-	-	-	0.7	-
Sylvite	-	-	-	0.8		-
Specific surface area, m^2/g						
	115	150	15	60	50	6
Average coherent scattering domain size along ***c***-axis, nm						
	5	4	12	6	-	46
Average coherent scattering domain size along ***b***-axis, nm						
	11	10	16	17	-	38
CEC (mmol/kg)						
	950[a]	1009[a]	698[b]	1331[a]	421[b]	-

[a]NH_4.Ac method, [b]Cohex method

monocation forms were interpreted from the XRD data (**Fig.3.5**). The interplanar spacing of the basal reflections $d_{(001)}$ were equal to 15.0 Å for the original FEBEX clay(without treatment) which reduced to $d_{(001)}$ = 13.5 Å for the Ca-form of the clay and to $d_{(001)}$ = 12.2 Å

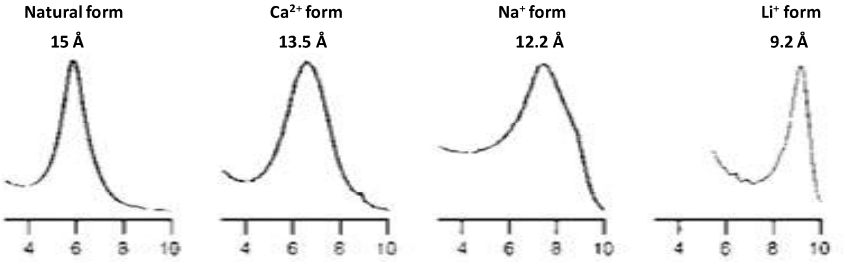

Fig. 3.5. The XRD pattern of the FEBEX clay with modified cation form

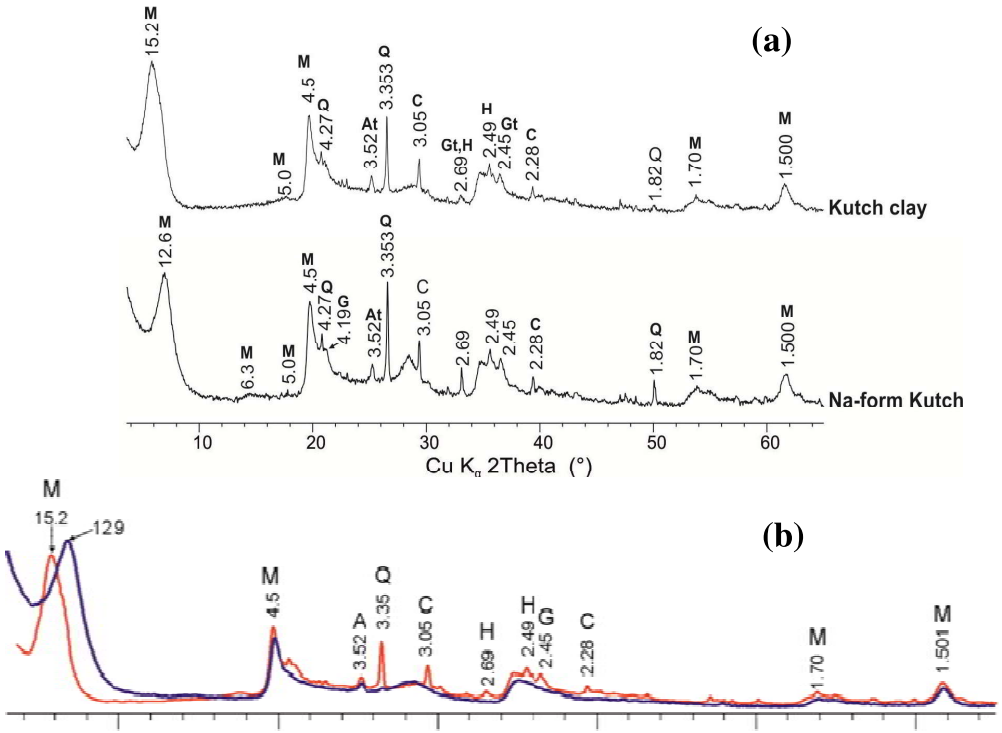

Fig. 3.6. The XRD pattern of modified Kutch clay (a) Kutch and Na-form of Kutch; (b) Kutch original (Red) and Kutch purified (after Fe-phase removal) (blue).

for the Na-form and $d_{(001)}$ = 9.2 Å for the Li-form. The $d_{(001)}$ = 9.2 Å for the Li-form of FEBEX can be explained as the lithium cation has a small ionic radius and hence, is capable of going to the vacant positions in the octahedral sheet of smectite (e.g. montmorillonite) to compensate the excess negative charge upon prolonged heating (Chapter 2, Section 2.8). As a

result, the Li-form of the FEBEX clay loses its ability to swell under ethylene glycol solvation and resulting in smaller interplanar spacing. The XRD spectrum of the Kutch sample was also recorded after iron removal by chemical treatment. The d-spacing of the non-basal reflection did not change after the chemical treatment, suggesting that the structure of the montmorillonite was not altered and Fe-containing octahedral were not damaged (**Fig. 3.6**). The decrease in the interplanar distances of the basal reflection $d_{(001)}$ from 15.2 to 12.9 Å occurred as a result of the substitution of Ca^{2+} and Mg^{2+} cations by Na^{+} ion in the interlayer spacing.

In short, all the studied bentonite clays were found to be enriched in smectite (montmorillonite), with some admixture of other clay minerals (chlorite, kaolinite), as well as carbonates, quartz, different iron oxides and hydroxides and other minerals in relatively small amounts. Due to the different position of the basal reflection $d_{(001)}$ reflections, the Na^{+} and Ca^{2+} forms were identified and estimated.

3.3. IRON SPECIATION IN CLAY MINERALS

The XRD data suggest the presence of Fe in the studies clay minerals. Iron being a redox-sensitive element can affect the sorption and speciation of redox active radionuclides such as U, Np, and Pu. Iron can be present is different mineralogical forms, and different forms may have different sorption behavior. Iron can also be present as either ferrous of ferric ions in its minerals. In view of different mineralogy and redox behaviors of iron, it's very important to have knowledge of iron speciation in the given system to better understand the behavior of the clay system.

3.3.1 Mössbauer Spectroscopy

The Mössbauer spectroscopy was used for iron (Fe) speciation in the bentonite clay samples. The Mössbauer spectra of the ^{57}Fe nuclei were measured at different temperatures for the bentonite clay samples. The Mössbauer spectra presented a superposition of broadened

quadrupole doublet and broadened magnetic component, which was attributed to a magnetically ordered Fe-phase. The minor components of the Khakassia clay sample are presented in the **Fig. 3.7**. The best fit hyperfine parameters of the de-convoluted spectra at various temperatures are shown in **Table 3.2.** From these studies, one can conclude that all the bentonite clay samples consist of ferric atoms in the high-spin state within an octahedral oxygen environment in accordance with the isomer shift values, which can be attributed to iron atoms within nonmagnetic minerals [130]. In addition, the Khakassia and FEBEX clay samples consisted of two nonmagnetic quadrupole doublets with large isomer shifts and quadrupole splitting (Table 3.2) indicating the presence of Fe^{2+} sites. The hyperfine parameters are also similar to those for Si and Al minerals but cannot be attributed to a specific source [122]. The hyperfine parameter analysis shows non-significant changes in the sub-spectra areas versus temperature. One may conclude that the Fe^{3+} atoms within all clay samples are separated into two essentially different states. The first can be presented as a distribution of quadrupole doublets, but it is impossible to fit it correctly with several quadrupole doublets of natural line width (**Fig. 3.7**). The average isomer shift of this distribution is indicative of high-spin ferric atoms within an octahedral oxygen environment. The wide distribution of quadrupole splitting values (**Fig. 3.9 (a, c, e))** is related to different forms of ferric hydroxides, surface atoms, and solid solutions of nonmagnetic Al and Si phases [122]. It can be observed that the profiles of the quadrupole splitting distribution are similar for all samples and do not change significantly with temperature. The second part is a broadened Zeeman component that is present in all samples, which could appear due to the size effects of nanocrystalline particles [131]. This hypothesis is logical as the magnetic component becomes more "classic" as the temperature decreases (**Fig. 3.7 and Fig. 3.8).** These components were fitted (**Fig. 3.9 (b, d, f))** as a distribution of Zeeman sextets with different frequencies of slow super-paramagnetic relaxation, which is a manifestation of the particle size effect [131]. The hyperfine parameters of these distributions (**Table 3.2**)

Table 3.2. ^{57}Fe hyperfine parameters of clay samples at different temperatures

Sample	Temp., K	Phase	<δ>, mm/s	<ε> or Δ/2, mm/s	<H_{hf}>, kOe	A, %	<Ω>, GHz
Rajasthan clay	295	Fe minerals	0.35(2)	-0.04(2)	530*	58(2)	12.0(25)
		Fe^{3+}-para	0.36(1)	0.33(1)	-	42(2)	-
	77	Fe minerals	0.48(1)	-0.11(1)	530*	61(2)	6.9(27)
		Fe^{3+}-para	0.47(1)	0.35(1)	-	39(2)	-
Kutch clay	295	Fe minerals	0.34(2)	-0.02(2)	530*	44(2)	700(200)
		Fe^{3+}-para	0.35(1)	0.31(1)	-	56(2)	-
	77	Fe minerals	0.48(1)	-0.13(1)	530*	44(2)	18.5(40)
		Fe^{3+}-para	0.47(1)	0.30(1)	-	56(2)	-
	15	Fe minerals	0.48(1)	-0.13(1)	530*	44(2)	7.7(25)
		Fe^{3+}-para	0.47(1)	0.31(1)	-	56(2)	-
Khakassia clay	295	Fe minerals	0.36(12)	-0.15(13)	530*	21(10)	100(60)
		Fe^{3+}-para	0.33(1)	0.36(1)	-	59(8)	-
		Fe^{2+}-I	1.17(4)	1.04(4)	-	5(2)	-
		Fe^{2+}-II	1.15(1)	1.33(1)	-	13(3)	-
	77	Fe minerals	0.39(1)	-0.15(5)	530*	29(6)	35(20)
		Fe^{3+}-para	0.39(1)	0.40(1)	-	57(5)	-
		Fe^{2+}-I	1.34(2)	1.09(2)	-	6(2)	-
		Fe^{2+}-II	1.31(1)	1.44(1)	-	8(2)	-
FEBEX original	295	Fe^{3+}-para	0.36(1)	0.28(3)	-	89(2)	-
		Fe^{2+}	1.18(2)	1.25(2)	-	11(1)	-
Kutch clay Purified	295	Fe^{3+}-para	0.35(1)	0.36(3)	-	100	-
	15	Fe^{3+}-para	0.47(1)	0.36(3)	-	100	-

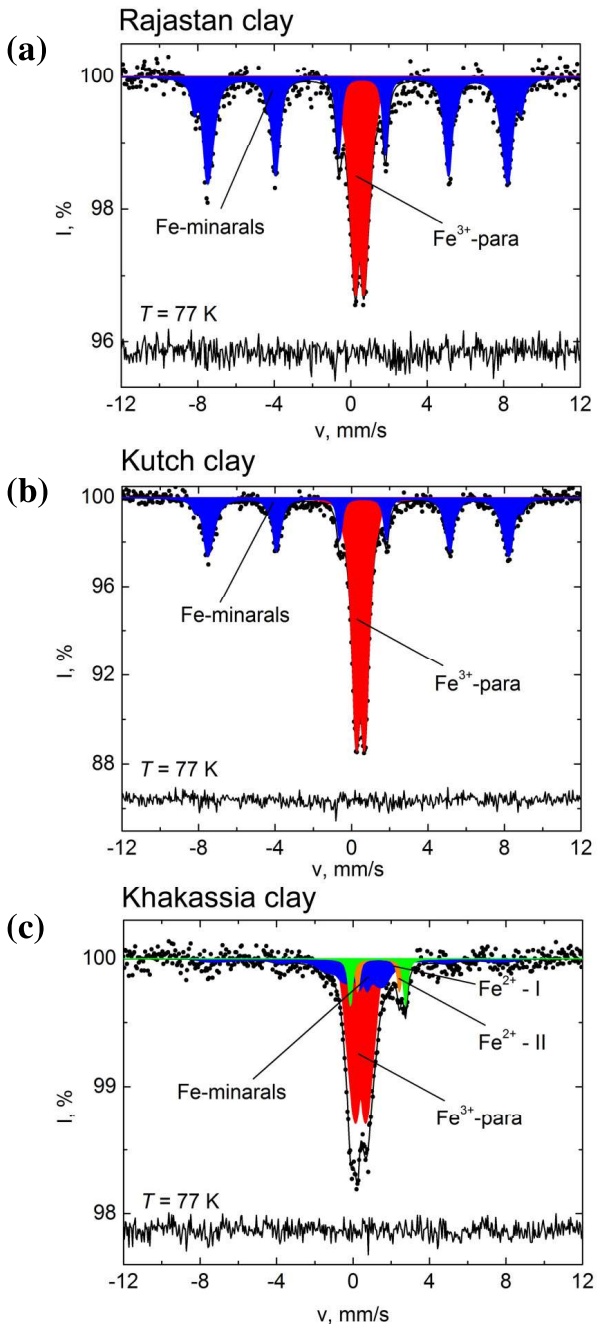

Fig. 3.7. Mössbauer spectra of (a) Rajasthan, (b) Kutch and (c) Khakassia clays measured at 77 K.

correspond to the goethite nanocrystalline phase for which the absolute value of the quadrupole shift ε is slightly higher than for the α-Fe_2O_3 hematite phase 132]. Thus, the Kutch and Rajasthan samples contain only a small amount (~3-6%) of "bulk" α-Fe_2O_3. The

weak changes in the quadrupole shift average values (**Table 3.2**) are related to the Morin transition (T_M ~260 K) of the hematite phase [133].The Mössbauer spectra of the Kutch clay, after Fe-phase removal, were recorded at 295 K and 15 K (**Fig.3.10**) and showed a quadrupole doublet with isomer shift (δ) and quadrupole splitting (Δ) (**Table 3.2**),

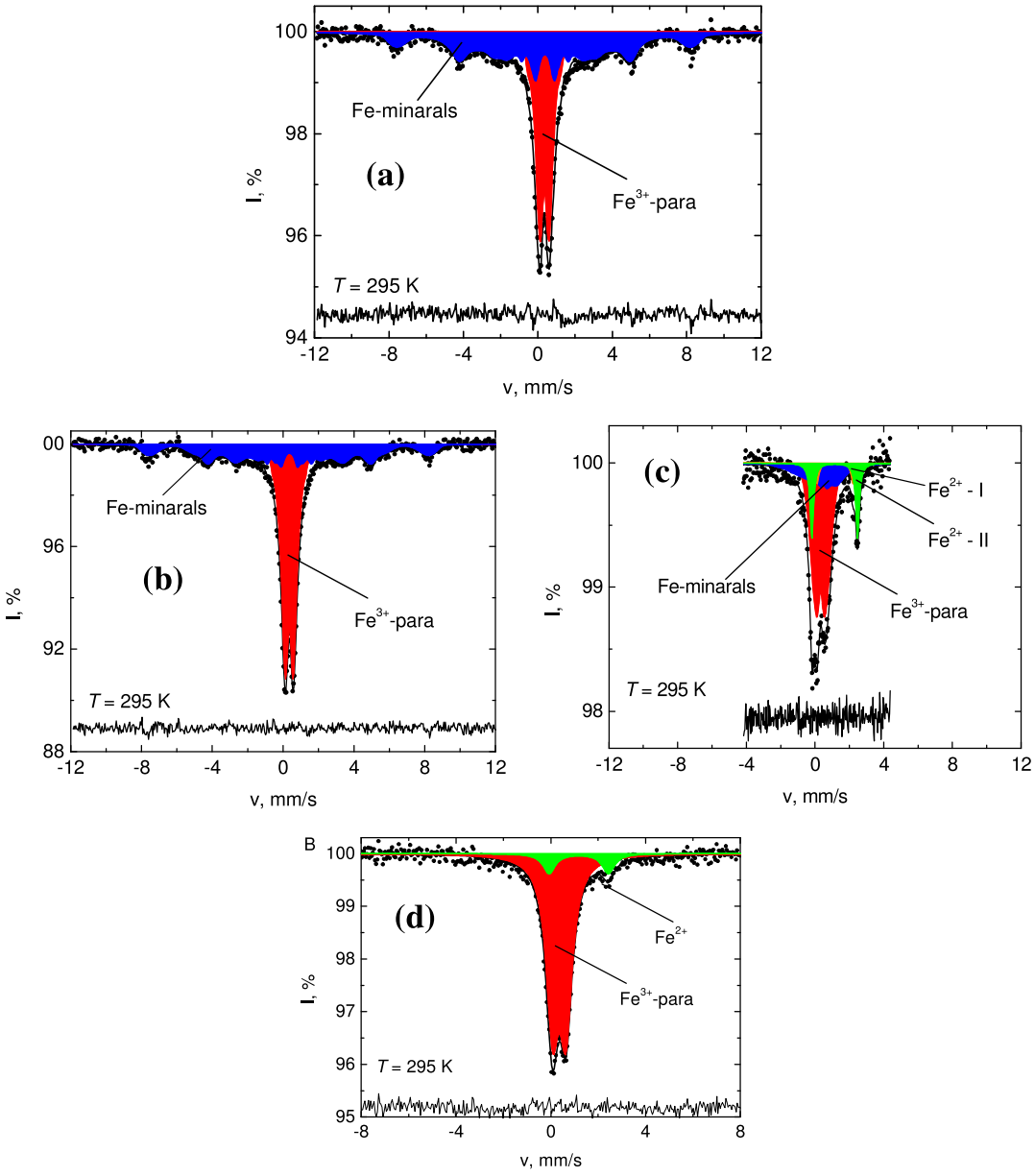

Fig. 3.8. Mössbauer spectra of (a) Rajasthan, (b) Kutch (c) Khakassia and (d) FEBEX clays measured at 295 K.

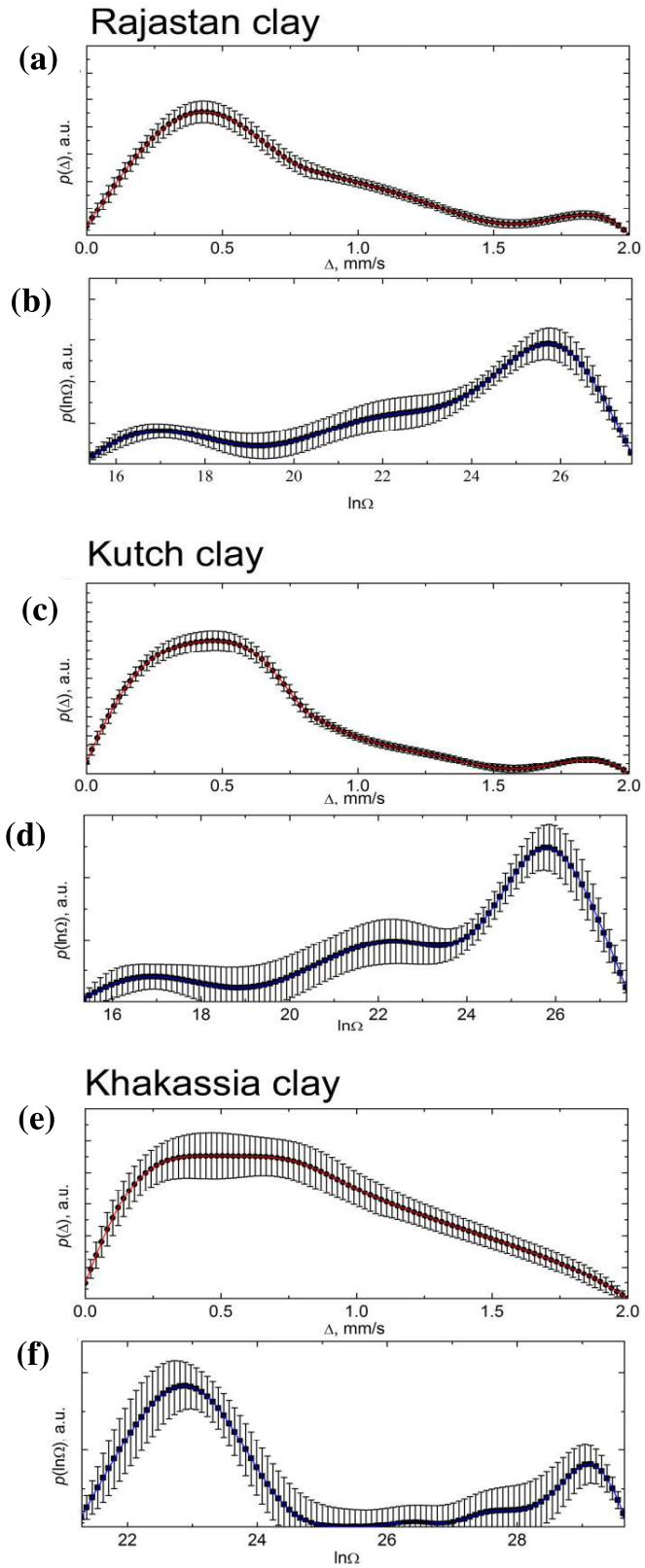

Fig. 3.9. Distributions (a, c, e) of the quadrupole splitting and (b, d, f) relaxation frequencies for Mössbauer spectra measured at 77 K of the Rajasthan, Kutch, and Khakassia clays.

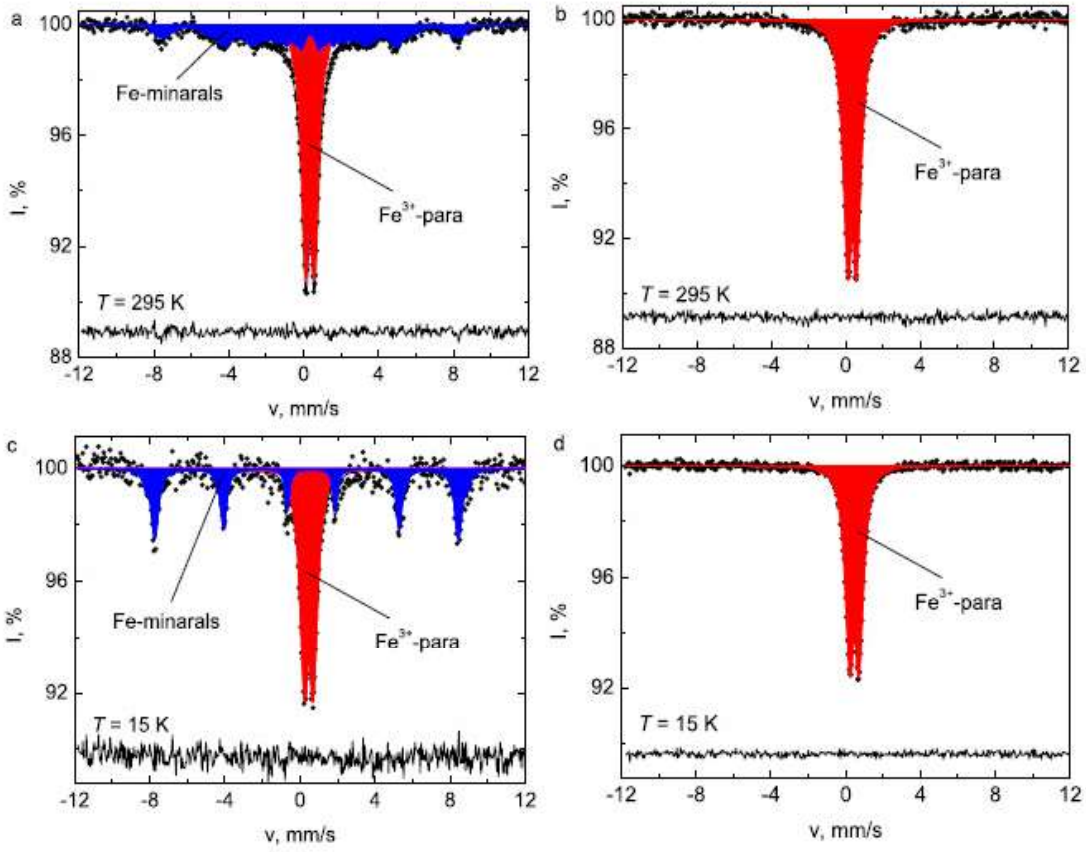

Fig. 3.10. Mössbauer spectra of the original (a,c) and modified (b,d) Kutch clays measured at 15 K (c, d) and 295 K (a,b).

corresponding to the high-spin Fe^{3+} ions in octahedral oxygen surroundings. Both the spectra have doublets which are "static" due to either the broad size distribution of fine particles or a mixed environment of Fe^{3+}. The mixed environment is caused by the presence of Si and Al atoms in the local environment and is not related, for example, by the super-paramagnetic relaxation effects of nanocrystalline particles. It was of interest to compare the observed spectra of purified Kutch clay with the original Kutch samples (**Fig. 3.10**). In addition to the quadrupole doublet, the spectra consist of a very diffuse Zeeman pattern indicative of the significantly inhomogeneous magnetic state of iron cations. For the analysis of this component, the distribution of hyperfine magnetic broadened components (W), which indicate the non-uniform crystal environment of Fe atoms within this mineral. The width of

the quadrupole doublet components does not change with temperature. Thus, the observed broadening of the quadrupole fields at ^{57}Fe nuclei (H_{hf}) was obtained. The average value of H_{hf}, is noticeably lower than the hyperfine magnetic fields for large particles, which could be due to the size effects of the nanocrystalline particles. The lack of this magnetically split sub-spectrum in the spectra of the purified sample recorded over a wide temperature range suggests that the treatment of the Kutch samples with citric acid solution completely washes out the goethite particles. Briefly, Kutch clay contains only Fe(III) in different forms: as structural iron (56%) and intrinsic iron phases (44%) (hematite and goethite). Khakassia clay contains both Fe(II) and Fe(III) out of which the latter is in the form of structural iron (57%) and iron oxides (29%). The remaining iron is structural divalent iron. The FEBEX original contains both Fe(III) (89%) and Fe(II) (11%). The modified Kutch (after iron phase's removal) contains only structural iron and addition phases were absent. The present studies show how Mössbauer spectroscopy is the most reliable and sensitive method of phase analysis in complex natural clay systems, since the fine goethite particles, due to their small size and low abundance, could not be detected by XRD analysis of clay minerals.

3.4. SURFACE PROPERTIES OF CLAY MINERALS

3.4.1. Fourier Transform Infrared Spectroscopy (FTIR)

The FTIR spectra of the studied clay samples in the ranges 3900-3000 cm^{-1} and 1800-500 cm^{-1} (recorded in the ATR mode) was shown in **Fig.3.11**. The correlation of the absorption bands' wave numbers with different types of vibrations was carried out in accordance with 134-136]. Based on the FTIR spectral data all the clays are mainly composed of dioctahedral Al-smectite, as evident by the position and profile of characteristic bands at 3623, 998, 916, and 525 cm^{-1}[135-138]. All the samples show broad maxima in the range 995 cm^{-1} to 1000 cm^{-1} for Si-O stretching vibrations. Small modulations at 916 and 844 cm^{-1} belong to the deformation vibrations of Al-OH-Al and Al-OH-Mg, respectively [136]. However, some difference can be seen depending on the present admixture in the clay samples. For example,

bentonite (Aldrich) shows broad maxima at 998 cm-1 Si-O stretching vibrations. In addition to the quartz (799 and 781 cm^{-1}) and carbonate (1431 and 877 cm^{-1}), kaolinite is easily identifiable in the clay minerals among the impurities on the strip at 3695 cm^{-1}. In the region of 600 to 1800 cm^{-1}, most of the bentonite clay samples were similar, except Rajasthan due to predominant peaks at 937 and 1025 cm^{-1}. The presence of quartz in the Khakassia can be seen from the presence of peaks at 797 and 776 cm^{-1}. The Si-O (longitudinal mode) stretching and OH deformation of water at 1116 cm^{-1} and 1630 cm^{-1} was found in all clays. In the region of the OH stretching vibrations, Khakassian and bentonite (Aldrich) look similar. The spectra of Kutch clay was dominated by broad spectrum at the 3000 to 3500 cm^{-1} region and a peak at 3616 cm^{-1}. More details about the origin of above wave number and the state of

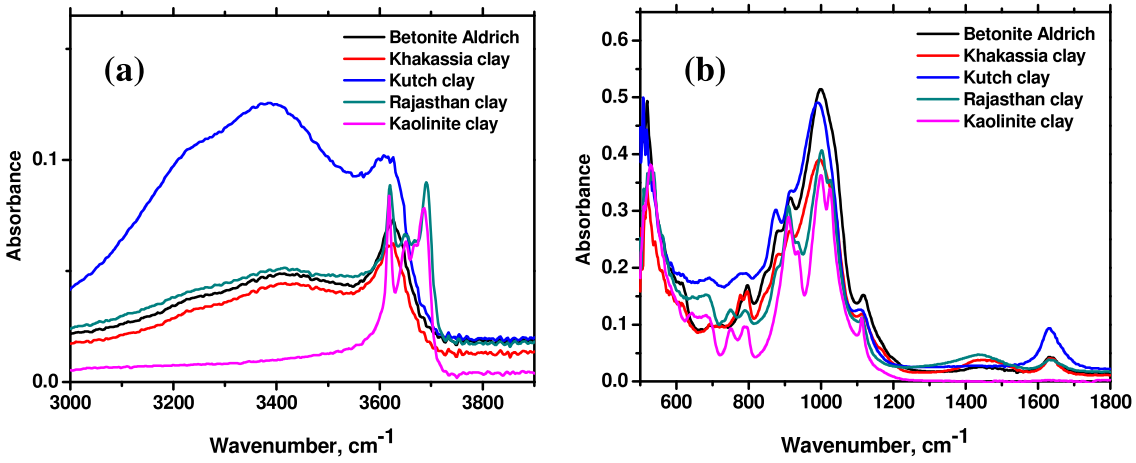

Fig. 3. 11. FTIR spectra (a) 500-1800 cm^{-1} region and (b) 3000 to 3900 cm^{-1} region, of studied clays using ATR-FTIR.

water in smectite in the interlayer can be found elsewhere. The FTIR of Rajasthan bentonite clay is dominated by OH stretching vibration characteristics of the kaolinite clay. The stretching vibrations of the OH^-groups, in addition to the wide bandwidth ~3418 cm^{-1} related to the vibrations of absorbed water, another broad intensive band is observed with the maximum absorption at 3624 cm^{-1}. This band is a superposition of the individual absorption bands of the cation-cation (Al-OH-Al, Al-OH-Mg, Mg-OH-Fe, Al-OH-Fe, Fe-OH-Fe, etc.)

[138]. Among the impurities in the FEBEX clay, a small amount of quartz (796 cm^{-1}) was found. **Fig. 3.12** shows the FTIR spectra of FEBEX, modified Kutch (after Fe-removal), Kutch and kaolinite in transmittance mode (using KBr pellets).

The FTIR spectra of the FEBEX clay also corresponded to that of the dioctahedral Al-smectite [135-138] where the most intense and relatively symmetrical absorption band at 1035 cm^{-1} belongs to the stretching vibrations of Si-O. Deformation vibrations of Si-O appear on the FTIR spectrum at 521 (Al-O-Si) and 468 (Si-O-Si), and as a shoulder at 622 cm^{-1} (Al-O-Si, Si-O-Si). Small modulations at 916 and 844 cm^{-1} belong to the deformation vibrations of Al-OH-Al and Al-OH-Mg, respectively [136]. In the region of the stretching vibrations of the OH^-groups, in addition to the wide bandwidth ~3418 cm^{-1} related to the vibrations of

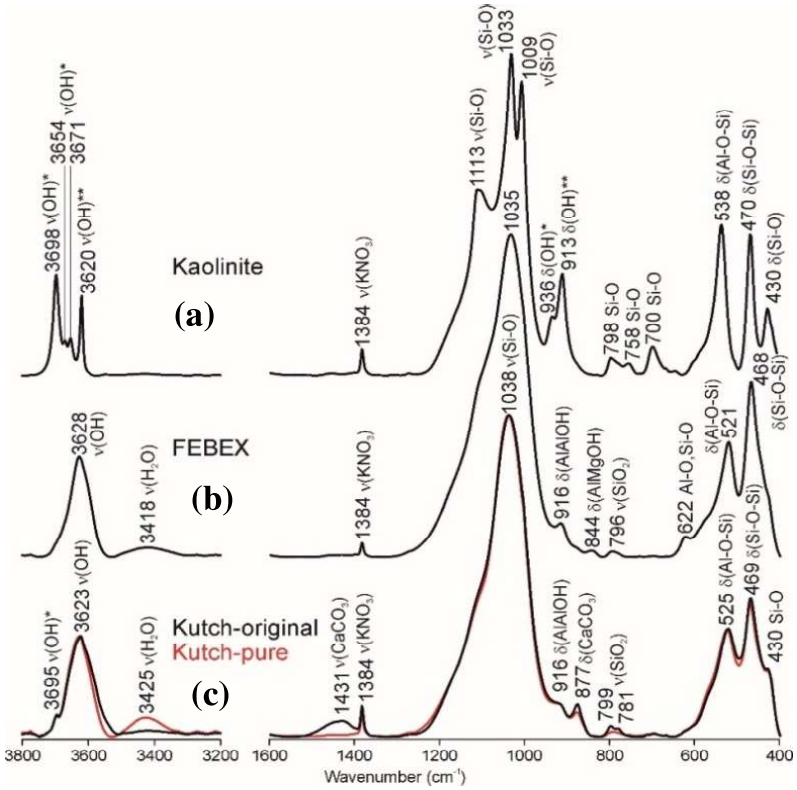

Fig. 3.12. FTIR spectra of studied clays: (a) kaolinite clay, (b) FEBEX clay, (c) Kutch clay (black line: original clay, red line: purified clay).ν stretching vibrations, δ deformation vibrations, * - valence vibrations of hydroxyl groups on the surface of the kaolinite layer, ** - valence vibrations of the hydroxyl groups.

absorbed water, another broad intense band was observed with the maximum absorption at 3628 cm^{-1}. Among the impurities in the FEBEX clay, a small amount of quartz (796 cm^{-1}) was found. The FTIR spectrum of the modified Kutch clay was very similar to the original Kutch clay.

The position and profile of the absorption bands of the FTIR spectrum of the kaolinite sample are typical for kaolin group. The region of stretching vibrations of the Si-O tetrahedral layer consists of two clear bands and the most intense bands of the FTIR spectra are those with the wave numbers of 1033 and 1009 cm^{-1}, while the more high frequency relatively wide band is at 1113 cm^{-1}. A less intense triplet of sharp bands at 538, 470 and 430 cm^{-1} corresponds to the deformation vibrations of Al-O-Si and Si-O-Si. In the region of the stretching vibrations of OH groups, the well-resolved diagnostic four narrow absorption bands were distinguished: common (3698 cm^{-1}) and antiphase (3671, 3654 cm^{-1}) on the surface of the kaolinite layer and 3620 cm^{-1} within the layer of kaolinite. The ratio of the intensities of the bands at 3671 and 3654 cm^{-1} and those at 3698 and 3620 cm^{-1} can give information about the degree of disorder of the kaolinite structure [139,140]. Bands at 936 and 913 cm^{-1} belong to the deformation vibrations of the hydroxyl groups on the kaolinite surface and inner layer, respectively. The four clearly resolved bands and the observed intensity distribution of the studied sample indicate its ordered structure located inside the kaolinite layer. The absorption band at 1384 cm^{-1} corresponds to an admixture of KNO_3 in KBr that was used during sample preparation.

3.5. MORPHOLOGY AND PARTICLE SIZE DISTRIBUTION

3.5.1. Electron Microscopy Studies

The Scanning and Transmission Microscopic studies were conducted to get an idea about the morphology and particle size distribution of different admixture phases present in the clay minerals. The preliminary studies with the clays in the suspension showed two fractions of

clays to be present in the clays. The two fractions were carefully separated from aqueous suspension based on density difference of the fraction and by the color of the individual fraction. The fraction with higher density and dark color was called as “dark fraction” while

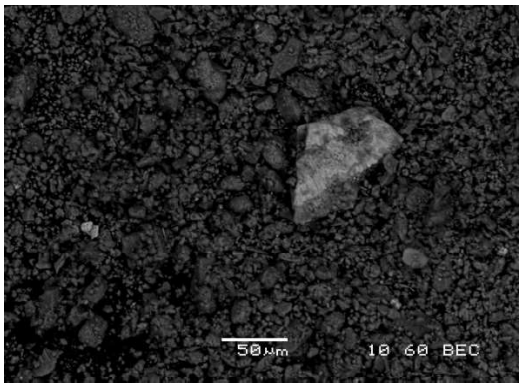

Khakassia “dark fraction”

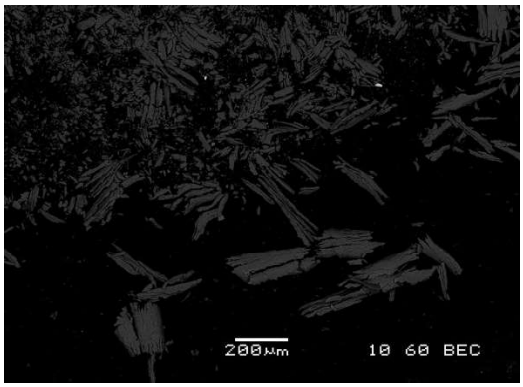

Khakassia “light fraction”

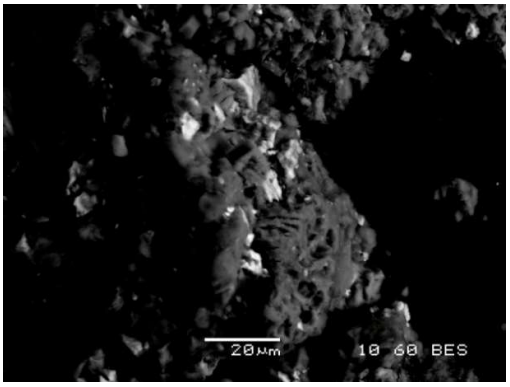

Kutch “dark fraction”

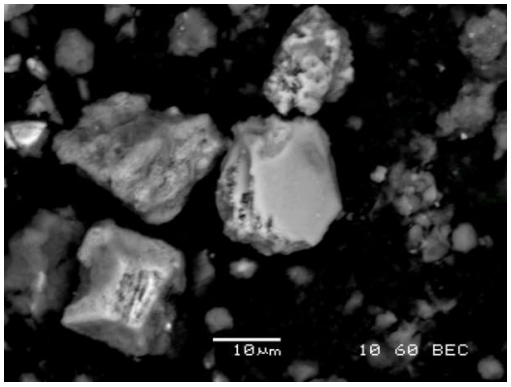

Kutch “dark fraction”

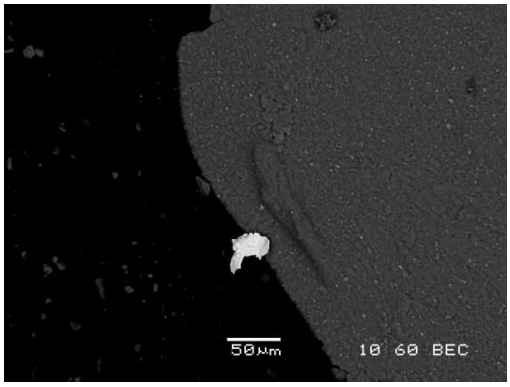

Kutch “light fraction”

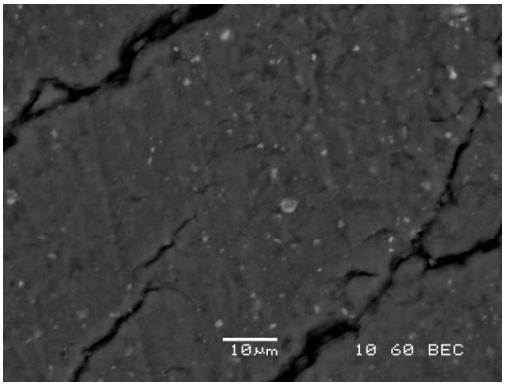

Kutch “light fraction”

Fig. 3.13. SEM images of the light and dark fraction of Kutch and Khakassia clays.

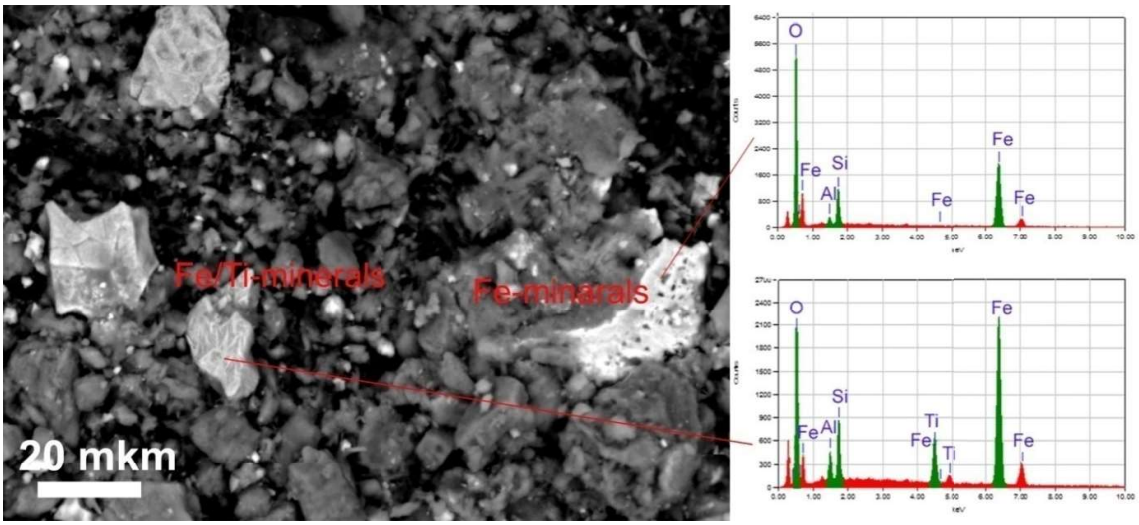

Fig. 3.14. SEM images together with EDX for the Rajasthan clay

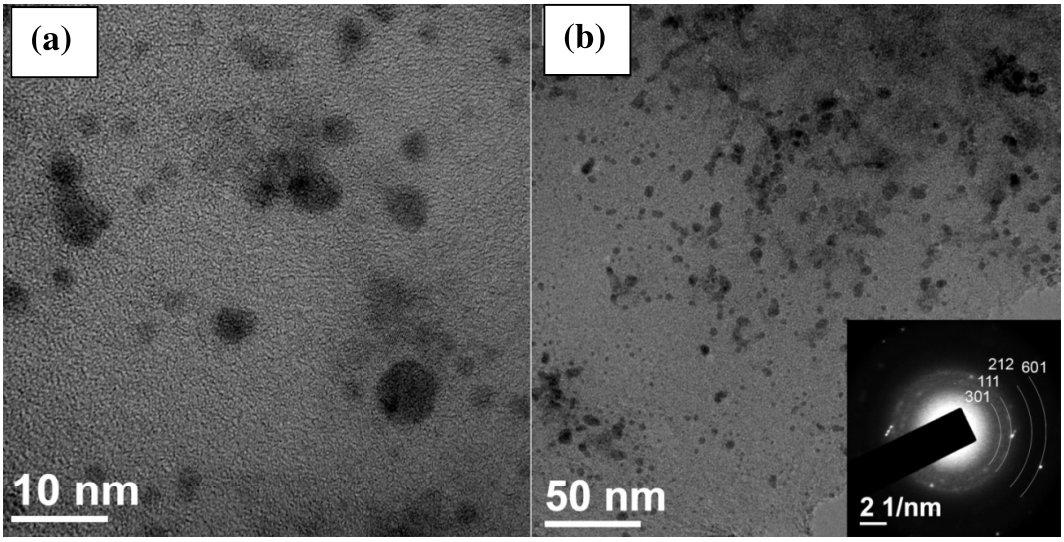

Fig. 3.15. (a), (b) HR-TEM images of goethite nanoparticles from Kutch clay samples. Selected area electron diffraction (SAED) are presented on the insert, white lines correspond to the position of the goethite reflexes.

the lighter part with relatively light color was called as “Light fraction”. The most plausible reason for the differentiation in color and density may be due to the presence of heterogeneous Fe-phase in the clay minerals. **Fig. 3.13** shows the typical SEM profile of light and a dark fraction of the studied clays. The SEM profile of the dark fraction shows the presence of bright spots due to the relatively high Z-elements, in this case, the Fe-minerals.

The light phase shows the presence of aluminosilicates without any bright spots. The typical SEM with EDX of Rajasthan clay samples clearly shows the presence of Fe-mineral, as expected, phases in the dark fraction **(Fig.3.14)**. The presence of iron oxide/hydroxide nanoparticles was confirmed by HR-TEM. **Fig. 3.15** shows typical HR-TEM images of goethite nanoparticles in the Kutch clay samples with particle size distribution in the range of 2 to 10 nm.

3.6. SPECIFIC SURFACE AREA AND CATION EXCHANGE CAPACITY

The specific surface area (SSA) of and the cation exchange capacity (CEC) of the clay minerals were determined by BET and Cohex method or NH_4Ac methods (, respectively and the results are listed in **Table 3.1 [141,142]**. As can be seen from the Table 2.1, the SSA values of Na- and Li-forms of FEBEX did not change much as compared to the original FEBEX clay and equals 63 and 59 m^2/g respectively, while the SSA of the Ca-form of FEBEX decreased to 45 m^2/g. This may be caused by the different microstructures of the samples as discussed in the literature by other authors [143, 144]. The increase in the SSA of the Kutch clay after iron removal may also be due to several reasons *viz.* i) on chemical treatment the impurities such as quartz and calcite that usually exist as large particles with small surface (**Table 3.1**) are removed, and hence help in an SSA increase, ii) during the purification step, montmorillonite was converted to the Na-form which has a higher surface area compared to the Ca-form because of a different microstructure [143,144] and iii)possible surface leaching or removal of Fe-oxide coating from the clay surface leading to exposure of more active surface area. The coherent scattering domain size (CSDS) that was calculated from XRD data is in good agreement with the SSA of the sample (**Table 3.1**). For example, purified Kutch clay with a minimal CSDS has a very high SSA (150 m^2/g). FEBEX clay has a relatively high total layer charge with a value of 0.79 per formula unit which may be the reason for the increase in particle size and decreasing surface area [145]. In contrast, montmorillonite from Kutch clay has a low total layer charge (0.56 per formula unit) that

may cause a smaller size of the clay particles and thus, a higher surface area value. The value of the total layer charge for montmorillonite from Khakassia clay is 0.61 per formula unit. Relatively high values of domain sizes are probably caused by the presence of vermiculite and beidellite layers in montmorillonite. The CEC of the clays used in this thesis work is presented in **Table 3.1**.

3.7. OTHER PROPERTIES

The elemental composition, the number of active surface site and charge onto the surface were determined by XRF, potentiometric titration and zeta potential measurements, respectively. An automatic titration system (Titrando 905, Metrohm) was employed for studies carried out at constant temperature (25 ± 1◦C). For the potentiometric titrations, about 40 ml volume of the clay suspension was taken in a conical flask of 100-mL volume (reactor vessel) with a particle concentration of 1 g/L at 0.01 M $NaClO_4$. The reactor vessel, equipped with a combined glass electrode, was agitated by a magnetic stirrer and purged with pure N_2 during the titration. After equilibration for about 1 h, the suspension was acidified using the standard $HClO_4$ to a pH of approximately 3.0 (acidimetric titration) and then divided into two equal parts, the first part was used for potentiometric titration while the second part was centrifuged at 10,000 rpm for 30 min, and the supernatant was utilized as the system blank[146]. This blank was subjected to a hydroxide titration identical to that of the first part. The titration curves of the clay samples were corrected with respect to the system blank. To subtract the influence of solid dissolution on the estimation of proton or hydroxide ion consumption by the clay itself, it was reasonable to use the supernatant produced under identical condition as the system blank. The Gran plot method was used to determine the specific volume of titrant added at the equivalent point (Ve) and to derive the total concentration of the reacting H^+ ions at each titration point (TOTH) [146]. The values of the Gran function (*G*) were calculated from the equations given below.

On the acidic side: $G_a = (V_0 + V_{at} + V_b) \cdot 10^{-pH} \cdot 100$ **(3.1)**

On the alkaline side: $G_b = (V_0 + V_{at} + V_b) \cdot 10^{-(13.8-pH)} \cdot 100$ **(3.2)**

where, V_0 is the initial volume of the clay suspension, and V_{at} and V_b are the total volumes of acid solution and those of hydroxide ions (OH^-) added at the different titration points, respectively. As the clay suspension was acidified before the alkalimetric titration, the OH^- added to the suspensions were consumed in the following three steps reflected in the Gran plot; (i) the neutralization of excess H^+ in the suspension (before V_{eb1}, see **Fig. 3.16**), (ii) the reaction with various surfaces active groups (between V_{eb1} and V_{eb2}, see **Fig. 3.16**), and (iii) the contribution to the system pH (after V_{eb2}).

The specific volumes, V_{eb1} and V_{eb2}, were obtained from the linear regression analysis of the Gran plots. The *V*eb1 was considered as the point the zero titration (The point before which there were no surface reactions consuming OH^- except simple acid–base neutralization of extra added protons to achieve acidic pH). The 'TOTH', as defined above, was calculated using the following equation:

$$TOTH = -(V_b - V_{eb1}) \times C_b / (V_0 + V_{at} + V_b)\ (mol/L), \quad \textbf{(3.3)}$$

where C_b is the concentration of the standard NaOH solution used for the titration. The data points from the hydroxide (OH^-) titration curve commencing after the point of zero charge calibration, were utilized in FITEQL 4.0 (a nonlinear least-squares optimization program) to estimate the surface acidity constants. The surface site concentration (H_S) was calculated from two equivalent points in the Gran plot, as given by the following equation

$$H_S = (V_{eb2} - V_{eb1})_{sample} \times C_b - (V_{eb2} - V_{eb1})_{blank} \times C_b\ V_0\ (mol/L) \quad \textbf{(3.4)}$$

Fig.3.16 shows the Gran plot for the bentonite (Aldrich) system at 0.01 M $NaClO_4$. The total number of active sites was found to be 5.4 (±0.1) $\times 10^{-4}$ mol/g of bentonite (Aldrich) clay and

was higher than the reported range. This value was imported into the FITEQL 4.0 program for the calculation of the surface acidity constants of the bentonite (Aldrich) samples used in

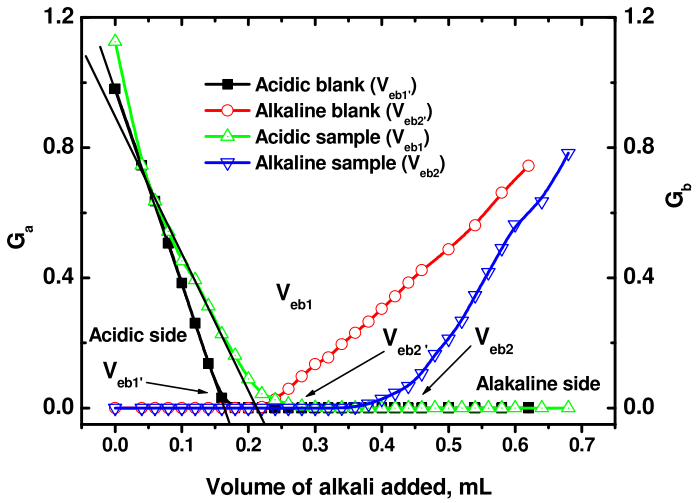

Fig. 3.16. Gran plot of the blank and bentonite suspension (5 g/L); *I*: 0.01 M $NaClO_4$; T: 298 K.

this work [147]. The XRF results are given in **Table 3.3**. The high Al and Si contents are due to the clay minerals present in the tetrahedral and octahedral sheets of montmorillonite, as

Table 3.3. The elemental composition of the studied clays

Sample	Composition, %										
	LOI*	Na_2O	MgO	Al_2O_3	SiO_2	K_2O	CaO	TiO_2	MnO	Fe_2O_3	P_2O_5
Rajasthan	20.06	1.15	4.64	16.28	35.12	0.30	6.67	3.09	0.16	12.27	0.11
Kutch	21.43	0.72	2.02	12.33	42.52	0.11	2.77	1.42	0.19	15.58	0.27
Aldrich	11.76	1.91	2.24	18.96	59.07	0.38	1.49	0.16	0.02	3.79	0.04
Khakassia	12.74	2.98	2.48	15.19	58.36	0.97	3.05	0.63	0.09	3.42	0.11
FEBEX	16.03	1.15	4.13	17.18	54.19	1.01	1.94	0.21	0.04	2.99	0.04
Kutch-purified	18.60	2.85	1.70	15.03	51.44	0.08	0.12	1.02	0.01	7.99	0.03

*Loss of ignition (LOI)

well, as due to the admixture of kaolinite and chlorite. The higher amount of Si in the Khakassia clay compared to the other samples is due to the higher quartz content, which was supported by the FTIR and XRD results (**Figs. 3.1 to 3.6**). The presence of a relatively high concentration of Ca and Mg can be partly attributed to the presence of carbonate minerals (calcite and dolomite), as indicated by FTIR and XRD data. The Rajasthan and Kutch clays were found to have high iron and titanium contents. Titanium was linked to the presence of anatase, which was identified by XRD. Iron can be included in the octahedral sheets of clay minerals, mostly smectites, and can also be found as separated accessory iron phases. The zeta potential measurements of the bentonite (Aldrich) done with varying pH values were found to be negative in the studied pH range (**Fig.3.17**).

3.8. CLAY AFFINITY FOR HUMIC ACID

Before going to do the experiments to understand the role of humic acid (HA) onto the radionuclide sorption, the pH-dependent interaction between bentonite and HA needs to be understood. HA being chromophoric, UV-vis spectrophotometry was used for the estimation of HA sorption onto bentonite as a function of pH. A calibration plot was generated from UV-vis spectrophotometric absorbance measurements to quantify the sorption of HA (**Fig. 3.17**) on the suspended bentonite (Aldrich). The absorbance of HA at the λ_{max}: 400 nm was also measured with increasing pH. The absorbance was found to be increasing with the pH, which may be due to the changes in the HA structural properties, such as the degree of dissociation of COOH and phenolic OH groups [99]. The sorption of HA on bentonite (Aldrich) was found to be decreasing with increasing pH values from 2 to 8. This behavior was attributed to the increased electrostatic repulsion between the negatively charged surface of bentonite (Aldrich) surface and anionic form of HA at higher pH values (**Fig. 3.17**). The measured Zeta potential of the bentonite suspension was found to be negative even in the acidic pH range and hence the PZC in the case of the bentonite is not seen in the present case.

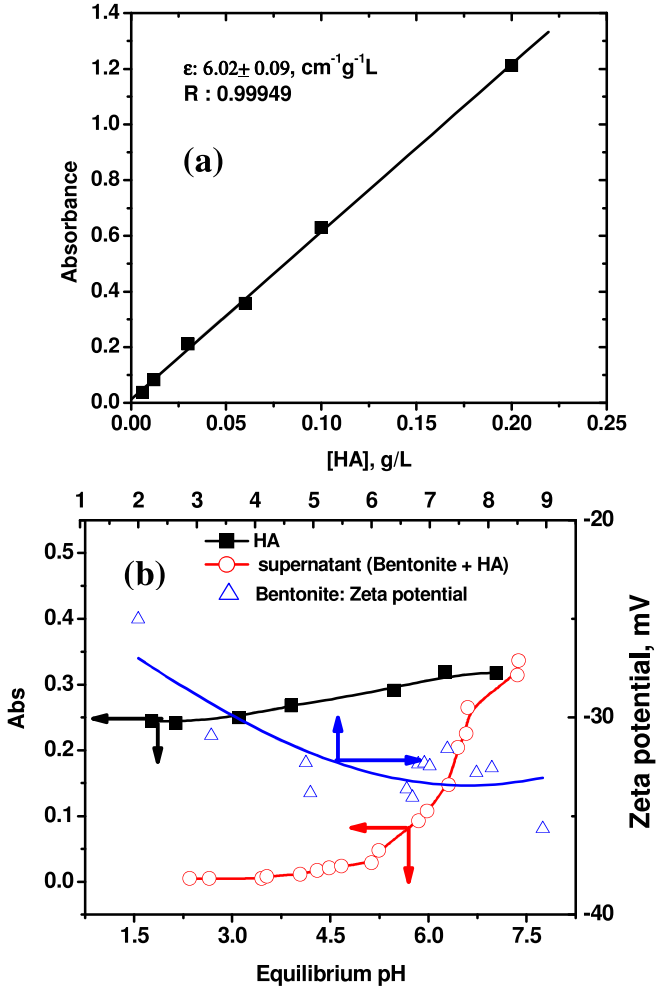

Fig. 3.17. (a) Calibration plot for estimation of HA at given pH; (b) Variation of humic acid (HA) absorbance with pH in the presence and absence of bentonite. [HA]: 50 mg/L; [bentonite]: 5 g/L; I: 0.01 M $NaClO_4$; λ_{max}: 400 nm; T: 298 K.

To summarise, we have used a host of physicochemical techniques to understand the composition of the natural and commercially available clay minerals used in the present study. The studied samples range from simple bi-layer clay systems, e.g., kaolinite, to trilayer systems, e.g. bentonite of both commercial (from Aldrich) and natural origins. These studies indicated that the present clays differ in their mineralogical compositions, Fe-speciation, have particle size inhomogeneity (e.g., TEM studies) and varying specific surface area. It would be interesting to see the effect of these variations on the sorption properties of these minerals toward a given radionuclide under different experimental conditions.

4

SORPTION AND MODELING STUDIES ON COMMERCIAL CLAY

4.1. INTRODUCTION

The sorption of actinides and fission products such as U(VI), Am(III) ((Eu(III) and Gd (III) were used as surrogates), Cs(I) and Sr(II) was studied onto commercially available bentonite clay. The sorption studies with kaolinite were also done to compare the behavior of the two classes of clay minerals (1:1 or bilayer and 1:2 or tri-layer) towards the sorption of trivalent actinides. As already discussed in Chapter 1, the presence of organic and inorganic complexants can modify the sorption behavior of the clay minerals. In this Chapter, the effect of organic acids starting from oxalic and citric acid to the relatively complex ethylenediaminetetraacetic acid (EDTA) and that of natural organic matters (NOM) such as humic acid are evaluated. The nature of the complexes formed at the aqueous-minerals interface is determined either by using spectroscopic techniques (which give direct information) such as EXAFS, EPR and fluorescence studies, or by indirect means such as SCMs. The batch sorption studies are carried out to understand the effects of various chemical parameters such as pH, ionic strength, etc on the sorption of radionuclides onto minerals surface. The experiments carried out at varying ionic strength help in identifying the nature of the complex formed, e.g., inner sphere or outer sphere, onto the clay minerals

surface. Speciation calculations of different complexed species are done to explain the experimental observations. An attempt has been made to fit the data, on the sorption of trivalent metal ions onto the bentonite clay to the well-known models viz. Freundlich, Langmuir, and Dubinin-Radushkevich (D-R) isotherms, to calculate the sorption capacity of bentonite and the mean energy of sorption. This Chapter starts with the uranium sorption studies, which is essential as these involve a radioactive contaminant from the very beginning or the front end of the nuclear fuel cycle. Starting from the mining to fuel fabrication, uranium can leach out either in large quantities, e.g. in trailing ponds or in very small quantity, from fuel fabrication facilities. The latter part of this Chapter deals with the sorption of fission products (Cs(I), Sr(II), and Am(III)) which are generated after the neutron irradiation of uranium fuel in the reactor for sufficient time and are of concern to the environment in the long term.

4.2. THE SORPTION OF URANIUM

> ***Caution: Being an α-emitter, working with the uranium requires glove box, fume hoods. The long half-life of this makes it relatively less hazardous when compared to other α-emitter with a shorter half-life. Care must be taken when working with this radioactive element.***

The preview about the uranium trailing and the associated risk were already discussed in Chapter 1. The comprehensive discussion about the uranium mining, management of waste generated and recent advances can be found on the world nuclear association websites.The uranium sorption experiments were performed in aerobic condition, with bentonite suspension (1 g/L), spiked with ^{233}U radiotracer (natural ^{238}U solution was used for EXAFS and TRLFS studies) at the required pH, and ionic strength. The kinetics of the uranium sorption onto bentonite was studied at pH 4 and 0.01 M $NaClO_4$ and the studies show that equilibrium could be achieved in ~ 2 h (**Fig. 4.1**). However, for the sorption experiments, samples were placed in polypropylene tubes and shaken mechanically at room temperature for ~ 24 h to ensure equilibrium. Suitable samples (100-200 µl) were taken out after

centrifugation and were assayed by liquid scintillation counting for % sorption calculation. **Fig. 4.2** shows the sorption behavior of U(VI)(~ 10^{-5} M) onto bentonite as a function of pH under aerobic conditions at I = 0.01 M ($NaClO_4$). The sorption of U(VI) onto bentonite (1 g/L) was not quantitative and was found to be increasing initially with increasing pH up to

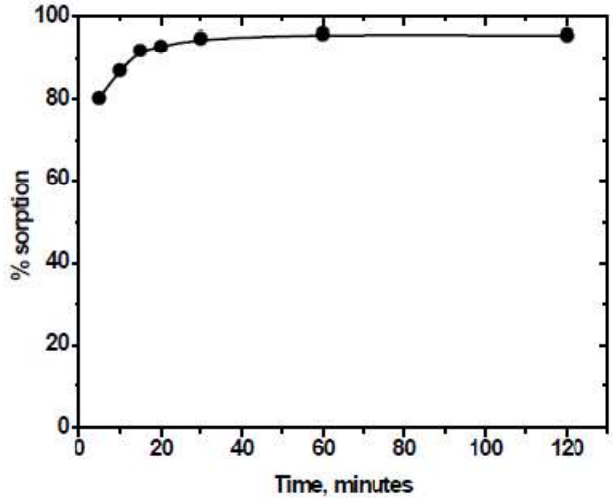

Fig. 4.1. Kinetics of U(VI) sorption onto bentonite (1g/L) pH : 4.0; I : 0.01 M; $NaClO_4$; T: 298 K.

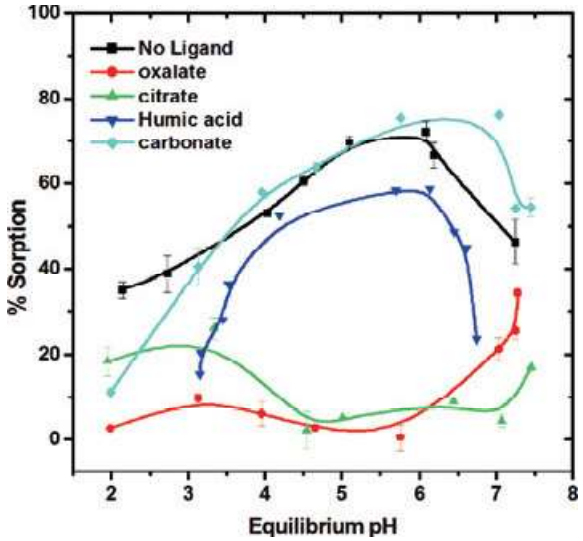

Fig. 4.2. Sorption of U(VI) (10^{-5} M) onto bentonite (1 g/L) in the absence and presence of different ligands; [Ligand]: 10^{-4} M; [Humic acid]: 100 mg/L; I: 0.01 M $NaClO_4$; T: 298 K.

pH 6. Any further increase in the system pH decreased the % sorption of U(VI) onto bentonite. While the initial increase in the U(VI) sorption was attributed to the surface complexation of UO_2^{2+}, (uranyl cation) with the deprotonated surface hydroxyl groups, the formation of anionic uranyl-carbonate species at higher pH (**Fig. 4.2**) was suggested to be responsible for the decrease in the % U(VI) sorption because of their electrostatic repulsive

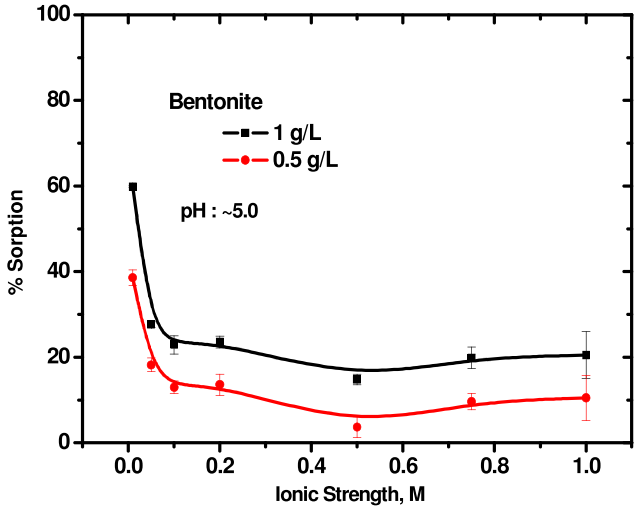

Fig. 4.3. U(VI) (10^{-5} M) sorption onto bentonite (0.5 and 1 g/L) with varying ionic strength; pH : ~5.0; T : 298 K

interactions with the negatively charged bentonite surface at higher pH values. Similar observations were reported elsewhere for the sorption of U(VI) [149-151]. To further investigate the nature of the sorbed complexes of U(VI) onto the bentonite (inner-/outer-sphere), the sorption experiments were carried out as a function of ionic strength (I = 0.01–1.0 M $NaClO_4$) at pH ~5. The sorption was found to be varying at lower ionic strengths, (< 0.1 M of $NaClO_4$ at pH 5), and remained almost constant beyond that (**Fig. 4.3**). This suggests that the sorption of U(VI) take place by the formation of inner-sphere complexes of U(VI) onto the bentonite surface.

The influence of different complexants (inorganic or organic) such as citrate (cit), HA, carbonate (CO_3^{2-}), oxalate (ox) on the sorption of U(VI) onto the bentonite clay (1 g/L)

was further investigated as a function of pH (2–8) at an ionic strength of 0.01 M ($NaClO_4$). There was a decrease in the U(VI) sorption onto bentonite in the presence of 10^{-4} M cit and ox which was attributed to the aqueous complexation of U(VI) with theses organic complexants in the pH range of 4–8 whereas the sorption of U(VI) onto bentonite was not affected significantly in the presence of 10^{-4} M of carbonate ions (Fig. **4.2**). These observations suggest that the amount of carbonate in the aqueous media due to the dissolved $CO_2(g)$ is sufficient for deciding the U(VI) sorption onto bentonite and the addition of the extra carbonate does not induce any more effect.

4.2.1. Spectroscopic Studies

4.2.1.1. Fluorescence Studies

The U(VI) aqueous complexation studies with different complexants were carried out to understand the changes in the aqueous speciation of the metal ion with/without complexing ligands/anion before/after contacting with the bentonite suspension (1 g/L) at pH ~ 5(±0.05) and I = 0.01M ($NaClO_4$). The emission intensity of U(VI) in the aqueous complexation

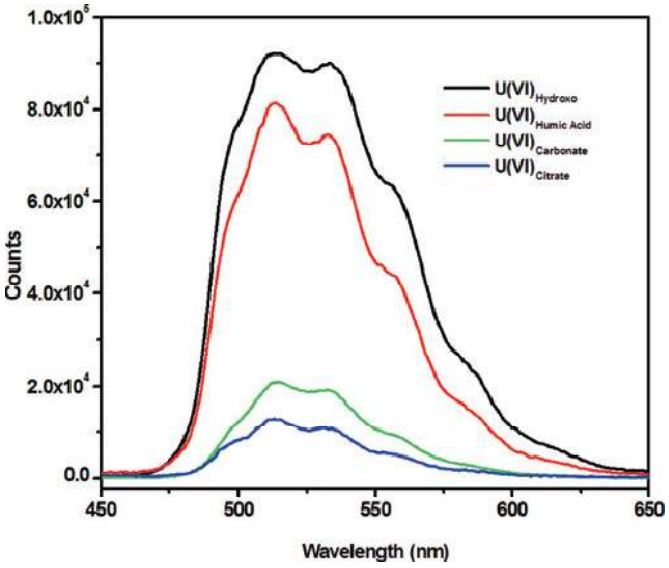

Fig. 4.4. Luminescence spectra for aqueous complexation of U(VI) with cit, HA and CO_3^{2-}; pH: 5.00 ± 0.05; I: 0.01 M $NaClO_4$.

studies with CO_3^{2-}, HA, cit (**Fig. 4.4**) followed the order: $U(VI)_{hydroxy}$ > $U(VI)_{HA}$ > $U(VI)_{carbonate}$ > $U(VI)_{citrate}$. The lower luminescence yield of $U(VI)_{carbonate}$ complex compared to others (except citrate) can be attributed to the strong dynamic quenching by the carbonate anion at room temperature[152]. The $U(VI)_{citrate}$ complex does not show any luminescence at room temperature[153]. Hence, the observed luminescence in the emission spectra of $U(VI)_{carbonate}$ and $U(VI)_{citrate}$ system can be attributed to the small amount of uncomplexed uranyl ion present in the hydroxo complexes of the uranyl ion. To gather more information

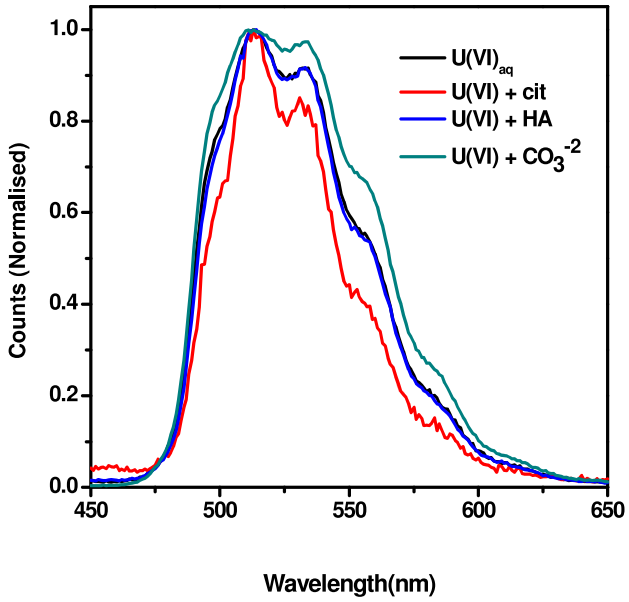

Fig. 4.5. Normalised fluorescence spectra for aqueous solutions of U(VI) containing cit, HA and CO_3^{2-}; pH: 5.00 ± 0.05; *I* : 0.01 M $NaClO_4$; T: 298 K.

about the nature of the luminescent U(VI) species formed with varying ligands at pH ~ 5(±0.05) and *I* = 0.01 M ($NaClO_4$), the luminescence spectra were normalized, as the shift in the peak position or variation in peak ratio in emission spectra can be related to the formation of different U(VI) species in the aqueous phase. However, the observed normalized spectra don't show any appreciable shift in the emission lines suggesting similar nature of the luminescent U(VI) species or absence of any noticeable change in its emission spectra without such a possibility (**Fig. 4.5**). As can be seen from the normalized luminescence

spectra, the emission profile of $U(VI)_{aq}$ with and without HA are super-imposable, suggesting, either the concentration of U(VI)-HA complex formed was very small and the emission spectra were dominated by aqueous U(VI)-hydroxo species present in the medium or the U(VI)-HA has spectra similar to that of $U(VI)_{aq}$. To confirm this, the lifetime of different U(VI) complexes were determined by luminescence decay at λ_{ex}: 230 nm and λ_{em}: 514 nm,

Table 4.1. Details of the samples used for the luminescence studies; [U(IV)]:10^{-4} M, [Ligand]: 10^{-4} M; [HA]: 10 mg/L; pH: 5.00 ± 0.05; *I*: 0.01M $NaClO_4$.

S.No.	Sample	τ_1(μs)	τ_2 (μs)
1	U(VI)	19	-
2	U(VI) + cit	20	-
3	U(VI) + HA	23	5
4	U(VI) +CO_3^{2-}	27	5
5	U(VI) + bentonite	19	5
6	U(VI) +cit+ bentonite	7	25
7	U(VI) +HA+ bentonite	19	100
8	U(VI) + CO_3^{2-}+ bentonite	21	100

owing to the fact that complexation with HA may give additional pathways for non-radiative decay to U(VI) causing if not substantial but significant decrease in the lifetime of U(VI) - HA complex as compared to that of $U(VI)_{aq}$. The lifetime of different complexes (**Table 4.1**) of the value of 23 ± 4 μs suggested the same luminescent U(VI) species. Higher lifetime value for U(VI)-carbonate and U(VI)-cit case is mainly due to higher uncertainties in the fitted data due to poor signal to noise ratio in the two cases (vide supra). From the analysis of the luminescence decay time (lifetime $\tau \sim 19$ μs) and prominent emission peak maxima at 498, 514, 534, and 557 nm, the most probable luminescence species can be ascribed to the

$(UO_2)_3(OH)_5^+$ complex [154]. Both life-time and peak position suggest the dominance of U(VI)- hydroxo species, possibly $(UO_2)_3(OH)_5^+$ complex, even in the case of uranyl-humate and uranyl-carbonate system, whereas the formation of ternary U(VI)-humate (UO_2 (OH)HA) complex at pH ~5 has been reported by others [155]. The ternary U(VI) humate complex, if formed in solution, either does not contribute to the luminescence signal or have similar lifetime and emission lines as $U(VI)_{aq}$, under present experimental conditions.

4.2.1.2. U(VI)-bentonite Suspension with/without Complexing Ligands

The emission spectra and lifetime profiles of $U(VI)_{aq}$, and U(VI)-bentonite suspension in the presence/absence of complexing ligands was also recorded under identical conditions and compared. The intensity of the emission lines followed the order: $U(VI)_{Hydroxy} > U(VI)_{Bentonite} > U(VI)_{Bentonite\text{-}Humic\ Acid} > U(VI)_{Bentonite\text{-}carbonate} \gg U(VI)_{Bentonite\text{-}citrate}$ at pH 5.00 (±0.05) and I = 0.01 M ($NaClO_4$) (**Fig.4.6(a)**). The observed trend can be explained with the help of the sorption profiles of U(VI) with bentonite in the presence/absence of different complexing ligands/anions.

The order of the luminescence intensity decrease in the emission spectra suggests that the residual $U(VI)_{hydroxo}$ species, after U(VI) sorption onto bentonite, are responsible for the observed luminescence spectra. The luminescence from that of the U(VI) or U(VI) complexes sorbed onto the bentonite is either quenched due to complexation (**Fig. 4.4**) or its intensity is very poor due to other associated non-radiative decay pathways as compared to that of the $U(VI)_{hydroxo}$ species. To confirm this hypothesis, the U(VI)-bentonite suspension was centrifuged to 16000 rpm for 30 min, and the solid residue was separated, air-dried and subjected to luminescence measurements. The U(VI) sorbed onto bentonite had very poor luminescence intensity (**Fig. 4.6(b)**) as compared to U(VI)-bentonite suspension. The poor emission spectra in the presence of citrate are due to the quenching of U(VI) luminescence upon citrate ion complexation[153]. The analysis of the luminescence decay curves for U(VI)-bentonite and U(VI)-cit-bentonite complexes shows one prominent luminescence

species with mean luminescence lifetime of 22 ± 3.0 μs (**Table 4.1**). This further supports the argument that only the U(VI)-hydroxo species in the supernatant is responsible for the observed emission. The higher lifetimes of the U(VI)-HA-bentonite and U(VI)-carbonate-bentonite samples along with 20 ± 1.0 μs (**Table 4.1**) suggest the presence of some different

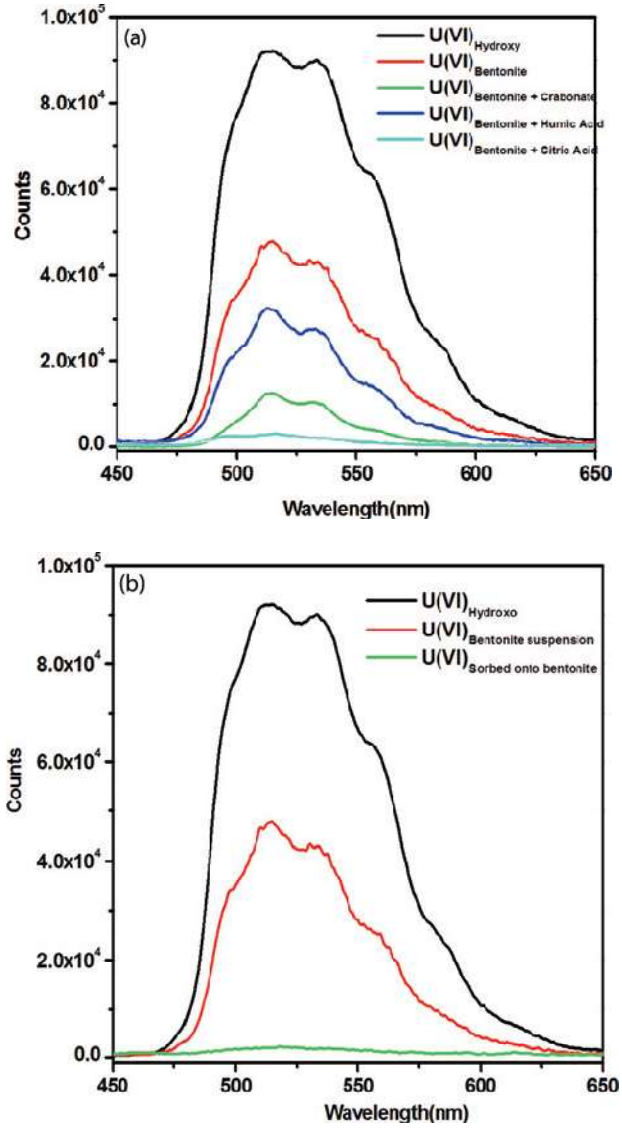

Fig. 4.6. (a) Luminescence spectra of U(VI)-bentonite suspension with and without complexing ligands; (b) Luminescence spectra of $U(VI)_{Hydroxo}$, $U(VI)_{bentonite\ suspension}$ and $U(VI)_{sorbed\ onto\ bentonite}$; pH: 5.00 ± 0.05; *I*: 0.01 M $NaClO_4$.

species, although no spectral shift was observed in the emission lines; this could be due to the formation of the surface sorbed mixed uranium-hydroxo complex as seen in the case of U(VI)

sorption onto alumina having a lifetime of ~ 120 μs [149]. The HA addition in the presence of bentonite is apparently not affecting the emission profile owing to the same reason, as discussed previously in the case of the emission spectra of U(VI) with/without HA.

4.2.1.3. UV-visible Spectroscopic Studies

The UV-Visible spectra of all the samples were recorded as complementary to the luminescence data. This study helps in assigning different species onto the bentonite, if present, which are non-fluorescent in nature or have very weak luminescence due to the

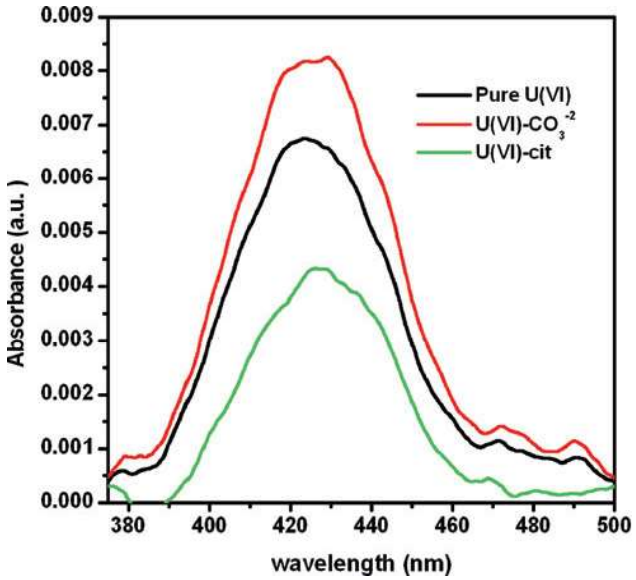

Fig. 4.7. UV-vis spectra of U(VI) species present in aqueous CO_3^{-2} (10^{-4} M) and cit (10^{-4} M) media; pH: 5.00 ± 0.05; *I*: 0.01 M $NaClO_4$.

quenching by the ligands or by any other means. The UV-vis absorption spectra were recorded for the liquid samples (the suspension and slurry were having very poor signal to noise ratio). The UV-vis spectra of different complexes of U(VI) shown in (**Fig. 4.7**) follow the order: U(VI)-CO_3^{2-} > $U(VI)_{aq}$ > U(VI)-cit (the UV-vis spectra for HA complexes of U(VI) were not shown as the high absorbance of HA mask the spectra of the U(VI)-HA

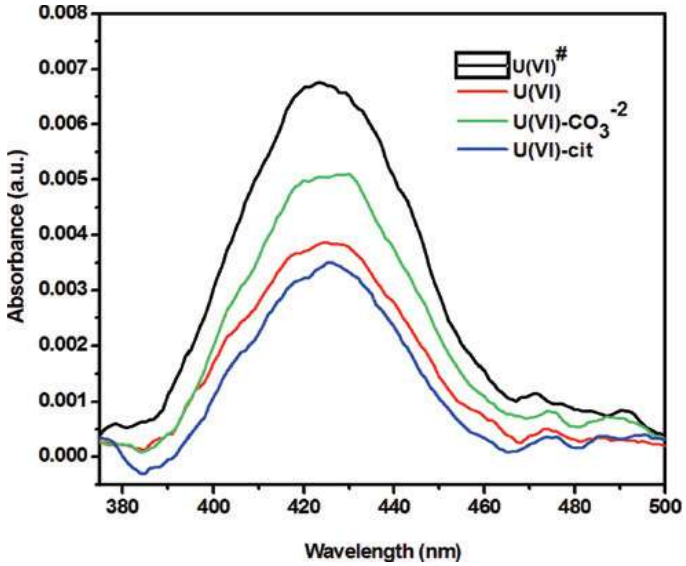

Fig. 4.8. UV-vis spectra of U(VI) species in the supernatant after centrifugation; pH: 5.00 ± 0.05; *I*: 0.01 M $NaClO_4$.

complex). The higher absorbance of the U(VI)-CO_3^{2-} complex compared to that of the $U(VI)_{aq}$, suggests the higher optical density value for U(VI)-CO_3^{2-} complex as compared to that of the pure $U(VI)_{aq}$ species under the present set of experimental conditions. The UV-vis

Table 4.2. U(VI) sorption onto bentonite with/without ligands from UV data (λ_{max}: 424 nm).

sample	Absorbance (x10)		Sorption (%)
	Without bentonite	Supernatant (after equilibration with bentonite)	
$U(VI)_{aq}$	0.0675	0.0386	42.8
U(VI)-carbonate	0.0819	0.0504	38.5
U(VI)-citrate	0.0433	0.0343	20.8

spectra of the supernatant, of the binary and ternary system of U(VI)-bentonite and ligands, were also recorded. The recorded UV-vis spectra show (**Fig.4.8**) a reduction in the absorbance value which was attributed to the U(VI) sorption onto bentonite in line with the results obtained from the radiometric studies (*vide supra*). The % sorption of U(VI) onto the bentonite clay was also calculated from the UV-vis absorbance data (**Table 4.2**). The lower

% sorption of U(VI) onto the bentonite in all the cases are expected due to a higher concentration of U(VI) employed (10^{-4} M) for the UV-vis spectrophotometric studies as compared to the radiometric studies (~ 10^{-5} M). The presence of U(VI)-cit complexes can be easily seen in the UV-vis spectrophotometric spectra, for both the aqueous complexation systems and supernatant of ternary system. Whereas we could not get any luminescence signal for similar systems, which clearly indicate luminescence quenching of U(VI) emission on citrate complexation.

4.2.1.4. EXAFS Studies on U(VI) Species Sorbed onto Bentonite

The U_{L3}-edge normalized EXAFS spectra for the U(VI) sorbed onto the bentonite surface (samples 2–4, **Table 4.1**) was shown in **Fig. 4.9.** The $k_2 \cdot (k)$ vs. k was plotted for samples 1 to 6. The XANES spectra of all the samples (2-5) are plotted along with those for U_3O_8 (used as standard) and UO_2^{2+} in pH 5 (pH adjusted using dilute perchloric acid; sample 1), and shows small shift towards higher energy side in the absorption edge indicating a higher positive charge on uranium, which could be attributed to a decrease in the electron density at uranium due to surface or ligand complexation. The guess structural parameters used for the simulation of theoretical EXAFS spectra of the samples have been taken from the crystal structure of Soddyite and uranyl acetate [156,157]. In the fitting process, though initial structure for the samples was taken as Soddyite, extra carbon atoms are included from the uranyl acetate structure for samples 3, 4 and 5. The (R) versus R spectra (**Fig. 4.10**) have been generated for all the samples from the (E) versus E spectra (**Fig.4.9**) data following the the methodology described above**.** The local structure parameters such as bond distances, coordination numbers (including scattering amplitudes) and disorder (Debye-Waller) factors (σ^2), which give the mean square fluctuations in the distances, have been used for the data fitting. for the U(VI)-L_3 edge measurements along with the paths taken from the initial guess structures, e.g. Soddyite, and uranyl acetate structure to carry out the fitting. The first Fourier

transform peak is the contribution of two oxygen shells, where Uranium is bonded to the two axial ($U–O_{ax}$) and six equatorial oxygen atoms ($U–O_{eq}$) in sample 2 sample 3, sample 4 and

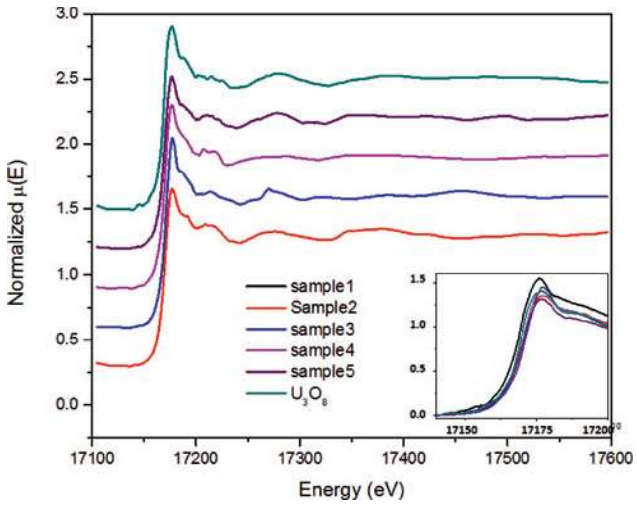

Fig. 4.9. Normalized EXAFS spectra of U(VI) species sorbed onto bentonite (samples 2-5) along with reference uranium oxide, U_3O_8. The inset shows an enlarged portion of the edge (with sample 1, e.g. $UO_2^{2+}{}_{aq}$).The best fit results are summarized in **Table 4.3.**

sample 5. For samples 3 and 4, the peak intensities are relatively smaller than those seen in the other two samples (2 and 5) suggesting higher disorder for sample 3 and 4. As the sample 1 was pure UO_2^{2+} in aqueous solution, it showed two prominent peaks (as expected) at 1.77Å and 2.27Å due to the back scattering of the two $U–O_{ax}$ and five $U–O_{eq}$ oxygen atoms which is in line with the literature values [158]. There were spectral features for U–U scattering, characteristics of oligomeric species in the recorded data, suggesting multinuclear species formation onto the surface of the bentonite. The $U–O_{eq}$ distance varied from 2.31Å to 2.35Å in different samples and are lower than the values (2.41– 2.46 Å) for the mononuclear outer-sphere U(VI) complexes reported at lower pH values [159]. The shorter value of $U–O_{eq}$ distances indicates inner sphere complexation under the present experimental conditions which was supported by the ionic strength variation experiments. These experiments suggested that the sorption of the metal ion changed marginally at higher pH values with

varying ionic strength, an indirect evidence for the inner-sphere complexation. As the montmorillonite is the major component of bentonite, different types of UO_2^{2+} ion bindings to the amphoteric surface sites (viz., aluminol and silanol) e.g., edge sharing, corner sharing in

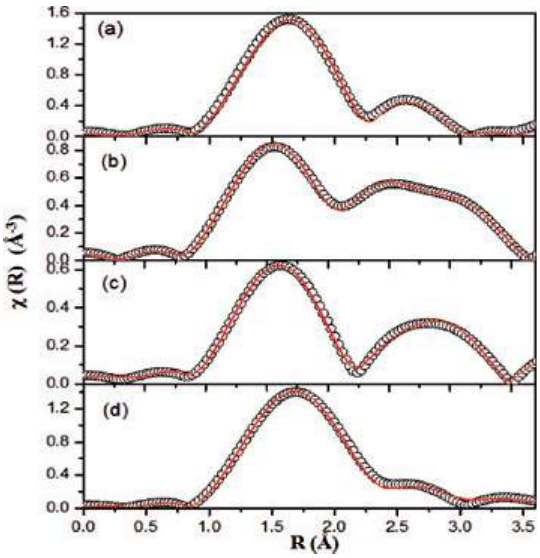

Fig. 4.10. Fourier transformed EXAFS spectra of U(VI) species sorbed onto bentonite (sample 2 to 5) at U L_3-edge (Scatter points) and theoretical fit (Solid line); (a) sample 2, (b) sample 3, (c) sample 4, and (d) sample 5.

mono-/bi-dentate manner can take place. However, exact sites and/or their proportion for UO_2^{2+} surface bindings is difficult to be judged from the EXAFS data in view of the similar scattering amplitudes of Si and Al. However, owing to structural differences in the silica tetrahedra and the alumina octahedra, the mode of binding of the UO_2^{2+} ion with surface could be predicted with great deal of accuracy using references like Soddyite, ($(UO_2)_2(SiO_4)\cdot H_2O$) which can serve as a reference for different binding types between$[UO_2O_{eq}]$ and $[SiO_4]$ polyhedra. In the Soddyite structure, the uranyl unit is connected to the $[SiO_4]$tetrahedra in a bi-dentate fashion (edge sharing) with a U–Si distance of 3.16Å and is bound via mono-dentate coordination (corner-sharing) with a U–Si distance of 3.81Å. It should be mentioned that the U–Si distance of around 3.08Å is considered as the uranyl ion bonded onto the silica in a bi-dentate manner [160-162]. Samples 2, 4 and 5 showed peaks at

3.11 Å, 3.19 Å and 3.22 Å due to the scattering of two Si atoms, which was in agreement with the bi-dentate bonding of UO_2^{2+} with the silica tetrahedron, On the other hand, the U–Si distance of 3.38 Å (expected rather large value of distance or 2 Si atoms from Soddyite

Table 4.3. The bond length, coordination number and disorder factor obtained by EXAFS fitting of $U(VI)_{aq}$ and U(VI) sorbed samples onto montmorillonite in the presence/absence of complexing agents

Paths	Parameters	Soddyite[a]	$UO_2(acetate)_2$[a]	Sample 2[b]	Sample 3[c]	Sample 4[d]	Sample 5[e]
U-O	R (Å)	1.66	1.75	1.81	1.79	1.83	1.83
	N	2.0	2.0	2	2.0	2.0	2.0
	σ^2			0.001	0.0042	0.0077	0.0016
U-O	R (Å)	2.31	2.39	2.31	2.33	2.35	2.32
	N	5.0	5.0	6.0	6	6	6.2
	σ^2			0.001	0.0179	0.0188	0.001
U-C	R (Å)		3.46		3.08	3.43	2.76
	N		2.0		7.02	4.16	2.29
	σ^2				0.001	0.0021	0.001
U-Si	R (Å)	3.17		3.11	3.38	3.19	3.22
	N	1		2.1	3.37	1	2.0
	σ^2			0.0012	0.001	0.0012	0.0013
U-U	R (Å)	3.79		3.86	3.84	3.83	4.08
	N	2.0		2	2.22	2.22	2.0
	σ^2			0.003	0.027	0.0097	0.001

[a] Theoretical values; [b] 1×10^{-4} M U(VI) + 1 g/L bentonite suspension; [c] 1×10^{-4} M U(VI) + 1×10^{-4} M cit + 1 g/L bentonite suspension; [d] 1×10^{-4} M U(VI) + 10 mg/L HA + 1 g/L bentonite suspension; and [e] 1×10^{-4} M U(VI) + 1×10^{-4} M carbonate + 1 g/L bentonite suspension.

structure) in Sample 3, with one scattering silicon atom can be attributed to mono-dentate corner sharing bonding of UO_2^{2+} with the silica tetrahedron. The U–U distance was varying in these samples (from 3.80 Å to 4.08 Å) showing the formation of inner-sphere multinuclear complexes at the montmorillonite surface [162]. It should be noted that there is a wide variation in the U-C bond lengths and carbon co-ordinations around uranium in samples 3 to

5 due to the presence of different types of coordinating modes of the ligands in this samples. In short, U(VI) binds to the bentonite surface by the formation of bi-dentate inner-sphere multinuclear complex. The complex of U(VI) in the presence of HA, showed a peak at 3.19 Å due to the scattering of a single Si atom, suggests edge sharing between Si tetrahedra and U(VI) whereas the U(VI) sorbed species onto the bentonite with or without carbonate shows similar EXAFS features, except for some U-C scattering, which may be due to the formation of mixed uranylhydroxocarbonates, $[(UO_2(OH)_x(CO_3)_y]^{2-x-2y}$, owing to the higher concentration of carbonate in sample 5. The U(VI)-cit showed higher U-Si coordination number (>3) with higher U-Si distance, suggesting U(VI)-silicate formation at the surface while the varying U–U distance in the studies samples (3.80Å to 4.08 Å) indicated the formation of inner-sphere multinuclear complexes at the surface [160-162].

4.3. SORPTION OF TRIVALENT ACTINIDES

The nuclear fuel, after achieving the required burn up, comes out of the nuclear reactor with a host of fission and activation products. After the required cooling period and reprocessing of the spent fuel, one is left with the “high-level liquid waste” whose safe management is a challenging task. The trivalent actinides in the waste, such as Am(III), are of concern, not only due to their short half-life (hence, higher dose) but also due to their decay leading to high energy α particles. The interactions of the trivalent metal ions such as Am(III), Eu(III) and Gd(III) with different backfill materials have been studied over the past years. Various aspects such as the presence of different complexing anions, the source, and form of the clay mineral, the presence of exchangeable cations, pre-treatment of the clay etc., require better insights to explain the sorption behavior of metal ion and also to predict the nature of the sorbed species onto mineral water interface. Different spectroscopic techniques, e.g., EXAFS (Extended X-ray Absorption Fine Structure), EPR (Electron Paramagnetic Resonance) and TRLFS (Time-Resolved Laser Fluorescence Spectroscopy) have been used to extract

information on the nature of the sorbed species onto mineral surface using suitable probe metal ion such as Gd(III) (EPR probe) and Eu(III) (fluorescence probe).

4.3.1. Effect of Complexing Agents on Eu(III) Sorption

The preliminary sorption experiments with Am(III), Eu(III) and Gd(III) showed similar sorption profiles as a function of pH. Therefore, detailed experiments were performed either using Eu(III) or Gd(III) (an EPR probe) to get a better insight into the metal ion sorption process under different experimental conditions. The complexation of Eu(III) (a surrogate of Am(III)) in natural waters with any naturally occurring ligand or those of anthropogenic

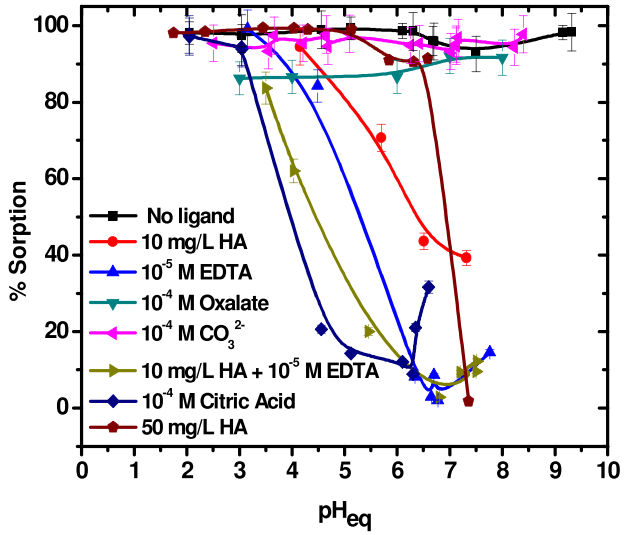

Fig. 4.11. Effect of different complexing ligands on Eu(III) sorption onto bentonite (1g/L) as a function of pH; *I*: 0.01 M $NaClO_4$; T:298 K.

origin, can affect its sorption onto bentonite clay. In this context, it was of interest to study the influence of different organic or inorganic complexing agents on Eu(III) sorption. The Eu(III) sorption studies onto bentonite were conducted with organic complexants such as, HA (10 and 50 mg/L), oxalate (10^{-4} M), citrate (10^{-6} to 10^{-4} M), EDTA (10^{-5} M) and carbonate (one of the more abundant inorganic complexants in natural media) with varying pH (2–8) at a constant ionic strength of 0.01 M ($NaClO_4$). The sorption of Eu(III) (10^{-5} M) onto the bentonite (1 g/L) surface was near quantitative (>95%) over the studied pH range in the

absence of any externally added complexant (**Fig. 4.11**) as seen by others [90,149]. There was a significant decrease in the Eu(III) sorption in the presence of 10^{-5} M EDTA which was attributed to the aqueous complexation of Eu(III) with EDTA in the pH range of 4–8 (**Fig. 4.11**). On the other hand, the sorption of U(VI) changes differently in the presence of HA (10 and 50 mg/L). The presence of 10 mg/L HA has a negligible effect on Eu(III) sorption in the lower pH range (2–4) beyond which a decrease was observed, whereas, for 50 mg/L, the sorption was almost invariant up to pH 5.5 and later decreases sharply. The sorption of Eu(III) onto bentonite was found not to be affected by the addition of carbonate ions. On the other hand, the sorption of Eu(III) decreased slightly (15-20%) in the presence of oxalic acid, The combined effect of HA (10 mg/L) and EDTA (10^{-5} M) on the Eu(III) sorption onto bentonite was also investigated. The drop in the % sorption was seen in the lower pH range where it appeared that complexation with EDTA and HA had a combined effect thereby reducing the sorption onto the bentonite clay. The presence of citric acid showed even sharer change in the % Eu(III) sorption which was attributed to the low pKa value of the complexant combined with its higher concentration used in these experiments and also to its the multidenticity.

4.3.2. Nature of the Sorbed Complex

The EPR and EXAFS studies were conducted to understand the nature of the sorbed complex at the clay surface. The Gd(III) sorption studies onto the bentonite clay were carried out at different pH conditions (4, 6 and 8) and also in the presence of 10 mg/L HA and 1×10^{-4} M cit at I = 0.01 M ($NaClO_4$). There was an enhancement in the sorption of Gd(III) onto bentonite in the presence of HA, while an opposite trend was seen in the presence of cit (**Fig. 4.12**). This observation is in line with the Eu(III) sorption data (*vide supra*).

4.3.2.1 EPR Studies

Gd(III) being an EPR active element, samples containing Gd(III) sorbed bentonite and aqueous Gd(III) solution was subjected to EPR spectral analysis. The g parameter gives information about unpaired electrons and their neighborhood and plays a role as a radical structure indicator. The EPR spectra of Gd(III) solution (10^{-4} M) in 0.01 M $NaClO_4$ at pH 4 (**Fig. 4.13**) was found to be different from that in the presence of 1 g/L bentonite suggesting immobilized metal ion at the bentonite surface. This is evident from the spectral parameters (g and width values) suggesting contrasting differences between the species at the surface and the hydrated Gd(III) ion and evidenced inner-sphere complex formation at the clay surface.

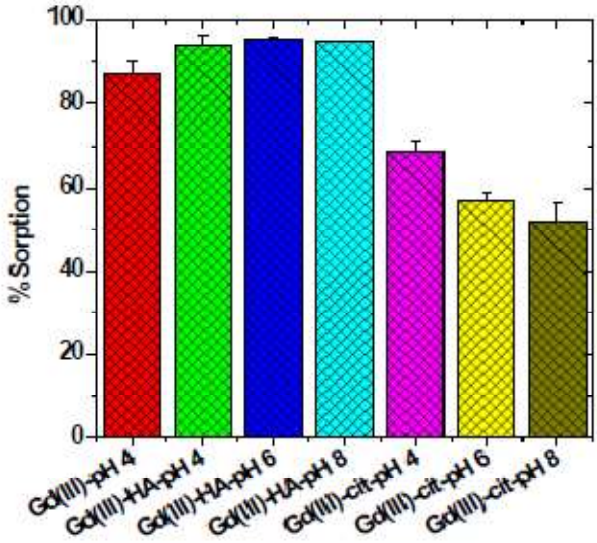

Fig. 4.12. Sorption of Gd(III) onto bentonite in the presence and absence of HA and cit at pH ~4, ~6 and ~8, *I*: 0.01 M $NaClO_4$, T: 298K

The results were further confirmed with the ionic strength variation experiments as the marginal change was seen in the % Eu(III) sorption with varying ionic strength at pH 4 and 8 (**Fig. 4.14**). The EPR signal observed at g = 1.98 with a line width of 175 G for the Gd(III) was attributed to the sorbed Gd^{3+} species [163]. Whereas the signal in the absence of bentonite at g = 1.98 with a line width of 80 G only was attributed to the metal ion coordinated with water molecules, three additional peaks were observed in the Gd(III)

solutions containing bentonite at g = 5.85, 4.20 and 2.78 (**Fig. 4.13**). The peak corresponding to g = 4.20 was attributed to the presence of ferric ions (Fe^{3+}) in the bentonite clay, which was also seen in Mössbauer spectra of clays [93-95]. On the other hand, the peaks at g = 5.85

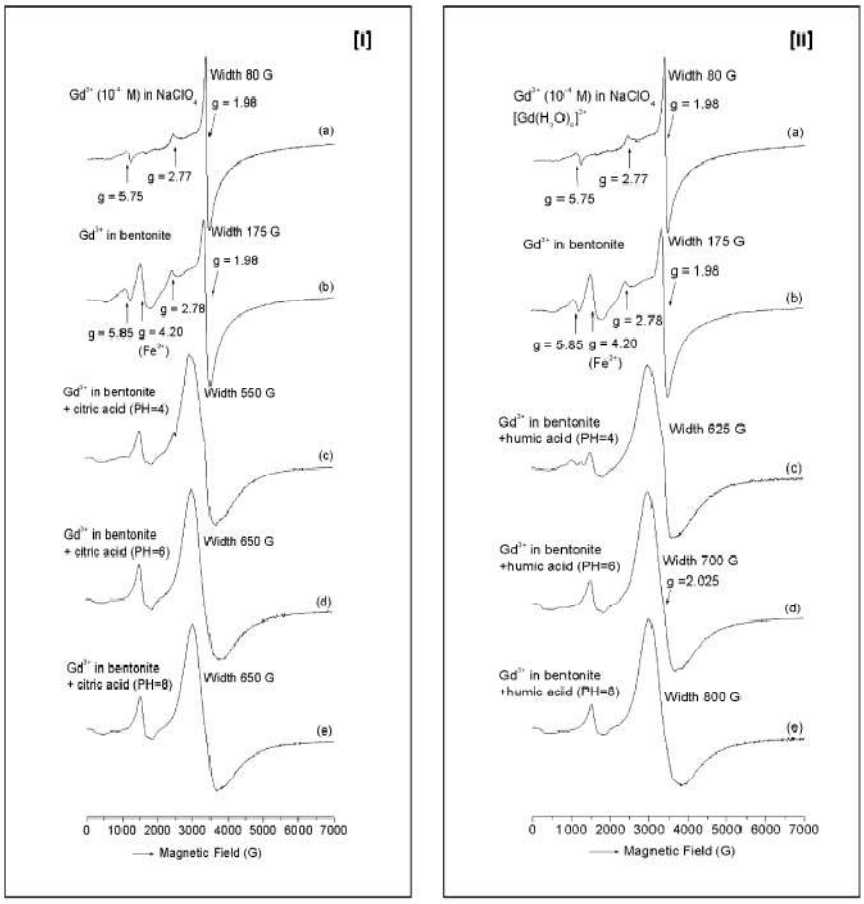

Fig. 4.13. EPR spectra of Gd(III) (10^{-4} M) under different experimental conditions. [**I**]: (a) at pH 4 (no bentonite), in the presence of bentonite (1 g/L), (b) at pH 4, (c) 10^{-4} M cit at pH 4, (d) 10^{-4} M cit at pH 6, and (e) 10^{-4} M cit at pH 8.; [**II**]: (a) at pH 4, in the presence of bentonite (1 g/L) (b) at pH 4, (c) 10 mg/L HA at pH 4, (d) 10 mg/L HA at pH 6, and (e) 10 mg/ L HA at pH 8; *I*: 0.01 M $NaClO_4$.

and 2.78 refer to the sorbed/coupled Gd(III) ions and a change in their chemical environment. The value of g = 5.85 indicated that the Gd(III) occupied a distorted tetrahedral environment when sorbed onto the bentonite surface, its rather difficult to say but g = 5.85 suggests that the Gd(III) ion are in rigidly bound state, which can only possible if it occupies the interlayer

space [163]. The presence of ligands such as citrate and HA led to the broadening of the EPR signals which was attributed to the anisotropy due to the change in the environment around the Gd(III) ions possibly due to its dehydration and sorption onto the bentonite clay. Typically, the bandwidth of the Gd(III) ions increased from 175 G at pH 4 in the absence of HA to 800 G at pH 8 in the presence of 10 mg/ L HA. On the other hand, the bandwidth increased to 650 G at pH 8 in the presence of 10^{-4} M cit. In the case of cit as the complexant, the EPR spectra changed from pH 4 to pH 6 but remained constant thereafter up to pH 8. This suggested that the species sorbed onto the bentonite surface may be changing when the pH was changed from 4 to 6 probably due to stronger complexing by cit at higher pH. However, no change in the nature of the sorbed species was seen beyond pH 6. The continuous increase

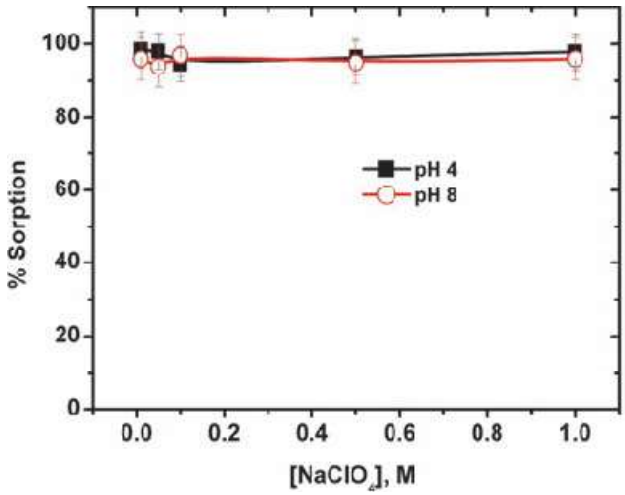

Fig. 4.14. Sorption of Eu(III) with varying ionic strength, pH ~4 and ~8, T:298 K

in the bandwidth with pH in the case of HA was attributed to the very complex nature of HA. The increase in the bandwidth at higher pH may be due to the deprotonation of the weak acidic functional groups of HA which cause progressive complexation with Gd(III) at higher pH values. The overall structure of HA can get modified at higher pH and may lead to the formation of complexed species. The relative value of the bandwidth at a given pH was found to be higher for HA as compared to cit which was attributed to the bulkier HA complex compared to the cit complex bound to the bentonite surface. The difference in the sizes shows

different rates of relaxation and hence, can have different bandwidths in EPR. These studies clearly demonstrate that the EPR spectral changes can be used to understand the changes in the chemical environment around the Gd(III) ions during the sorption process.

4.3.2.2. XAFS Studies

The XAFS studies of Eu(III) sorbed species on bentonite were carried out to get an insight into the speciation of sorbed Eu(III) species. The XAS measurements were performed for a representative set of differently prepared bentonite samples. The experiments were performed at the Eu L_2- edge as the presence of Fe in the clay caused interference during the EXFAS studies at the Eu L_3- edge. The XANES spectra are shown in **Fig. 4.15**. The positions of the X-ray absorption edges at ca. 7617 eV are very close to those expected for trivalent Eu ion, and no spectral evidence of the reduction of Eu to its divalent state was found. The XAS data

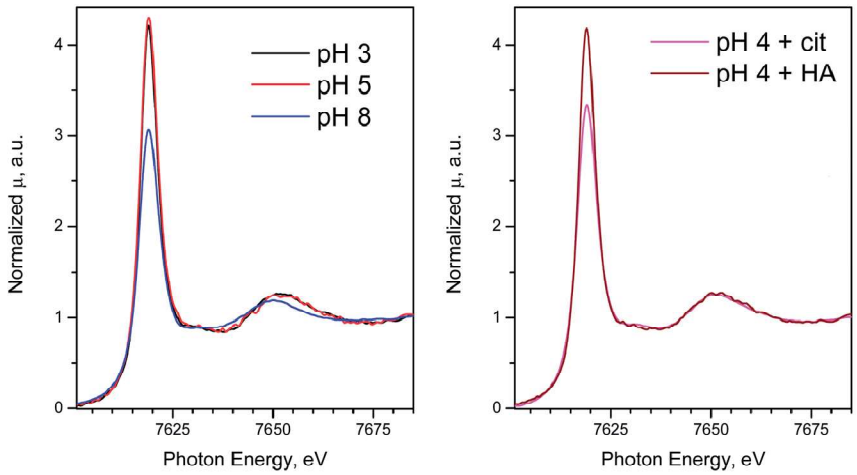

Fig. 4.15. Eu L_2-edge XANES spectra for representative Eu-sorbed bentonite samples.

revealed a dependence of Eu(III) sorption behavior on the equilibrium pH value. Firstly, the concentration of Eu(III) adsorbed onto the bentonite increased with increasing pH which was evidenced by the absolute intensity of the X-ray fluorescence signal from the similarly prepared samples. For the bentonite sample treated at pH 8, the XANES spectrum was characterized by noticeably attenuated “white line” intensity (see a panel of Fig. 4.15), which indicated a change in the chemical nature of the adsorbed species compared to the other two

samples. Additional information on the local structure of the adsorbed Eu(III) species were obtained from a quantitative analysis of the full EXAFS spectra (**Fig. 4.16**).Fourier transforms (FTs) for all the studies samples were dominated by the first coordination sphere contribution, which is unambiguously attributed to Eu–O interactions. No strong interaction in the second coordination sphere was observed, which indicated that the adsorbed

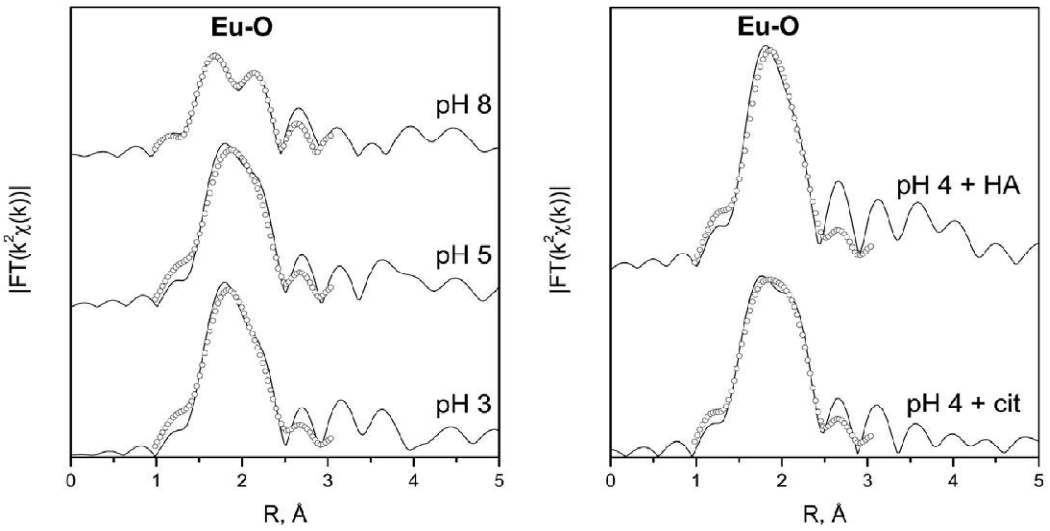

Fig. 4.16. Fourier transforms of the Eu L_2-edge EXAFS spectra for representative Eu-sorbed bentonite samples: experimental data (solid lines) and best fits (open circles). The local structure parameters corresponding to the fits are summarized in **Table 4.4**.

Eu(III) ions could not form any ordered clusters, structurally similar to either $Eu(OH)_3$ or Eu_2O_3. On the other hand, the Eu(III) ions remained as mononuclear species coordinated to the surface hydroxyl/ion-exchange sites of the clay [90]. The irregular shapes of the Eu–O dominant maxima observed for all FTs indicated non-equivalent distances within the coordination environment of the Eu(III) ions. The structural model refined against experimental EXAFS data included two different Eu–O interactions with variable inter-atomic distances and coordination numbers (CN). The parameters corresponding to the best-fit models are listed in **Table 4.4**. For the samples prepared at pH 3 and 5, the structural parameters are found to be comparable; the total Eu–O CN is close to 9, and the interatomic distances span the range 2.30 – 2.48 Å. In contrast, the sample prepared at higher pH, (pH 8)

was distinctly different; the total CN being smaller (7.8) with shorter the Eu–O distances. Such differences could be attributed to the fact that at lower pH the possibility of the outer-

Table 4.4. Bond length, coordination number and disorder factor obtained by EXAFS fitting.

Sample	Coordination sphere	N	R, Å	R_f
pH 3	Eu-O	4.3	2.30	0.033
		4.7	2.48	
pH 5	Eu-O	3.9	2.30	0.032
		5.1	2.48	
pH 8	Eu-O	3.6	2.24	0.020
		4.2	2.45	
pH 4 + cit	Eu-O	3.8	2.30	0.017
		4.8	2.48	
pH 4 + HA	Eu-O	4.0	2.31	0.041
		4.7	2.47	

sphere ion exchange behavior of Eu(III) in the bentonite suspension was possible, while its sorption was dominated by surface complexation/ inner-sphere with aluminol (≡AlOH) or silanol (≡SiOH) groups at higher pH values [84]. Since the information about the second shell atoms is difficult to get from the above recorded data, the distinction between the outer and inner sphere complexation is not very clear. On the other hand, the EPR studies on the Gd(III) complexes and ionic strength variation studies suggest the inner sphere complexation mechanism being the most prominent one for the Eu(III) sorption even at a low pH (ca. 4).

In addition to the pH variations studies, the effects of two sorption modifiers, viz. cit and HA, were also investigated. According to the XAFS results, the introduction of citric acid mimics to some extent the effects of the pH increase on the surface, the absolute intensity of the X-ray fluorescence (proportional to Eu concentration) is being strongly enhanced and the white line in the XANES spectrum being attenuated. This behavior can be attributed to the poor sorption of cit on the clay mineral [164]. Interestingly, the spectral characteristics and

structural parameters of Eu (III) species in the presence of HA are essentially the same as in the samples obtained at similar pH values without any modifiers.

4.3.3. Thermodynamic Modeling Studies

The double layer model (DLM) was used to model the surface characteristics (e.g. protonation and deprotonation) of bentonite. The data points from the acid-base titration curve commencing after the point of zero charge (PZC) calibration were utilized in a non-linear least-squares optimization program (FITEQL 4.0) to estimate the surface acidity constants. The quality of fit was evaluated by using the values WSOS/DF, where WSOS is defined as the weighted sum of squares and DF stands for the degree of freedom. Values of WSOS/DF of < 20 suggest a good match of theoretically predicted data with those obtained experimentally. The log K_a value of protonation for aluminol sites (≡XOH) (log K_{a1}: 4.06) is higher than that of deprotonation (log K_{a2}: -2.93). On the other hand, the deprotonation constant of silanol sites is (log K_{a3}:-4.3). This suggests that the aluminol sites (≡XOH) are more prone towards protonation and deprotonation as compared to the silanol sites (≡YOH) (**Table 4.5**). The calculated surface protonation constants were used for the modeling of the data on the Eu(III) sorption onto the bentonite surface. During the optimization process, the values of K_{a1}, $K_{a2,}$ and K_{a3} were fixed and the values of ≡YOEu^{2+}, ≡YOEu(OH)$^{+}$, ≡XOEu^{2+} and ≡XOEu(OH)$^{+}$ were allowed to vary for optimization purposes. The surface complexation equations for the formation of different surface species can be shown as follows:

$$\equiv YOH + Eu^{+3} \rightarrow \equiv YOEu^{2+} + H^{+} \qquad K_{a4} \qquad \textbf{(4.1)}$$

$$\equiv YOH + Eu^{+3} + H_2O \rightarrow \equiv YOEu(OH)^{+} + 2H^{+} \qquad K_{a5} \qquad \textbf{(4.2)}$$

$$\equiv XOH + Eu^{+3} \rightarrow \equiv XOEu^{2+} + H^{+} \qquad K_{a6} \qquad \textbf{(4.3)}$$

$$\equiv XOH + Eu^{+3} + H_2O \rightarrow \equiv XOEu(OH)^{+} + 2H^{+} \qquad K_{a7} \qquad \textbf{(4.4)}$$

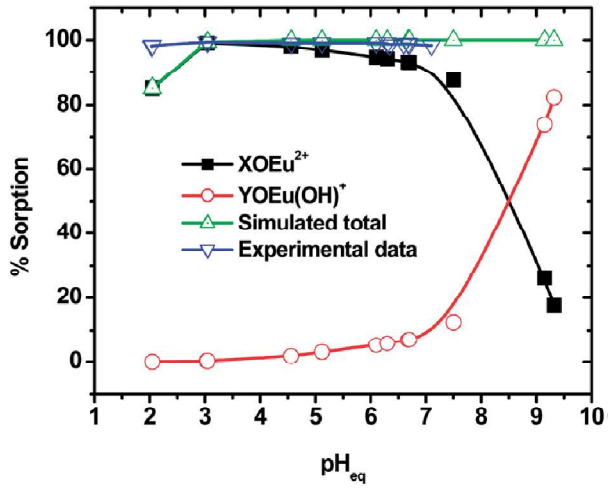

Fig. 4.17. Modeled profiles of Eu(III) sorption onto the bentonite clay, *I*: 0.01 M $NaClO_4$; T:298 K.

Table 4.5: Optimized and used values for the modeling studies

Species	*log K*	*WSOS/DF*
$Eu(OH)^{+2}$	-7.9[a]	
$Eu(OH)_2^{+1}$	-14.9[a]	
$Eu(OH)_3$	-24.9[a]	
$\equiv YOH_2^+$	4.06[b]	11.75
$\equiv YO^-$	-2.93[b]	
$\equiv XO^-$	-4.30[b]	
$\equiv YOEu^{2+}$	2.90[b]	
$\equiv YOEu(OH)^+$	1.03[b]	
$\equiv XOEu^{2+}$	4.45[b]	20.35
$\equiv XOEu(OH)^+$	-5.21[b]	

[a] ref [165], [b] p.w.

The optimized values of the variables, e.g. the surface constants (protonation and deprotonation) and the corresponding WSOS/DF, along with the Eu(III) aqueous complexation thermodynamic database used in the present modeling studies, are listed in **Table 4.5**. The various Eu(III) surface species considered in the present modeling studies are

$\equiv XOEu^{+2}$ and $\equiv YOEu(OH)^{+}$ while species such as $\equiv XOEu(OH)_2$, $\equiv YOEu(OH)_2$, $\equiv XOEu(OH)_3^{-1}$, and $\equiv YOEu(OH)_3^{-1}$ were neglected as the contribution of these species was negligible in the pH range studied. The optimized log K values for different species were

used for the construction of the speciation plots to get the probable species distribution onto the bentonite surface. The modeling results show the predominant formation of $\equiv XOEu^{+2}$ up to pH < 7 beyond which $\equiv YOEu(OH)^{+}$ is dominating and decide the sorption of Eu(III) onto bentonite in the studied pH range (**Fig. 4.17**).

4.3.4. Sorption Isotherms

The retention or release of any compound/contaminant onto a solid controls its mobility in the environment and has been quantified in terms of the ‘‘sorption isotherm’’. Among all phenomena governing the mobility of substances in aqueous media and aquatic environments, the transfer of substances from a mobile phase (a radioactive contaminant in the present case) to a solid phase (clay surface here) is a key phenomenon. That is the reason why the ‘‘isotherm’’, a curve describing the retention of a solute on a solid at its various concentrations, is a major tool to describe and predict the mobility of this substance in the environment. These retention or release phenomena are sometimes strongly kinetically controlled so that time-dependence of the sorption isotherm must be specified.

4.3.4.1. Eu(III) Sorption Isotherm onto Bentonite

To gain an insight into the sorption phenomena, viz. monolayer, multi-layer formation, physisorption, chemisorptions, etc, the sorption data are generally fitted into different models showing the relationship between the bulk activity of sorbate and the amount sorbed at a given temperature. The sorption of Eu(III) (10^{-5} – 10^{-2} M) onto bentonite (1 g/L) was studied at pH ~ 4.00(±0.05) and I = 0.01 M ($NaClO_4$). The experimental data was fitted with different isotherms such as Langmuir, Freundlich and D-R isotherms.

4.3.4.2. Langmuir Isotherm

The Langmuir sorption isotherm in the liquid phase can be represented by the following equation:

$$\frac{C_e}{q_e} = \frac{1}{q_0 b} + \frac{C_e}{q_o} \qquad \textbf{(4.5)}$$

where C_e (mol/L) is the equilibrium concentration of metal ions in the aqueous phase, q_e (mol/g) is the amount of metal ions sorbed (mol) , on the solid phase (g) , at equilibrium, q_0 (mol/g) and b (L/mole) are the Langmuir constants related to sorption capacity and sorption

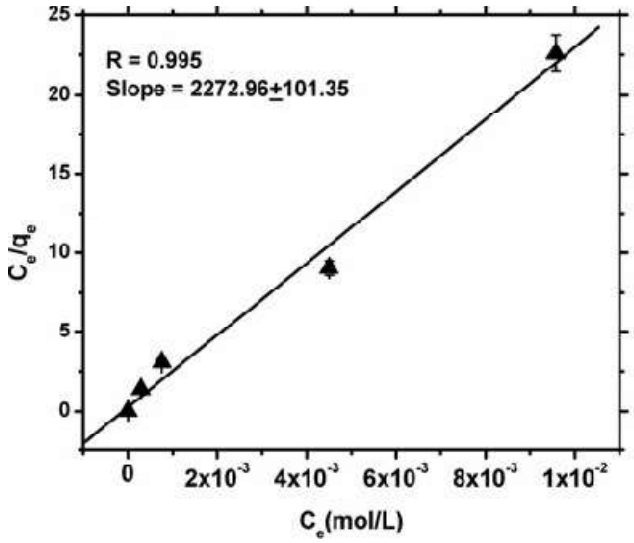

Fig. 4.18. The Langmuir isotherm of Eu(III) sorption onto the bentonite clay; pH: 4.00 ± 0.10; *I*: 0.01 M $NaClO_4$, T: 298K.

equilibrium constant respectively. The best fit to the linear plot of C_e/q_e *vs* C_e suggested that the adsorption of Eu(III) on bentonite obeys the Langmuir adsorption model (**Fig. 4.18**). The correlation coefficient for the linear fit of the plot was found to be >0.99. The Langmuir constant, q_0, determined from the slope of the above plot were found to be 4.4(±0.3) × 10^{-4} mol/g of bentonite. Similarly, the value of 'b' was calculated from the intercept as 9.09 × 10^3 L/mole. The maximum sorption capacity (q_0) represents the monolayer coverage of Eu(III)

on the bentonite and 'b' represents the equilibrium constant for sorption of Eu(III) onto the bentonite.

4.3.4.3. Freundlich Isotherm

The Freundlich sorption isotherm was also applied to the present binary system, which assumes that the enthalpy of sorption varies logarithmically with the initial concentration of metal ion, e.g., Eu(III), in the liquid phase. The Freundlich isotherm can be expressed by the equation **4.6**

$$\log\frac{x}{m} = \log k_f + \frac{1}{n}\log C_e \qquad \textbf{(4.6)}$$

where C_e is the concentration of metal ions in the aqueous phase at equilibrium, x/m is the concentration of metal ions sorbed onto sorbent per unit mass of the sorbent, k_f and n is the

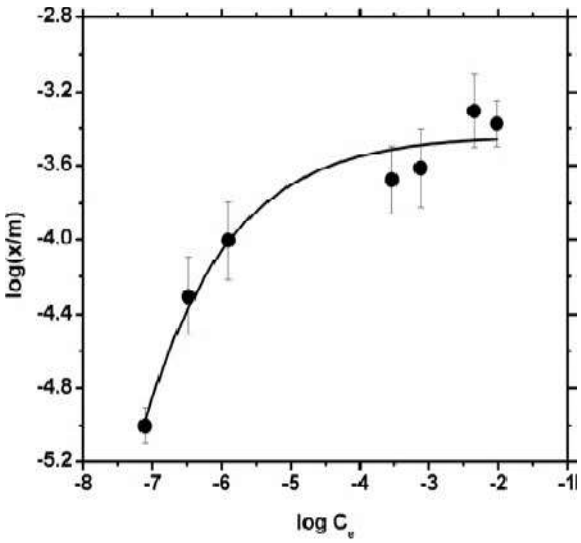

Fig. 4.19. The Freundlich isotherm of Eu(III) sorption onto the bentonite clay; pH: 4.00 ± 0.10; *I*: 0.01 M $NaClO_4$, T: 298K.

constants related to the sorption capacity and sorption intensity, respectively. The plot of log(x/m) vs. log C_e which is the linear form of the Freundlich sorption isotherm, for the sorption of Eu(III) onto bentonite shows that the points do not fit to a straight line (**Fig. 4.19**) suggesting the non-applicability of the Freundlich isotherm for this system. This suggested

the absence of multi-layer adsorption of Eu(III) on the bentonite surface under present experimental conditions.

4.3.4.4. Dubinin-Radushkevich (D-R) Isotherm

To have a better insight into the sorption mechanism, the following linear form of the D-R equation was used to fit the data on the sorption of Eu(III) onto bentonite:

$$lnq_e = lnX_m - \beta\varepsilon^2 \qquad \textbf{(4.7)}$$

where qe is the amount of Eu(III) sorbed onto the bentonite at equilibrium, X_m is the maximum sorption capacity, β is the activity coefficient which is related to the mean sorption energy, and ε is Polanyi potential and expressed as equation 4.8:

$$\varepsilon = RT.\ln(1 + {}^{1}/_{C_e}) \qquad \textbf{(4.8)}$$

where Ce is the equilibrium concentration of Eu(III) in the aqueous phase, R is the gas constant (kJ/mole) and T is the absolute temperature. The saturation limit (X_m) may represent

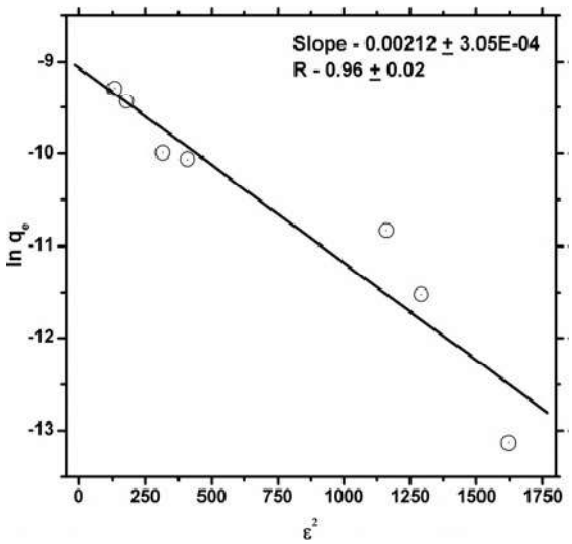

Fig. 4.20. Linearized form of the Freundlich isotherm of Eu(III) sorption onto the bentonite clay; pH: 4.00 ± 0.10; *I*: 0.01M ($NaClO_4$), T:298 K

the total specific active sites on the sorbent. The plot of ln Ce vs. ε^2 is a straight line (**Fig. 4.20**) and from the slope of the plot the value of β was calculated as – 2.12 (±0.3) × 10^{-3}. The

sorption energy (E), which is the measure of the free energy required for the transfer of one mole of metal ion from infinity to the sorbent surface, was calculated using the following relation:

$$E = \frac{1}{\sqrt{-2\beta}} \qquad \textbf{(4.9)}$$

The value of E for the present system was estimated to be 15.3 (±0.2) kJ/mol suggesting that the Eu(III) sorption on bentonite followed mainly an ion exchange mechanism or surface complexation which was in line with our earlier studies (*vide supra*) [166,167]. The sorption capacity of bentonite clay was determined to be 3.8 (±0.1) × 10^{-4} moles/g (average value) using both, the Langmuir and the D-R isotherm models.

4.3.5. Eu(III) De-sorption Studies

Batch studies were carried out to understand the role of aqueous phase acidities on the desorption of Eu(III) already sorbed onto the bentonite clay. It was expected that increasing hydrogen ion concentration in the aqueous phase should facilitate the desorption of Eu(III) sorbed by two ways, (a) either by ion exchange between Eu(III) and H^+ or (b) by the protonation of the bentonite surface leading to the release of the bound Eu(III). Desorption

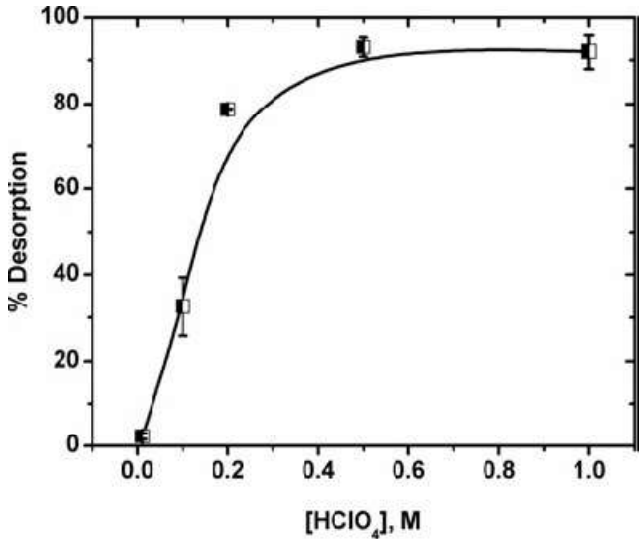

Fig. 4.21. Desorption of the loaded Eu(III) from the bentonite as a function of $HClO_4$ concentration; *I*: 0.01 M $NaClO_4$; *T*: 298 K.

studies were performed on ^{152,154} Eu sorbed onto bentonite clay (1 g/L) samples (prepared at pH 6.00(±0.05), I = 0.01 M ($NaClO_4$)) employing varying $HClO_4$ concentrations (0.01 M–1.0 M). The desorption of the sorbed Eu(III) from bentonite increased with acid concentration from ca. 2% (0.01 M $HClO_4$) to > 94% (1 M $HClO_4$) (**Fig. 4.21**). The data suggests that if the clay mineral loaded with Eu(III) ions comes in contact with an acidic effluent, it is quite probable that the radionuclide may be desorbed and start moving with the flow of water.

4.4. SORPTION OF FISSION PRODUCTS (FP)

It was of interest to compare the relative sorption behavior of trivalent [[Am(III)] ~10^{-10} M, [Eu(III)] ~10^{-6} M)], divalent [[Sr(II)] ~ 10^{-6} M], and monovalent [[Cs(I)] ~ 10^{-9} M] ions onto bentonite as a function of pH. **Fig. 4.22** shows that the % sorption of these metal ion shows

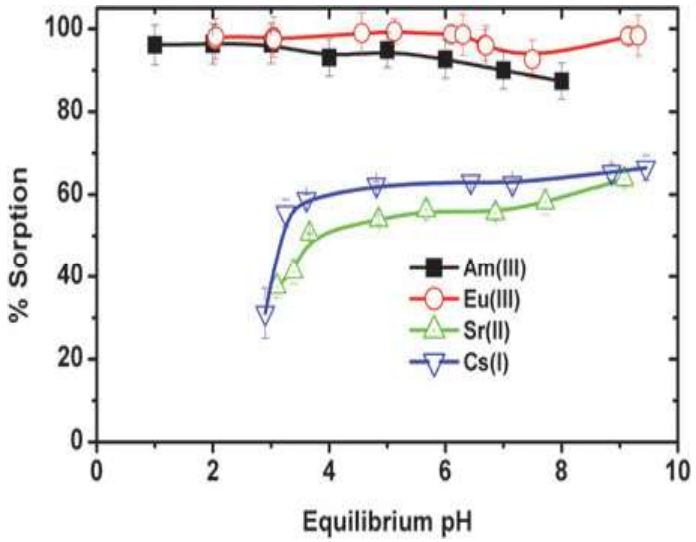

Fig. 4.22. Sorption profile of different metal ions (tracer concentrations) onto bentonite (1g/L) as a function of pH; I: 0.01 M $NaClO_4$; T: 298 K.

the following order: Am(III) > Eu(III) > Cs(I) > Sr(II). It is important to mention that the sorption studies were performed using a comparable count rate (cpm) for each of the radionuclides to have reproducible sorption data. Under this condition, it was difficult to perform the experiments with nearly the same concentrations of the metal ions. However, it was worth noting that despite having two order higher concentration of Eu(III) in solution, its

sorption onto bentonite was comparable to that of Am(III). The higher % sorption of trivalent metal ions was due to their higher charge which led to better electrostatic attraction and stronger complexation with the bentonite surface. However, the same argument should hold for the sorption of a divalent ion like Sr(II) as compared to that of a monovalent ion such as Cs(I). In contrast, a reverse order of sorption was observed under the present experimental conditions. This could be explained in terms of their hydration sizes. The reported hydration diameters of Cs(I) and Sr(II) are ~ 250 pm and 500 pm, respectively [168]. Therefore, the resulting electrostatic attraction between Cs(I) and the negatively charged bentonite surface is expected to be more as compared to that of Sr(II). This may lead to an enhanced sorption of Cs(I) as compared to that of Sr(II). Similar observations have been reported elsewhere during the sorption of Sr(II) and Cs(I) on smectite rich clay [169-173]. It is also probable that swelling characteristics of the bentonite might be helping in the creation of ion exchange sites, which prefer a less hydrated metal ion like Cs(I) with smaller size over the highly hydrated metal ions such as Sr(II) with a larger size.

4.5. Eu(III) SORPTION ONTO KAOLINITE: A BI-LAYER SYSTEM

Kaolinite come under another class of clay minerals having bi-layer system, 1:1 (silica: alumina), which are also used by several researchers for the sorption of trivalent lanthanide/actinides under a variety of experimental conditions. In the present work, the sorption of Eu(III) onto kaolinite was investigated in the presence/absence complexing agents such as cit and HA. The data were compared with that of bentonite in different conditions.

4.5.1. Kinetics and Sorption Edge

The kinetics of Eu(III) sorption onto kaolinite was investigated at different pH (3.0, 5.5, and ~7.5) and ionic strengths (0.01, 0.1 and 1 M $NaClO_4$) (**Fig. 4.23**). The sorption equilibrium was reached in about 1 h under the present experimental conditions. The % sorption of

Eu(III) varied with ionic strength in acidic pH, e.g., pH 3.0 and 5.5, whereas comparable sorption data were obtained with varying ionic strengths at pH 7.5. The difference in the %

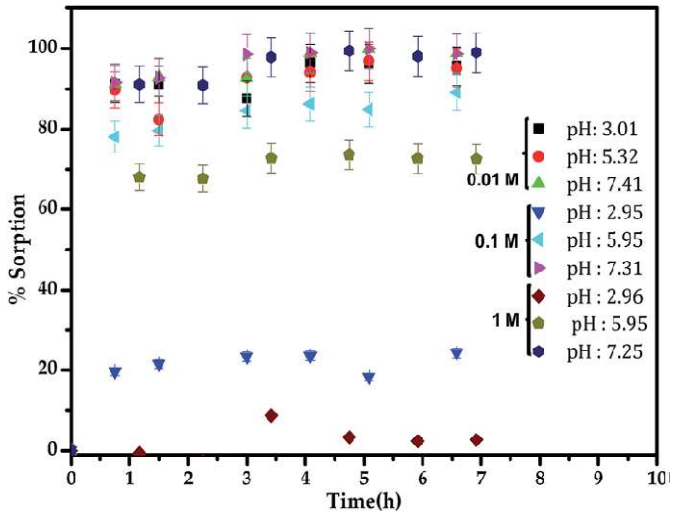

Fig. 4.23. Kinetics of Eu(III) (10^{-6} M) sorption onto kaolinite (1 g/L) at different pH and ionic strengths.

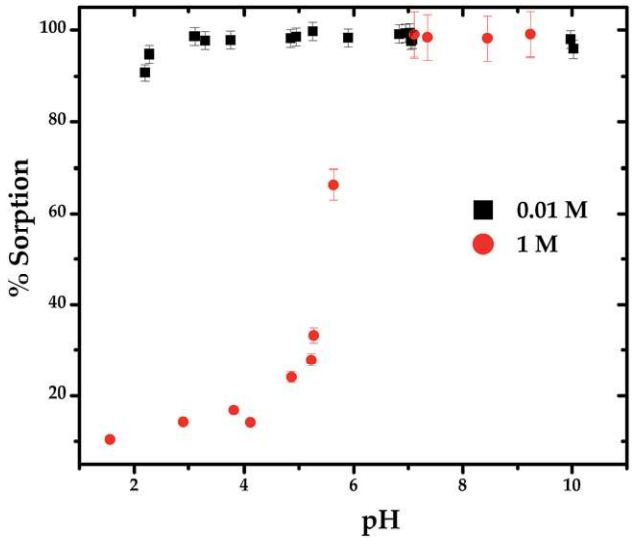

Fig. 4.24. pH edge for the Eu(III) (10^{-6} M) sorption onto kaolinite (1 g /L) at different ionic strengths (*I:* 0.01 and 1 M $NaClO_4$).

sorption data with the ionic strength at different pH values suggest the prevalence of different mechanisms of Eu(III) sorption at different pH values. These data suggest that the Eu(III) sorption follows an ion-exchange mechanism of sorption in acidic pH range, while complexation reactions with the surface hydroxyl groups are seen to be dominating at higher

pH values (pH > 6.0), (**Fig. 4.24**). In order to obtain the range of pH values where the sorption mechanism changes from ion-exchange to surface complexation, pH edge for Eu(III) sorption was determined at different ionic strengths. From the sorption profiles at different ionic strengths, one can say that,the Eu(III) sorption follows an outer-sphere complexation mechanism at the kaolinite surface up to pH <6, beyond which, surface complexation (inner-sphere) is predominantly responsible for its sorption onto kaolinite [111]. The lower % sorption at the higher ionic strength and at low pH, can be attributed to competition between Na^{+} and Eu^{3+} for the binding sites available on the kaolinite surface, whereas at higher pH, the nature of the interaction changes and the % sorption becomes similar in both the cases.

4.5.2. Effect of Complexing Agents

As discussed previously, the presence of different complexing agents in the geosphere can affect the interaction mechanism between the clay and the metal ions of interest. The organic complexants such as oxalic acid (10^{-4} M), citric acid (10^{-4} M), and natural organic matters (NOM) e.g., humic acid (10 mg/L) were used as representatives of the organic complexants found in the ecosphere, as these molecules owe their complexing ability due to the presence

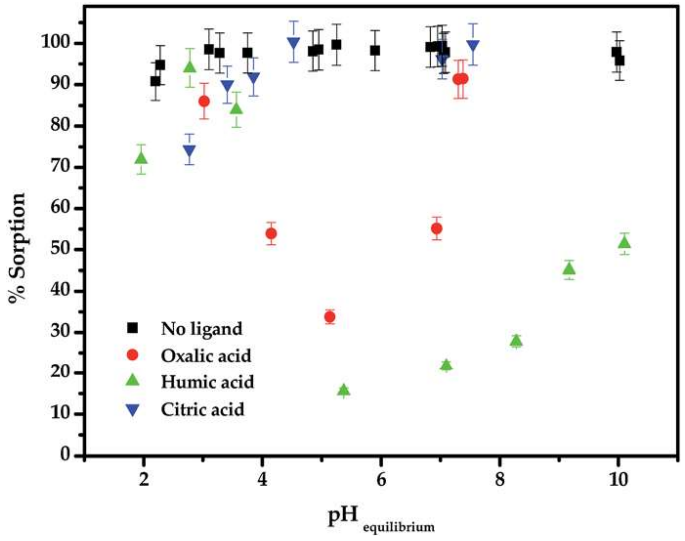

Fig. 4.25.: Effects of oxalic acid (10^{-4} M), citric acid (10^{-4} M), and humic acid (10 mg/ L) on the Eu(III) (10^{-6} M) sorption onto kaolinite (1 g/ L).

of carboxylate (-COO) and/or hydroxyl (-OH) groups, which are the most common functional groups found in naturally occurring organic molecules. For the sorption experiments, organic complexants and Eu(III) tracer were added simultaneously to 1 g/L Kaolinite suspension and the mixture was equilibrated overnight. The sorption of Eu(III) in the presence of oxalic acid initially decreased up to 30% from pH 3.0 to 5.5 and subsequently increased to yield quantitative sorption (pH >8.0). The initial decrease in the % sorption values is due to the aqueous complexation of Eu(III) with oxalic acid up to pH 5.5, beyond which the formation of neutral species (**Fig. 4.25**) reduces the complexing ability of the metal ion resulting in a rise in the Eu(III) sorption. In sharp contrast, the addition of citric acid does not change Eu(III) sorption as compared to the bare Eu(III) sorption. The difference in the nature of the Eu(III) sorption profile in the two cases is still not understood. For studies involving HA, the sorption of Eu(III) followed a trend similar to that in the case of oxalic acid and hence, a similar explanation can be made. Fluorescence studies were carried out to further investigate the interactions of Eu(III) with kaolinite at the molecular level.

4.5.2.1. Fluorescence Studies

The nature of the complexes (inner or outer sphere) of Eu(III) with kaolinite in the presence/absence of the complexing anions was studied with fluorescence spectroscopy (FS). The FS experiments were performed for oxalic acid and HA. The emission spectra of $Eu(III)_{aq}$, Eu(III) – kaolinite, and Eu(III) – oxalic acid/HA were recorded and compared with those obtained for the ternary systems, e.g., Eu/kaolinite–oxalic acid/ HA to correlate the luminescence spectral data with the speciation of Eu(III) in the different systems. The fluorescence studies for the ternary systems were carried out using 10^{-4} M Eu(III) for better signal to noise (S/N) ratio. The fluorescence spectra of the suspensions were recorded for both the systems. In the case of oxalic acid, the fluorescence spectra of the suspensions were recorded with varying pH at a higher kaolinite concentration of 2.5 g/ L (**Fig. 4.26**). The fluorescence spectra of the Eu(III)–kaolinite–oxalic acid ternary system was found to be

similar to that of the Eu(III)–oxalic acid complex (binary system) obtained in aqueous media. This suggests the presence of a Eu(III)–oxalate complex on the surface of kaolinite, even in

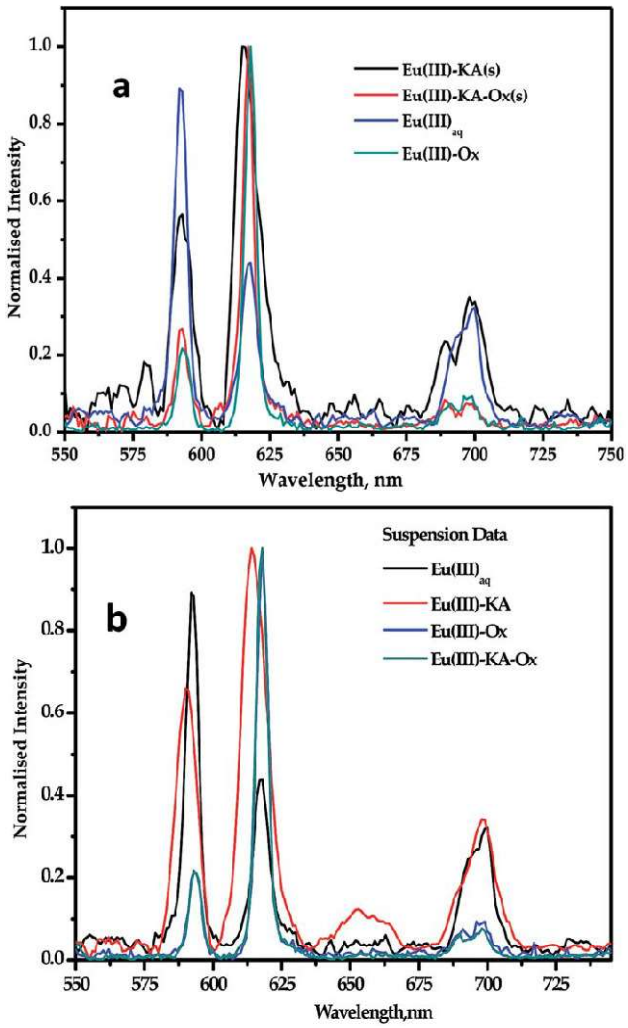

Fig. 4.26. Comparison of luminescence spectra of Eu(III) (10^{-4} M) sorbed onto kaolinite (2.5 g/L) (a) solid smeared onto glass slide; (b) suspension in the presence and absence of oxalic acid (10^{-4} M); T: 298 K.

the ternary system. The lifetime data conformed to a mono-exponential decay pattern with a calculated lifetime of 232 ±10 μs, which was close to the lifetime of the Eu(III)–oxalate complex (within the limits of experimental error). Since the suspension was directly used for fluorescence studies, the emission may arise from Eu(III)–oxalate complex present as an aqueous soluble species or may be sorbed onto the kaolinite surface. To confirm this, the

suspension was centrifuged at 20,000 rpm and the supernatant and the solid residue were separated and individually used for the fluorescence studies. The fluorescence spectra of the supernatant showed no emission lines for Eu(III)–oxalate complex (either no Eu–oxalate

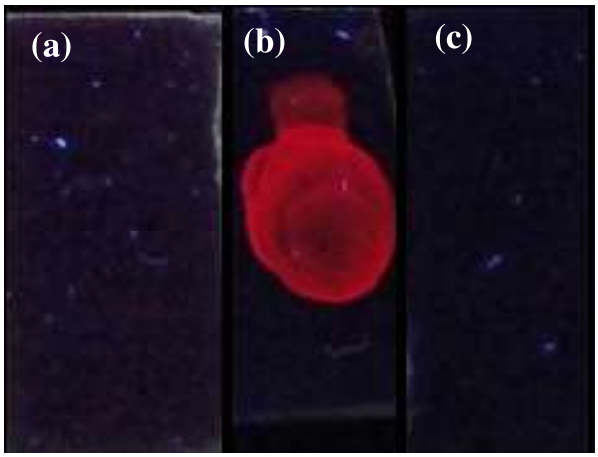

Fig. 4.27. Fluorescence under UV lamp (a) Eu-Kaolinite-oxalate, (b) Eu(III)-oxalate spot, (c) blank (only kaolinite)) (λ_{ex}: 254 nm), of Eu(III) (10^{-4} M) sorbed onto kaolinite (2.5g/L).

complex present or the emission is below the detection limit of the instrument). A thin layer of the slurry (residue) was kept on a glass plate, air-dried at room temperature and used for the luminescence spectral analysis. The recorded emission spectra were very similar to those of the aqueous Eu(III)–oxalic acid complex (**Fig. 4.27**). The peak ratio values and lifetime data are in close agreement (within the experimental uncertainties) with those of the Eu(III)–oxalic acid complex. The glass plate with deposited solid residue was also seen under a UV lamp at 254 nm excitation and it emits red luminescence from the surface, confirming the presence of Eu(III) as the Eu(III)–Ox complex on the kaolinite surface. The addition of 10 mg/L HA did not change either the lifetime or the emission spectra of Eu(III). On the other hand, increasing the HA concentration to 100 mg/L resulted in a change in the peak ratio ($^5D_0 \rightarrow {}^7F_2$ to $^5D_0 \rightarrow {}^7F_1$ transition) from 0.59 for $Eu(III)_{aq}$ to 1.24 for Eu(III)-HA_{aq} onto kaolinite surface keeping the lifetime as 111±3 μs.

To summarise, the sorption profile of the studied radionuclides have quite different affinities for any given clay. For example, the sorption of various radionuclides onto bentonite follows the order Am(III) ~ Eu(III) > Cs(I) > Sr(II), which can be explained either on the basis of the difference in their hydration radius or their ionic potential values. The presence of complexing agents behave differently for different radionuclides, for example, the presence of humic acid decreases the sorption of Eu(III) at circumneutral pH conditions but for U(VI) the decrease is marginal. EXAFS and fluorescence are important tools to understand the mechanism of sorption. In general, the presence of the complexing agents modifies the sorption profiles of a radionuclide onto the mineral surface and hence, serves as an additional and important parameter to ascertain the migration of radionuclides in the geosphere and metal ion binding to the surface for ternary (radionuclide+ clay + complexants) systems.

5

SORPTION AND MODELING STUDIES ON NATURAL CLAYS

5.1. INTRODUCTION

Though ^{237}Np has a very long half-life ($2.14x10^{6}$ y), primordial Np no longer exists as it must have decayed since the age of the Earth is considerably larger (4.5×10^{9} y). Holleman and Wiberg instead give an abundance of 4×10^{-17} % for ^{237}Np in the earth's crust which equals $2.4\ x10^{5}$ kg [174]. The natural background of most radioactive isotopes has been increased significantly by anthropogenic activities, particularly by the atmospheric and underground nuclear weapon tests and mid-air explosion of satellites containing ^{238}Pu as a power source [174.] The resulting total global fallout is estimated at 2500 kg of ^{237}Np [175]. By far the largest amount of Np released into the environment can be attributed to the operation of nuclear power plants. The total amount of ^{237}Np produced by the nuclear industry was estimated to be 5.4×10^{4} kg by the end of 2003, and increasing by about 3000 kg each year [176].

Neptunium, a by-product during the fission reaction involving ^{235}U fuelled nuclear reactors, is also present in all stages of the nuclear fuel cycle. ^{237}Np is the daughter product of

^{241}Am (by α-decay) and the granddaughter of ^{241}Pu (beta decay followed by alpha decay), is also formed through the radioactive decay in vitrified nuclear waste blocks containing these isotopes. Np, due to its comparably poor sorption properties, can escape from the repository more easily than its parent elements. In a considerably large timescale, it is possible that water may infiltrate the repository and can corrode the containers, releasing radiotoxic long-lived radionuclides like ^{237}Np into the geosphere. For such a scenario, the natural water concentration of actinides in general and of ^{237}Np, in particular, is anticipated to be very low [106].

The actinides behave differently depending on the site-specific chemical conditions determined by the mineral composition of the repository. The two key natural barriers to the spreading of such radionuclides buried underground are their solubility in water and their sorption onto clay minerals. The present Chapter will concentrate on the latter aspect. On the basis of availability, decay properties, and distribution, only 6 of the 14 actinide elements are of long-term environmental concern, namely Th, U, Np, Pu, Am, and Cm [177]. Resulting from the effective charges of the ions (e.g., ionic potential) and considering hydrolysis and polymerization of the +IV oxidation state, the ionic species like M^{3+} form the strongest while MO_2^+ form the weakest complexes [106]. Np can exist in the oxidation states from III to VII, most of which are formed under rather unusual conditions such as extreme redox potentials, radiolysis, or elevated temperatures [177]. Np(V) is stable under ambient conditions; Np(IV) is only present in the absence of oxygen, whereas Np(III) and Np(VI) can exist under extremely reducing or oxidizing conditions or under the influence of radiation [19]. Hence, the redox reactions encountered in far-field conditions (away from the nuclear repositories) as well as in most groundwater environments do not induce considerable changes in the neptunium speciation. Under a wide range of environmental conditions, Np speciation is dominated by its pentavalent state as the NpO^{+2} cation [63]. In aqueous media, Np(V) and Np(VI) exist as linear trans-dioxo cations NpO_2^+ and NpO_2^{+2}, which are linear and

symmetric[106,178]. Np(VI) is stable in acidic solutions predominating at pH 3-5 but is rather easily reduced to Np(V) [179]. At high Np concentration and acidity, the two species are additionally connected via the disproportionation reaction given below for which the reaction rate is extremely slow [19].

$$2NpO_2^+ + 4H^+ \rightarrow Np^{4+} + 2NpO_2^{+2} + 2H_2O \qquad \textbf{(5.1)}$$

The simple pentavalent aquo ion comprises about 95% of the total soluble neptunium, again suggesting that Np(V) is the most stable oxidation state in aqueous solutions. All actinides, except the pentavalent ions, are significantly vulnerable to hydrolysis at pH-values encountered in the natural water. The fifth oxidation state is the most stable oxidation state in water and does not hydrolyze significantly at pH < 7 [179]. The products of hydrolysis can be monomeric, polynuclear, or colloidal Neptunium hydroxides [180]. Np(V) forms the hydrolyzed products such as $NpO_2(OH)$ and $NpO_2(OH)_2^-$ only at high pH values [177]. Under such conditions, Np(V), similar to Np(VI), exist as hydroxides and hydrated oxides [181]. The amphoteric character of Np(V) is shown as follows:

$$NpO_2(OH)_2^- \pm OH^- \leftrightarrow NpO_2(OH) \pm H^+ \leftrightarrow NpO_2^+ + H_2O \qquad \textbf{(5.2)}$$

Regarding the reaction chemistry, actinide ions in all common solution oxidation states are hard Lewis acids. The pentavalent actinyl ions (AnO_2^+) behave like large singly charged alkali metal cations without any noteworthy tendency for precipitation and complexation reactions [174]. Consequently, the stability constants of Np(V) complexes are relatively low compared to those of Np(III), Np(IV), and Np(VI) [182].

The exact character of the bonding in actinides, however, is determined by the oxidation state of the actinide and the hard or soft properties of the ligand(s). Neptunium is perhaps the only actinide favoring the fifth oxidation state under a wide range of environmental conditions. Therefore, it is predicted to be the most easily soluble and mobile

actinide in the environment, considering similarly the repository surroundings as well as most natural waters [106]. For example, the apparent diffusivity for Np(V) in compacted bentonite is ten to 100 times higher compared to lower oxidation state actinide species like Am(III) or Pu(IV) [183]. Np(V) also forms the weakest complexes among the actinides. At rather low neptunium concentrations, which can be expected after a possible release from a repository, sorption onto particulates or clay minerals is the main factor influencing the environmental fate of neptunium and, thus, is the most vital geochemical mechanism for limiting its migration.

5.2. Np(V) SORPTION STUDIES ONTO CLAYS

Clay minerals are the major part of many argillaceous formations proposed as host rocks for deep geological repositories. Some of these are the Opalinus clay in Switzerland, Callovo-Oxfordian, Toarcian clays in France, Boom and Ypresian clays in Belgium and Horonobe sediments in Japan, etc. The bentonite based backfill barrier materials are considered in most disposal concepts worldwide [184]. Together with iron oxides, clay minerals are the major constituent of soils and sediments, which represent the interface between geo-, atmo-, bio-, and hydrosphere. They also serve as the most important sink for metals once introduced into the environment.

5.2.1 Np(V) Sorption Kinetics and pH Edge

The Np(V) uptake studies were performed as described in the experimental part. The kinetics of Np(V) uptake onto bentonites of different origins viz. Kutch, Rajasthan, and Khakassia were studied at 0.01 M and 1 M $NaClO_4$ at pH ~8.0 **(Fig. 5.1(a) and 5.1(b)).** The sorption equilibrium for Np(V) sorption was reached in ~ 24 h for all the studied bentonite samples at different ionic strengths (**Fig. 5.1(a) and 5.1(b)**). Although there were mineralogical differences in the bentonite from different origins, the sorption kinetics of Np(V) on these samples were similar. The lower Np(V) sorption onto Khakassia bentonite is attributed to the

difference in its mineralogy when compared to other clays and will be discussed later. The % sorption of $^{239}Np(V)$ (4×10^{-14} M) onto different bentonite samples was studied at varying pH

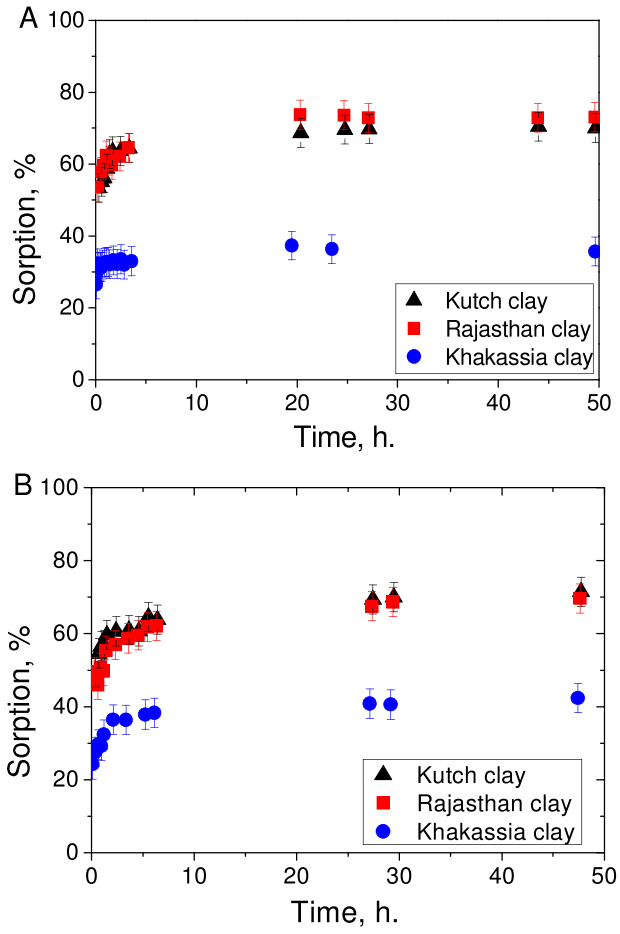

Fig. 5.1. Kinetics of Np(V) sorption onto natural bentonite of different origins at (a) *I*: 0.01 M and (b) *I*: 1.0 M $NaClO_4$ ($pH_{initial}$:8.5, [solid phase]: 0.5 g/L).

values in 0.01 M and 1 M $NaClO_4$ (**Fig. 5.2**). For all the studied clay systems, %sorption of Np(V) increased with increasing pH at a given ionic strength. The shape and position of the pH sorption edge differ for the different bentonite samples discussed above. The Khakassia bentonite has the lowest sorption efficiency in all the studied clays. The experimental conditions for the Np(V) sorption experiments correspond to a high excess of the solid phase (0.5g/L) compared to the Np(V) concentration (4×10^{-14} M), with a constant solid to liquid ratio of 0.5 g/L. However, the specific surface area of the studied bentonite samples differs

and therefore the changes in pH-edges from sample to sample can be affected by this difference in the specific surface area (*vide infra*). The sorption of Np(V) may also depend strongly on the mineral composition of the studied clay systems. The changes in radionuclide sorption at different ionic strengths are indicative of their sorption mechanism onto the clay surface (*vide infra*) [185]. For the present system, the Np(V) sorption onto Rajasthan and

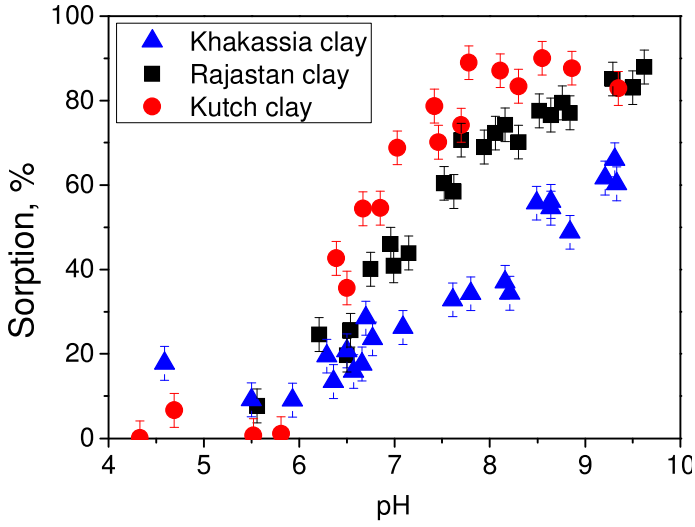

Fig. 5.2. The pH-dependent Np(V) sorption onto natural bentonite of different origins; *I* : 0.01 M, [Np(V)] : 4×10^{-14} M; [solid phase]: 0.5 g/L; T: 298 K.

Khakassia bentonite clays at different ionic strength, e.g., 0.01 M and 1 M ionic strengths, are similar, suggesting inner-sphere complexation of Np(V) under the studied pH range. In earlier reports, it was shown that the Np(V) sorption onto clay minerals depends on the pH of the medium. At lower pH, ion-exchange is dominant whereas, at higher pH, surface complexation of Np(V) is the major mechanism of metal ion uptake by the clay [186-187]. In the present experiments, Np(V) sorption at pH values < 6 was low and barely changes with increasing ionic strength. This may be partially due to the hindered exchange of Np(V) with interlayer cations e.g. Ca^{2+} and Mg^{2+} (especially in the case of Kutch and Rajasthan clays) as well as due to the competition with these cations for sorption sites. These cations may be present in solution due to the partial dissolution of accessory minerals such as calcite,

dolomite, and others and their presence may affect the ion-exchange of Np(V) with the interlayer cations of clay minerals. In the case of Kutch clay, the Np(V) sorption changes

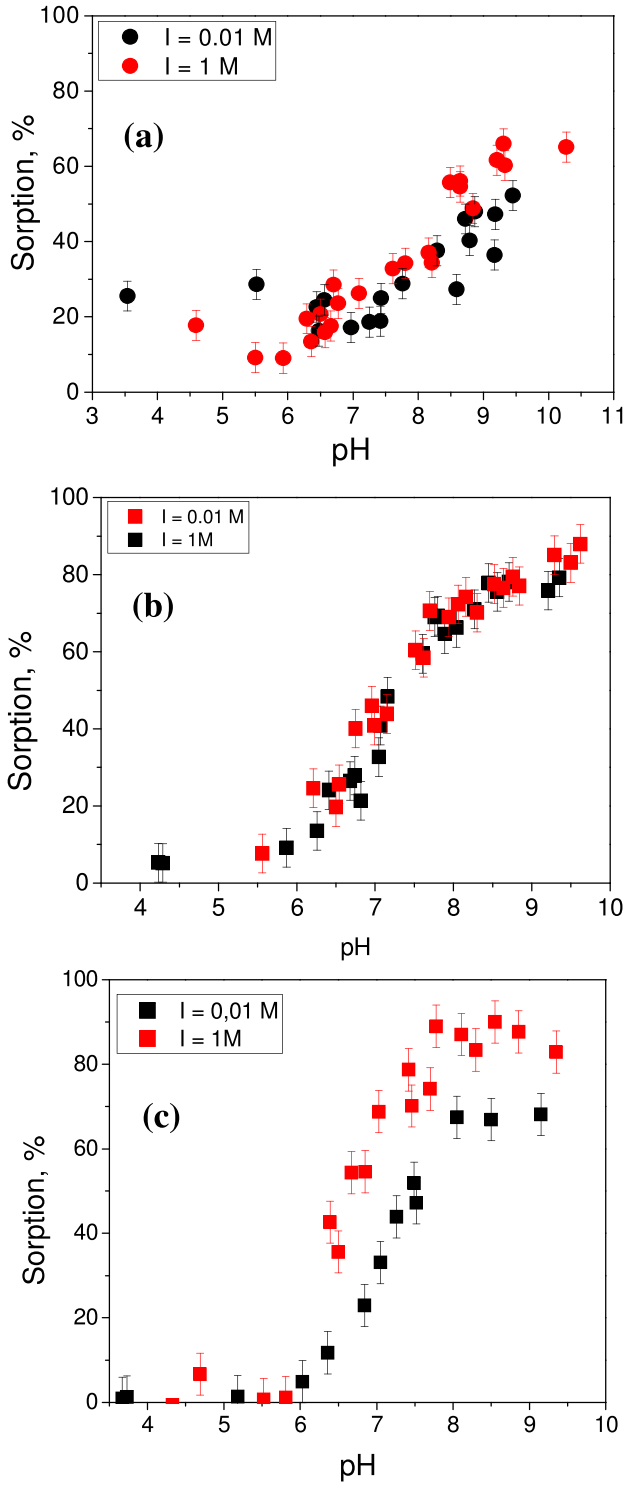

Fig. 5.3. The pH-dependent Np(V) sorption onto (a) Khakassia; (b) Rajasthan and (c) Kutch bentonites at different ionic strengths, [Np(V)] : 4×10^{-14} M; [solid phase]:0.5 g/L; T: 298 K.

with varying ionic strengths though the trend is opposite to the expected results. The experimental results demonstrate higher sorption of Np(V) onto the Kutch clay at higher ionic strength values. To understand this, some more experiments were carried out to arrive at logical conclusions. The Kutch clay contains Mg^{2+} and Ca^{2+} substituted smectite may influence the Np(V) sorption. Consistent with previously published data, Np(V) sorption was found to be higher onto Na-smectite than onto Ca-smectite, which could explain the lower Np(V) sorption onto Kutch clay at lower ionic strength [186,188]. To determine the impact of the changes, the following experimental approach was undertaken. The natural Kutch

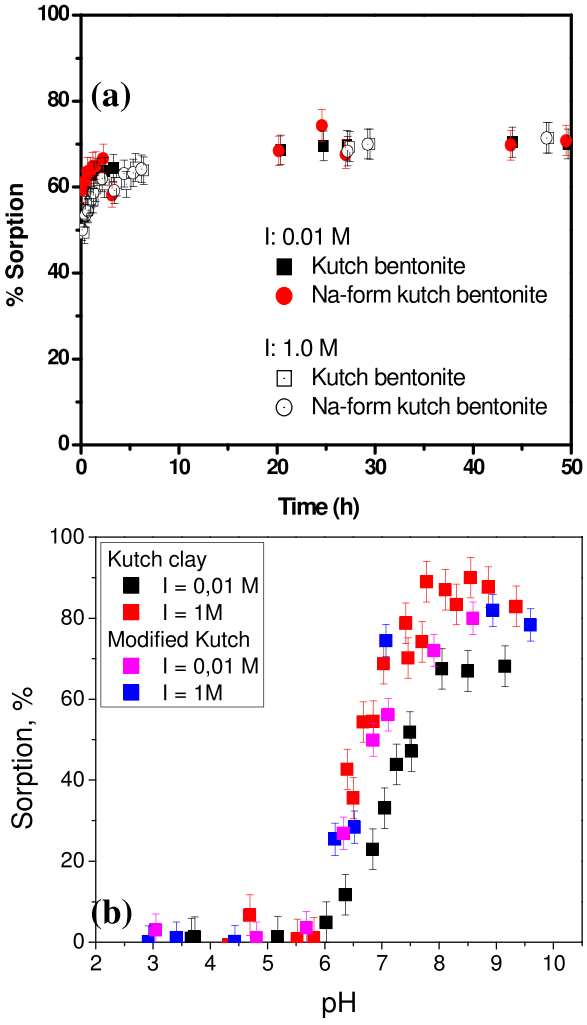

Fig. 5.4. The comparison of Np(V) (a) sorption kinetics and (b) pH dependence onto the Na-form of Kutch bentonite with pristine Kutch bentonite at different ionic strengths; [Np(V)]:4 $\times 10^{-14}$ M; [solid phase]: 0.5 g/L; T: 298 K.

bentonite was treated with 1 M $NaClO_4$ to convert the Ca/Mg^{2+}-smectite form of Kutch to the Na- form. This treated Kutch bentonite (Na-smectite form), now called as the Na-form Kutch clay, was characterized by XRD (see Chapter 3, Section 3.2.1). The XRD pattern confirms the smectite modification to Na-form Kutch bentonite as showed two visible basal reflections with $d_{(001)}$ =12.6 Å and $d_{(002)}$ = 6.3 Å, which indicated interlayer cation exchange to convert to the Na^+ form. The sorption kinetics and pH-edge for Np(V) sorption onto the Kutch clay and the Na-form of Kutch clay were compared (**Fig. 5.4(a & b)).** From the comparison of the pH edges of Np(V) sorption **(Fig. 5.4(b)),** it is clear that the sorption of Np(V) onto the Na-form Kutch clay is higher than that onto the natural bentonite at lower ionic strength values. The Np(V) sorption pH edge onto the Na-form Kutch bentonite is similar at different ionic strengths and is comparable to the sorption data for the pristine Kutch clay at a higher ionic strength (1 M $NaClO_4$). This suggests that even the preliminary treatments such as washing can also alter the Np(V) sorption onto the clay minerals. It may be seen from the above experiment that the change of smectite from the Mg/Ca form to the Na-form may have increased the Np(V) uptake at a higher pH range. Other factors contributing to the enhanced Np sorption onto Kutch and Rajasthan bentonite when compared with those of the Khakassia clay suggested those due to the presence of other minor components or accessory minerals phases present in it. Experimental and theoretical protocols were planned to understand the two aspects, i.e., i) the role of interlayer cation and ii) the effect of the presence of accessory minerals, on the Np(V) sorption.

5.2.2 Role of Accessory Minerals onto Np(V) Sorption

To understand the role of the accessory minerals and to probe the specific phases responsible for the Np(V) sorption, a combination of two techniques, viz. SSNTD (for α-radiography) and SEM-EDX were used. The local distribution of Np(V) on the studied clays was studied at higher surface loading with ^{237}Np compared to the batch experiments where ^{239}Np was used. The samples were divided into “light” and “dark” fractions by centrifugation (for details see

Chapter 3, Section 3.5.1). Both the fractions were placed on glass slides and covered with CR-39 polycarbonate films for α-radiography. The exposed (for 17 h) CR-39 film was etched with 6 M NaOH at 75 ± 1 ºC for 6 h and the α-track images along with the corresponding areas of the solid samples were observed using an optical microscope. (See Chapter 2, Section2.3.4). **Fig. 5.5** shows optical microscope and corresponding α-track analysis images for Np(V) sorbed onto different clays. In the case of the "light" bentonite fraction, Np(V) was

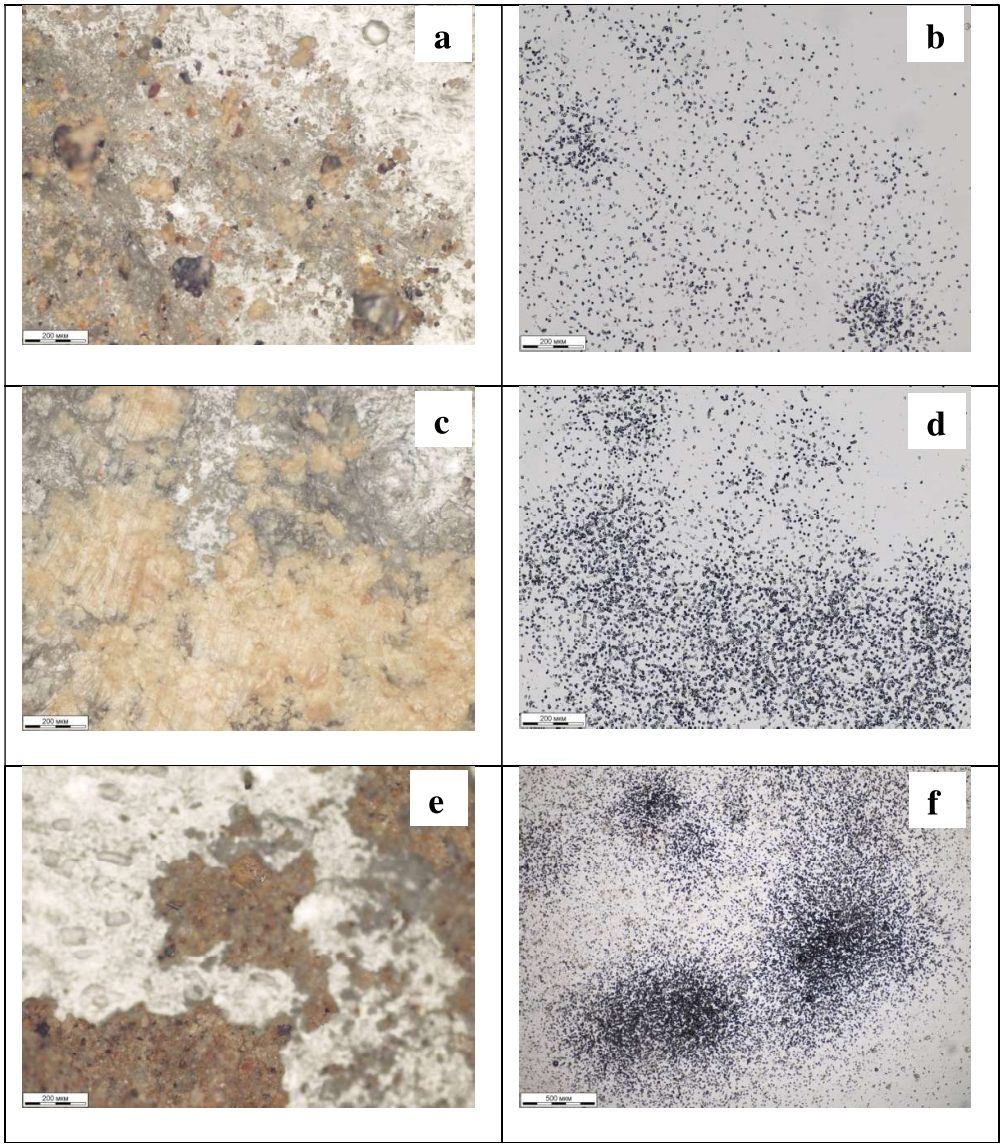

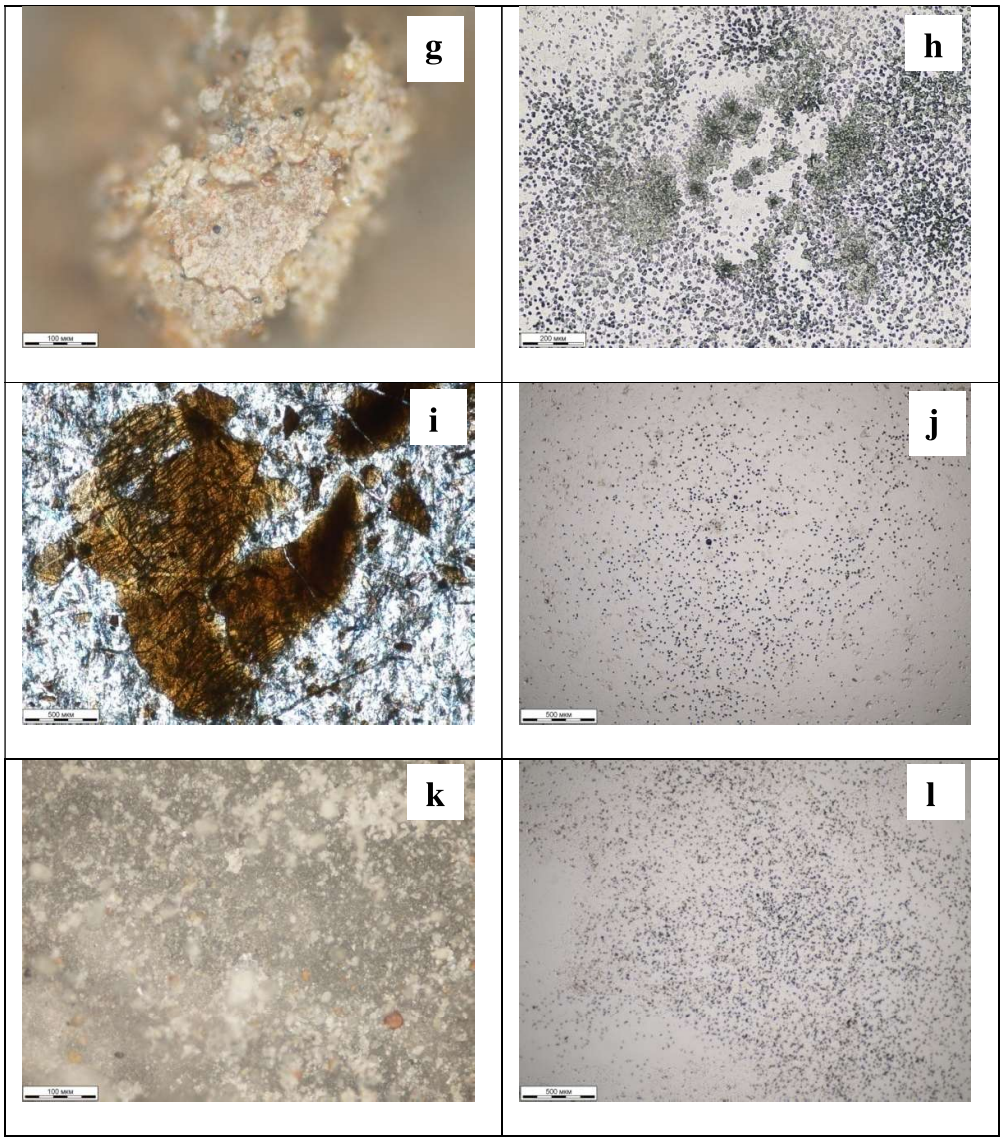

Fig. 5.5. Optical microscope images (a) Dark-Rajasthan; (c) light-Rajasthan; (e,g) Dark-Kutch; (i) light-Kutch; (k) light-Khakassia and corresponding α-track analysis (b) Dark-Rajasthan; (d) light-Rajasthan; (f,h) Dark-Kutch; (j) light-Kutch; (l)light-Khakassia images for Np(V) sorbed onto different clays. The two fractions were separated by centrifugation and were given name based on relative appearance.

found to be evenly distributed, whereas the "dark" fraction showed hot-spots where ^{237}Np was concentrated. The SEM-EDX of the same samples showed that the "dark" bentonite fraction contained mainly the Fe- and Fe/Ti containing oxides and hydroxides (**Fig. 5.6**),

whereas the "light" fraction was predominantly rich in clay minerals. Thus, even under high surface loading conditions, the presence of accessory minerals, such as iron oxides/hydroxides, in clays can greatly influence the Np(V) sorption. To further support the argument that the Fe containing phases present in the clay minerals play an important role in deciding the Np(V) sorption, another set of sorption experiments was carried out under identical conditions with the Fe-mineral-free Kutch clay (Fe-phases were removed by chemical treatments; (see Chapter 2, Section 2.8 for details). The characterization of the Fe-mineral-free Kutch clay was given in Chapter 3, Section 3.2.2. In short, it contains montmorillonite (> 96 mass %) with the relatively high amount of structural iron (approximately 6 wt%) compared to other studied montmorillonites. **Fig. 5.7** shows the sorption of Np(V) onto raw and purified Kutch clay in 0.01 M $NaClO_4$. A decreased Np(V)

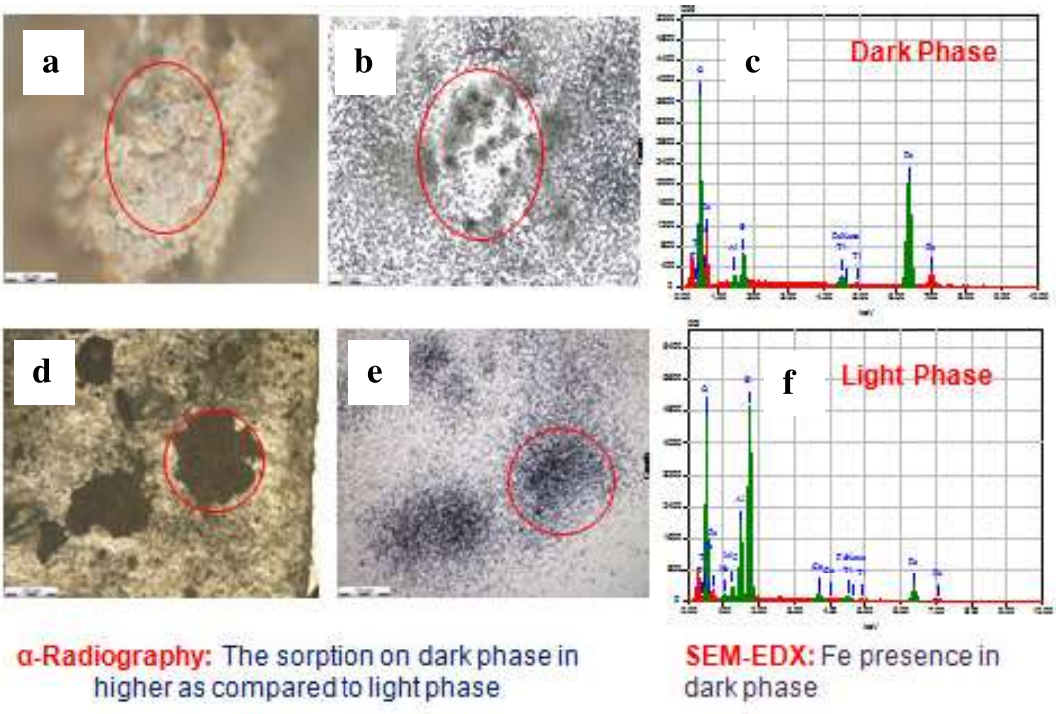

Fig. 5.6. Representative optical microscope images (a,d) and corresponding α-track analysis images (b,e) for Np(V) sorbed onto different clays (a,d); The SEM-EDX profile of the dark and light phase (c,f).

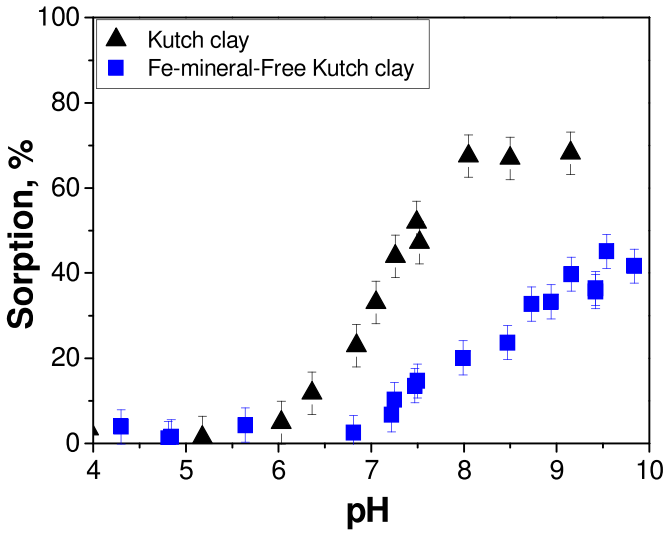

Fig. 5.7. pH-dependent Np(V) sorption onto pure and Fe-mineral free Kutch clay; [Np(V)] = 4×10^{-14} M, [solid phase] = 0.5 g/L, Ionic strengths = 0.01 M $NaClO_4$

sorption onto the Fe-mineral- free Kutch clay was observed as compared to the pristine Kutch clay (without any chemical treatment). This behavior of the Fe-mineral- free Kutch clay supported the explanation given on the basis of the presence of small amounts of Fe- phases which dramatically affected the Np(V) sorption behavior. The other factor, *i.e.,* the nature of the interlayer cations and the nature of clay e.g., bi-layer or tri-layer can also affect the Np(V) sorption.

5.2.3 Effect of Interlayer Cation onto Np(V) Sorption

To examine the impact of interlayer cations on the Np(V) sorption, Na-, Ca- and Li-forms of montmorillonite were used. The FEBEX bentonite (from Spain) was chosen for this study as the starting material. **Fig. 5.8** demonstrates the pH dependence of Np(V) sorption onto homo ionic montmorillonite forms containing different interlayer cations. The Np(V) pH edges for all the studied bentonites, clearly show that the ionic form of the montmorillonite has no or negligible influence on the Np(V) sorption (within experimental error limits) onto them. In acidic range, e.g., at pH values < 6, ion-exchange is the dominant Np(V) sorption mechanism onto the clay minerals, whereas at higher pH values, surface complexation with different

edge surface sites dominates [186,187]. The effect of interlayer cations on the cation exchange of Np(V) was studied by Kozai et al. who reported a strong dependence of Np(V) sorption on the natural cation exchange of the clay minerals at pH < 4.5 [188]. On the other hand, Np(V) sorption is studied in the present work over an extended pH range (up to pH11.5) and did not show much dependence on the interlayer cation. Under the present experimental conditions, surface complexation with an edge surface site may be the main mechanism of interaction of Np(V) with clay. The Li-form of FEBEX clay, where the interlayer space contains Li^+ ions, loses its ability to swell suggesting no possible interaction of Np(V) with the interlayer space. The observed sorption of Np(V) onto the Na-form and Li-form of FEBEX is very similar in the studied pH region of 5.0–10, suggesting that the interlayer spaces do not participate in the Np(V) interaction and supports our assumption that the metal ion interacts with an edge surface site. At pH > 10, sorption of Np(V) onto the Ca-

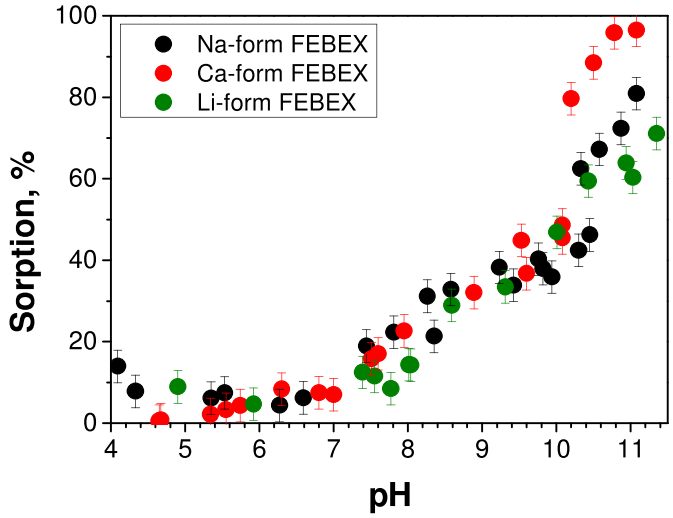

Fig. 5.8.. The pH-dependent Np(V) sorption onto Na-, Ca- and Li-forms of FEBEX clay. [Np(V)]: 4×10^{-14} M, [solid phase] :0.5 g/L, *I*: 0.01 M $NaClO_4$.

form FEBEX increases compared to that onto the respective Na- and Li-forms of FEBEX clay. Two possible reasons may be given for this observation. Rabung et al. proposed a hypothesis on the co-precipitation of Cm(III) with Ca-silicate hydrate or Ca-hydroxide

phases, that increased the metal ion sorption in that region [189] Most likely, an analogous co-precipitation was present in our system. At the same time, the interlayer distances for this clay decreased in the order: Ca-form > Na-form > Li-form. The Ca-form of FEBEX clay contains two water layers in the interlayer space, and the Na-form has only one water layer, while the Li-form contains almost no molecular water in the interlayer space suggesting that the Np(V) uptake is also decreased in the same order. This may be an indication that the interlayer distance is playing a role in the Np(V) sorption in some other ways in this pH region as the interlayer exchange is not possible (vide supra). However, a further investigation in this direction is needed to strengthen the hypothesis.

5.2.4 Effect of Clay Internal Structure onto Np(V) Sorption

The sorption behavior of Np(V) onto Na-FEBEX (tri-layer clay mineral) and kaolinite (bi-layer clay mineral) was compared and the results are discussed here. Kaolinite, 1:1 clay, is the main mineral component of many natural clays and an important component of various soils and fracture filling materials of crystalline hard rock.

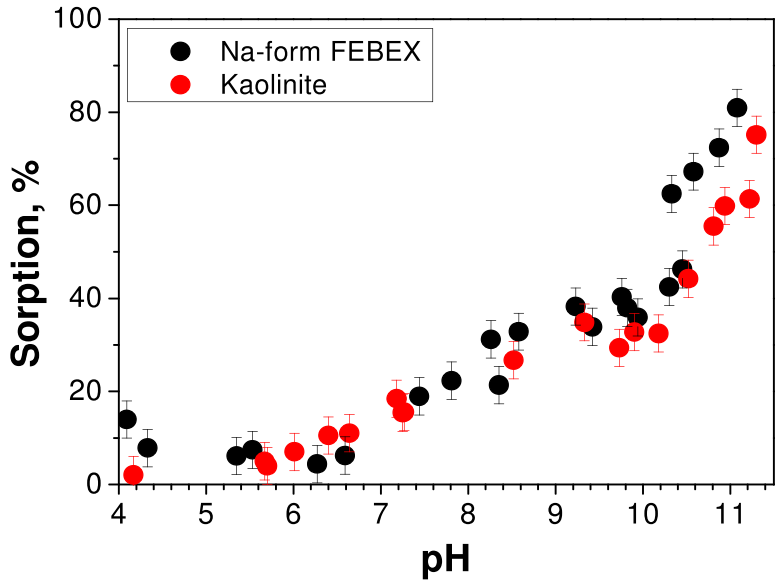

Fig. 5.9. pH dependence of Np(V) sorption onto Na-form of FEBEX and Kaolinite clay.([Np(V)]: 4×10^{-14} M, [solid phase]: 0.5 g/L, *I*: 0.01 M $NaClO_4$

The kaolinite minerals are known for having poor cation exchange capacity but despite the absence of an exchangeable interlayer cation, kaolinite has edge surfaces site that can interact with Np(V). The experimental results (**Fig. 5.9**) for Np(V) sorption onto kaolinite and Na-FEBEX agree with our previous assessment that the metal ion sorption is not influenced substantially by ion exchange and that surface complexation is the dominating mechanism. The similarity in the Np(V) sorption onto kaolinite and the Na-form of FEBEX clay, despite kaolinite having a low cation exchange capacity and poor specific surface area (□one-tenth of Na-FEBEX) compared to Na-FEBEX, suggests the predominant role of edge sites for Np(V) uptake.

5.3 THERMODYNAMIC MODELING OF SORPTION DATA

The thermodynamic modeling was done to further strengthen the conclusions drawn earlier about the role of accessory phase, the effect of interlayer cation and clay internal structure for Np(V) sorption.

5.3.1. Role of Accessory Minerals onto Np(V) Sorption

Among the vast literature devoted to thermodynamic modeling of Np(V) sorption onto bentonite clays, the papers by Bradbury and Baeyens (1997) and Tachi et al. (2014) were chosen for getting the surface complexation constants for the bentonite surface [190,191]. In both, the manuscripts SCM of Np(V) sorption onto purified montmorillonite was performed, and the findings were fitted using a linear free-energy relationship (LFER). The notable difference in the above two papers is that while Bradbury and Baeyens studied the sorption of Np(V) at very low concentrations ($<10^{-13}$ M) and used two-site protolysis nonelectrostatic surface complexation (2SPNE SC/CE) model for SCM, Tachi et al. performed their experiments at comparatively higher Np(V) concentrations (1×10^{-6} M) and used one-site protolysis non-electrostatic surface complexation modeling (1SPNE SC/CE). These two models and the corresponding surface complexation constants (**Table 5.1**) were used to

model our experimental data using the component additivity approach of SCM. The concentration of smectite in different bentonites samples was determined from the characterization experiments as detailed before (see Chapter 3, Section 3.2; Table 3.1). In view of the lack of equilibrium constant data for Np(V) sorption onto the Ca^{2+}/ Mg^{2+} forms of smectite, the surface complexation modeling was done only for Np(V) sorption onto Na^{+}-smectite. This is based on the assumption that at 1 M $NaClO_4$ all smectite forms are converted to the Na^{+}-form. Two modeling curves for Np(V) sorption onto montmorillonite are presented for the Indian clays. In **Fig. 5.10**, the values of concentration of each proposed phase in the legend correspond to the values given in **Table 5.1**. Since in 1 M $NaClO_4$ smectite is completely converted to the Na^{+}-form (see discussion below), two modeling curves for Np(V) sorption onto montmorillonite are presented for Indian clays e for initial sample and after complete conversion to Na^{+}-form. For the Kutch clay, the black and red lines in **Fig. 5.10** were calculated for 23% of the mass fraction of montmorillonite in the sample (at 0.01 M $NaClO_4$) and 90% of the mass fraction for montmorillonite in the sample (at 1 M $NaClO_4$). Increased Np(V) sorption with the mass fraction of montmorillonite was observed by modeling which correlates well with experimental data on Np(V) sorption onto the Kutch clay with an increase in the ionic strength. However, modeling of Np(V) sorption onto pure montmorillonite (100% of the mass fraction) did not result in any agreement with the experimental data in the case of the Kutch clay. Np(V) sorption onto the Rajasthan clay also did not converge well with the models of Np(V) sorption onto pure montmorillonite, whereas that onto the Khakassia bentonite was satisfactorily fitted by the model of Bradbury and Baeyens[192]. On the other hand, the modeling of sorption data with equilibrium constants from Tachi et al. did not fit in all cases (shown only for Khakassia clay). This suggests that the admixture phases (e.g. anatase, titania etc) present in the presently studied bentonites clearly have an influence on the Np(V) sorption onto these clays. The candidates contributing to the Np(V) sorption are suggested to be goethite, hematite, and anatase. For the

present modeling case, sorption onto goethite was taken into account because of two reasons; firstly, its higher concentration than another accessory phases in the Kutch and Rajasthan clay samples and secondly, its higher Np(V) sorption constant than hematite and anatase 193-196]. Both of these factors suggest strong competition for Np(V) by goethite compared to the

Table 5.1: The surface complexation constants and other parameters of modeling that were used in the present work.

Reaction	log *K*	Surface site concentration, sites/nm^2	Reference
Montmorillonite (NEM)			
$\equiv S^sOH + H^+ \Leftrightarrow \equiv S^sOH_2^+$	4.5	0.034	[192]
$\equiv S^sOH \Leftrightarrow \equiv S^sO^- + H^+$	-7.9		
$\equiv S^sOH + NpO_2^+ \Leftrightarrow \equiv S^sONpO_2 + H^+$	-2.0		
$\equiv S^sOH + NpO_2^+ + H_2O \Leftrightarrow \equiv S^sONpO_2OH^- + 2H^+$	-12.0		
$\equiv S^sOH + H^+ \Leftrightarrow \equiv S^sOH_2^+$	5.75		[191]
$\equiv S^sOH \Leftrightarrow \equiv S^sO^- + H^+$	-8.30		
$\equiv SOH + NpO_2^+ \Leftrightarrow \equiv SOHNpO_2$	2.8		
$\equiv SOH + NpO_2^+ \Leftrightarrow \equiv SONpO_2 + H^+$	-4.45		
$\equiv SOH + NpO_2^+ + H_2O \Leftrightarrow \equiv SONpO_2OH^- + 2H^+$	-14.5		
Goethite (DDL)			
$\equiv S^sOH + H^+ \Leftrightarrow \equiv S^sOH_2^+$	7.9	2.31	[193]
$\equiv S^sOH \Leftrightarrow \equiv S^sO^- + H^+$	-9.9		
$\equiv FeOH + NpO_2^+ \Leftrightarrow \equiv FeONpO_2 + H^+$	-1.57		

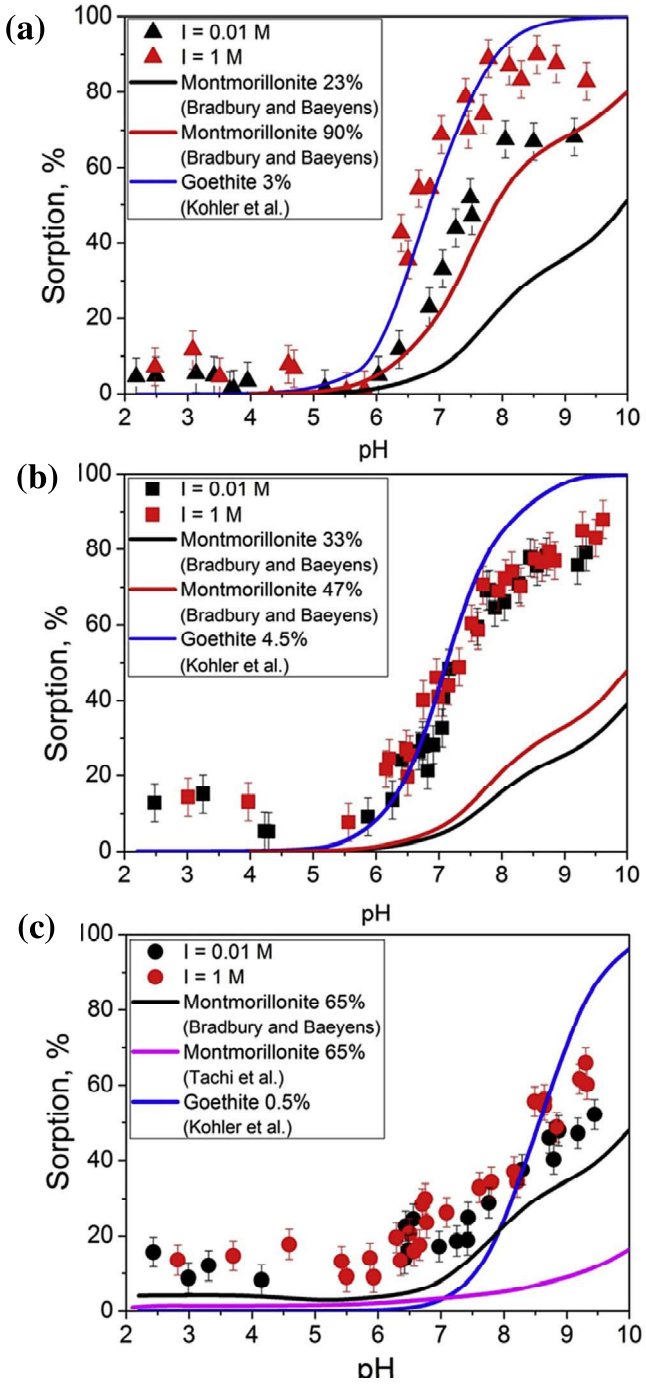

Fig. 5.10. Thermodynamic modeling and experimental data of the pH dependence of Np(V) sorption onto (a) Kutch, (b) Rajasthan and (c) Khakassia clay at different ionic strengths. Black and red lines: sorption profiles of Np(V) onto Na^+-form of montmorillonite using the constants from ref [192] Blue lines: sorption profiles of Np(V) onto goethite using the constants from ref [193]; Magenta line: sorption profile of Np(V) onto Na^+-form of montmorillonite using the constants from ref [191]; ([Np(V)]: 4×10^{-14} M, [solid phase]: 0.5 g/L).

other components. The sorption of Np(V) onto goethite phase was modeled using its total mass fraction obtained from XRD studies and by assuming that the specific surface area of goethite, *i.e.*, the surface area per unit mass of goethite, is identical with the specific surface area of the sample as a whole, namely 115 m^2/g for the Kutch clay, 50 m^2/g for the Rajasthan clay, 15 m^2/g for the Khakassia clay (**Fig. 5.10**). The surface area of each mineral phase within the sample is made proportional to its mass fraction. The modeling studies were also used to understand the role of interlayer cations on Np(V) sorption and to compare the sorption of the metal ion onto the different class of clays.

The experimental determination of the surface area of the individual phases in a complex mineral mixture is a challenging task. The sorption of Np(V) onto Kutch and Rajasthan bentonites fit well by the addition of goethite contribution to the Np(V) sorption (blue line in **Fig. 5.10**), indicating that the presence of even a relatively small amount of iron hydroxide/oxide into the natural clays have higher influence on the Np(V) uptake. This observation is also supported by our individual experiments using α-radiography coupled with SEM-EDX and sorption experiments with the Fe-phase free Kutch clay.

5.3.2 Effects of Interlayer Cation and Clay Structure

The pH-profiles of Np(V) sorption onto the bentonites of different cationic forms together with onto the kaolinite clay was shown in **Fig. 5.11**. The CA approach of the SCM was used to simulate the Np(V) sorption data with two-site protolysis non-electrostatic surface complexation (2SPNESC) model with the sorption constants. At present, we didn't find any thermodynamic data for Np(V) sorption onto different ionic forms of montmorillonite, and hence, it is not very clear how these interlayer cations influence Np(V) sorption onto edge sites. All of our experimental data for the sorption of Np(V) on different clays (with different interlayer cations and different structures) matched well with the simple modeling curve using the reported data (Bradbury and Baeyens) for Na^+-form of montmorillonite [192].

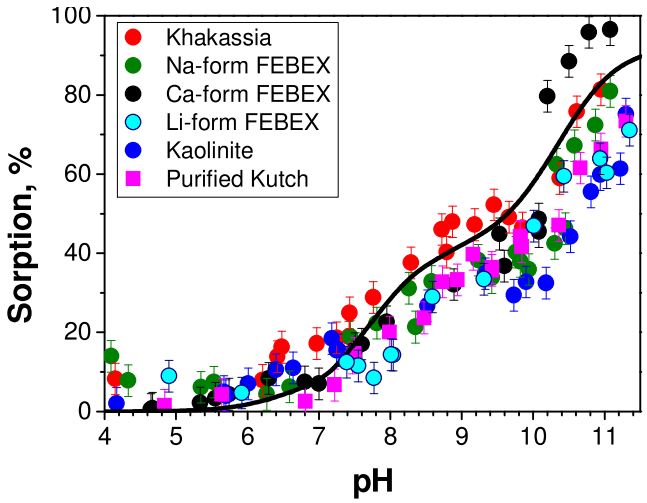

Fig. 5.11. The pH-dependent Np(V) sorption onto different clays. The black line is the thermodynamic modeling of Np(V) sorption onto a strong site of Na-montmorillonite; [Np(V)]: $4x10^{-14}$ M, [solid phase]: 0.5 g/L, *I*: 0.01 M $NaClO_4$ (sorption constants and concentration of sorption site are taken from ref [192].

The improvement in the modeling of the sorption profiles for individual clay can be done separately by varying different parameters such as the binding site concentration, surface protonation constants, etc. The surface areas of the studied samples also differed significantly from 6 m^2/g for the kaolinite sample to 150 m^2/g for the purified Kutch clay. We did not optimize the fitting by varying the SCM parameters as we preferred to use the CA approach. Reasonably good fitting of the experimental data was seen with the theoretical line. From the experimental data, the effect of specific surface areas on the Np(V) sorption onto different clays is not very clear. In view of the fact that changing the specific surface area can cause a shift in the sorption edge (**Fig. 5.12**), one can propose the following. Either the surface area of 6 m^2/g (the lowest one) may be enough for the Np(V) sorption under the present conditions or the edge sites with similar properties and concentration much higher than Np(V) concentration exists on the surfaces of all the studied clay minerals under present experimental conditions. This makes the sorption profiles of Np(V) at trace concentration (10^{-14} M) looks similar.

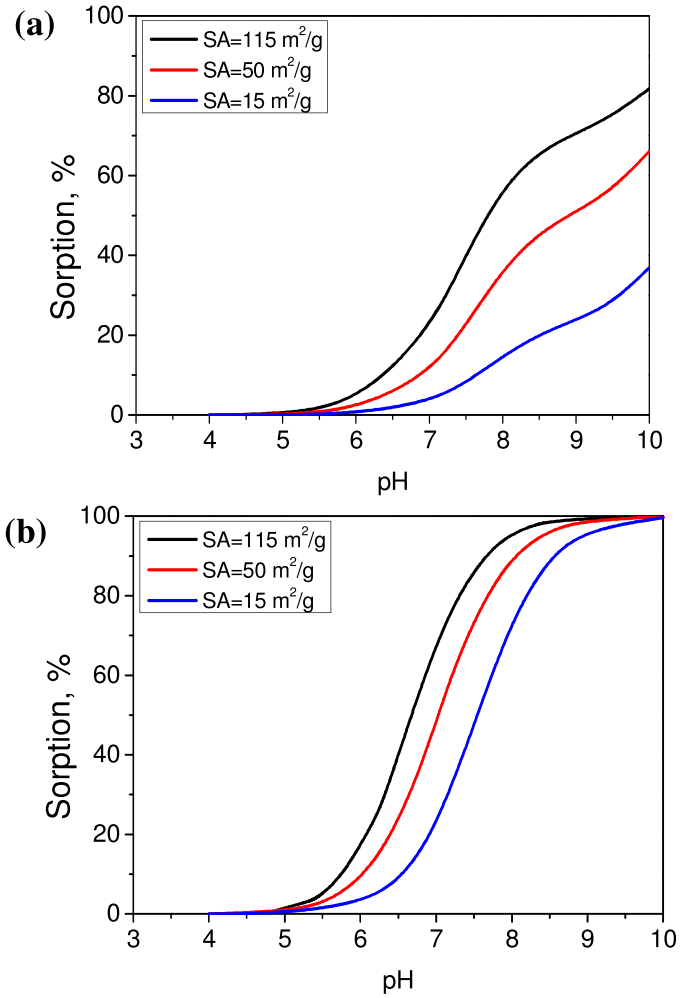

Fig. 5.12. Modeling of sorption onto (A) – montmorillonite (constants from ref [192]) and (B) goethite (constants from ref [193]), [montmorillonite] = 0.5 g/L, [goethite] = 0.025 g/L. from Bradbury and Baeyens [192]. The concentration of the strong surface site was taken as $2x10^{-3}$ mol/kg. Bradbury and Baeyens reported the data for the sorption onto the Na-form of montmorillonite [192].

The Np(V) sorption onto the Khakassia clay, which has a relatively high quartz content, compares well with the other studied clays. This suggests that the presence of quartz does not influence Np(V) sorption to any significant extent. Fröhlich has tried to compare the Np(V) sorption onto different clays using normalized distribution coefficients with respect to the specific surface area (K_a), which could be more appropriate than comparing the K_d values [197]. However, from our results, it seemed that such a comparison was not very helpful in

the case of sorption of radionuclides at trace concentrations onto different clay minerals (**Fig. 5.13**). A better understanding of the relation between specific surface area and concentration of the edge sorption sites for clay minerals is needed for further understanding. The shape of

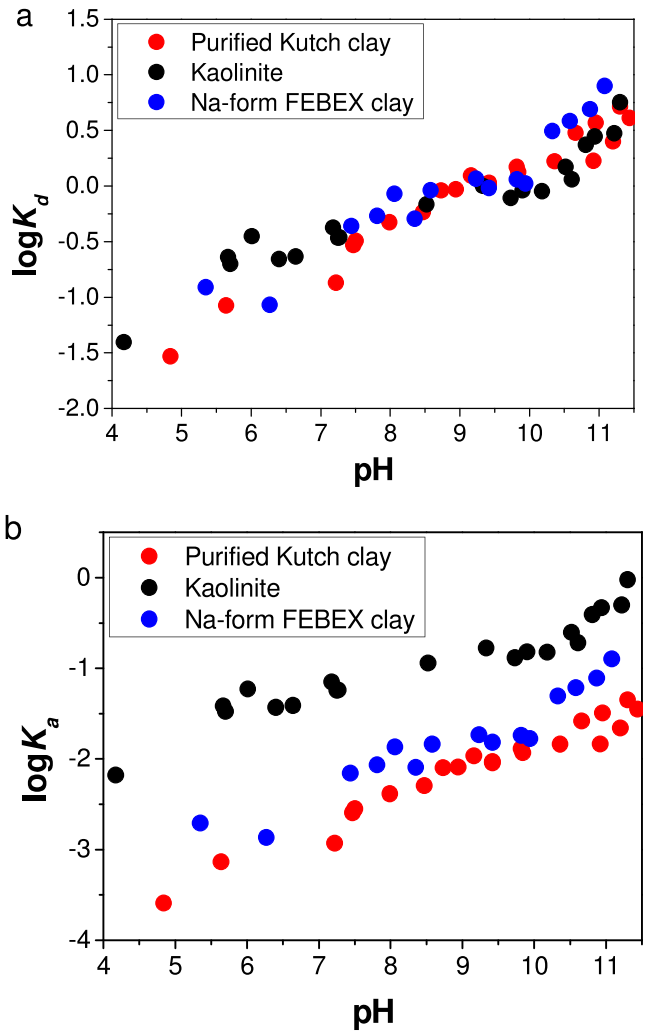

Fig. 5.13. Sorption of Np(V) onto studied clays expressed in (a) K_d and (b) K_a units. K_d is the distribution coefficient and equals the Np(V) concentration sorbed on the mineral is divided by concentration remaining in solution (mol/g). K_a is coefficient normalizing t to the specific surface area of clay minerals (mol/m^2).

pH-edges shows two distinct maxima or have curvatures caused by sorption of different hydrolyzed species of Np(V), e.g., NpO_2^+ and neutral NpO_2OH (**Fig. 5.14**) as predicted by equation 5.3 and 5.4.

$\equiv SOH + NpO_2^+ \Leftrightarrow \equiv SONpO_2 + H^+$, $\log K_1 = -2.0$ **(5.3)**

$\equiv SOH + NpO_2^+ + H_2O \Leftrightarrow \equiv SONpO_2OH^- + 2H^+$, $\log K_2 = -12.0$ **(5.4)**

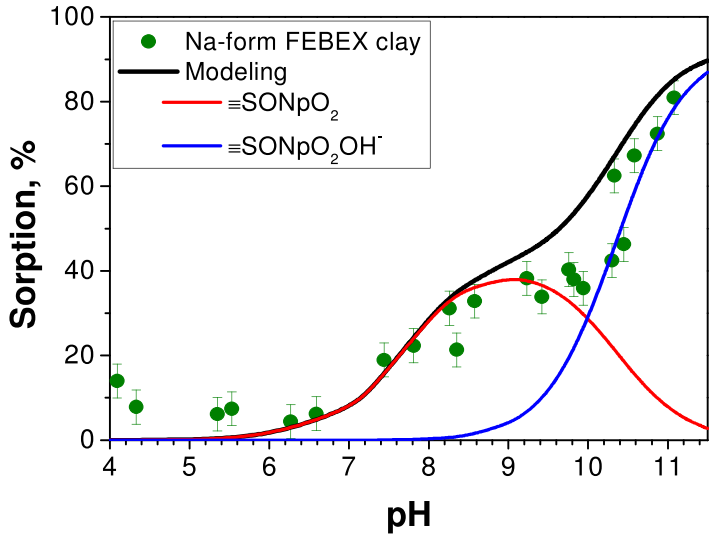

Fig. 5.14. Sorption data together with thermodynamic modeling, sorption constants and concentration of sorption site are taken from ref [192]; [Np(V)] = 4×10^{-14} M, [solid phase] = 0.5 g/L, I = 0.01 M $NaClO_4$.

5.4. THE pE-pH DIAGRAM

Previous reports have suggested that the presence of Fe(II) in the clay minerals may cause Np(V) reduction to Np(IV) which would result in a higher Np sorption onto the given clay minerals due to higher ionic potential of Np(IV) compared to Np(V)[188]. We have not observed any reduction of Np(V) to Np(IV) under the experimental conditions used in the present studies even for clay minerals containing the structural Fe(II). The sorption of Np was evaluated on to different clays for 8 days, assuming slower kinetics of Np(V) reduction to Np(IV), but even after such a long time interval we have not observed any enhancement in the Np sorption, hence reduction of Np(V) to Np(IV) is negated. The Eh-Ph diagram was also plotted to further confirm the existence of the Np as NpO_2^+ under the present experimental conditions (**Fig.5.15**). The comparison of the slopes in the two graphs **Fig 5.15 (a)** and **Fig**

5.15 (b) suggests the presence of Np as NpO_2^+ (all the data points would lie in the light orange shaded region) under the present experimental conditions.

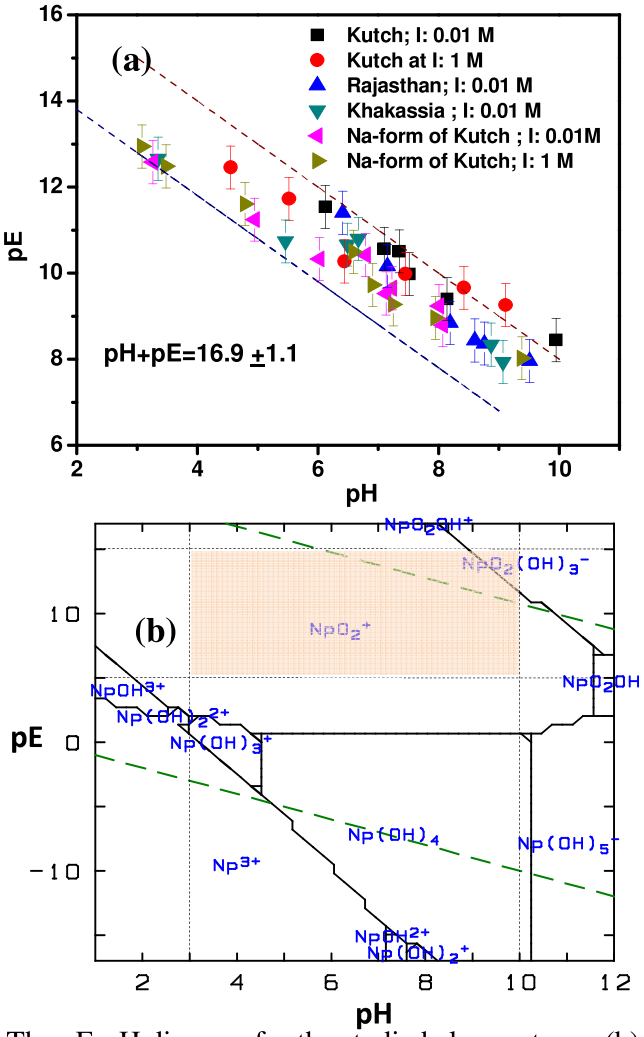

Fig. 5.15. (a) The pE-pH diagram for the studied clay systems; (b) the pE-pH diagram for Np; T: 298K.

5.5. SORPTION OF TRIVALENT ACTINIDES

The preliminary studies on sorption of Eu(III) (as a surrogate for Am(III)) (2×10^{-11} M) onto bentonite (0.5 g/L) clays of different origin were initiated. The sorption of Eu(III) was studied as a function of time to arrive at the steady state equilibrium for Eu(III) sorption. The kinetic studies indicated that < 6 hrs was required to attain the sorption equilibrium onto the studied clay systems (**Fig. 5.16**). To further understand the variation of Eu(III) (2×10^{-11} M) sorption onto different clay systems (0.5 g/L), pH edge for Eu(III) sorption was also studied at 0.01 M

$NaClO_4$. The sorption of Eu(III) was near quantitative for all the studied clays at lower ionic strength values. This showed that the sorption of Eu(III) was neither dependent on the form

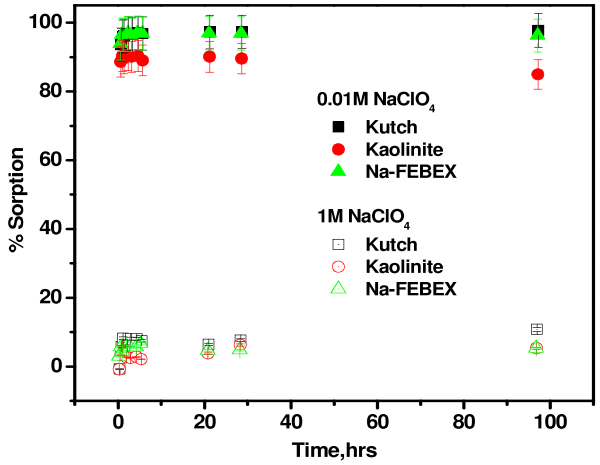

Fig. 5.16. The kinetics of Eu(III) (2×10^{-11} M) sorption onto different clays with varying ionic strength; pH: 4.00 ± 0.05.

nor the presence of any accessory minerals as seen in the case of Np(V) sorption at low ionic strength solution. The subsequent studies at higher ionic strength showed that the sorption followed an outer sphere complexation at the mineral surface at pH values < 6 and later dominated by inner-sphere complexation. This pH edge at higher ionic strength values also showed slight variation for different clay systems.

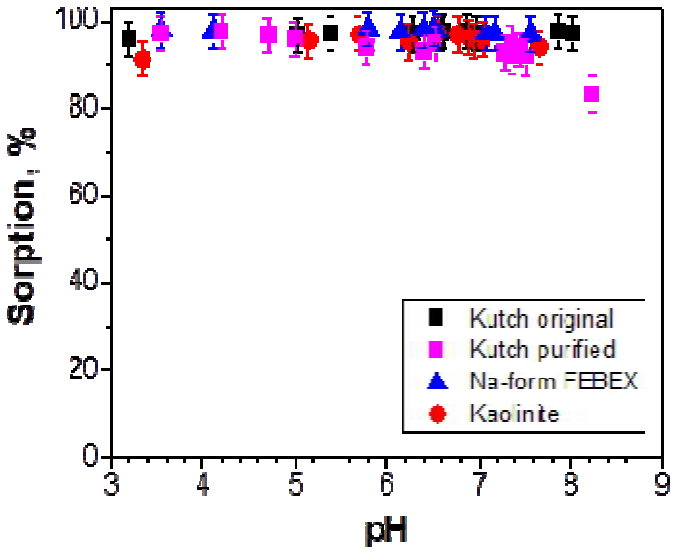

Fig. 5.17. The pH edge for Eu(III) sorption onto different clays, *I*: 0.01 M $NaClO_4$

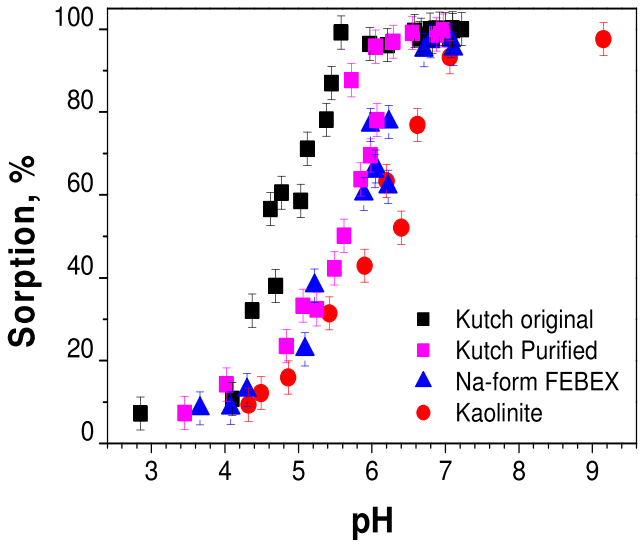

Fig. 5.18. The pH edge for Eu(III) sorption onto different clays, *I*: 1 M $NaClO_4$

The original Kutch bentonite clay showed pH edge at lower pH values when compared to other clays. This could be due to the presence of additional Fe-phases in the pristine Kutch clay as the purified Kutch bentonite showed sorption profiles similar to the other clays. The two forms of clays *e.g.,* bi-layer (kaolinite) and tri-layer (bentonite) also showed similar trends for Eu(III) sorption. Further studies are needed to conclude about the role of accessory minerals and other factors governing the sorption of trivalent actinides onto natural sediments.

To summarise, the present Chapter deals with the sorption of Np (V) onto the natural clays varying in their mineralogical composition and accessory Fe-mineral. The Np(V) sorption data showed that the presence of Fe-phases (e.g. goethite in the present case), even at very low concentrations (few percents) plays an important role in deciding Np(V) sorption and speciation onto natural sediments. The surface complexation modeling alone with a set of different experiments such as α-radiography and SEM-EDX independently support the role of Fe-phases towards Np (V) sorption. The interlayer cation and the form had no influence on the Np (V) sorption for pH > 5.

6

SUMMARY AND CONCLUSIONS

The present Thesis deals with the characterization of natural/commercial clays from different origins and effect of clay composition on the sorption of different radionuclides onto these clays are discussed using various experimental and theoretical approaches. Various physio-chemical methods were used in this Thesis work for the characterization of clay minerals and these obtained data, in turn, were used for understanding the interactions of radionuclides with these clay minerals. The Thesis can be broadly divided into two parts. The first part deals with the characterization of natural sediments of different origins for accessory minerals phases, Fe-speciation, etc. This analysis is one of the most important parts before any radioactive land decontamination process or for choosing a suitable remediation strategy. It not only provides the information about the most abundant phases present in soil but also assists in the prediction of the behavior of the contaminants (*e.g.,* speciation) in the presence of these minerals phases. This analysis will help in understanding the sorption behavior of the given radioactive contaminants onto these sediments. The second part deals with the studies on the sorption of different radionuclides, under different chemical conditions, onto these previously characterized sediments. The sorption results were modeled, wherever required, to

further understand the role of different components of the sediments in deciding the sorption of the radioactive contaminants.

A host of physicochemical techniques were used to understand the composition of the clay mineral used in the present study. The studied clay samples range from simple bi-layer clay system such as kaolinite to a more complex tri-layer system such as bentonite of both commercial (from Aldrich) as well as natural origins. Briefly, the XRD studies showed that all the clay samples used in this study were enriched in smectite (montmorillonite), with some admixture of other clay minerals (chlorite, kaolinite), as well as carbonates, quartz, different iron oxides and hydroxides and other minerals in relatively small amounts. The difference in the ionic form of the clays was identified and estimated due to the different positions of the basal (001) reflections. The elemental composition, determined by ICP-AES, of the studied clays, supported the XRD data. The Fe speciation was done using Mossbauer spectroscopy and the results indicated that the Kutch clay contains iron, as a ferric ion (Fe (III)) only. However, the Fe speciation in the clay minerals suggested its presence as: as structural iron in 56% sites and as intrinsic iron phases at 44% sites (hematite and goethite). The Khakassia clay contained both Ferrous (Fe(II)) and Fe(III) out of which the latter was present in the form of structural iron (57%) and iron oxides (29%) while the remaining iron was as the structural divalent iron. On the other hand, the FEBEX original contained both Fe(III) (89%) and Fe(II) (11%). The modified Kutch (after the removal of the Fe containing phases) contained only structural iron and as expected the addition Fe-phases were absent. The present studies used Mössbauer spectroscopy as the most reliable and sensitive technique for Fe-phase analysis in complex natural clay systems. This was due to the fact that many Fe-phases (such as the fine goethite particles) were difficult to characterize or even difficult to get detected due to their small size and low abundance in the clay minerals. The FTIR studies showed that the investigated clay samples were composite of different phases and the nature of clay, ordered or not, were detected. Other characterization studies such as SEM-EDX,

TEM, BET etc. indicated that the clays studied in the present. The studied clays differed in their mineralogical compositions and had inherent particle size inhomogeneity with varying specific surface area. It would be interesting to see the effect of these variations on the sorption properties of these minerals toward a given radionuclide.

The sorption of radionuclides of different oxidation states e.g., monovalent (Cs(I)) divalent (Sr(II)), Trivalent (Am(III)/Eu(III)/Gd(III)), pentavalent (Np(V)) and hexavalent (U(VI)) was studied onto the previously characterized clays. The sorption behavior of different metal cations viz. Am(III) ($\sim 10^{-10}$ M, carrier free), Eu(III) (10^{-6} M, with carrier), divalent Sr(II) ($\sim 10^{-5}$ M, with carrier), and monovalent Cs(I) ($\sim 10^{-9}$ M, carrier free), onto bentonite followed the order: Am(III) ~ Eu(III) > Cs(I) > Sr(II). Whereas higher sorption in the case of trivalent metal ions was due to their higher charge, higher sorption of Cs (I) compared to Sr (II) was attributed to the higher hydrated radius of the latter. Sorption of Eu(III) onto bentonite was invariant with the ionic strength (I = 0.01 to 1.0 M ($NaClO_4$)) at pH 4 and 8 suggesting inner-sphere nature of the sorbed species. The presence of different complexing ligands such as EDTA, HA and their combination suppressed the sorption of Eu (III) which was attributed to the aqueous complexation. On the other hand, the presences of ligands like oxalate and carbonate (10^{-4} M) had an only marginal influence on the sorption profiles which was due to poor aqueous complexation by these ligands. This was supported by speciation calculation of the metal ions in the presence of these ligands. Eu (III) sorption increased with bentonite concentration in the sample solutions which was attributed to the availability of the surface sites for the sorption process.

The isotherm studies showed that the sorption of Eu(III) onto bentonite followed the Langmuir model and not the Freundlich model suggesting a monolayer sorption process. The D-R isotherm was used for the calculation of sorption energy (E) as 15.3(±0.2) kJ/mol which suggested ion exchange mechanism was operative during the sorption of Eu (III) onto the bentonite clay. The sorption capacity of bentonite clay was determined to be $3.8(\pm 0.1) \times 10^{-4}$

moles/g using Langmuir and D-R isotherms. Desorption of Eu(III) could be achieved using 0.5–1 M $HClO_4$ solutions.

These batch sorption studies showed that the sorption of U(VI) increased with increasing pH up to a value < 6 beyond which a decrease was seen which was attributed to the formation of anionic carbonate species. Marginal variation in the U(VI) sorption with ionic strength at higher pH suggested inner-sphere complexation. The addition of complexing ligands modified the sorption behavior of U(VI) onto the bentonite clay. While humic acid showed an increase in the metal ion sorption followed by a plateau and finally a decrease thereafter, as a function of the aqueous phase pH, which was attributed to the formation of aqueous U(VI)-humate complexes, low sorption (max. 20%) in the entire pH range was noticed in the case of oxalate and citrate due to dominating complexation reactions. The presence of carbonate did not have any significant influence on the sorption profile of the uranyl ion. The intensity in the emission spectra of the aqueous complexes of U (VI) with OH^-, CO_3^{2-}, HA, and cit followed the order: U(VI)-hydroxyl > U(VI)-humate > U(VI)-carbonate > U(VI)-citrate. The lower luminescence yield of U(VI) carbonate complex can be attributed to the strong dynamic quenching by the carbonate ion at room temperature. Similarly, the U(VI) citrate complex did not emit any luminescence at room temperature. The residual luminescence observed in the emission spectra was contributed by the small amount of uncomplexed uranyl ion present in the form of the uranyl hydroxo complexes. On the other hand, the luminescence yield of UO_2^{2+}-HA complex and $UO_2^{2+}{}_{aq}$ were comparable, suggesting the dominance of the aqueous U(VI)-hydroxo species even in U(VI)-HA system. The normalization of spectra did not show any appreciable shift in the emission spectra suggesting similar nature of the complexed UO_2^{2+}species in different samples. This was further confirmed by the luminescence lifetime spectra which ranged between 19–27 μs. Similarly, the luminescence intensities in the emission spectra for U(VI)-bentonite suspensions in the presence, as well as in the absence, of complexing ligands followed the

order: U(VI)-hydroxy > U(VI)-bentonite > U(VI)-bentonite-humate > U(VI)-bentonite-carbonate ≫ U(VI)-bentonite-citrate. The observed trend followed the sorption profiles of U(VI) onto bentonite in the presence or absence of different complexing ligands. In addition, no peak shift was observed in the luminescence lines, which was also supported by the lifetime data (19–27 μs) and by the UV-vis spectrophotometry. The XANES spectra of the U(VI) sorbed onto bentonite showed a shift in absorbance edge, which could be attributed to the decrease in the electron density at the uranium center due to the surface or ligand complexation. The Fourier transformed EXAFS spectra in the *R* space were mainly dominated by the back-scattering from the two axial oxygen atoms in the first shell. On the other hand, the second shell or higher *R* value fittings suggested predominantly bi-dentate inner sphere multinuclear complex formation during the sorption of U(VI) onto the bentonite surface.

The sorption of Np(V) onto the natural clays varying in their mineralogical compositions and accessory Fe-mineral content was investigated. The sorption data showed that the presence of Fe oxides/hydroxide phases (e.g., goethite in the present case), even at very low concentrations (<5%) plays an important role in deciding Np(V) sorption and speciation onto the natural sediments. This could influence both the kinetics of sorption (especially the pH sorption edges at the steady state) and possibly on the reversibility of the metal ion sorption. It is important to conclude that the surface complexation data are highly important to the modeling of such complex heterogenic systems as soils or bottom sediments. The effect of interlayer cation and the form of the clay (1:1) was also investigated. The sorption behavior of Np(V) at trace concentrations onto different clays and clay minerals were compared. At pH > 5, the interlayer cations in montmorillonite clays had no influence on the metal ion sorption. The dominant mechanism in this pH range was complexation with edge surface sites. As a result, clay minerals with 2:1 type and different interlayer cations and 1:1 type clay minerals demonstrated similar sorption profiles. The most important

characteristic of the clay that changed the Np(V) sorption dramatically was the presence of iron oxyhydroxide as an accessory mineral. The sorption studies of Eu(III) onto natural sediments were attempted and shows that the Eu(III) sorption was not very much dependent on the presence of accessory mineral phases in clays as seen in the case of Np(V) sorption.

The present Thesis makes an important addition towards the understanding of the role of the different constituents of the natural clay minerals towards the sorption and migration behavior of actinides and long-lived fission products in the geosphere. With the advancement in the synchrotron source based experimental techniques and laser-based spectroscopic instruments, molecular level speciation of actinides at very low concentrations at mineral water interface can be obtained, which in turn would help in better understanding of the chemistry of interaction between the two and also help in validating the models proposed for the prediction of the migration pathways of different radionuclides in the geosphere upon their accidental release from the deep geological repositories.

The knowledge from the present Thesis can be extended to understand the sorption behavior of the radionuclides onto the natural sediments. The importance and role of accessory phases present in the natural sediment onto the sorption of radionuclides are highlighted in the present Thesis but need more understanding and further research. Although, the natural sediments used in the present Thesis were of different origin with variable composition and Fe-content, still the majority of the minerals phases fall in smectite form of clay. These studies can be taken as guide for understanding of other types of natural sediments rich in different forms of clays to better understand the actinide sorption and speciation in natural media. The presence of NOMs and thin oxide layer of accessory mineral phase onto the natural sediments can change the way of radionuclide interaction with the natural sediments and requires detailed investigation. In the present Thesis, we have tried to characterize the natural sediments with respect to its mineral composition, elemental analysis and Fe-speciation using host of techniques. But still lots of challenges are remaining such as,

the presences of amorphous phase of minerals are invisible to most of the characterization techniques, the role of biotic or abiotic layers onto the minerals towards radionuclides sorption are still wage, etc. The thorough characterization of naturals sediments, as done in the present Thesis, will not only help in better understanding of the sorption results but also helps in designing the remediation strategies for radioactive contaminant removal from environments.

The nature believe in change and hence, the geochemistry, hydrochemistry, biochemistry, etc. of the natural systems keeps on changing, not only from one point to other point but also variable in time at a given place. It is very difficult to get sorption characteristics of a soil system by studying only its pure analogues or from studies of soil system at different regions but these studies can definitely help, at least to some extent, to predict the radionuclides retention using suitable modelling approach such as CA-SCM. Further studies are also needed for the better understanding of, how the intrinsic properties of actinides combined with site-specific conditions (e.g., temperature, ionic strength, complexing agents etc.) and control reaction kinetics and pathways of migration and thus, the ultimate environmental fate of the radioactive contaminants.

It is very difficult at this point to that which clay can be chosen for effective retardation of radionuclide mobility in to the environment as different clay minerals may act differently toward the sorption of a given radionuclide. Besides that, the redox behavior, redox reaction and speciation of actinides at the mineral-water interface require more detailed investigations under different chemical conditions before arriving at any conclusion. The overall outcome from these studies would help to understand of the role of accessory minerals, interlayer cation, clay form, NOMs etc. towards the sequestration of actinides in the environment. The information obtained will be also useful in design and planning of suitable methods for remediation of actinides and/or others long-lived radioactive contaminated land or aquifer.

REFERENCES

1. Devell, L., Tovedal, H., Bergström, U., Appelgren, A., Chyssler, J., Andersson, L. *Nature*, (1986) **321**,192–193.
2. Kastenberg, W.E., Ethics, risk, and safety culture: reflections on Fukushima and beyond. Journal of Risk Research, (2015) **18**(3), 304-316.
3. Katata G., Chino M., Kobayashi T., Terada H., Ota M., Nagai H., Kajino M., Draxler R., Hort M. C., Malo A., Torii T., Sanada Y.; *Atmos. Chem. Phys.,* (2015) **15**, 1029-1070.
4. Muto S. Fukushima accident: What happened and lessons learned. Geotechnics for Catastrophic Flooding Events - Proceedings of the 4th International Conference on Geotechnical Engineering for Disaster Mitigation and Rehabilitation, GEDMAR 2014. (2015), 79-91.
5. Saito K, Tanihata I, Fujiwara M, T. Saito, Shimoura S., Otsuka T., Onda Y., Hoshi M., Ikeuchi Y., Takahashi F., Kinouchi N., Saegusa J., Seki A., Takemiya H., Shibata, T.; (2015) 139, 308-319.
6. Sutou S., Monitoring of radio-contamination in returnees from evacuation zones in Fukushima and sporadic measurements of radiation in contaminated areas of Ibaraki and Fukushima prefectures. In "Fukushima Nuclear Accident: Global Implications, Long-Term Health Effects, and Ecological Consequences." (2015), 203-216.
7. Suzuki K, Yamashita S: Perspective: Health-risk implications of the Fukushima nuclear power plant accident. In "Fukushima Nuclear Accident: Global Implications, Long-Term Health Effects, and Ecological Consequences." (2015), 1-25.
8. Buesseler K., Aoyama M., Fukasawa M.; *Environ. Sci. Technol.*; (2011) **45**(23), 9931–9935.

9. Clint A. Sharrad, Laurence M. Harwood, Francis R. Livens; Chapter 2; Nuclear Fuel Cycles: Interfaces with the Environment; in Nuclear power and the Environment, (2011), 40 – 56.
10. Joanna C. Renshaw, Stephanie Handley-Sidhu and Diana R. Brookshaw; Chapter 7: Pathways of Radioactive Substances in the Environment, in Nuclear power and the Environment, (2011), 152 – 176.
11. Bleise A., Danesi P.R., Burkart W., *J. Environ. Radio.*; (2003) **64**, 93–112.
12. http://world-nuclear.org/harmony accessed on May 15th, 2018.
13. G. Friedlander, J. W. Kennedy, E. S. Macias, J. M. Miller, Nuclear and Radiochemistry, Third Edition, John Wiley & Sons, USA, (1981).
14. Rao K. R., *Current Science* (2001) **81**, 1534-1546..
15. Kastenberg W. E., Gratton L. J., *Physics Today*, (1997) **50,** 41-47.
16. McCombie C., *Physics Today*, (1997) **50**, 56-64.
17. Egorov N.N., Zakharov M.A., Lazarev L.N., Lyubtsev R.I., Nikiforov A.S., Strakhov M.V. ,Filippov E.A., "New approaches to solving the management problem of long-lived radionuclides", In Proceedings of the third international conference on nuclear fuel reprocessing and waste management, RECOD-91, (1991) **1**, p. 357.
18. J. J. Katz and G. T. Seaborg, "The chemistry of actinide elements", *Willy Publications* (1957) 315.
19. Choppin G. R., Jensen M. P., Actinides in solution: complexation and kinetics, in The Chemistry of Actinide and Transactinide Elements (Eds.) L.R.Morss, N.K.Edelstein, and J.Fuger, Springer, (2006), 2524-2621.
20. Ahrland S., Liljenzin J. O., Rydberg J., Solution Chemistry, In "Comprehensive Inorganic Chemistry", J.C. Bailar Jr., H.J. Emeleus, R. Nyhlom and A.F.T. Dickenson (Eds.), Pergamon Press, Oxford (1973) **5**, 465-535.
21. Janes A. D., Choppin G. R., *Actinides Rev.,* (1969) **1,** 311.

22. Choppin, G. R., *J. Nucl. Radiochem. Sci,;* (2005) **6**, 1-5.

23. Choppin, G. R., *Mar. Chem.* (2006) **99**, 83-92.

24. Choppin, G. R.*, J. Radioanal. Nucl. Chem*, (2007) **273**, 695-703.

25. Choppin G.R., Allard B. Complexes of actinides with naturally occurring organic compounds in Handbook on the physics and chemistry of the Actinides (Eds.) A.J. Freeman and C. Keller, Elsevier Science Publ, (1985).

26. UNSCEAR 2016 Report: "Sources, Effects And Risks of Ionizing Radiation; Report of the United Nations Scientific Committee on the Effects of Atomic Radiation general assembly, United state Nations; NY, USA, (2016).

27. UNSCEAR 2008 Report: "Sources and effects of ionizing radiation; Report of the United Nations Scientific Committee on the Effects of Atomic Radiation to the general assembly, United state Nations; NY, USA, (2008).

28. Simon S. L; Bouville A.; Beck H. L.; *J Environ. Radio.* (2004) **74**, 91–105.

29. Ewing R.C. in "Energy, Waste and the Environment: A Geochemical Perspective (Geological Society Special Publication) by R. Giére and P. Stille, The Geological Society : London, UK, (2004), p.7.

30. Christensen G.C., Romanov G.N., Strand P., Salbu B., Malyshev S.V., Bergan T.D., Oughton D., Drozhko E.G., Glagolenko Y.V., Amundsen I., Rudjord A.L., Bjerk T.O., Lind B.; *The Science of the Total Environment,* (1997) **202,** 237-248.

31. Standring W. J. F., Oughton D. H., Salbu B.; *Environ. Sci. Technol.* (2002) **36**, 2330-2337.

32. Børretzen P., Standring W. J. F., Oughton D. H., Dowdall M., Fifield L. K. *; Environ. Sci. Technol.,* (2005) **39 (1)**, 92–97.

33. UNSCEAR 1993 Report: "Sources and effects of ionizing radiation; Report of the United Nations Scientific Committee on the Effects of Atomic Radiation to the general assembly, United state Nations; NY, USA, 1993.

34. Standring W.J.F., Stepanets O., Brown J.E., Dowdall M., Borisov A., Nikitin A.; *J. Environ. Radio.* (2008) **99,** 665-679.

35. Tompson A.F.B., Bruton C.J., Pawloski G.A., Smith D.K., Bourcier W.L., Shumaker D.E., Kersting A.B., Carle S.F., Maxwell R.M.; *Environ. Geo.*, (2002) **42**,235–247.

36. National Securities Technologies, Nevada Test site report environmental report summery, US department of energy, Nevada Test site; Nevada, USA, (2008).

37. Smith D. K, Finnegan D. L, Bowen S. M; *J. Environ. Radio.* (2003) **67**, 35-51.

38. Nikipelov B. V., Romanov G. N., Buldakov L. A., Babaev N. S., Kholina Y. B. and Mikerin E. I., Accident in the Southern Urals on 29 September 1957, International Atomic Energy Agency, Vienna, Austria, (1989).

39. Smith J.T.; Chapter 3: Nuclear Accidents in Nuclear power and the Environment, (2011), 57 – 81.

40. Hu Qin-Hong, Weng Jian-Qing, Wang Jin-Sheng; *J Environ. Radio.,* (2010) **101**(6), 426-437.

41. Renshaw J. C., Lloyd J. R, Livens F. R., *Comptes Rendus Chimie*, (2007) **10**, 1067-1077.

42. Abdelouas A.; *Elements* (2006) **2**, 335-341.

43. Morris K., Raiswell R., in Interactions of Microorganisms with Radionuclides, ed. M. Keith-Roach J., Livens F. R., Elsevier, London, UK, (2002), 101.

44. McKenzie H., McCord J., Groundwater Annual Report Sellafield Ltd, Cumbria, UK, (2009).

45. Banaszak J. E., Rittmann B. E., Reed D. T., *J. Radioanal. Nucl. Chem.,* (1999) **241**, 385-435.

46. Webb G. A. M., Anderson R. W., Gaffney M. J. S., *J. Radiol. Prot.,* (2006) **26**, 33-50.

47. Van Der Stricht S., Janssens A., Radioactive Effluents from Nuclear Power Stations and Nuclear Fuel Reprocessing Sites in the European Union, 1999–2003, European Commission Directorate-General for Energy and Transport, Luxembourg, (2005).
48. Landa E. R.,*J. Environ. Radioact.*, (2004) **77**, 1-27.
49. Mudd G. M.,*J. Environ. Radioact., (*2008) **99**, 288-315.
50. Rozanski K., Froehlich K., *IAEA Bulletin*, (1996) **38**, 9-15.
51. IAEA, Naturally occurring radioactive material (NORM V), in Proceedings of the Fifth International Symposium on Naturally Occurring Radioactive Material, IAEA, Seville, Spain, (2007).
52. Michalik B.,*J. Environ. Monitor.*, (2009) **11**, 1825-1833.
53. Othman I., Al-Masri M. S., *Appl. Radiat. Isot*., (2007) **65**, 131-141.
54. Betti, M., De Las Heras, L.A., Janssens, A., Henrich, E., Hunter, G., Gerchikov, M., Dutton, M., Van Weers, A.W., Nielsen, S., Simmonds, J. and Bexon, A., J. *Environ. Radioact.,* (2004) **74**, 255-277.
55. Papastefanou C., *J. Environ. Radioact*., (2010) **101**, 191-200.
56. Flues, M., Moraes, V. and Mazzilli, B.P., *J. Environ. Radioact.,* (2002) **63**, 285-294.
57. National Cancer Institute, Radon Cancer, https://www.cancer.gov/about-cancer/causes-prevention/risk/substances/radon/radon-fact-sheet, (July 2018).
58. P. D. Wilson, The Nuclear Fuel Cycle – From Ore to Waste, Oxford University Press, Oxford, UK, (1996).
59. J. R. Lloyd and L. E. Macaskie, in Environmental Microbe-Metal Inter-actions, ed. D. R. Lovley, ASM Press, Washington DC, USA, (2000), p.277.
60. Koch-Steindl, H., Pröhl, G, *Radiat. Environ. Biophys*., (2001) **40**, 93-104.
61. Lloyd J. R., Renshaw J. C., in Metal Ions In Biological Systems, ed. Sigel A., Sigel H., Sigel R. K. O., Taylor & Francis, Boca Raton, FL, USA, (2005), p.205

62. Siegel M. D., Bryan C. R., in Treatise on Geochemistry Volume 9: Environmental Geochemistry, ed. B. S. Lollar, Elsevier, Oxford, UK, (2003), p.205.
63. Lieser K. H., in Nuclear and Radiochemistry, ed. Lieser K. H., Wiley-VCH, Weinheim Germany, (2001), p.395.
64. Collins, R.N. and Kinsela, A.S., *Chemosphere*, (2010) **79**, 763-771.
65. Brooks, S.C., Taylor, D.L., Jardine, P.M.*Geochim. Cosmochim. Acta* , (1996) **60** , 1899-1908.
66. Salbu, B., Lind, O.C., Skipperud, L., *J. Environ. Radioact.,* (2004) **74**, 233-242.
67. Beck, H.L., Bennett, B.G., *Health Phys*., (2002) **82**, 591-608.
68. UNEP, Depleted Uranium in Serbia and Montenegro: Post-conflict Environmental Assessment in the Federal Republic of Yugoslavia , United Nations Environment Programme, Geneva, Switzerland, (2002).
69. UNEP, Depleted Uranium in Kosovo: Post-conflict Environmental Assessment , United Nations Environment Programme, Geneva, Switzerland, (2001).
70. UNEP, Depleted Uranium in Bosnia & Herzegovina: Post-conflict Environmental Assessment , United Nations Environment Programme, Geneva, Switzerland, (2003).
71. Brown G. E., Foster A. L., Ostergren J. D.,*Proc. Natl. Acad. Sci.*U. S. A., (1999) **96**, 3388-3395.
72. Warren L. A., Haack E. A.,*Earth Sci. Rev*., (2001) **54**, 261–320.
73. Waychunas G. A., Kim C. S., Banfield J. F.,*J. Nanopart. Res*., (2005) **7**, 409-433.
74. Utsunomiya A. S., Geipel G., Ewing R. C., Baumann N., Brendler V., *Environ. Sci. Technol*., (2006) **40**, 4646-4652.
75. Singer D. M., Maher K., Brown G. E., *Geochim. Cosmochim. Acta,* (2009) **73** , 5989-6007.
76. Lieser K. H*., Radiochim. Acta*, (1995) **70**, 355-375.

77. Langley S., Gault A. G., Ibrahim A., Takahashi Y., Renaud R., Fortin D., Clark I. D., Ferris F. G., *Environ. Sci. Technol.,* (2009) **43**, 1008-1014.

78. Sahai N., Carroll S. A., Roberts S., O'Day P. A., *J. Colloid Interface Sci.,* (2000) **222**, 198-212.

79. Parkman R. H., Charnock J. M., Livens F. R., Vaughan D. J., *Geochim. Cosmochim. Acta*, (1998) **62**, 1481-1492.

80. McKinley J. P., Zachara J. M., Heald S. M., Dohnalkova A., Newville M. G.,Sutton S. R., *Environ. Sci. Technol.,* (2004) **38**, 1017-1023.

81. Koning A. de, Konoplev A. V., Comans R. N. *J.Appl. Geochem.*, (2007) **22**, 219-229.

82. Bostick B. C., Vairavamurthy M. A., Karthikeyan K. G., Chorover J.,*Environ. Sci. Technol.*, (2002) **36**, 2670-2676.

83. Hinton T. G., Kaplan D. I., Knox A. S., Coughlin D. P., Nascimento R. V., Watson S.I., Fletcher and D.E., Koo B.J., *Environ. Sci. Technol.* , (2006) **40**, 4500-4505.

84. Geckeis H., Lutzenkirchen J., Polly R., Rabung Th., Schmidt M.,*Chem. Rev.,* (2013) **113**, 1016-1062.

85. Engineered Barrier Systems and the Safety of Deep Geological Repositories: State-of-the-art Report, Nuclear Energy Agency Organisation for Economic Co-Operation and Development, OECD 2003, ISBN 92-64-18498-8, in co-operation with the European Commission EUR 19964, (2003), EN.

86. Nadeau P. H., Bain, D. C.,*Clays Clay Miner.* (1986) **34**, 455–464.

87. Pusch R., *Nuclear Engineering and Technology*, (2006) **38**, 483-488.

88. Steefel C., Rutqvist J., Tsang C.-F., Liu H.-H., Sonnenthal E., Houseworth J., Birkholzer J., Reactive transport and coupled THM processes in engineering barrier systems (EBS), LBNL Report, (2010).

89. Fan Q.H., Tan X.L., Li J.X., Wang X.K., Wu W.S.,Montavon G., *Environ. Sci. Technol.*, (2009) **43**, 5776-5782.

90. Tan X., Fang M.,Wang X., *Molecules*, (2010) **15**, 8431-8468.

91. Denecke M.A., *Coord. Chem. Rev*., (2006) **250**, 730-754.

92. Von Z., A., Bemtgen J.M., *Inorg. Chem.,* (1982) **21**, 1771-1777.

93. Matsuda T., Yamanaka C., Ikeya M, *Adv. EPR Appl*., (2002) **18**, 217-220.

94. Matsuda T., Yamanaka C., Ikeya M., *Radiat. Meas*., (2003) **37**, 371-375.

95. Matsuda T., Yamanaka C., Ikeya M., *Appl. Radiat. Isot*., (2005) **62**, 353-357.

96. Kowal-Fouchard A., Drot R., Simoni E., Marmier N., Fromage F., Ehrhardt J.J., *New J. Chem*., (2004) **28**, 864-869.

97. Bryan N.D., Abrahamsen L., Evans N., Warwick P., Buckau G., Weng L., Van Riemsdijk, W.H.,*Applied geochemistry*, (2012) **27**, 378-389.

98. Choppin, G. R. Role of humics in actinide behavior in ecosystem, in: Chemical Separation technologies and related methods of nuclear waste management (Eds.) G.R. Choppin and M.Kh Khankhasayev, Kluwer Academic Publishers , Dordrecht, (1999) 247-260.

99. Stevenson F. J., Humus Chemistry Genesis, Composition, Reactions, Wiley Interscience Publication, New York, (1982) , p. 221.

100. Steinberg C.E., Kamara S., Prokhotskaya V.Y., Manusadžianas L., Karasyova T.A., Timofeyev M.A., Jie Z., Paul A., Meinelt T., Farjalla V.F., Matsuo A.Y.,*Freshwater Biol*., (2006) **51**, 1189-1210.

101. Sutton R., Sposito G.,*Environ. Sci. Technol.,* (2005) **39**, 9009-9015.

102. Reiller P.E., Evans N.D., Szabo G., *Radiochim. Acta*, (2008) **96**, 345-358.

103. Keepax R. E., Jones D. M., Pepper S. E., Bryan N. D., in Interactions of Microorganisms with Radionuclides, ed. Keith-Roach M. J., Livens F. R., Elsevier, London, UK, (2002), p.143.

104. Nash K., Fried, S., Friedman, A.M.,Sullivan, J.C., *Environ. Sci.Technol.,*(1981) **15**, 834-837.

105. Silva R.J., Nitsche H.,*Radiochim. Acta*, (1995) **70(s1)**, 377-396.

106. Runde W.H., *Los Alamos Science* , (2000) **26**, 392-411.

107. Choy C.C., Korfiatis G.P., Meng X.*, J. Hazard. Mater.*, (2006) **136**, 53-60.

108. Brookins D. G., Eh-pH Diagrams for Geochemistry , Springer-Verlag, Berlin, Germany, (1988).

109. Wang P., Anderko A.,Turner D. R., *Industrial and Engineering Chemical Research* (2001) **40**, 4428–4443.

110. Payne T.E., Brendler V., Ochs M., Baeyens B., Brown P.L., Davis J.A., Ekberg C., Kulik D.A., Lutzenkirchen J., Missana T., Tachi Y.,*Environmental Modeling and Software*, (2013) **42**, 143-156.

111. Stumm W., Chemistry of the Solid Water Interface. Processes at the Mineral-Water and Particle Water Interface in Natural Systems. Wiley-interscience Publication,Chapter 3, (1992), p 43.

112. Dähn R., Baeyens B., Bradbury M.H.,*Geochimica et Cosmochimica Acta*, (2011) **75,** 5154–5168

113. Davis J.A., Coston J.A., Kent D.B., Fuller C.C.,. *Environ. Sci. Technol.* (1998) **32**, 2820-2828.

114. Davis J.A., Ochs M., Olin M., Payne T.E., Tweed C.J., NEA Sorption Project Phase II. Interpretation and Prediction of Radionuclide Sorption onto Substrates Relevant for Radioactive Waste Disposal Using Thermodynamic Sorption Models. OECD, (2005), p. 5992.

115. Srinivasan, N., Nadkarni, M.N., Balasubramanian, G.R., Chitnis R.T., Siddiqui, H.R. (1972). *Pilot plant for separation of U-233 at Trombay*, BARC Report, Report-643, Bhabha Atomic Research Centre, Mumbai, India.

116. Rattan S.S., Reddy A.V.R., Mallapurkar V.S., Singh R.J, Prakash S., *J. Radioanal. Nucl.Chem.* (1981) **67**, 95-99.

117. Sill C.W.,*Anal. Chem.* (1966) **38**, 802-804.

118. McDowell W. J., "*Organic scintillators and liquid scintillation counting*", Horrocks D.L., Peng L.T. (Eds.), Academic Press, Inc., New York (1971) 937.

119. Ihle H., Karayannis M.,urrenhoff A., "*Organic scintillators and liquid scintillation counting*", Horrocks D.L., Peng L.T. (Eds.), Academic Press, Inc., New York (1971) 879.

120. Jenkins 1988:6; http://archaeometry.missouri.edu/ xrf_overview.html

121. http://www.rsc.org/membership/networking/interestgroups/mossbauerspect/intropart1.asp

122. Murad, E., Properties and behavior of iron oxides as determined by Mossbauer spectroscopy. In: Stucki, J.W., Goodman, B.A., Schwertmann, U. (Eds.), Iron in Soils and Clay Minerals, (1988), 309-350.

123. Matsnev M.E., Rusakov V.S., *AIP Conf. Proc.* (2012) **1489**, 178-185.

124. Altmaier M., Metz V., Neck V., Muller R., Fanghanel Th, *Geochim. Cosmochim. Acta* (2003) **67**, 3595-3601.

125. Bond D.L., Davis J.A., Zachara J.M.,. Uranium(VI) release from contaminated vadose zone sediments: estimation of potential contributions from dissolution and desorption. In: Barnett M.O., Kent D.B. (Eds.), Adsorption of Metals to Geomedia. II: Variables, Mechanisms, and Model Applications. Elsevier,(2008).

126. Kent D.B., Abrams R.H., Davis J.A., Coston J.A., Leblanc D.R.,(2000) **36**(12), 3411-3425.

127. Guillaumont R., Fanghanel T., Neck V., Fuger J., Palmer D.A., Grenthe I., Rand M.H.,. Update on the Chemical Thermodynamics of Uranium, Neptunium, Plutonium, Americium and Technecium. OECD Nuclear Energy Agency, Amsterdam, The Netherlands (Chemical Thermodynamics), (2003).

128. Moore D.M., Reynolds R.C., X-Ray Diffraction and the Identification and Analysis of Clay Minerals. Oxford University Press, (1997).

129. Bish D.L., Post J.E., (1993) **78**, 932-940.

130. Menil F.,*J. Phys. Chem. Solids,* (1985) **46**, 763-789.

131. Morup S., Knudsen J.E., *J. Phys. C: solid state physics,* (1985) **18**, 2943.

132. Vandenberghe R.E., De Grave E., De Geyter G., Landuydt C.,*Clays Clay Minerals* (1986) **34**, 275 -280.

133. Nininger J., Schroeer D., *J. Phys. Chem. Solids* (1978) **39**, 137-144.

134. Farmer V.C. (Ed.), The Infrared Spectra of Minerals. Mineralogical Society of Great Britain and Ireland (1974).

135. Madejová J., Komadel P., *Clays and Clay Miner.* (2001) **49**, 410–432.

136. Madejová J., Komadel P., Information available from infrared spectra of the fine fractions of bentonites. Clay Miner. Soc., Aurora, Colo. (2005) **13**, 65–98.

137. Russell J.D., Fraser A.R., Infrared methods, in: Wilson, M.J. (Ed.), Clay Mineralogy: Spectroscopic and Chemical Determinative Methods. Springer Netherlands, Dordrecht, (1994), 11–67.

138. Zviagina B.B., McCarty D.K., Środoń J., Drits V.A., *Clays and Clay Miner*. (2004) **52**, 399–410.

139. Brindley G.W., B.G., Crystal Structures of Clay Minerals and Their X-ray Identification (1980), 305-360.

140. Plançon A., Zacharie C., *Clay Min.* (1990) **25**, 249–260.

141. Kyllonen J., Hakanen M., Lindberg A., Harjula R., Vahkamaki M., Lehto J., Radiochim. Acta (2014) **102**, 919–929.

142. Mohamedharoonbasha A., Chandramohan R., *J. Pure Appl. & Ind. Phys*. (2012) **2**(3), 234-240.

143. Neaman A., Pelletier M., Villieras F., *Appl. Clay Sci*. (2003) **22**, 153–168.

144. Deng L., Yuan P., Liu P., Annabi-Bergaya F., Zhou J., Chen F., Liu Z., *Appl. Clay Sci*., (2017) **143**, 184–191.

145. Fernández A.M., Baeyens B., Bradbury M., Rivas P., *Phys. Chem. Earth,* (2004) **29**, 105–118.

146. Duc, M., Gaboriaud, F., Thomas, F.J. *Colloid Interface Sci*., (2005) **289**, 139-147.

147. Westall J., FITEQL User Guide. A computer programme for the determination of chemical equilibrium constants from experimental data Version 4.0, Oregon, USA, January 1999, (1999).

148. https://www.world-nucler.org &https://www.wise-uranium.org

149. Kowal-Fouchard A., Drot R., Simoni E., Ehrhardt J. J., *Environ. Sci. Technol*., (2004) **38**, 1399–1407.

150. Boult K. A., Cowper M. M., Heath T. G., Sato H., Shibutani T., Yui M., *J. Contaminant Hydrology* (1998) **35**, 141–150.

151. Bachmaf S., Merkel Broder J, *Environ. Earth Sci.,* (2011) **63**, 925–934.

152. Saini R. D., Bhattacharyya P. K., Iyer R. M., *J. Photochem. Photobio. A,* (1989) **47**, 65–81.

153. Günther A., Steudtner R., Schmeide K., Bernhard G.,. *Radiochim. Acta* (2011) **99**, 535–541.

154. Sachs S., Brendler V., Geipel G., *Radiochim. Acta* (2007) **95**, 103–110.

155. Krepelov A., Sachs S., Bernhard G.,. *Radiochim. Acta* (2006) **94**, 825–833.

156. Nozik Yu. Z., Kuznetsov L. M., *Kristallografiya* (1990) **35**, 1563–1564.

157. Howatson J., Grev D. M., Morosin B., *J. Inorg. Nucl. Chem*. (1975) **37**,1933–1935.

158. Allen P. G., Bucher J. J., Shuh D. K., Edelstein N. M., Reich T., *Inorg. Chem.*(1997) **36**, 4676–4683.

159. Dent A. J., Ramsay J. D. F., Swanton S. W., *J. Colloid Interface Sci*. (1992) **150**, 45–60.

160. Demartin F., Gramaccioli C. M., Pilati T. *Acta Crystallogr. C,*(1992) **48**, 1–4.

161. Catalano J. G., Brown G. E. Jr. *Geochim. Cosmochim. Acta,* (2005) **69**, 2995–3005.

162. Sylwester E. R., Hudson E. A., Allen P. G., *Geochim. Cosmochim. Acta,* (2000) **64**, 2431–2438.

163. Kucherov A.V., Lakeev S.G., Shelef M., *Appl. Catal., B*, (1998) **16**, 245-254.

164. Marcussen H., Holm P.E., Strobel B.W., Hansen H.C.B., *Environ. Sci. Technol.*, (2009) **43**, 1122-1127.

165. Baik M.H., Cho W.J., Hahn P.S., *Environ. Eng. Res.,* (2004) **9**, 160-167.

166. Atun G., Bilgin B., Mardinli A., *J. Radioanal. Nucl. Chem.* (1996) **211**, 435–442.

167. Saeed M.M., Hasany S.M., Ahmed M., *Talanta,* (1999) **50**, 625–634.

168. Kielland J., *J. Am. Chem. Soc.,* (1937) **59**, 1675–1678.

169. Mulyutin V. V., Gelis V. M., Nekrasova N. A., Kononenko O. A., Vezentsev A. I., Volovicheva N. A., Korol'kova S. V., *Radiochemistry* (2012) **54**, 75–78.

170. Kasar S., Kar A. S., Kumar, S., Pente, A. S., Kaushik, C. P., Bajpai, R. K., Tomar, B. S.: Sorption of Cs(I) and Sr(II) on smectite rich clay. In: *Proceedings of Nuclear and Radiochemistry Symposium*, NUCAR-2013, held at Jabalpur, India during February 19–23, (2013), 581–582.

171. Dmitriev S. A., Barinov A. S., Kuptsov V.M.,. *Radiochemistry* (2011) **53**, 437–442.

172. Dmitriev S. A., Barinov A. S., Kuptsov V.M., *Radiochemistry* (2011) **53**, 443–448.

173. Fan Q. H., Xu J. Z., Niu Z.W., Li P., Wu W. S., *Appl. Radiat. Isotopes*, (2012) **70**, 13–19.

174. Holleman A. F.,Wiberg E.. Die Actinoide, *Lehrbuch der Anorganischen Chemie*, de Gruyter, Chapter 36,(2007),1948–1976.

175. Yoshida Z., Johnson S. G., Kimura T., Krsul J. R. Neptunium, *in* L. R. Morss, N. M. Edelstein and J. Fuger (eds), *The Chemistry of the Actinide and Transactinide Elements, Third Edition*, Springer, Chapter 6,(2006), 699–812.

176. Albright D., Kramer K., Neptunium 237 and americium: World inventories and proliferation concerns, *Global stocks of nuclear explosive material*, Institute for Science and International Security (ISIS), Washington, D.C., Chapter 10 (2005).

177. Clark, D. L., Hobart, D. E. and Neu, M. P, *Chemical Reviews*, (1995) **95**: 25–48.

178. Gutowski K. E., Bridges N. J., Rogers R. D. Actinide structural chemistry, *in* Morss L. R., Edelstein N. M., Fuger J. (eds), *The Chemistry of the Actinide and Transactinide Elements, Third Edition*, Springer,Chapter 22, (2006) 2380–2523.

179. Lemire R. J., Fuger J., Nitsche H., Potter P., Rand M. H., Rydberg J., Spahiu K., Sullivan J. C., Ullman W. J., Vitorge P., Wanner H., *Chemical Thermodynamics of Neptunium and Plutonium*, Vol. 4 of *Chemical Thermodynamics Series*, Elsevier, OECD Nuclear Energy Agency, (2001).

180. Loveland W. D., Morrissey D. J. and Seaborg G. T., *Modern Nuclear Chemistry*, John Wiley & Sons Inc., (2006).

181. Konings R. J. M., Morss L. R., Fuger J. Thermodynamic properties of actinides and actinide compounds, *in* Morss L. R., Edelstein N. M., Fuger J. (eds), *The Chemistry of the Actinide and Transactinide Elements, Third Edition*, Springer, Chapter 19, (2006), 2113–2224.

182. Lieser K. H., Mühlenweg U., *Radiochimica Acta,* (1988) **43**, 27–36.

183. Allard B., Olufsso, U., Torstenfelt B., *Inorganica Chimica Acta,* (1984) **94**, 205–221.

184. Bradbury M.H., Baeyens B.,*Appl. Clay Sci.,* (2011) **52**, 27-33.

185. Goldberg S., Criscenti L.J., Turner D.R., Davis J.A., Cantrell K.J., *Vadose Zone J.* (2007) **6**, 407-435.

186. Benedicto A., Begg J.D., Zhao P., Kersting A.B., Missana T., Zavarin M., *Appl. Geochem.* (2014) **47**,177 -185.

187. Zavarin M., Powell B.A., Bourbin M., Zhao P., Kersting A.B.,. *Environ. Sci. Technol.* (2012) **46**, 2692-2698.

188. Kozai N., Ohnuko T., Matsumoto J., Banba T., Ito Y., *Radiochim. Acta* (1996) **75**, 149-158.

189. Rabung T., Pierret M.C., Bauer A., Geckeis H., Bradbury M.H., Baeyens B., *Geochem. Cosmochim. Acta* (2005) **69**, 5393–5402.

190. Bradbury M.H., Baeyens B., *J. Cont. Hydrol.* (1997) **27**, 223-248.

191. Tachi Y., Ochs M., Suyama T., J. Nucl. Sci. Technol. (2014) **51**, 1177-1190.

192. Bradbury M.H., Baeyens B., *Radiochim. Acta,* (2006) **94,** 619-625.

193. Kohler M., Honeyman B.D., Leckie J.O., *Radiochim. Acta*.,(1999) **85***,* 33-48.

194. Muller K., Groschel A., Rossberg A., Bok F., Franzen C., Brendler V., Foerstendorf H., *Environ. Sci. Technol.*, (2015) **49**, 2560-2567.

195. Romanchuk A.Yu, Kalmykov S.N., *Radiochim. Acta* (2014) **102**, 303-310.

196. Gracheva N.N., Romanchuk A.Y., Smirnov E.A., Meledina M.A., Garshev A.V., Shirshin E.A., Fadeev V.V., Kalmykov S.N., *Appl. Geochem.,* (2014) **42**, 69-76.

197. Fröhlich D.R.,.*Clays and Clay Miner.* (2015) **63**, 262–276.